Women claim discrimination at NIH's child health institute p. 21

Emotions in the faces of mice pp. 33 & 89

Hominin genera in South Africa 2 million years ago pp. 34 & 47

Science

$15
3 APRIL 2020
sciencemag.org

AAAS

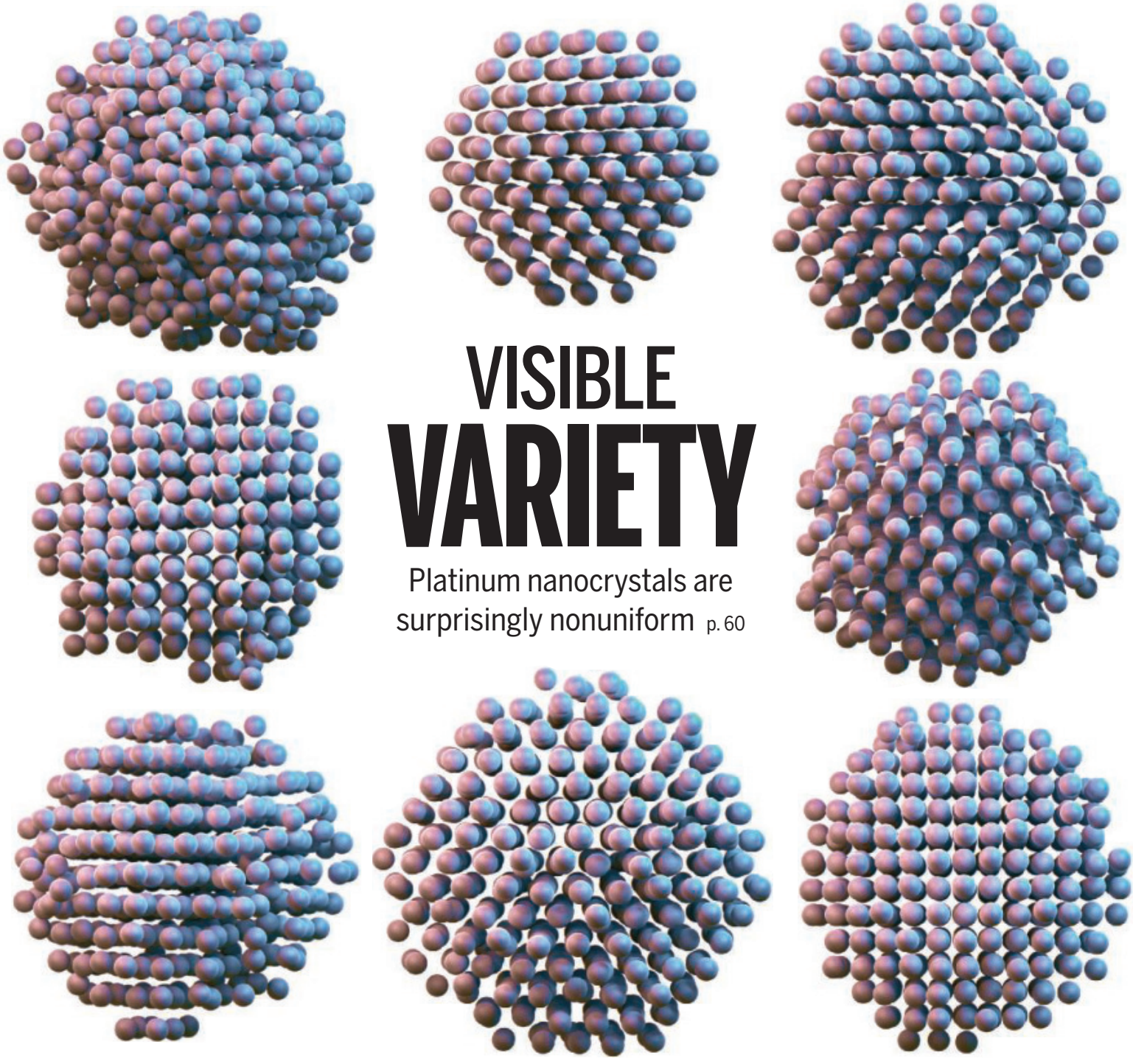

VISIBLE VARIETY

Platinum nanocrystals are surprisingly nonuniform p. 60

2019 Cozzarelli Prize

Please join us in congratulating the recipients of the 2019 Cozzarelli Prize!

Awarded annually to six PNAS articles, one in each of the National Academy of Sciences' six broadly defined scientific classes, this year's winners represent exceptional scientific achievement, originality, and innovation in their fields.

The 2019 Cozzarelli Prize–winning papers are:

PHYSICAL AND MATHEMATICAL SCIENCES

The end of ice I, Daniel R. Moberg, Daniel Becker, Christoph W. Dierking, Florian Zurheide, Bernhard Bandow, Udo Buck, Arpa Hudait, Valeria Molinero, Francesco Paesani, and Thomas Zeuch

BIOLOGICAL SCIENCES

Mosaic origin of the eukaryotic kinetochore, Eelco C. Tromer, Jolien J. E. van Hooff, Geert J. P. L. Kops, and Berend Snel

ENGINEERING AND APPLIED SCIENCES

Mechanics unlocks the morphogenetic puzzle of interlocking bivalved shells, Derek E. Moulton, Alain Goriely, and Régis Chirat

BIOMEDICAL SCIENCES

Widespread soil bacterium that oxidizes atmospheric methane, Alexander T. Tveit, Anne Grethe Hestnes, Serina L. Robinson, Arno Schintlmeister, Svetlana N. Dedysh, Nico Jehmlich, Martin von Bergen, Craig Herbold, Michael Wagner, Andreas Richter, and Mette M. Svenning

BEHAVIORAL AND SOCIAL SCIENCES

Bioarchaeology of Neolithic Çatalhöyük reveals fundamental transitions in health, mobility, and lifestyle in early farmers, Clark Spencer Larsen, Christopher J. Knüsel, Scott D. Haddow, Marin A. Pilloud, Marco Milella, Joshua W. Sadvari, Jessica Pearson, Christopher B. Ruff, Evan M. Garofalo, Emmy Bocaege, Barbara J. Betz, Irene Dori, and Bonnie Glencross

APPLIED BIOLOGICAL, AGRICULTURAL, AND ENVIRONMENTAL SCIENCES

Economics of the disintegration of the Greenland ice sheet, William Nordhaus

Visit **pnas.link/cozzarelli** to learn more.

PNAS
www.pnas.org

The Cozzarelli Prize

CONTENTS

3 APRIL 2020 • VOLUME 368 • ISSUE 6486

21

NEWS

IN BRIEF

IN DEPTH

FEATURES

INSIGHTS

LETTERS

PERSPECTIVES

POLICY FORUM

BOOKS *ET AL.*

ILLUSTRATION: STEFANIA INFANTE

UNDERSTANDING DYNAMIC ECOSYSTEMS

AAAS | ANNUAL MEETING
Phoenix, AZ | February 11–14, 2021

Join us in Phoenix!

We are embedded in a variety of ecosystems, including the environments that we inhabit and the many social systems in which we live and work. Finding ways of maintaining the stable balance of these ecosystems in the face of rapidly changing circumstances is critical for our advancement. Drawing on a multitude of scientific perspectives, this Annual Meeting seeks to feature diverse ways of understanding the complexities and dynamics of biological, physical, social, and economic systems across scales, as well as strengthening and activating new connections to address underlying problems in various spheres.

SESSION PROPOSAL DEADLINE EXTENDED!

Session proposals for the 2021 AAAS Annual Meeting are now being accepted through **July 14, 2020.**

aaas.org/meetings

Excavations in the Drimolen quarry in South Africa have yielded several distinct, contemporaneous hominin species fossils from 2 million years ago.

RESEARCH

IN BRIEF

REVIEW

RESEARCH ARTICLES

REPORTS

DEPARTMENTS

ON THE COVER

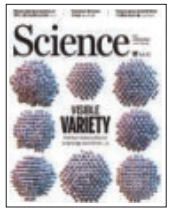

A selection of three-dimensional (3D) atomic structures of platinum nanocrystals in solution. Transmission electron microscopy images of individual rotating nanocrystals were reconstructed to generate the 3D density maps. The resultant atomic structures represent the intrinsic structural heterogeneity of ligand-protected nanocrystals synthesized in a single batch. See page 60. *Illustration: Younghee Lee*

PHOTO: ANDY HERRIES

SCIENCE (ISSN 0036-8075) is published weekly on Friday, except last week in December, by the American Association for the Advancement of Science, 1200 New York Avenue, NW, Washington, DC 20005. Periodicals mail postage (publication No. 484460) paid at Washington, DC, and additional mailing offices. The title SCIENCE is a registered trademark of the AAAS. Domestic individual membership, including subscription (12 months): $165 ($74 allocated to subscription). Domestic institutional subscription (51 issues): $2148; Foreign postage extra: Air assist delivery: $98. First class, airmail, student, and emeritus rates on request. Canadian rates with GST available upon request, GST #125488122. Publications Mail Agreement Number 1069624. **Printed in the U.S.A.**
Change of address: Allow 4 weeks, giving old and new addresses and 8-digit account number. **Postmaster:** Send change of address to AAAS, P.O. Box 96178, Washington, DC 20090–6178. **Single-copy sales:** $15 each plus shipping and handling available from backissues.sciencemag.org; bulk rate on request. **Authorization to reproduce** material for internal or personal use under circumstances not falling within the fair use provisions of the Copyright Act can be obtained through the Copyright Clearance Center (CCC), www.copyright.com. The identification code for *Science* is 0036-8075. *Science* is indexed in the *Reader's Guide to Periodical Literature* and in several specialized indexes.

Science AAAS

Editor-in-Chief Holden Thorp, hthorp@aaas.org

Executive Editor Monica M. Bradford

Editors, Research Valda Vinson, Jake S. Yeston **Editor, Insights** Lisa D. Chong

DEPUTY EDITORS Julia Fahrenkamp-Uppenbrink (UK), Stella M. Hurtley (UK), Phillip D. Szuromi, Sacha Vignieri **SR. EDITORIAL FELLOW** Andrew M. Sugden (UK) **SR. EDITORS** Gemma Alderton (UK), Caroline Ash (UK), Brent Grocholski, Pamela J. Hines, Paula A. Kiberstis, Marc S. Lavine (Canada), Steve Mao, Ian S. Osborne (UK), Beverly A. Purnell, L. Bryan Ray, H. Jesse Smith, Keith T. Smith (UK), Jelena Stajic, Peter Stern (UK), Valerie B. Thompson, Brad Wible, Laura M. Zahn **ASSOCIATE EDITORS** Michael A. Funk, Priscilla N. Kelly, Tage S. Rai, Seth Thomas Scanlon (UK), Yury V. Suleymanov **LETTERS EDITOR** Jennifer Sills **LEAD CONTENT PRODUCTION EDITORS** Harry Jach, Lauren Kmec **CONTENT PRODUCTION EDITORS** Amelia Beyna, Jeffrey E. Cook, Chris Filiatreau, Julia Katris, Nida Masiulis, Suzanne M. White **SR. EDITORIAL COORDINATORS** Carolyn Kyle, Beverly Shields **EDITORIAL COORDINATORS** Aneera Dobbins, Joi S. Granger, Jeffrey Hearn, Lisa Johnson, Maryrose Madrid, Ope Martins, Shannon McMahon, Jerry Richardson, Alana Warnke, Alice Whaley (UK), Anita Wynn **PUBLICATIONS ASSISTANTS** Jeremy Dow, Alexander Kief, Ronmel Navas, Hilary Stewart (UK), Brian White **EXECUTIVE ASSISTANT** Jessica Slater **ASI DIRECTOR, OPERATIONS** Janet Clements (UK) **ASI SR. OFFICE ADMINISTRATOR** Jessica Waldock (UK)

News Editor Tim Appenzeller

NEWS MANAGING EDITOR John Travis **INTERNATIONAL EDITOR** Martin Enserink **DEPUTY NEWS EDITORS** Elizabeth Culotta, Lila Guterman, David Grimm, Eric Hand (Europe), David Malakoff **SR. CORRESPONDENTS** Daniel Clery (UK), Jon Cohen, Jeffrey Mervis, Elizabeth Pennisi **ASSOCIATE EDITORS** Jeffrey Brainard, Catherine Matacic **NEWS REPORTERS** Adrian Cho, Jennifer Couzin-Frankel, Jocelyn Kaiser, Kelly Servick, Robert F. Service, Erik Stokstad, Paul Voosen, Meredith Wadman **INTERNS** Eva Frederick, Rodrigo Perez Ortega **CONTRIBUTING CORRESPONDENTS** Warren Cornwall, Ann Gibbons, Mara Hvistendahl, Sam Kean, Eli Kintisch, Kai Kupferschmidt (Berlin), Andrew Lawler, Mitch Leslie, Eliot Marshall, Virginia Morell, Dennis Normile (Shanghai), Elisabeth Pain (Careers), Charles Piller, Michael Price, Tania Rabesandratana (Barcelona), Emily Underwood, Gretchen Vogel (Berlin), Lizzie Wade (Mexico City) **CAREERS** Donisha Adams, Rachel Bernstein (Editor), Katie Langin (Acting Editor) **COPY EDITORS** Julia Cole (Senior Copy Editor), Cyra Master (Copy Chief) **ADMINISTRATIVE SUPPORT** Meagan Weiland

Creative Director Beth Rakouskas

DESIGN MANAGING EDITOR Marcy Atarod **GRAPHICS MANAGING EDITOR** Alberto Cuadra **PHOTOGRAPHY MANAGING EDITOR** William Douthitt **WEB CONTENT STRATEGY MANAGER** Kara Estelle-Powers **SENIOR DESIGNER** Chrystal Smith **DESIGNER** Christina Aycock **GRAPHICS EDITOR** Nirja Desai **INTERACTIVE GRAPHICS EDITOR** Xing Liu **SENIOR SCIENTIFIC ILLUSTRATORS** Valerie Altounian, Chris Bickel **SCIENTIFIC ILLUSTRATOR** Alice Kitterman **SENIOR GRAPHICS SPECIALISTS** Holly Bishop, Nathalie Cary **SENIOR PHOTO EDITOR** Emily Petersen **PHOTO EDITOR** Kaitlyn Dolan

Chief Executive Officer and Executive Publisher Sudip Parikh

Publisher, Science Family of Journals Bill Moran

DIRECTOR, BUSINESS SYSTEMS AND FINANCIAL ANALYSIS Randy Yi **DIRECTOR, BUSINESS OPERATIONS & ANALYSIS** Eric Knott **DIRECTOR OF ANALYTICS** Enrique Gonzales **MANAGER, BUSINESS OPERATIONS** Jessica Tierney **SENIOR BUSINESS ANALYST** Cory Lipman, Meron Kebede **FINANCIAL ANALYST** Alexander Lee **ADVERTISING SYSTEM ADMINISTRATOR** Tina Burks **SENIOR SALES COORDINATOR** Shirley Young **DIGITAL/PRINT STRATEGY MANAGER** Jason Hillman **QUALITY TECHNICAL MANAGER** Marcus Spiegler **ASSISTANT MANAGER DIGITAL/PRINT** Rebecca Doshi **SENIOR CONTENT SPECIALISTS** Steve Forrester, Jacob Hedrick, Antoinette Hodal, Lori Murphy **DIGITAL PRODUCTION MANAGER** Lisa Stanford **CONTENT SPECIALIST** Kimberley Oster **ADVERTISING PRODUCTION OPERATIONS MANAGER** Deborah Tompkins **DESIGNER, CUSTOM PUBLISHING** Jeremy Huntsinger **SR. TRAFFIC ASSOCIATE** Christine Hall **SPECIAL PROJECTS ASSOCIATE** Sarah Dhere

ASSOCIATE DIRECTOR, BUSINESS DEVELOPMENT Justin Sawyers **GLOBAL MARKETING MANAGER** Allison Pritchard **DIGITAL MARKETING MANAGER** Aimee Aponte **JOURNALS MARKETING MANAGER** Shawana Arnold **MARKETING ASSOCIATES** Tori Velasquez, Mike Romano, Ashley Hylton **DIGITAL MARKETING SPECIALIST** Asleigh Rojanavongse **SENIOR DESIGNER** Kim Huynh

DIRECTOR AND SENIOR EDITOR, CUSTOM PUBLISHING Sean Sanders **ASSISTANT EDITOR, CUSTOM PUBLISHING** Jackie Oberst

DIRECTOR, PRODUCT & PUBLISHING DEVELOPMENT Chris Reid **DIRECTOR, BUSINESS STRATEGY AND PORTFOLIO MANAGEMENT** Sarah Whalen **ASSOCIATE DIRECTOR, PRODUCT MANAGMENT** Kris Bishop **SR. PRODUCT ASSOCIATE** Robert Koepke **DIGITAL PRODUCT STRATEGIST** Michael Hardesty **SPJ ASSOCIATE** Samantha Bruno Fuller

DIRECTOR, INSTITUTIONAL LICENSING Iquo Edim **ASSOCIATE DIRECTOR, RESEARCH & DEVELOPMENT** Elisabeth Leonard **MARKETING MANAGER** Kess Knight **SENIOR INSTITUTIONAL LICENSING MANAGER** Ryan Rexroth **INSTITUTIONAL LICENSING MANAGER** Marco Castellan **MANAGER, AGENT RELATIONS & CUSTOMER SUCCESS** Judy Lillibridge **SENIOR OPERATIONS ANALYST** Lana Guz **FULFILLMENT COORDINATOR** Melody Stringer **SALES COORDINATOR** Josh Haverlock

DIRECTOR, GLOBAL SALES Tracy Holmes **US EAST COAST AND MID WEST SALES** Stephanie O'Connor **US WEST COAST SALES** Lynne Stickrod **US SALES MANAGER, SCIENCE CAREERS** Claudia Paulsen-Young **US SALES REP, SCIENCE CAREERS** Tracy Anderson **ASSOCIATE DIRECTOR, ROW** Roger Goncalves **SALES REP, ROW** Sarah Lelarge **SALES ADMIN ASSISTANT, ROW** Bryony Cousins **DIRECTOR OF GLOBAL COLLABORATION AND ACADEMIC PUBLISHING RELATIONS, ASIA** Xiaoying Chu **ASSOCIATE DIRECTOR, INTERNATIONAL COLLABORATION** Grace Yao **SALES MANAGER** Danny Zhao **MARKETING MANAGER** Kilo Lan **ASCA CORPORATION, JAPAN** Kaoru Sasaki (Tokyo), Miyuki Tani (Osaka) **COLLABORATION/CUSTOM PUBLICATIONS/JAPAN** Adarsh Sandhu

DIRECTOR, COPYRIGHT, LICENSING AND SPECIAL PROJECTS Emilie David **RIGHTS AND LICENSING COORDINATOR** Jessica Adams **RIGHTS AND PERMISSIONS ASSOCIATE** Elizabeth Sandler **CONTRACTS AND LICENSING ASSOCIATE** Lili Catlett

---

MAIN HEADQUARTERS
Science/AAAS
1200 New York Ave. NW
Washington, DC 20005

SCIENCE INTERNATIONAL
Clarendon House
Clarendon Road
Cambridge, CB2 8FH, UK

SCIENCE CHINA
Room 1004, Culture Square
No. 59 Zhongguancun St.
Haidian District, Beijing, 100872

SCIENCE JAPAN
ASCA Corporation
Sibaura TY Bldg. 4F, 1-14-5
Shibaura Minato-ku
Tokyo, 108-0073 Japan

EDITORIAL
science_editors@aaas.org

NEWS
science_news@aaas.org

INFORMATION FOR AUTHORS
sciencemag.org/authors/science-information-authors

REPRINTS AND PERMISSIONS
sciencemag.org/help/reprints-and-permissions

MEDIA CONTACTS
scipak@aaas.org

MULTIMEDIA CONTACTS
SciencePodcast@aaas.org
ScienceVideo@aaas.org

INSTITUTIONAL SALES AND SITE LICENSES
sciencemag.org/librarian

PRODUCT ADVERTISING & CUSTOM PUBLISHING
advertising.sciencemag.org/products-services
science_advertising@aaas.org

CLASSIFIED ADVERTISING
advertising.sciencemag.org/science-careers
advertise@sciencecareers.org

JOB POSTING CUSTOMER SERVICE
employers.sciencecareers.org
support@sciencecareers.org

MEMBERSHIP AND INDIVIDUAL SUBSCRIPTIONS
sciencemag.org/subscriptions

MEMBER BENEFITS
aaas.org/membercentral

AAAS BOARD OF DIRECTORS
CHAIR Steven Chu
PRESIDENT Claire M. Fraser
PRESIDENT-ELECT Susan G. Amara
TREASURER Carolyn N. Ainslie
CHIEF EXECUTIVE OFFICER Sudip Parikh
BOARD Cynthia M. Beall, Rosina M. Bierbaum, Ann Bostrom, Stephen P.A. Fodor, S. James Gates, Jr., Laura H. Greene, Kaye Husbands Fealing, Maria M. Klawe, Robert B. Millard, Alondra Nelson, William D. Provine

EDITORIAL

This is real

H. Holden Thorp
Editor-in-Chief, *Science* journals.
hthorp@aaas.org;
@hholdenthorp

Last week, we ran what is likely to be one of the most widely read *Science* news stories ever—an interview with Dr. Anthony Fauci, director of the U.S. National Institute of Allergy and Infectious Diseases (NIAID). Fauci was strikingly candid about his desire for extraordinary measures to combat coronavirus disease 2019 (COVID-19), and he was unusually direct about the challenges in getting the administration to see how important it is for the country to maintain social distancing.

Despite the exceptional job they are doing providing factual updates during White House press conferences, Fauci and his accomplished colleague Dr. Deborah Birx have become targets for political attacks from allies of the administration who are not qualified health advisers and don't know what they are talking about. This is unacceptable. Facts about the spread of the virus and its dangerous health and societal consequences are not political. A survey of health officials shows this to be the case.

When I was chancellor of the University of North Carolina (UNC), I was fortunate to work closely with Dr. William Roper, who was then dean of the UNC School of Medicine and the chief executive officer of UNC Health Care. Before we worked together, Bill had done separate stints running the U.S. Centers for Disease Control and Prevention (CDC) and the Centers for Medicare and Medicaid Services in the 1980s and early 1990s during Republican presidencies.

I tracked Bill down in North Carolina, where he is now interim president of the UNC system, to seek his thoughts about the coronavirus crisis and the response of the administration. "I would trust Tony Fauci with my life," he told me. Roper and Fauci worked closely together when Bill ran the CDC and Fauci was already the NIAID's director. Bill disagrees with statements by the current administration that minimize the importance of sustained social distancing. When I asked him when social distancing should end, he said we'll know it's time when the hospitals tell us that they are no longer overwhelmed. Or as Fauci said, "the virus makes the timeline."

> **"...we'll know it's time when the hospitals... are no longer overwhelmed."**

Bill has always been measured in his statements about everything, but he became very exasperated when I asked about the international implications of this political fighting. He talked about a time in the past when the CDC director and Tony Fauci were treated like rock stars abroad, particularly in China, reflecting the respect for U.S. leadership in global health. The nationalism that now has flared up around the White House threatens to undermine the effort to manage a global crisis.

In looking at the papers coming to *Science* and posted on preprint servers, it is clear that the only way we can get a handle on the situation is with international collaboration. The data coming out of Chinese labs studying the virus—how it spreads and the disease that it causes—as well as the findings of Chinese scientists on the ground, are indispensable in finding a solution. That's why the racist labeling of the virus is doubly dangerous. In his interview with *Science*, when Fauci was asked if he would ever call it the "Chinese virus," he simply said, "No."

Bill Roper isn't the only former Republican health official sounding the alarm. Earlier this week, just as President Trump was shifting to messages about accelerating a return to work, his own former director of the Food and Drug Administration, Scott Gottlieb, struck a somber tone. Gottlieb has been an important and vocal advocate of prioritizing public health. He said in a *Wall Street Journal* op-ed on 22 March that "America's coronavirus epidemic is only beginning" and that "COVID-19 can't be allowed to rage through the country untamed."

Still, Fauci, Gottlieb, and Roper all believe that the United States can avoid the worst if it stays focused. Fauci has been pleading for a few more weeks of strong action and reminding people that the pandemic won't last forever. Roper is optimistic that students in the UNC system will return to classes in the fall. And Gottlieb ended his *Wall Street Journal* article by stating, "With the right mix of controlling transmission, expanding testing and deploying promising drugs, American ingenuity can beat back this pathogen."

But they're sober about the short term. I ended my conversation with Roper by asking what message he had for our readers. He was succinct: "This is real."

–H. Holden Thorp

PHOTO: CAMERON DAVIDSON

Published online 27 March 2020; 10.1126/science.abb9223

EDITORIAL

Emerging from AI utopia

A future driven by artificial intelligence (AI) is often depicted as one paved with improvements across every aspect of life—from health, to jobs, to how we connect. But cracks in this utopia are starting to appear, particularly as we glimpse how AI can also be used to surveil, discriminate, and cause other harms. What existing legal frameworks can protect us from the dark side of this brave new world of technology?

Facial recognition is a good example of an AI-driven technology that is starting to have a dramatic human impact. When facial recognition is used to unlock a smartphone, the risk of harm is low, but the stakes are much higher when it is used for policing. In well over a dozen countries, law enforcement agencies have started using facial recognition to identify "suspects" by matching photos scraped from the social media accounts of 3 billion people around the world. Recently, the London Metropolitan Police used the technology to identify 104 suspects, 102 of whom turned out to be "false positives." In a policing context, the human rights risk is highest because a person can be unlawfully arrested, detained, and ultimately subjected to wrongful prosecution. Moreover, facial recognition errors are not evenly distributed across the community. In Western countries, where there are more readily available data, the technology is far more accurate at identifying white men than any other group, in part because it tends to be trained on datasets of photos that are disproportionately made up of white men. Such uses of AI can cause old problems—like unlawful discrimination—to appear in new forms.

"...cracks in this utopia are starting to appear..."

Right now, some countries are using AI and mobile phone data to track people in self-quarantine because of the coronavirus disease 2019 pandemic. The privacy and other impacts of such measures might be justified by the scale of the current crisis, but even in an emergency, human rights must still be protected. Moreover, we will need to ensure that extreme measures do not become the new normal when the period of crisis passes.

It's sometimes said that existing laws in Western countries don't apply in the new world of AI. But this is a myth—laws apply to the use of AI, as they do in every other context. Imagine if a chief executive officer of a company preferred to recruit people of a particular race, unfairly disadvantaging other people, or if a bank offered credit more readily to men than women. Clearly, this is unlawful discrimination. So, why would the legal position be any different if discrimination occurred because these people were similarly disadvantaged by the use of an algorithm?

The laws that many countries already use to protect citizens—including laws that prohibit discrimination—need to be applied more rigorously and effectively in the new technology context. There has been a proliferation of AI ethics frameworks that provide guidance in identifying the ethical implications of new technologies and propose ways to develop and use these technologies for the better. The Australian Human Rights Commission's Human Rights and Technology Discussion Paper acknowledges an important role for ethics frameworks but notes that to date, their practical impact has been limited and cannot be a substitute for applying the law. Although this project has considered how Australia specifically should respond to the challenges of emerging technologies such as AI, the recommendations are general. The Commission sets out practical steps that researchers, government, industry, and regulators should take to ensure that AI is accountable in its development and use. It also suggests targeted reform to fill the gaps that have been exposed by the unprecedented adoption of AI and related technologies. For example, our laws should make crystal clear that momentous decisions—from sentencing in criminal cases to bank loan decisions—cannot be made in a "black box," whether or not AI is used in the decision-making process. And where the risk of harm is particularly severe, such as in the use of facial recognition for policing, the Commission proposes a moratorium in Australia until proper human rights safeguards are in place.

The proposals in the discussion paper are written in pencil rather than ink and are open for public comment until the end of this month (tech.humanrights.gov.au) before the final report is released later this year. AI offers many exciting possibilities and opportunities for humanity, but we need to innovate for good and ensure that what we create benefits everyone.

–Edward Santow

Edward Santow
is Australia's Human Rights Commissioner.
humanrights.commissioner@humanrights.gov.au

10.1126/science.abb9369

CREDITS: (PHOTO) HUMAN RIGHTS COMMISSIONER EDWARD SANTOW © AUSTRALIAN HUMAN RIGHTS COMMISSION; (ILLUSTRATION) WILLIAM DUKE/PHOTO BY DAXIAO PRODUCTIONS/SHUTTERSTOCK

NEWS

Workers build an emergency field hospital in New York City's Central Park for COVID-19 patients.

PHOTO: MARY ALTAFFER/AP PHOTO

IN BRIEF

Edited by **Jeffrey Brainard**

INFECTIOUS DISEASE

A COVID-19 battle on multiple fronts

Scientists raced this week to help patients, save research, navigate obstacles, and counter misinformation.

U.S. bailout may fall short

FUNDING | The $2.2 trillion stimulus package the U.S. Congress approved on 27 March includes $1.25 billion to help federal research agencies combat the COVID-19 pandemic. But the amount for research is far below what will be needed, science advocates say; they plan to seek more money in the next relief bill. For now, the National Institutes of Health will get an additional $945 million to speed development of vaccines and therapies, and the National Science Foundation will receive $76 million more for researchers to pursue new approaches to understanding and coping with the pandemic. The Department of Energy's national laboratories will get an extra $100 million to continue operations. And a $14 billion allocation will help universities cover overall operating costs.

Disease risk dwarfs suicide peril

POLICY | Research contradicts U.S. President Donald Trump's claim on 23 March that suicides from a poor economy would greatly outnumber deaths from the new coronavirus disease. In fact, the microbe could kill nearly 500 times as many Americans as did suicides connected to the 2008 Great Recession, according to researchers at the University of Bristol wrote in a blog reviewing past studies.

Emergency OK for malaria drugs

DRUG DEVELOPMENT | The U.S. Food and Drug Administration this week allowed the use of two antimalarial drugs to treat people hospitalized with COVID-19—despite only anecdotal evidence that either is effective against the illness. President Donald Trump has touted hydroxychloroquine sulfate and chloroquine phosphate as potential treatments. The agency's emergency use authorization allows supplies of the drugs in the Strategic National Stockpile to be distributed to hospitalized patients when a clinical trial is not available or feasible. Sandoz, a division of Novartis, alone donated 30 million doses of hydroxychloroquine sulfate to the stockpile last week for patient care and clinical trials. This is the agency's first such authorization for a drug intended to treat COVID-19.

Polio fight is paused

GLOBAL HEALTH | In an unprecedented move, the Global Polio Eradication Initiative (GPEI) has recommended that countries suspend all polio vaccination campaigns until the second half of this year to help prevent the spread of COVID-19. The decision comes at a bad time: Before that disease surged, polio was on the rise in Afghanistan and Pakistan; so-called vaccine-derived viruses are spreading fast in Africa. The campaign is caught between two "terrible situations," says Michel Zaffran of the World Health Organization, who heads GPEI. It will reassess the timeline as the pandemic evolves.

Hawaii telescopes shut

ASTRONOMY | Telescope operations atop Mauna Kea on Hawaii closed on 29 March as the state ordered residents to stay at home to counter the COVID-19 pandemic. The shutdown is the second in less than 1 year at one of the world's leading observing sites; another was forced last summer by demonstrations over the planned construction of the Thirty Meter Telescope. Some 500 astronomers and support staff members work at the 12 independent observatories on the summit, the *Honolulu Star-Advertiser* reports. A major casualty will be the Event Horizon Telescope, a global array involving one

instrument on Mauna Kea that last year provided the first image of a black hole. Its 2020 campaign has been canceled.

A science task for a rainy day

CITIZEN SCIENCE | "The British love talking about the weather. They also love measuring it." That's the motto of a U.K. research team hoping to lure the public to help a scholarly study while stuck at home sheltering from the COVID-19 virus. Last week, the team asked people to digitize data recorded by hand from about 5500 U.K. rain gauges from the 1820s to the 1950s. Researchers with the Rainfall Rescue project, funded by the National Centre for Atmospheric Science and the University of Reading, hope to analyze the data to better understand historical periods of wet and dry conditions and compare them with recent changes caused by global warming.

Clinical trials put on hold

BIOMEDICINE | Thousands of clinical trials have been delayed as ripples from the COVID-19 pandemic continue to spread. Drug giants Bristol-Myers Squibb and Eli Lilly announced in March they will defer launching most new trials. And a survey of 73 research sites, reported last week by Clinical Research IO, a clinical trials software vendor, suggested widespread disruption: Twenty-four percent of investigators said they have halted enrolling new volunteers, and another one-third are considering doing the same. Meanwhile, clinical researchers testing novel cancer drugs and therapies for many other diseases are assessing how to ship drugs to volunteers to avoid inperson visits.

MORE FROM ONLINE

Highlights from *Science*'s online coverage of the pandemic; read more at sciencemag.org/tags/coronavirus.

Featured interview

Top China scientist: Wear masks

George Gao has been at the center of China's efforts to control COVID-19 as director-general of the Chinese Center for Disease Control and Prevention. In January he was part of a team that first isolated and sequenced severe acute respiratory syndrome coronavirus 2, the virus that causes COVID-19.

"The big mistake in the U.S. and Europe, in my opinion, is that people aren't wearing masks," he said. "It can prevent droplets that carry the virus from escaping and infecting others."

But evidence supporting suggestions like Gao's is spotty, according to a separate online news article in *Science*, **Would everyone wearing face masks help us slow the pandemic?**

More online headlines from *Science*

How sick will the coronavirus make you? The answer may be in your genes. Genetic analysis using large biobanks may enable predictions.

New coronavirus leaves pregnant women with wrenching choices—but little data to guide them. Parents and doctors must weigh benefits of breastfeeding versus risks of possible infection.

Iran confronts coronavirus amid a battle between science and conspiracy theories. Sanctions and distrust hamper pandemic response.

The lockdown's environmental upside

Satellites have detected sharp drops in concentrations of nitrogen dioxide (NO_2), a precursor to smog, in populated areas around the globe after vehicles and other sources were idled by COVID-19 prevention measures.

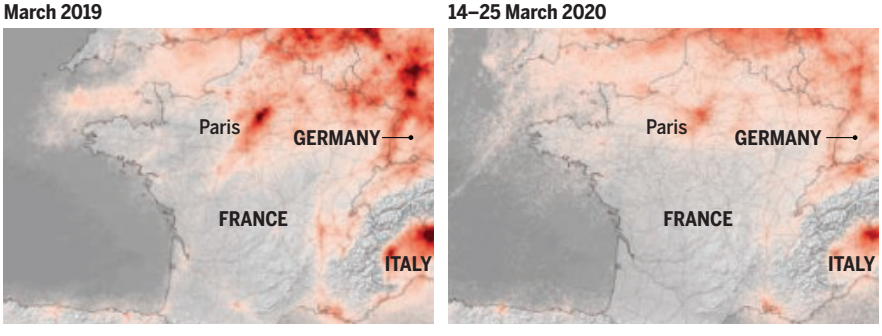

GRAPHIC: © CONTAINS MODIFIED COPERNICUS SENTINEL DATA (2019–20), PROCESSED BY KNMI/ESA

BIOMEDICINE

U.S. outlines path for pot research

After nearly 4 years of what some researchers saw as foot dragging, the U.S. Drug Enforcement Administration (DEA) last week proposed rules that would allow it to process 37 applications to grow marijuana for medical research. For more than 50 years, federal authorities have allowed only one source, the University of Mississippi, Oxford, to cultivate research cannabis. But as interest in the plant's potential medical benefits has grown, some cannabis researchers have said the Mississippi supply lacks sufficient potency and diversity for studies of chronic pain, post-traumatic stress disorder, and other conditions. An applicant, the Scottsdale Research Institute (SRI), sued the agency in June 2019 to compel it to process the requests. DEA proposed the rules on 23 March. George Hodgin, CEO of another applicant, the Biopharmaceutical Research Company, called them "the most meaningful and material progress made in federal cannabis policy in decades." But the federal rulemaking process can take years, notes Shane Pennington, a lawyer for SRI, adding, "DEA basically has ... found a way to put this on the back burner a lot longer."

Who will lead NSF?

LEADERSHIP | France Córdova completed her 6-year term this week as the 14th director of the U.S. National Science Foundation (NSF), and the $8 billion agency had no acting director as *Science* went to press. NSF's chief operating officer, chemist Fleming Crim, is the odds-on favorite to fill in until the U.S. Senate confirms Sethuraman Panchanathan, who was nominated as director in December 2019. But the White House could also name a temporary head from another

CONSERVATION ECOLOGY

Elephants restore depleted soil

By defecating and toppling trees, African elephants can help enrich savanna soils, replacing nutrients lost to cattle ranching, a study says. Even at moderate densities, cattle remove nutrients from grasslands because they are herded into corrals at night—robbing the soil of the dung and urine they would otherwise deposit on the savanna. A study begun in 1995 called the Kenya Long-term Exclosure Experiment now reports nearly twice as much soil carbon in controlled grazing areas that included elephants; soil nitrogen was also higher. The explanation, researchers say in the 16 March issue of *Nature Sustainability*, is that elephants spread dung as they roam, and they knock down trees, whose decomposition adds nutrients to the soil. The higher nutrient content provides more nutritious grasses, benefiting gazelles and other wild herbivores. The rich grasses could improve grazing for cattle, too, offering a reason for ranchers to protect elephants. Their numbers have been increasing in Kenya but are in decline elsewhere because of poaching.

Cattle and elephants coexist at a research station in Kenya.

federal agency. "NSF has a strong leadership team" ready to soldier on, says agency spokesperson Amanda Greenwell.

U.S. eases up on emissions

ENVIRONMENT | The Trump administration this week finalized its plan to roll back auto fuel efficiency standards, from an average of 54 miles per gallon (23 kilometers per liter) to 40 miles per gallon (17 kilometers per liter) by 2025. The move, if it survives legal challenges, will add at least 1 billion tons to annual U.S. greenhouse emissions.

Rochester settles #MeToo case

LITIGATION | The University of Rochester and its accusers in a high-profile sexual harassment lawsuit agreed on 27 March to a $9.4 million settlement for the plaintiffs, ending a bitter episode that divided its Department of Brain and Cognitive Sciences. Nine now-former professors and students sued in 2017, saying the university retaliated against and defamed them after they alleged sexual harassment by faculty member and linguist Florian Jaeger. The university did not find Jaeger guilty of sexual harassment. Nor did it admit fault in the settlement, which the plaintiffs called a major victory. Jaeger, through his lawyer, continued to deny the allegations. The university says it has expanded training to prevent and address sexual misconduct. Driven in part by the case, New York state enacted sweeping changes in 2019 to its sexual harassment laws.

Physics pioneer Anderson dies

THEORETICAL PHYSICS | Philip Anderson, a feisty theorist whose shaped physics far beyond his métier, condensed matter, died on 29 March at age 96. In the 1950s he showed how disorder could trap free-flowing electrons in a crystalline solid, a quantum effect for which he shared the 1977 Nobel Prize in Physics. He also revolutionized physicists' understanding of magnetism and superconductivity. He nearly invented the Higgs boson, the most famous of fundamental particles, before it was hypothesized by Peter Higgs in 1964. "Phil was a true giant of physics," says Michael Norman, a theorist at Argonne National Laboratory. "One of the greatest ever."

Tooth hints at humanity's history

BIOANTHROPOLOGY | A molecular analysis of tooth enamel from an 800,000-year-old ancestor of modern humans showcases the promise of ancient proteins for reconstructing our species' tangled family tree, researchers say. Analysis of the tiny specimen from *Homo antecessor* offers new evidence that the extinct hominin was most likely a close relative of the last common ancestor of Neanderthals, Denisovans, and modern humans, says a study published this week in *Nature*. Researchers used mass spectrometry to study the specimen, found in Spain's Atapuerca Mountains. They identified seven proteins, which are much hardier than DNA, and compared the genetic sequences that would have coded for the proteins with those of other hominins.

PHOTO: DINO J. MARTIN

Science Webinars

AAAS

Science Webinars help you keep pace with emerging scientific fields!

Stay informed about scientific breakthroughs and discoveries.

Gain insights into current research from top scientists.

Take the opportunity to ask questions during live broadcasts.

Get alerts about upcoming free webinars.

Sign up at: webinar.sciencemag.org/stayinformed

IN DEPTH

Jennifer Haller receives the first administration of an mRNA vaccine, made by the biotech firm Moderna, against the pandemic coronavirus.

PHOTO: AP PHOTO/TED S. WARREN

INFECTIOUS DISEASES

Vaccine designers take first shots at COVID-19

Two candidate vaccines start trials while dozens more are rushed into development

QQ group:1067583220

By **Jon Cohen**

The coronavirus that for weeks had been crippling hospitals in her hometown of Seattle changed Jennifer Haller's life on 16 March—but not because she caught it. Haller, an operations manager at a tech company in the city, became the first person outside of China to receive an experimental vaccine against the pandemic virus, and in the days since, she has experienced an outpouring of gratitude. "There's been overwhelming positivity, love, and prayers coming at me from strangers around the world," Haller says. "We all just feel so helpless, right? This was one of the few things happening that people could latch on to and say, 'OK, we've got a vaccine coming.' Disregard that it's going to take at least 18 months, but it's just one bright light in some really devastating news across the world."

The vaccine Haller volunteered to test is made by Moderna, a well-financed biotech that has yet to bring a product to market (*Science*, 3 February 2017, p. 446). Moderna and China's CanSino Biologics are the first to launch small clinical trials of vaccines against coronavirus disease 2019 (COVID-19) to see whether they are safe and can trigger immune responses. (The CanSino vaccine trial also began on 16 March, according to researchers from the Chinese military's Institute of Biotechnology, which is collaborating on it.) As *Science* went to press, a World Health Organization tally of other vaccine candidates that could follow stood at 52 (see table, p. 15).

"This is a wonderful response from the biomedical community to an epidemic," says Lawrence Corey, a virologist at the Fred Hutchinson Cancer Research Center who has run many vaccine trials but is not involved with a COVID-19 effort. "It's both gratifying and problematic in the sense of how do you winnow all this down?"

Science's COVID-19 coverage is supported by the Pulitzer Center.

Broadly speaking, these vaccines group into eight different "platforms"—among them old standbys such as inactivated or weakened whole viruses, genetically engineered proteins, and the newer messenger RNA (mRNA) technology that is the backbone of the Moderna vaccine—and their makers include biotechs, academia, military researchers, and a few major pharmaceutical companies. On 30 March, Johnson & Johnson (J&J) announced what it said could be a $1 billion COVID-19 vaccine project, with about half the money coming from the U.S. Biomedical Advanced Research and Development Authority if milestones are met.

Many viruses, including HIV and hepatitis C, have thwarted vaccine developers. But the new enemy, severe acute respiratory syndrome coronavirus 2 (SARS-CoV-2), doesn't appear to be a particularly formidable target. It changes slowly, which means it's not very good at dodging the immune system, and vaccines against the related coronaviruses that cause SARS and Middle East respiratory syndrome (MERS) have worked in animal models. Corey heads the United States's HIV Vaccine Trials Network, which has seen one candidate vaccine after another crash and burn, but he is optimistic about a SARS-CoV-2 vaccine. "I don't think this is going to be that tough."

One concern is whether people develop durable immunity to SARS-CoV-2, which is crucial given that vaccines try to mimic a natural infection. Infections with the four human coronaviruses that typically cause minor colds don't trigger long-lasting immunity. Then again, researchers have found long-

lasting immune responses to the viruses causing SARS and MERS, and genetically they are far more like SARS-CoV-2. And unlike cold-causing viruses, which stay in the nose and throat, the new coronavirus targets the lower respiratory tract, where the immune response can be stronger, says Mark Slifka, an immunologist who studies vaccines at the Oregon National Primate Research Center. "When you get an infection in the lungs, you actually get high levels of antibodies and other immune cells from your bloodstream into that space."

Even with an all-out effort, Anthony Fauci, director of the U.S. National Institute of Allergy and Infectious Diseases (NIAID), predicts a vaccine "is going to take a year, a year and a half, at least." Side effects, dosing issues, and manufacturing problems can all cause delays. Already some are calling for an ethically fraught shortcut to speed up clinical trials: giving people candidate vaccines and then intentionally attempting to infect them (see sidebar, p. 16).

A vaccine candidate might also be made available to health care workers and others at high risk even before final efficacy trials are completed. Stanley Perlman, a veteran coronavirus researcher at the University of Iowa, suggests a vaccine that only offers limited protection and durability could be good enough—at first. "In this kind of epidemic setting, as long as you have something that tides us along and prevents a lot of deaths, that may be adequate," he says.

A BETTER SPIKE

On 13 January, 3 days after Chinese researchers first made public the full RNA sequence of SARS-CoV-2, NIAID immunologist Barney Graham sent Moderna an optimized version of a gene that would become the backbone of its vaccine. Sixty-three days later, the first dose of the vaccine went into Haller and other volunteers participating in the small trial at the Kaiser Permanente Washington Health Research Institute. In 2016, Graham had made a Zika virus vaccine that went from lab bench to first volunteer in what was then a lightning-fast 190 days. "We beat that record by nearly 130 days," he says.

The effort benefited from lessons Graham learned from his past vaccine efforts, including his work on respiratory syncytial virus (RSV). The search for an RSV vaccine has a checkered past: In 1966 a trial of a candidate vaccine was linked to the death of two children. Later studies identified the problem as vaccine-triggered antibodies that bound to the surface protein of the virus but did not neutralize its ability to infect cells. This antibody-viral complex, in turn, sometimes led to haywire immune responses.

Studying structures of the RSV surface protein, Graham discovered that it had different orientations before and after fusing with a cell. Only the pre-fusion state, it turned out, triggered high levels of neutralizing antibodies, so in 2013 he engineered a stable form of the molecule in that configuration. "It was so clear at that point that if you didn't have structure, you didn't really know what you were doing," Graham says.

The experience came in handy in 2015, when a member of Graham's lab made a pilgrimage to Mecca, Saudi Arabia, and came back ill. Worried that it might be MERS, which is endemic in Saudi Arabian camels and repeatedly jumps into humans there, Graham's team checked for the virus and instead pulled out a common cold coronavirus. It was relatively easy to determine the structure of its spike, which then allowed the team to make stable forms of the ones for the SARS and MERS viruses, and, in January, for SARS-CoV-2's. That's the basis of the Moderna COVID-19 vaccine, which contains mRNA that directs a person's cells to produce this optimized spike protein.

No mRNA vaccine has yet reached a phase III clinical trial, let alone been approved for use. But producing huge numbers of doses may be easier for mRNA vaccines than for traditional ones, says Mariola Fotin-Mleczek of the German company CureVac, which is also working on an mRNA vaccine for the new coronavirus. CureVac's experimental rabies vaccine showed a strong immune response with a single microgram of mRNA, suggesting 1 gram could vaccinate 1 million people. "Ideally, what you have to do is produce maybe hundreds of grams. And that would be enough," Fotin-Mleczek says.

Many companies are relying on time-tested techniques. Sinovac Biotech is making a SARS-CoV-2 vaccine by inactivating whole virus particles with formaldehyde and adding an immune booster called alum. Sinovac used the same strategy for a SARS vaccine it developed and tested in a phase I clinical trial 16 years ago, says Meng Weining, a vice president at Sinovac. "We immediately just restarted the approach we already know."

Florian Krammer, a virologist at the Icahn School of Medicine at Mount Sinai, says inactivated virus vaccines have the advantage of being a tried-and-true technology that can be scaled up in many countries. "Those manufacturing plants are out there, and they can be used," Krammer says.

CanSino is now testing another approach. Its vaccine uses a nonreplicating version of adenovirus-5 (Ad5), which also causes the common cold, as a "vector" to carry in the gene for the coronavirus spike protein. Other vaccine researchers worry that because many people have immunity to Ad5, they could mount an immune response against the vector, preventing it from delivering the spike protein gene into human cells—or it might even cause harm, as seemed to happen in a trial of an Ad5-based HIV vaccine made by Merck. But the same Chinese collaboration produced an Ebola vaccine, which Chinese regulators approved in 2017, and a company press release claimed its new candidate generated "strong immune responses in animal models" and has "a good safety profile."

Other COVID-19 vaccine platforms include a laboratory-weakened version of SARS-CoV-2, a replicating but harmless measles vaccine virus that serves as the vector for the spike gene, genetically engineered protein subunits of the virus, a loop of DNA known as a plasmid that carries a gene from the virus, and SARS-CoV-2 proteins that self-assemble into "viruslike particles." J&J is using another adenovirus, Ad26, which does not commonly infect humans, as its vector. These approaches can stimulate different arms of the immune system, and researchers are "challenging" vaccinated animals with SARS-CoV-2 to see which responses best correlate with protection.

Many researchers assume protection will largely come from neutralizing antibodies, which primarily prevent viruses from entering cells. Yet Joseph Kim, CEO of Inovio Pharmaceuticals, which is making a DNA COVID-19 vaccine, says a response by T cells—which clear infected cells—proved a better correlate of immunity in monkey studies of the company's MERS vaccine, which is now in phase II trials. "I think having a balance of antibody and T cell responses probably is the best approach."

Kim and others applaud the variety of strategies. "At this early stage, I think it makes sense to try anything plausible," he says. As Stéphane Bancel, CEO of Moderna, says, "Nobody knows which vaccines are going to work."

FINAL PRODUCTS

Spurring many of the efforts has been the Coalition for Epidemic Preparedness Innova-

Best shots

The World Health Organization has tallied dozens of vaccine candidates, based on a variety of technologies. Two have started human safety trials (*).

PLATFORM	CANDIDATES
Protein subunit	18
RNA	8*
DNA	3
Non-replicating vector	8*
Replicating vector	5
Inactivated virus	2
Attenuated virus	2
Viruslike particle	1

DATA: WHO

Infect volunteers to speed a coronavirus vaccine?

As desperately as the world wants a shot that provides protection from the new coronavirus afflicting one country after another, proving that a vaccine works safely can be painfully slow. Clinical trials start with small numbers of people and at first only look for side effects and immune responses, slowly building up to a large study that tests efficacy—a process that will take at least 1 year for the new virus (see main story, p. 14). But as the scale of the pandemic becomes clearer, a provocative, ethically complicated proposal to shave many months off that timeline is gaining traction: Give people an experimental vaccine and then deliberately try to infect them.

Stanley Plotkin of the University of Pennsylvania, inventor of the current rubella vaccine, says a carefully designed "human challenge" trial could offer clear proof of a vaccine's worth at blinding speed. "We're talking 2, 3 months," says Plotkin, who has co-authored a commentary submitted for publication that describes how this might be ethically done. "People who are faced with a terrifying problem like this one will opt for measures that are unusual. And we have to constantly rethink our biases." A similar proposal from three other scientists was published this week in the *Journal of Infectious Diseases*.

Human challenge studies have been done ever since 1796, when Edward Jenner infected a boy with the smallpox virus after immunizing him with cowpox. Some are still underway for dengue, cholera, and other diseases (*Science*, 20 May 2016, p. 833). Today, such trials have careful designs and undergo extensive ethical reviews. Yet even researchers who conduct them argue against human challenges for the new coronavirus.

Matthew Memoli, an immunologist at the U.S. National Institute of Allergy and Infectious Diseases who stages human challenge studies of influenza, notes that the virus is so new it is not clear how often it makes people seriously ill or leaves them with long-term complications. "When you're going to give somebody a virus on purpose, you really want to understand the disease so that you know that what you're doing is a reasonable risk."

He also questions how quickly a proper human challenge of the new pathogen could be done. The challenge virus would first have to be grown under contamination-free, high-quality standards, and researchers would also have to determine the proper dosing of the challenge virus with, say, a monkey model, and confirm the dose in unvaccinated people.

Myron Levine, a vaccine researcher at the University of Maryland School of Medicine who has conducted challenge experiments for decades, doubts traditional clinical trials for vaccine candidates will be as slow as some fear. "I think we're going to move very, very fast," he says. Because of the high levels of new infections in many places, conventional trials will reveal a vaccine's worth on the same timeline as a human challenge, Levine says. "I cannot imagine that this would be ethical and would really speed up what we have to do."

Plotkin and other proponents of coronavirus challenge studies say risks could be reduced by only enrolling young adults, who seem to rarely suffer severe symptoms. To further decrease risks, the challenge could use a coronavirus strain from a person who had mild symptoms, a natural virus weakened in the laboratory, or a coronavirus mimic made by adding genes, such as the one for its surface "spike" protein, into a different, harmless virus.

Levine and Memoli agree that the risks would become more acceptable if an effective drug for the virus were available. And Seema Shah, a bioethicist at Northwestern University who also has strong misgivings, says the ethical scales might tip in favor of the experiment if the volunteers were people already "trained to take on these risks," like health care workers.

Shah would like to see a standing committee set up to address the ethics of challenge trials, especially during outbreaks, and spell out when they are justified. "The public is not familiar with these trials," she says. "They sound completely counterintuitive and opposed to the standard notion of what researchers or doctors are supposed to be doing."

Given the urgency, Shah adds, the vaccine community would be wise to quickly work out all the devilish details. "We're all going through these complicated emotions right now. If we're going to say we're making an exception to the standard way we do things, then we really have to get that right." —*J.C.*

tions (CEPI), a nonprofit set up to coordinate R&D for vaccines against emerging infectious diseases. So far, CEPI has invested nearly $30 million in vaccine development at Moderna, Inovio, and six other groups. "We have gone through a selective process to pick the ones that we think have the greatest likelihood of meeting our goals—which we think ought to be the world's goals—of speed, scale, and access," says CEPI CEO Richard Hatchett.

But he is rooting for other candidates as well. "We don't want to be in a situation where we have [one] successful vaccine and we have a contamination event [during manufacturing] and suddenly we don't have any vaccine supply."

CEPI invests in manufacturing facilities at the same time it puts money into staging clinical trials. "By doing things in parallel rather than in serial fashion, we hope to compress the overall timelines," Hatchett says. After reviewing phase I data and animal data, CEPI plans to move six of the eight products into larger studies to arrive at three that are worthy of full-scale efficacy trials that enroll perhaps 5000 participants. CEPI has less than $300 million in its coffers for fully developing a vaccine, however. and Hatchett estimates the price tag at $2 billion.

Seth Berkley, who heads Gavi, the Vaccine Alliance, argued in an editorial in *Science* last week that the world needs to come together even more to streamline the search for a COVID-19 vaccine. "If ever there was a case for a coordinated global vaccine development effort using a 'big science' approach, it is now," Berkley wrote, stressing that there must be extraordinary sharing of data, coordination of clinical trials, and funding. "You can't move 100 vaccines forward," he says.

Moderna and J&J both say that if everything goes perfectly, they could launch efficacy trials with about 5000 people in late fall and determine by January 2021 or so whether the vaccine works. Meng says, depending on approval from Chinese regulatory agencies, Sinovac could move its vaccine through small phase I and II tests by June. But, because of China's success at controlling its epidemic, the company may have to find another country that has high transmission of SARS-CoV-2 to stage an efficacy trial quickly.

Haller has had no serious side effects from the mRNA injected into her arm, but realizes that the phase I study will not determine whether the vaccine is effective. "The chances of the one that I got being really anything? I don't know," Haller says. "This is just the first of many, many vaccines, and it's just stupid luck that I was the first one." ■

With reporting by Kai Kupferschmidt.

PANDEMIC RESPONSE

United States strains to act as cases set record

Conflicting messages, lack of coordination plague chaotic efforts to slow coronavirus

By ***Science*** **News Staff**

The United States is first, and not in a good way. Last week, it set a grim record, surpassing all other nations in the reported number of people infected with the coronavirus that causes COVID-19. Officials had documented nearly 200,000 cases as *Science* went to press on 31 March; the death toll neared 4000. Even President Donald Trump—who just 1 month ago claimed the virus was "very much under control"—warned that the pandemic is about to get much worse.

To limit the damage, Trump on 29 March announced that federal recommendations to practice physical distancing would remain in place at least through the end of April, dropping his much-criticized push for a faster return to business as usual. In the meantime, officials across the nation are scrambling to find enough ventilators, protective gear, and supplies for hospitals overwhelmed with COVID-19 patients—or about to be (see graph, below right). Many state governors ratcheted up restrictions intended to slow the pandemic, imposing stay-at-home orders that some said could last into June.

Despite such actions, the U.S. pandemic response remains a work in progress—fragmented, chaotic, and plagued by contradictory messaging from political leaders. "We don't have a national plan," says epidemiologist Michael Osterholm of the University of Minnesota, Twin Cities. "We are going from press conference to press conference and crisis to crisis … trying to understand our response." Others are dismayed that the U.S. Centers for Disease Control and Prevention (CDC), which has prominently provided national leadership in past outbreaks, hasn't been more visible. "I sure would like to see a lot more of CDC," says Julie Gerberding, a former director of the agency. The United States is "in a reactive mode," says Jeremy Konyndyk, a senior policy fellow at the Center for Global Development. "We're still chasing the virus."

To catch up, Osterholm and other researchers have released a flurry of battle plans in the past week. Many officials have welcomed the recommendations and signaled their support. But the question now is whether the United States—a patchwork of more than 50 state and territorial governments marked by political polarization and a history of fierce resistance to centralized authority—can follow through.

The urgency is great. A review of 12 mathematical models conducted by federal scientists concluded the United States is likely to see millions of people infected. The death toll is now likely to reach more than 100,000 (see graph, below right) even with distancing and other measures, Deborah Birx, White House coronavirus response coordinator, has said repeatedly. Some experts fear even those numbers are too optimistic, given that outbreaks are now poised to explode in places—including Louisiana, Michigan, and Florida—that are ill-prepared for the surge of people needing hospitalization.

The new battle plans generally agree several moves need to be taken immediately. Federal, state, and local governments must consistently urge, if not order, most people to stay home and keep their distance from others. Federal officials must take a stronger role in directing medical supplies to areas most in need. Testing for the virus must accelerate and expand, so that people who are infected can be quarantined.

But there are numerous obstacles. Testing could soon be hampered by a shortage of reagents, caused in part by the disruption of supply chains in Asia, Osterholm notes. Instead, health officials may have to rely on less precise illness surveillance—documenting the frequency of COVID-19 symptoms to estimate the number of cases.

Persuading more than 320 million Americans to take the pandemic seriously, meanwhile, will require a radical change in messaging from political leaders at every level, from the White House to city halls. "Rule one of communication in a pandemic is have a message and stick to it," says politi-

Perilous slopes

Exponentially rising case numbers (left, as of 30 March) indicate outbreaks are exploding in some states, while modeling (right) suggests the U.S. death toll will be large.

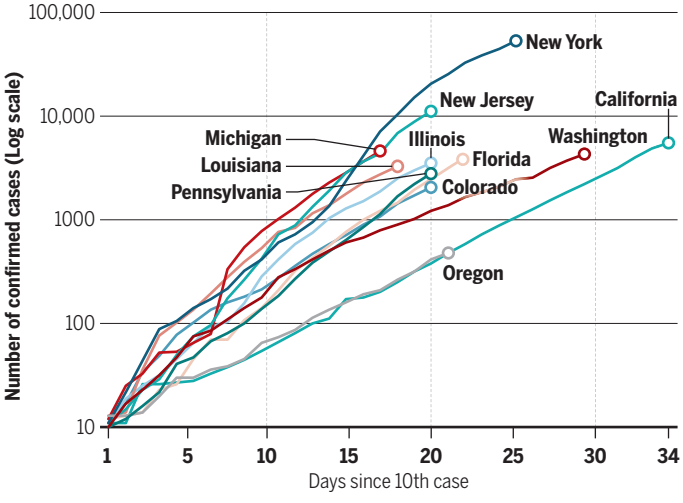

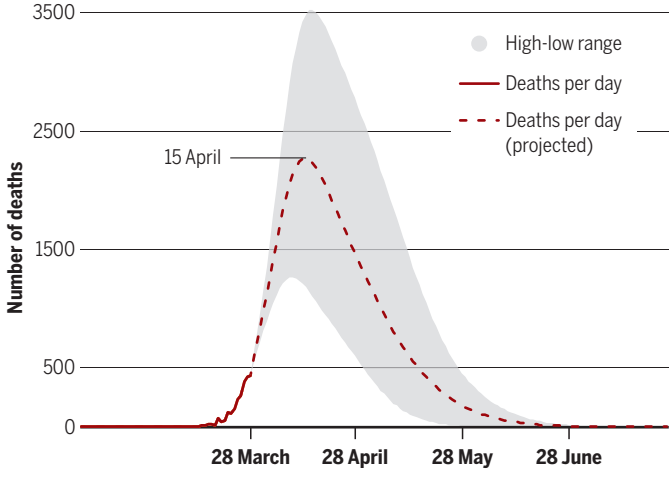

CREDITS: (GRAPHICS) N. DESAI/*SCIENCE*; (DATA, LEFT TO RIGHT) JOHN HOPKINS UNIVERSITY; INSTITUTE FOR HEALTH METRICS AND EVALUATION

cal scientist Scott Greer of the University of Michigan, Ann Arbor, who has studied the U.S. response to the 2014 Ebola epidemic. So far, that's been the exception, as Trump and state and local officials have delivered a cacophony of conflicting messages, from indifference to alarm.

Even if lockdowns succeed at halting the virus, as they have in China, the country needs to marshal massive resources to monitor for new outbreaks and quickly contain them, Konyndyk says. Identifying cases and contacts and isolating them will require a huge increase in public health workers at the local level. "Most of what we would need to do to transition away from large-scale social distancing is not in place, and there don't appear to be plans to put it in place," he says.

The absence of nationwide coordination highlights the division of legal power between the federal and state governments, observers say. Governors, not federal officials, typically hold police powers to shut businesses and enforce curfews. But many are reluctant to invoke those powers and suffer the political costs without clear direction from above, Greer says. Political division over the pandemic has also hampered decisive action: Polls show Republicans perceive the threat as less serious than Democrats and independents.

To see the consequences of such divides, Greer points to Florida, where Governor Ron DeSantis (R) delayed ordering a statewide closure of beaches, apparently unwilling to cross the powerful tourism industry—and his political base. DeSantis "is dependent on a large bloc of voters who are Republicans and many are very pro-Trump. If I've got Donald Trump saying essentially, 'Don't lock down,' what political cover do I have?" Greer says. Epidemiologists predict the delay will worsen Florida's outbreak.

New research suggests partisan leanings are influencing pandemic response in other states, too. In a preprint released on 28 March, researchers at the University of Washington, Seattle, found that states with a Republican governor or where Trump fared better in the 2016 election were less likely to have instituted a range of social distancing measures than states led or dominated by Democrats.

Bridging such divisions will be essential if the United States is to defeat the coronavirus, says Harvard University epidemiologist William Hanage. "The closest comparison here, in terms of national mobilization, is a war. And there is no way the United States would fight a war as 50 separate states." ■

With reporting by Warren Cornwall, David Malakoff, Kelly Servick, and Kai Kupferschmidt.

PHOTO: FEATURE CHINA/BARCROFT MEDIA/GETTY IMAGES

INFECTIOUS DISEASES

As normalcy returns, can China keep COVID-19 at bay?

Infected travelers pose a continuing threat, but local coronavirus transmission still occurs as well

By **Dennis Normile**

Life is almost back to normal in much of China. Shops, restaurants, bars, and offices are open. Manufacturing activity is picking up. Traffic once again jams the highways of major cities. Three-quarters of China's workforce was back on the job as of 24 March, according to one company's estimate. Wuhan, where the COVID-19 pandemic originated, is lagging, as is the rest of Hubei province—but even there, the lockdown is set to lift 8 April.

China has done what few believed was possible: Bring a blazing epidemic of a respiratory virus to a virtual standstill. On 18 March, the country reported zero locally transmitted COVID-19 cases for the first time. Since then, only eight such infections have been reported, only one of them in Wuhan. Now, the key question is: Can China keep it that way?

Public health experts worldwide are watching closely. "China is addressing an issue every country and location in the world will eventually face: how to normalize and restore societal activities, while at the same time minimizing disease-related dangers from the outbreak," says epidemiologist Keiji Fukuda of the University of Hong Kong (HKU).

New infections now mostly come from outside—623 cases have been confirmed in incoming air passengers between 18 and 30 March. At midnight on 27 March, China banned virtually all foreigners from entering the country and required returning Chinese to be quarantined for 2 weeks, whether coming by air or over land. But there is still danger at home as well. The smattering of locally transmitted cases shows SARS-CoV-2, the virus that causes COVID-19, isn't entirely gone. And the low case numbers may be deceptive. Until early this week, tallies from China's National Health Commission did not include people who tested positive for the virus but had no symptoms, and local authorities have reportedly suppressed data on new infections to meet the target of zero local cases.

Still, "I believe that there are few local cases," says HKU epidemiologist Ben Cowling. But with most of the population still susceptible to infection, fresh outbreaks remain a constant danger. "How to balance getting back to work and a normal state versus maintaining the current status [of few new cases] is certainly critical," says Ding Sheng, director of the Global Health Drug Discovery Institute at Tsinghua University.

Officials are relaxing restrictions slowly

Workers at Dongfeng Honda in Wuhan, China, eat lunch while sitting 1.5 meters away from each other.

and methodically, Ding says. Many restaurants at first reopened with shortened hours and for a limited number of customers; now, doors are open to all. Primary and secondary schools in several provinces have reopened, but only in communities free of the disease, and schools must check students' temperatures and watch for symptoms. Universities, where students from around the country mix, remain closed. Events that draw crowds are still banned or discouraged. Live music venues and gyms in many cities remain closed. There are temperature checks at subway entrances and factory gates. And habits developed during the epidemic persist. Face masks are ubiquitous. People keep their distance in public and at work. Millions continue to work from home.

To guard against flare-ups, investigators trace and quarantine close contacts of every newly confirmed COVID-19 case, including those who may be asymptomatic, Wu Zunyou, an epidemiologist at the Chinese Center for Disease Control and Prevention (China CDC), told the communist party newspaper *China Daily* last week. In another precaution, everyone visiting fever clinics in Beijing and other major cities is now tested for the virus. And many provinces check the health status of migrant workers and others crossing their borders. "Any new transmission will be identified quickly and controlled swiftly," Ding says.

The 27 March travel ban—which the government implemented even though it strenuously objected when the United States banned visitors from China in January—addresses the other main risk: reintroduction of the virus from the rest of the world. Flights into China have also been severely curtailed. Chinese citizens who arrive undergo strict screening en route and upon arrival and go into quarantine for 2 weeks.

A European academic who returned to China 1 week before the ban took effect described the process to *Science*. His temperature was taken twice during the flight and he filled out a form detailing his recent whereabouts, the health status of family members and colleagues, and his use of medications. Another temperature check followed at the Beijing airport, after which the scholar—who asked not to be identified—was escorted to his own apartment for a 14-day quarantine. A community official pasted a quarantine notice across the door jamb, which was removed and replaced for grocery deliveries. Authorities ordered him to a "quarantine hotel" 3 days later, after a fellow passenger on the plane turned positive for COVID-19. The academic remains "very understanding," and says he was treated well.

China's strategy "seems to have been effective thus far in preventing a resurgence," says Benjamin Anderson, an epidemiologist at Duke Kunshan University. But with the virus now circulating around the world, "repeated importations to China will inevitably lead to local transmission," Cowling says. "Authorities will need to get on top of the cases very quickly," he says, in a game of whack-a-mole. Remaining pockets of local infection could be a problem as well, says Ira Longini, a disease modeler at the University of Florida. "The models say the disease will come back once the restrictions are lifted. I hope that's not correct, but I can't imagine why it wouldn't be," Longini says.

Much is at stake. Economists predict China's gross domestic product may shrink 10% in the first quarter of this year, the worst contraction since 1976, and demand for China's manufactured goods has collapsed. The Chinese strategy is aimed at buying time until a vaccine or drugs are available, says George Gao, director of China CDC. A group led by Chen Wei of the Academy of Military Medical Sciences has already started a phase I study of a candidate vaccine, according to *China Daily*. Dozens of other vaccine studies are underway around the world (see p. 14).

Ding, who lived in Beijing through the worst of the crisis, believes China can keep its guard up until these efforts bear fruit. Although minor flare-ups could happen any time, he says, a large-scale reemergence of COVID-19 "is very unlikely given what we have learned." ■

With reporting by Jon Cohen, Martin Enserink, and Bian Huihui.

ARCHAEOLOGY

Lead pollution tracks the rise and fall of medieval kings

Ice core preserves precise record of lead dust from English mines

By **Ann Gibbons**

In the Peak District of England, the picturesque village of Castleton nestles at the foot of a limestone outcrop crowned by a medieval castle. Today, hikers flock to the natural beauty of this region, home to the United Kingdom's first national park. But 800 years ago, the wild moors and wooded gorges were "covered in toxic lead pollution," says archaeologist Chris Loveluck of the University of Nottingham. "The royal hunting forest near the castle was an industrial landscape."

Here, farmers mined and smelted so much lead that it left toxic traces in their bodies—and winds blew lead dust onto a glacier 1500 kilometers away in the Swiss Alps. Loveluck and his colleagues say the glacier preserves a detailed record of medieval lead production, which they have deciphered with a new method that can track deposition over a few weeks or even days.

Lead tracks silver production because it is often found in the same ore, and the team found that the far-flung lead pollution was a sensitive barometer of the medieval English economy. As they report in a study published this week in *Antiquity*, lead spiked when kings took power, minted silver coins, and built cathedrals and castles. Levels plunged when plagues, wars, or other crises slowed mining and the air cleared. "This is extraordinary—lead levels correlate with the transition of kings," says historian Joanna Story of the University of Leicester, who was not part of the study.

Most people associate lead pollution with the Industrial Revolution, when lead became widely used in paints, pipes, and ceramics. But researchers have long known that the Romans also absorbed high levels of lead as they smelted silver and other ores. Recently, scientists have identified startling spikes of lead deposited in medieval times in Arctic

ice cores and in lake sediments in Europe. A study last year suggested most of the pollution came from mines in Germany.

The new study, however, points to England. In collaboration with Loveluck and historians at Harvard University, glaciologist Paul Mayewski and his team at the University of Maine, Orono, analyzed lead in an ice core drilled in 2013 in the Colle Gnifetti Glacier in the Swiss Alps. The 72-meter-long core preserves more than 2000 years of fallout from pollution, volcanoes, and Saharan dust storms. To decipher this record at the highest possible resolution, the team used a laser to carve 120-micron slivers of ice, each representing just a few days or weeks of snowfall, along the length of the core. They analyzed the samples—some 50,000 from each meter of the core—for about a dozen elements, including lead.

The ice core data reveal the scale of regional pollution, showing dramatic lead spikes between 1170 and 1219 C.E.—"the highest levels of lead pollution before modernity," says historian Alexander More, of Harvard and Long Island University, Brooklyn. Lead levels matched those recorded in 1890, at the height of the Industrial Revolution. (Lead in the core peaked in the 1970s, spurred by leaded gasoline.)

To find the source of the medieval spikes, the team modeled how winds carry pollution. They found that during summer, lead-laced winds blew to the glacier from the northwest—from England. Summer, between spring and fall harvests, was also when Peak District farmers mined the most lead. "You have women and children breaking the rocks and smelting the ore in Castleton, and the lead is getting picked up and transported over the western Alps," says historian Ann Carmichael of Indiana University, Bloomington.

The ice core data spurred Loveluck to groundtruth the method with the English Pipe rolls, historic scrolls that record annual taxes paid by miners for cartloads of lead. At a 2018 workshop at Harvard, the geo-scientists and historians found they could match lead pollution in the Swiss ice core, taxes paid, and events in English history. For example, when Mayewski showed on a graph that lead pollution plummeted in 1170, Loveluck and Harvard historian Michael McCormick immediately knew why: "1170 was the year that Henry II's assassins killed the archbishop of Canterbury [Thomas Becket] and Henry was excommunicated," Loveluck says. "Nobody paid any taxes." Mining stopped.

Ten years later, lead pollution peaked. That's when Henry II had finally made up with the pope and "began to bankroll the rebuilding of Cistercian abbeys," Loveluck says. "He has massive lead orders" for building roofs, gutters, and cisterns, which are reflected in taxes on mines in the Peak District and at Carlisle in Northern England.

Lead in the core surged again in 1193, when Richard I (the "Lionheart") was imprisoned in Germany by the Holy Roman Emperor Henry VI, who demanded a ransom. "There appears to be a very concerted effort to pay the ransom," McCormick says, which gave a turbo boost to lead and silver mining.

But Richard I left his successor and brother, John I, a depleted treasury. John lost Normandy in a war with France and was perceived as weak. Emboldened, his barons revolted in 1215, when John was forced to sign the Magna Carta, giving the church and barons more rights and reducing John's ability to raise taxes, McCormick says. John died in 1216 and during the rocky transition to his son, Henry III, coins were not minted and mining stopped. Lead levels in the core plummeted.

For miners and their families, economic good times—when lead production spiked—may have also spurred devastating health effects, says Loveluck, who is part of an ongoing study of Castleton skeletons.

Other nations' mines may also have contributed to the surges in the ice core, cautions geochemist Paolo Gabrielli of Ohio State University, Columbus. And snow hydrologist Joe McConnell of the Desert Research Institute, part of the rival group that proposed German mines as the source of high lead levels in Arctic ice cores, questions the precision of the new study. He notes that much of the snow that drops on Swiss glaciers is blown away, leaving an incomplete record in the ice.

One way to settle the debate would be to check mining records: McCormick says silver and lead mining peaked in one German region before this period. Researchers could also study whether lead from English and German mines has distinctive isotopic signatures; if so, isotopes in the ice record could settle which region polluted most. Meanwhile, other teams are analyzing ice cores elsewhere in the Alps for lead. "We've got to do this work fast, before all of these glaciers melt," Carmichael says. ■

The fortunes of kings, written in ice

Historical events influenced the amount of taxes paid on lead from English mines (blue). They also had broader effects, shaping lead pollution deposited 1500 kilometers away in a Swiss glacier (red).

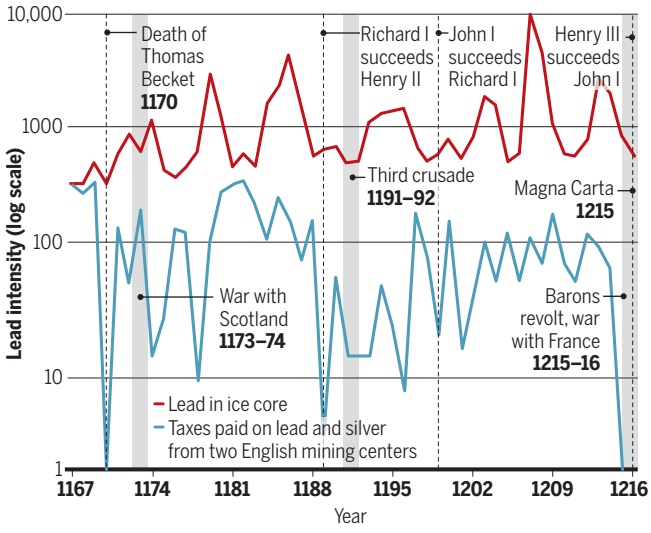

Peveril Castle in England's Peak District draws hikers today, but it was once a center of lead and silver mining.

CREDITS: (GRAPHIC) N. DESAI/*SCIENCE*; (PHOTO) ROBJEM/ISTOCK

ILLUSTRATION: STEFANIA INFANTE

WHERE ARE THE WOMEN?

Female scientists allege discrimination and neglect of research on women at NIH's child health institute

By **Meredith Wadman**

In November 2014, nine senior female scientists at the National Institute of Child Health and Human Development (NICHD) requested a meeting with their director. Their concern: that the careers of women at the institute's Division of Intramural Research (DIR) were being stymied by its powerful scientific director, Constantine Stratakis. They complained that the number of tenured and tenure-track female scientists in the then–$177 million division was at a historic low, and they said women were starkly lacking among its leaders. They wanted more women recruited and better retention of female talent.

After the meeting, then-NICHD Director Alan Guttmacher wrote in an email forwarded to the women: "There is wide agreement that we have a serious problem." He added that he looked forward to "action … which actually makes a difference."

But today, fewer female scientists run labs in DIR than in 2014, when one in four lab leaders was a woman. In 2011, the year Stratakis became permanent scientific director, 27% of DIR labs were run by women, compared with 23% today. At leading children's research hospitals canvassed by *Science*, comparable percentages range from 30% to 47% (see table, p. 23).

Stratakis's critics charge that the numbers form one piece of a picture of sex discrimination at the division he led; that picture, they say, includes a slew of equal employment opportunity (EEO) complaints and the dismantling of research on reproduc-

tive disease in adult women. Between 2013 and 2019, at least eight female professionals at NICHD filed EEO complaints naming Stratakis. Other women who did not file complaints also felt ill-treated by Stratakis, and some of them left the institute.

"Constantine Stratakis does not value the diversity, perspective, and contributions that women bring to the table as physicians and as scientists," says Lynnette Nieman, an endocrinologist who filed a complaint charging him with sex bias in 2014. "That has shown in his actions, in how he has treated women here, and his poor record in enhancing the diversity of the institute."

Stratakis, 54, a pediatrician and expert in the genetics of pituitary and adrenal gland tumors, vehemently counters those arguments. "The NICHD intramural program is highly supportive of women scientists," he said in a statement. He notes that he recently hired three female gynecologists to staff a new program on gynecological disease in children and teens. He adds that women comprise nine of 10 DIR clinical investigators, who treat patients, staff trials, and train physicians. (In contrast to lab-running scientists, clinical investigators typically lack independent research budgets and labs and have time-limited, renewable appointments.) "I have made demonstrative strides to diversify not only my leadership team but also the Board of Scientific Counselors," an external advisory board, Stratakis adds. In 2008, one of 12 board members was a woman; today, eight of 14 are women. And, he notes, in 2015, after the senior women complained, he eliminated a heavily male layer of middle managers, replacing them with eight associate scientific directors—four men and four women.

Some women at NICHD staunchly support Stratakis, saying he faced structural obstacles to boosting the numbers of women running DIR labs. Other women say he advanced their careers and had reason to curtail those of others, including some who filed EEO complaints. "He tried to seriously elevate this institute by eliminating people who he saw as nonproductive, whether male or female," says Kristina Rother, a National Institutes of Health (NIH) pediatric endocrinologist who has worked with Stratakis for decades and whom he hired in July 2019 to direct a physician training program. "NICHD is by far not the worst—instead, it is one of the better NIH institutes for women's careers."

Stratakis plans to leave NICHD at the end of May to become executive director and chief scientific officer at the Research Institute of the McGill University Health Centre. He stepped down as NICHD scientific director in February, but remains an NICHD scientist. He leaves behind an institute that is, by some accounts, scientifically stronger but, according to others, has earned a reputation that keeps female scientists away. Stratakis "makes you small," says one female scientist at NICHD who feels Stratakis treated her unfairly. She did not file an EEO complaint, she says, because "I just didn't feel like fighting."

THE $1.56 BILLION NICHD is the seat of U.S. government research on infant and child health. Because NIH has no dedicated institute for women's health, NICHD is also the home of much U.S.-funded obstetrics and gynecology research, including an intramural OB-GYN research program mandated by Congress in 1993. As scientific director, Stratakis had the final word on staff, space, equipment, lab supply budgets, and salaries for DIR's scores of lab-running scientists; he also controlled hiring and firing, shaping the direction of the division's research.

Pediatrician Constantine Stratakis has run NICHD's Division of Intramural Research for 10 years.

That research explores topics as diverse as protein synthesis in yeast and synapse formation in embryonic fruit flies. Some DIR scientists conduct additional clinical research, enrolling patients in trials at NIH's Clinical Center, where NICHD physicians also oversee gynecological patient care throughout the hospital.

In 2012, the year after Stratakis became permanent director, a blue-ribbon panel convened to address financial and other problems in DIR that predated him (*Science*, 18 May 2007, p. 968). The panel's 2013 report proclaimed that "the poor representation of women and minorities in the DIR has a broad negative impact on training, morale, and quality of science and leadership. Addressing this problem should be a priority."

That task fell to Stratakis, a leading Greek-born geneticist who discovered the genetic basis of several rare tumors. A charismatic figure who spouts Greek aphorisms and drives a midnight blue Porsche, Stratakis has been spotted stooping to tie a patient's shoelaces. He earned his M.D. and a doctorate from the University of Athens and then completed a pediatrics residency and subspecialty training at Georgetown University. Hired to launch a lab in DIR in 1996, he has been there since, becoming acting scientific director in 2009 and taking over the permanent job in 2011.

In response to financial pressures and later to Trump administration hiring controls, Stratakis shrank the ranks of lab-running scientists in DIR in Bethesda, Maryland, from 84 to 57 between 2011 and March 2020. To do so, he forced or eased out aging scientists; he also did not retain four female physicians in a temporary program grooming them to become tenure-track scientists. The number of women running labs fell from 23 to 13 (a 43% drop); the number of men fell from 61 to 44 (28%), according to annual DIR reports and recent public announcements.

Despite the overall reduction, between 2013 and this January Stratakis oversaw the hiring of eight tenure-track scientists in DIR; two—just 25%—were women. More than half of U.S. Ph.D. graduates in biological sciences have been women since 2008; nearly half of postdocs in health research are women. According to the most current public data, today 29% of DIR's tenure-track scientists are women, compared with 45% across NIH. (NIH notes that a separate, smaller intramural division at NICHD, focusing on the health of populations, has two female tenure-track investigators. Stratakis became acting director of this division in late 2017; both women were hired in 2012.)

Agency observers acknowledge that administrators across NIH face a challenge in quickly boosting the proportion of women running intramural labs. Many intramural scientists remain in their positions for decades, resulting in a workforce heavy with aging male scientists and relatively few chances to make new tenure-track hires. According to NIH data, as of September 2019, 76% of tenured scientists across NIH are men. "To actually affect the percentage per se takes a lot," says Hannah Valantine, NIH's chief diversity officer.

But Stratakis's critics say that doesn't excuse his failure to recruit and retain young female scientists or explain why propor-

PHOTO: THE CHILDREN'S INN AT NIH

tionally more women than men left DIR. And some current and former female scientists at NICHD, both young and older, say Stratakis badly damaged their careers.

IN 2015, DIANA BLITHE, a Ph.D. biochemist who is chief of NICHD's Contraceptive Development Program, met with Nieman and Stratakis. Nieman, Blithe, and others had co-patented a drug, ulipristal acetate, that was marketed in different dosages as an emergency contraceptive and as a treatment for uterine fibroids. (Fibroids are noncancerous growths that lead to more than 150,000 hysterectomies in the United States each year.) At the meeting, Blithe recalls, Stratakis prohibited further clinical studies of the fibroid drug that Nieman had proposed. Blithe says Stratakis "was speaking to Lynnette in a very disrespectful, demeaning way. He was just saying that her work wasn't good enough."

Blithe, who filed her own EEO complaint against Stratakis and another senior NICHD administrator last year, was infuriated on Nieman's behalf. "I said words to the effect of 'How dare you treat her in this way? NICHD is getting hundreds of thousands of dollars in royalties from work that she did, developing a drug that's helping hundreds of thousands of women avoid hysterectomies. And she was just elected president of the Endocrine Society.' I got very upset."

One year earlier, Nieman, 66, had filed an EEO complaint claiming that Stratakis had crippled her clinical research by shrinking her staff and budget because she was female. Reviews written by external experts in 2011, given to *Science* by Nieman, were lukewarm about some of her lab studies. But the reviewers were enthusiastic about her clinical studies of a serious disease on which she is a world authority: Cushing syndrome, in which the body makes too much of the stress hormone cortisol. "Her work is recognized as invaluable by peers," one reviewer wrote. The reviewers also worried about her "modest" budget. Stratakis nonetheless downsized Nieman's research team, which fell from seven in 2011 to five in 2012, three in 2013, and one in 2014, according to DIR annual reports. By 2014, Nieman says, Stratakis had also reduced her $118,000 budget for items including supplies and travel to $20,000.

NICHD's director, Diana Bianchi, declined to allow Stratakis to comment on specific cases and added that she would not address Nieman's or other women's cases, saying the agency does not comment on personnel matters.

Nieman and NIH agreed on a settlement of her EEO complaint in 2015. But she says she despairs at how Stratakis harmed her career. "I know that I won't ever be able to do things I could have done."

Stratakis's defenders note that Nieman and Stratakis, who also studies Cushing syndrome, have clashed for years. In 1999, when she was NICHD's clinical director, Nieman reprimanded Stratakis, writing that he had failed to follow the rules for protecting human subjects.

Employment lawyers say the collection of eight complaints against Stratakis is extraordinary. The number suggests "an environment that is not welcoming or fair towards women because statistically speaking, there are going to be many other women who haven't come forward and haven't complained," says Deborah Dixon, a lawyer with Gomez Trial Attorneys who has represented female scientists in sex discrimination cases.

From 2015 to 2019, an average of 36 EEO complaints alleging sex discrimination were filed annually across NIH—about 1.3 sex discrimination complaints per NIH institute per year. That figure suggests that from 2013 to 2019, the period during which the eight complaints were filed, Stratakis received roughly as many complaints as would be expected in the entire NICHD, which had between 550 and 600 full-time employees during those years, about half of whom were in DIR.

For comparison, NIH's National Institute of Neurological Disorders and Stroke (NINDS) is about the same size as NICHD. But Story Landis, NINDS's scientific director from 1995 to 2003 and its director from 2003 to 2014, says she was not named in a single EEO complaint.

Of the eight EEO complaints filed by women against Stratakis, six alleged sex discrimination, sometimes combined with age discrimination, and two alleged age discrimination alone. Three complaints have been settled. A fourth complainant lost a lawsuit on appeal, a fifth dropped her complaint after quitting the agency, and a sixth complaint was dismissed. Two others are ongoing.

One of those in process is Blithe's, which alleges sex bias by Stratakis and by pharmacologist Karim Calis, NICHD's director of clinical research and compliance and a member of Stratakis's leadership team. Blithe, a world-leading contraceptive expert, alleged that Calis made disparaging, false public statements that she was doing science without appropriate supervision and endanger-

NIH's child health institute trails peers

Science canvassed research-intensive children's hospitals about the gender of scientists who head experiment-running labs. NICHD appears unusually male-dominated. (These numbers exclude clinical researchers without lab space and scientists who run dry labs studying topics like epidemiology or population science.)

NAME OF INSTITUTION	LOCATION	NUMBER OF LABS	NUMBER OF LABS RUN BY WOMEN	PERCENTAGE OF LABS RUN BY WOMEN
National Institute of Child Health and Human Development	Bethesda, Maryland	57	13	23%
Boston Children's Hospital	Boston	200	60	30%
Cincinnati Children's Hospital Medical Center	Cincinnati	195	60	31%
Hospital for Sick Children Research Institute	Toronto	155	51	33%
Children's Hospital Los Angeles	Los Angeles	56	19	34%
St. Jude Children's Research Hospital	Memphis	101	34	34%
Children's Hospital of Philadelphia	Philadelphia	142	52	37%
UCL Great Ormond Street Institute of Child Health	London	74	32	43%
Texas Children's Hospital	Houston	256	121	47%

GRAPHIC: X. LIU/*SCIENCE*

How women at NIH's Clinical Center lost childbearing chances

In 2014, Kelsey Taylor of Norwood, Massachusetts, was 19 years old, ill with severe sickle cell disease, and about to be treated at the Clinical Center, the research hospital at the National Institutes of Health (NIH). But the toxic drugs and radiation used in her treatment were likely to injure her ovaries and leave her infertile.

Even at 19, Taylor knew she wanted the chance to have biological children someday. "For me that was huge," she says. She was fortunate: NIH was just starting to freeze patients' eggs before fertility-damaging therapies, so that women might start a pregnancy after their medical odyssey. But the next year, the National Institute of Child Health and Human Development (NICHD), which launched the egg-freezing program, suspended it, dismaying infertility experts.

The program originated with OB-GYN Erin Wolff, then a scientist in training at NICHD. Several months earlier, Wolff had proposed to NICHD's scientific director, pediatrician Constantine Stratakis, that she provide egg freezing to patients like Taylor. Several young women had decided not to enter potentially lifesaving research studies when they learned they were likely to lose their fertility, Wolff says.

The American Society for Reproductive Medicine had declared in 2012 that egg freezing was no longer experimental, and major hospitals across the country were offering it. But Stratakis and his clinical director, pediatrician Forbes Porter, told Wolff she would need to offer the egg freezing as a research study, she says. (NICHD declined to make Stratakis or Porter available for comment.)

Wolff launched the study in August 2014, and Taylor was her first patient. Wolff retrieved and froze the eggs of 20 more women and teens over the coming 16 months. But in December 2015, NICHD's Institutional Review Board, an ethics committee, suspended the study because of protocol deviations. Wolff says the lapses, such as adjusting pregnancy test timing by a few days to accommodate patients' schedules, were well within the standard of clinical care. She failed to win a permanent job at NICHD and left (see main story, p. 21).

After Wolff's protocol was suspended, "I was upset," says Barbara Collura, president and CEO of Resolve: the National Infertility Association. She served on NICHD's external advisory council from 2015 to 2019. "This was standard of care; it was not experimental. This is supposed to be our nation's preeminent research facility."

Before leaving, Wolff wrote to NIH Director Francis Collins in February 2016, asking him to protect the egg-freezing program. She noted that in the 6 weeks since the trial's suspension, four women had already undergone therapies toxic to their ovaries without being offered egg freezing. She

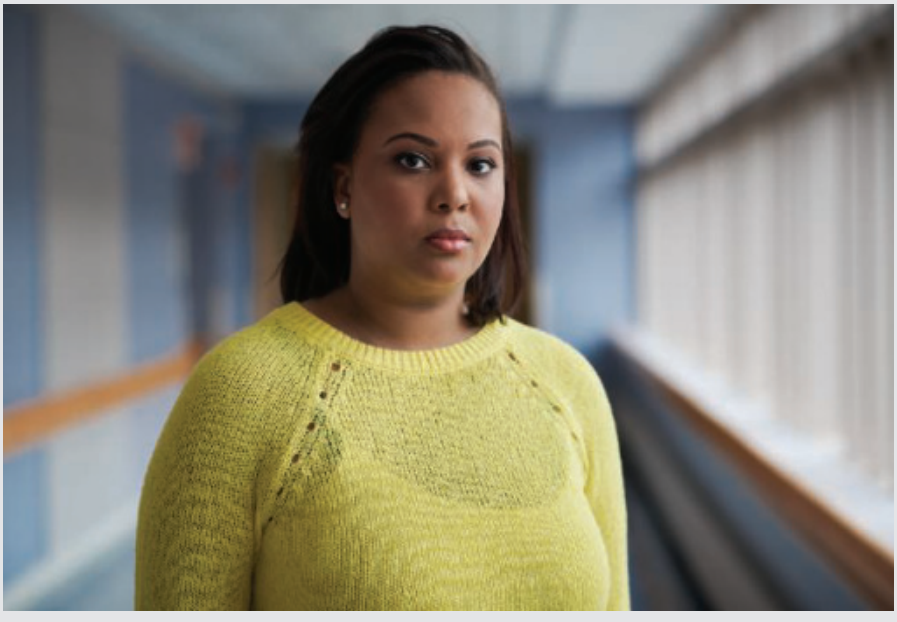

Kelsey Taylor was able to freeze her eggs before receiving therapy toxic to her ovaries.

PHOTO: ANGELO MERENDINO

ing safety, for which she says he offered no evidence or examples. She added that Stratakis refused to curb Calis, who has no expertise in contraception, and that Stratakis instituted unnecessary and discriminatory surveillance of her work.

"[Stratakis] gave deferential treatment to Dr. Calis and, without reason, gave more weight to Dr. Calis's comments about my program than to mine," Blithe alleges.

Calis referred questions to NICHD, which declined to comment.

"No leader of long standing, in my experience, can please everyone," says Brenda Hanning, Stratakis's chief of staff from 2011 until her 2016 retirement. (Hanning was not referring to Blithe, who came to the intramural program after Hanning retired.) "I was involved in cases where some women with problems in their careers looked for someone to blame for their own failings. It was shameful when they targeted him."

CRITICS OF STRATAKIS also blame him for gutting gynecological research on adults, a field that tends to attract female investigators. "The in-house gynecology research program has been subjected to drastic cuts," says James Segars, a veteran OB-GYN who left his fibroids-focused NICHD lab in 2015 after Stratakis refused, against the recommendation of external reviewers, to put Segars on tenure track. He is now director of reproductive science and women's health research at Johns Hopkins Medicine.

Segars was part of NICHD's answer to the 1993 law that requires an intramural research program with lab and clinical studies in both obstetrics and gynecology. The obstetrics research is carried out at a $15.5 million satellite intramural research program at Wayne State University. Stratakis oversees the tenured NICHD investigator Roberto Romero, who runs the program and supervises its 21 contract physicians and scientists, four of whom are women.

Gynecology research is headquartered in Bethesda where under Stratakis five veteran OB-GYNs left DIR. Three were women. All four labs conducting adult gynecology or infertility research have closed as well, including those of Nieman and Segars. "I am concerned that there is no meaningful basic science research going on in gynecologic disease at the moment," Serdar Bulun, chair of OB-GYN at Northwestern University's Feinberg School of Medicine, told Stratakis

Science Webinars

AAAS

Science Webinars help you keep pace with emerging scientific fields!

Stay informed about scientific breakthroughs and discoveries.

Gain insights into current research from top scientists.

Take the opportunity to ask questions during live broadcasts.

Get alerts about upcoming free webinars.

Sign up at: webinar.sciencemag.org/stayinformed

told him that the patients she had treated were mostly poor, with many uninsured. Virtually all had told her they could not pay the procedure's $16,000 price tag at private fertility clinics. "We at NIH are failing to do what is well within our means to protect [patients'] ability to bear children," she wrote.

Collins passed the letter to Michael Gottesman, NIH's deputy director for intramural research, who wrote to Wolff in March 2016 that he had concluded that egg freezing was "both appropriate and feasible" for Clinical Center patients. He added: "I can assure you that all patients whose fertility might be affected by these treatments will be offered the option of egg freezing."

More than 3 years passed before NIH resumed offering egg freezing to Clinical Center patients in July 2019. By late January of this year, 10 patients had taken advantage of it. NIH declined to explain the delay, saying only that in the interim the agency had "counseled" patients about getting egg freezing done outside NIH.

The lapse was "really unethical," says Joyce Reinecke, executive director of the nonprofit Alliance for Fertility Preservation. "You are potentially sterilizing people."

Infertility physician Kenan Omurtag of Washington University in St. Louis says his institution began to offer egg freezing as a service in 2012, "the minute" the experimental label was lifted. He calls the 3.5-year delay outrageous and says, "The right response is: 'What happened? Why did it happen? And how can we make sure it doesn't happen again?'" —*M.W.*

at a December 2019 meeting of his Board of Scientific Counselors. "There are major missed opportunities" for research on topics such as abnormal uterine bleeding, Bulun said.

In the meeting, Stratakis acknowledged the "thin" gynecology lab program but said relevant basic research also occurs in nonobvious places. Today, NICHD in Bethesda has one tenured OB-GYN, Alan Decherney, 78, whose lab Stratakis closed in 2015 and who now helps train infertility physicians. Stratakis also recently hired three female non–tenure-track gynecologists who focus on pediatric and adolescent gynecology.

One gynecologist who left DIR is Alicia Christy, who in 2013, after a mission trip to Uganda, applied for a Bill & Melinda Gates Foundation grant to assess how reducing barriers to the use of intrauterine devices would affect rates of unintended pregnancy in female farmers in sub-Saharan Africa. Stratakis signed her application. But Christy recalls him standing in her office returning the application to her, looking down at her and saying: "That's not our mission. Even if you get the money, I would never support you." She did not win the grant.

Beyond her own experience, Christy says, "I saw what he did to other women." She recalls a promising female DIR physician who won a highly competitive $360,000 research award from the American Association of Obstetricians and Gynecologists Foundation. NICHD said it could not spend the money on the young woman's research and returned it. She soon left the institute for private practice.

After her experience with the Gates Foundation grant, Christy moved out of DIR to the institute's extramural branch. "I took a lower position to not be under [Stratakis's] authority," she says.

NICHD declined to allow Stratakis to comment on Christy's account and declined to explain why the young physician's award was returned.

"I took a lower position not to be under [Stratakis's] authority."
Alicia Christy, formerly of NICHD

Another OB-GYN who left was Erin Wolff, 44, now an infertility consultant in McLean, Virginia. From 2011 to 2016, she was an assistant clinical investigator, part of an NICHD program grooming her to become a tenure-track scientist. She studied the uterine lining in monkeys and human patients, with the goal of designing therapies for abnormal uterine bleeding and infertility.

In 2015, Wolff accused Stratakis of sex discrimination in an EEO complaint, alleging that he set her up for failure, failed to find effective mentors for her, stared at her chest, and spoke to her condescendingly. She claims Stratakis pushed her to take over NICHD's infertility physician training program, a job she feared would compromise her chances to win a tenure-track research job. When she resisted and asked for a raise, presenting data showing that the next highest paid NIH physician in her job category was making $40,000 more than she was, Stratakis went on a "tirade," she alleges. He told her he had a plan for her future as a physician, not a scientist, she says. He "tried to belittle me, telling me that I had little potential."

Several months later, Wolff alleges, Stratakis and other NICHD officials targeted her, investigating all of her clinical studies for what Wolff contends were minor paperwork mistakes and protocol deviations in two of them—lapses of a sort that NICHD tolerated in male colleagues, she alleges. Her male mentor, who was associate investigator on one trial, was not investigated, she says. She adds that NICHD insisted that a program she launched to freeze eggs from young women faced with losing their fertility be structured as a research trial. Wolff contends it should have been offered as a patient service (see sidebar, p. 24).

In December 2015, Calis, vice chair of the institute's ethics committee, sent Wolff a memo saying it had suspended all her clinical studies.

NIH declined to comment. But in a 2018 affidavit responding to another woman's EEO complaint, pediatrician Forbes Porter, whom Stratakis had promoted to NICHD clinical director, wrote: "The decision to audit and suspend [Wolff's] protocols was a decision by the NICHD Institutional Review Board (IRB). The Wolff case has undergone multiple levels of review. None have found in favor of Dr. Wolff."

Wolff left the institute in June 2016 for a job with a company. In fall 2019, she and the agency agreed on a settlement.

"Constantine Stratakis effectively gutted our research division for women's health, and then my career, everything that I personally had invested in making this my life's mission," Wolff says. "It's tremendously heart-wrenching."

NICHD declined to comment and would not allow Stratakis to respond.

ON 1 JUNE, Stratakis is scheduled to assume his new position at the Research Institute of McGill University, overseeing 445 researchers, nearly 1200 trainees, and more than 1100 staff.

His departure will open a new chapter at NICHD, where his boss, Bianchi, said in a statement in response to questions from *Science*, "We absolutely support women." Bianchi became the institute's first permanent female director in 2016; she retained Stratakis after a performance review in 2018. Her statement noted that several other senior administrators at the institute are women.

Dixon says the individual women's stories, combined with the paucity of women running DIR labs and the loss of DIR gynecological research on adult women, "reveal that change is unfortunately slow." She says NICHD should be concerned. "They want to ensure the best and the brightest and the most capable researchers and doctors are addressing child health. Which means you can't exclude women." ■

This story was supported by the *Science* Fund for Investigative Reporting.

CALL FOR PAPERS

SPJ
SCIENCE PARTNER JOURNALS

spj.sciencemag.org/bmef

BME Frontiers

OPEN ACCESS

Biomedical Engineering (BME) Frontiers is a **Science Partner Journal** distributed by the **American Association for the Advancement of Science** (AAAS) in collaboration with the **Suzhou Institute of Biomedical Engineering and Technology, Chinese Academy of Sciences** (SIBET CAS). *BME Frontiers* aims to serve as an effective platform for the multidisciplinary community of biomedical engineering. The journal will publish breakthrough research in the fields of pathogenic mechanisms as well as disease prevention, diagnosis, treatment, and assessment.

The Science Partner Journals (SPJ) program was established by the American Association for the Advancement of Science (AAAS), the nonprofit publisher of the *Science* family of journals. The SPJ program features high-quality, online-only, open access publications produced in collaboration with international research institutions, foundations, funders and societies. Through these collaborations, AAAS expands its efforts to communicate science broadly and for the benefit of all people by providing top-tier international research organizations with the technology, visibility and publishing expertise that AAAS is uniquely positioned to **offer as the world's largest general science membership society**.

Submit your research to *Biomedical Engineering Frontiers* today!
Learn more at: **spj.sciencemag.org/bmef**

ARTICLE PROCESSING CHARGES WAIVED UNTIL 2021

NEXTGEN VOICES: ASK A PEER MENTOR

Seeking career clarity

We asked young scientists to serve as peer mentors for "Seeking Career Clarity," the author of the question below. By asking reflective questions, sharing relevant personal experiences, and offering advice, these scientists provide support and perspective. Follow NextGen Voices on Twitter with hashtag #NextGenSci. Read previous NextGen Voices survey results at https://science.sciencemag.org/collection/nextgen-voices. **—Jennifer Sills**

Dear NextGen VOICES peer mentors,

I am the first of my family to go to graduate school, and I'm about to defend my Ph.D. It has been a really tough few years, but I've finally completed all the requirements in my program. I published two papers and was a coauthor on several more. I was even given an "outstanding student" grant to attend a conference this year! Even so, this all feels quite average for a Ph.D. student, and I feel like I can attribute most of my achievements to luck. The support of my peers and adviser also helped me a lot. As I apply for jobs, I can often think of a colleague who seems more qualified for the position than I am. I fail to meet many of the requirements listed for jobs outside of academia, but the jobs I do qualify for seem like they're all for people with less education than I have. I want a job commensurate with my experience, but I don't want to oversell myself in applications or interviews. How can I realistically assess my own potential and avoid wasting time applying to jobs I could never get?

Sincerely,
Seeking Career Clarity

Prioritize, then go for it!

How can you win the lottery (i.e., get the job) if you haven't even bought a ticket (applied)? I was also the first in my family to go to college, let alone pursue a Ph.D. When my Ph.D. adviser sent me a postdoc ad for a position at one of the best universities in the United States, I asked her if such positions are worth applying to given that I didn't think I would be selected. She told me, "I think you can! I wouldn't have sent you the ad if I thought you couldn't do it." I thought, if someone believes in me so much, the least I can do is give it a shot! I ended up getting interviews for the first two applications I submitted and receiving offers for both positions. Make sure to set priorities; there are several factors to consider, including field of work, type of position, salary, location, and benefits. Once you have established your goals, start testing the waters. Be motivated, positive, and determined, and treat failures as opportunities for growth.

Chloe Antoniou
Department of Basic and Clinical Sciences, University of Nicosia Medical School, Nicosia, Cyprus. Email: antoniou.c@unic.ac.cy

Why are you worried that others are more qualified when you don't even know if they have applied for the job? List the types of

ILLUSTRATION: DAVIDE BONAZZI/THEISPOT

jobs you want (such as academia, industry, and government), the geographic areas where you'd like to go, and your skills. Apply for any jobs that fit at least two of those. No applicant is perfect. Apply for jobs you want, and don't worry about finding a "perfect" job. You might be surprised at where you find yourself in 5 years.

Katie Burnette
Department of Evolution, Ecology, and Organismal Biology, University of California, Riverside, Riverside, CA 92521, USA. Email: Katiec@ucr.edu

What are the parts about science and research that you most enjoy? For example, you might like troubleshooting tricky assays or explaining science to junior researchers. The answer to this question can help guide your career search. Ph.D. training has been described as intellectual hazing, and it can take some time to accept that you are our future's best hope. I've enjoyed the gradual realization that I am on the front lines of solving the world's most difficult and pressing questions.

Aaron Christensen-Quick
Inovio Pharmaceuticals, San Diego, CA 92121, USA. Email: AaronCQ85@gmail.com

Make connections

Have you considered using your network to find direct points of contact in the companies you apply to? Once you have a personal connection, you can point out that completing your Ph.D. highlights your research, analytical, organizational, and time management skills, which you can apply to any job. Demonstrating to potential employers that you are keen to learn and invest time into personal development (such as online courses) will show that you can soon fulfill their requirements and are a good investment. If you find a position that you are interested in and enthusiastic about, apply for it, even if you don't fulfill all the requirements.

Monika Lewinska
Biotech Research and Innovation Centre, University of Copenhagen, Copenhagen, 2200, Denmark. Twitter: @LewinskaMonika

Have you considered the conference you will attend this year as a career opportunity? I got my job after I did a presentation at a conference. If you are giving an oral presentation at the conference, prepare it and practice it at journal club. Highlight your scientific findings and emphasize your future research interests. If you participate in a poster session, describe your study logically and clearly and actively discuss it with others. Confidently presenting your work and making your career aspirations clear will increase the likelihood of a potential employer taking interest in you.

Yongsheng Ji
Department of Human Parasitology, Anhui Medical University, Hefei, Anhui, 230032, China. Email: jiyongshengkey@hotmail.com

Can you articulate specific differences between generic impostor syndrome and your assessment of your skills versus the job requirements? If yes, you may have identified an area to pursue some growth and development. If not, it may be time to give yourself a little more credit and tune out the inner naysayer. Before getting job offers, I constantly wondered whether I could make it into industry. Even after accepting an offer, I noticed how much better qualified my incoming cohort of colleagues seemed to be. Impostor syndrome never goes away, but I found that soliciting feedback helps to allay my fears and identify areas for growth. Seek out people who are already on the path(s) you wish to take, try to understand their journey, and solicit their feedback on your current skill set and experiences to identify areas you should work on to prepare for your own.

Muhammad M. Khalifa
Pharmaceutical Sciences Division, University of Wisconsin-Madison, Madison, WI 53703, USA. Email: mkhalifa503@gmail.com

Scientifically analyze self-doubt

When considering colleagues who seem better qualified for a position, ask yourself: "But did they apply for it?" No, you did. The competition is steep enough; do not add imaginary competition in your head. The attribution of achievements to luck is common in academia. Indeed, luck is part of life. If your luck corresponds only to positive achievements, it deviates from the gaussian distribution of randomness. Ask yourself how to explain that. You will find that your argument for luck does not stand statistical scrutiny. Meanwhile, keep in mind that a single universal CV will not be appropriate for all positions. Write a different application for each job, highlighting only what is relevant. Keep applying for positions that you find interesting, and think of an interview as a two-way process. You want to see what they provide as much as they want to see what you can do.

Athanasia Nikolaou
Department of Physics, Sapienza University of Rome, Rome, 185, Italy. Email: athanasia.nikolaou@uniroma1.it

You are asking many questions, but most of them seem to be about external factors. What are your interests? What is it that you would really like to do? Prioritize your career interests based on your passion, resources, and constraints such as time, training required to fill in the skill gaps, geography, and finances. If you are able to argue against yourself, you should also be able to argue for yourself. As a scientist, consider which argument is more evidence-based. Since you seem to have a good support network of advisers and peers, it is also worth relying on their assessment of you (keeping in mind that you don't want to become overly dependent on others' opinions and validation). Once you have made your personal profile, align it to the job market. Identify the skill gaps and actively seek the resources and networks to fill them in. Balance your internal profile by considering your past achievements and also what you strive to do and learn in the future.

Pragya Srivastava
Department of Bioengineering, University of Pennsylvania, Philadelphia, PA 19104, USA. Twitter: @pragya_srivas

Remember that you are unique

Congratulations on defending your Ph.D.! What a huge accomplishment! To help me give you better advice, what types of work or experiences did you enjoy during graduate school and what aspects did you not like? Are there any types of work or fields that you tangentially experienced but would like to explore more? Trust that you know yourself better than anyone. No job is a life sentence. If you don't like it, find another one. Regarding the feeling that you're just an average Ph.D., remember that getting a Ph.D. is very difficult and equivalent to 4 to 5 years of work experience plus project management and possibly supervisory experience. Your skeptical mind-set is beneficial for experiment planning and data analysis but not for assessing your own self-worth. Write out all of your accomplishments, lab responsibilities, and skills, no matter how obscure or common. You are the only person with that specific set of work experience in the whole world! Sell that!

Brynn Anne Hollingsworth
American Association for the Advancement of Science (AAAS) Science and Technology Policy Fellow, Rockville, MD 20850, USA. Email: bahsynchro@gmail.com

Have you thought about where you were at the start of your Ph.D. and what you have achieved now? I have found that comparing myself to others leads to imposter syndrome. Others tend to share their successes while being less open about failures. It might help to make a list with your strengths and achievements and use it to build your

application for the job you desire. A Ph.D. program gives you many marketable skills that are not obvious, such as project management and managerial skills.

Norman van Rhijn
Manchester Fungal Infection Group, University of Manchester, Manchester, Lancashire, M13 9XX, UK. Twitter: @NormanRhijn

Have you tried focusing on the processes that led to your achievements? By doing such an exercise, you may discover what you enjoy most about science. Next, look for positions where you will experience challenges that force you to refine the processes you enjoy. This way, you will keep doing what you love and loving what you do.

Saumya Saurabh
Department of Developmental Biology, Stanford University, Stanford, CA 94305, USA. Twitter: @saumya_s

Have you considered the possibility that you are not overselling but underselling yourself? I have encountered many situations where I thought I was not qualified for a position or workshop, but when I attended, I realized that I could fit right in. I suggest that you apply for the positions that you feel you are not qualified for, and you will be surprised by how many times you will hear back and be invited for interviews. Eventually, you will realize that your experience and knowledge are unique, and there will be places where you are the perfect fit and much more qualified than any other candidate. Remember that the safest way not to get a job is not to apply for it.

Nikos Konstantinides
Department of Biology, New York University, New York, NY 10003, USA. Twitter: @nkonst4

Value your own hard work

Have you considered why you think your scholarly achievements have been attributed to luck rather than your dedication, hard work, and good support system? I am a first-generation student, and despite recognition for my achievements, I still sometimes feel imposter syndrome creeping up, forcing me to question myself. However, my advice to you is: Just go for it! If you find your dream job and are lacking in some of the necessary skills or content areas, be honest with the employer. Discuss both your strengths and weaknesses and how you would be willing to improve those weaknesses if offered the position. For example, I am not an expert in some of the statistical analyses I will be conducting during my postdoc research, but I emphasized in my interview and application materials how I would be willing to participate in professional development opportunities to gain the relevant skills. Be confident that your Ph.D. is proof of your perseverance, knowledge, and skills.

Ashley Barbara Heim
School of Biological Sciences, University of Northern Colorado, Greeley, CO 80631, USA. Email: ashley.heim@unco.edu

Why do you attribute most of your achievements to luck rather than work ethic and talent? My first semester of graduate school was punctuated with feelings of being an impostor. I felt as though sheer luck had been the only thing that brought me as far as I had come, and I feared that others too would see me as an impostor. However, I soon discovered that I was not alone, and that I had overexaggerated the accomplishments of my peers while undervaluing my own accomplishments and intellect. Work ethic and dedication are the primary determinants of success. You have boundless potential to have a successful career as long as you remember that hard work and diligence will propel you forward.

Eric Britt Moore
Department of Agronomy, Iowa State University, Ames, IA 50011, USA. Email: ebm256@iastate.edu

Why do you attribute your Ph.D. accomplishments to luck? There is a reason why Pasteur's quote, "Chance favors the prepared mind," has stood the test of time. I have found it's helpful not to measure yourself against others. Instead, I measure myself by asking whether I am doing the best that I can and whether there are things I can improve. I would suggest applying first for the jobs you want the most. If new skills are needed, learn them. If you don't succeed in the first round, assess the feedback and broaden your search. What may look like a suboptimal job posting may in fact turn out to be your life passion, so steer the wheel, mind the rudder, and chart your own path that will bring you fulfillment and satisfaction.

Michael Strong
Center for Genes, Environment, and Health, National Jewish Health and University of Colorado, Anschutz Medical Campus, Denver, CO 80206, USA. Email: strongm@njhealth.org

Trust your support network

Have you asked your adviser and peers to list your strengths in researching, presenting your work, and as a person? I do not believe that finishing your Ph.D. has anything to do with luck. It is a result of hard work and perseverance. The only luck I could see in your case is a positive and supportive working environment. I would trust the people who believe in you to boost your self-esteem and not be afraid that you will oversell yourself.

Aleksandra Kosanic
Zukunftskolleg, University of Konstanz, Konstanz, D 78457, Germany. Twitter: @SashaKosanic

Have you asked your colleagues (peers and professors) about the role that serendipitous circumstances played in helping them to get their first postdoctoral job? While publications and awards are important for the screening process, your personal traits and organizational fit will determine whether you get the position. My doctoral colleagues who had more advanced technical skills and publications served as a poor benchmark for assessing whether I had a realistic opportunity of being considered for a job. The recent hires in the company or department were a better indicator: If they had eclectic backgrounds and achievements as well as skills similar to my own, then I would often be interviewed and shortlisted.

Samuel Nathan Kirshner
School of Information Systems and Technology Management, University of New South Wales, Sydney, NSW 2052, Australia. Email: s.kirshner@unsw.edu.au

Have you talked to your contemporaries to find out whether they are feeling the same way? Many of them are probably equally doubtful about the novelty of their achievements and may consider you to be more qualified for jobs, just as you perceive them to be more deserving. You can also contact your seniors who are already pursuing the career of your choice. They can help you reshape your profile according to the requirements of a specific job.

Antarip Halder
Solid State and Structural Chemistry Unit, Indian Institute of Science, Bengaluru, Karnataka, 560012, India. Email: antarip.halder@gmail.com

Have you reached out to someone more experienced and well-respected in your field? Seek opinions and feedback from senior researchers you trust and respect, such as your Ph.D. supervisor or other faculty members. Ask them to evaluate your achievements and identify your potential with complete honesty and objectivity. The confirmations you receive will fuel your self-confidence.

Khor Waiho
Institute of Tropical Aquaculture and Fisheries, Universiti Malaysia Terengganu, Kuala Nerus, Terengganu, 21030, Malaysia. Email: waiho@umt.edu.my

10.1126/science.abb6859

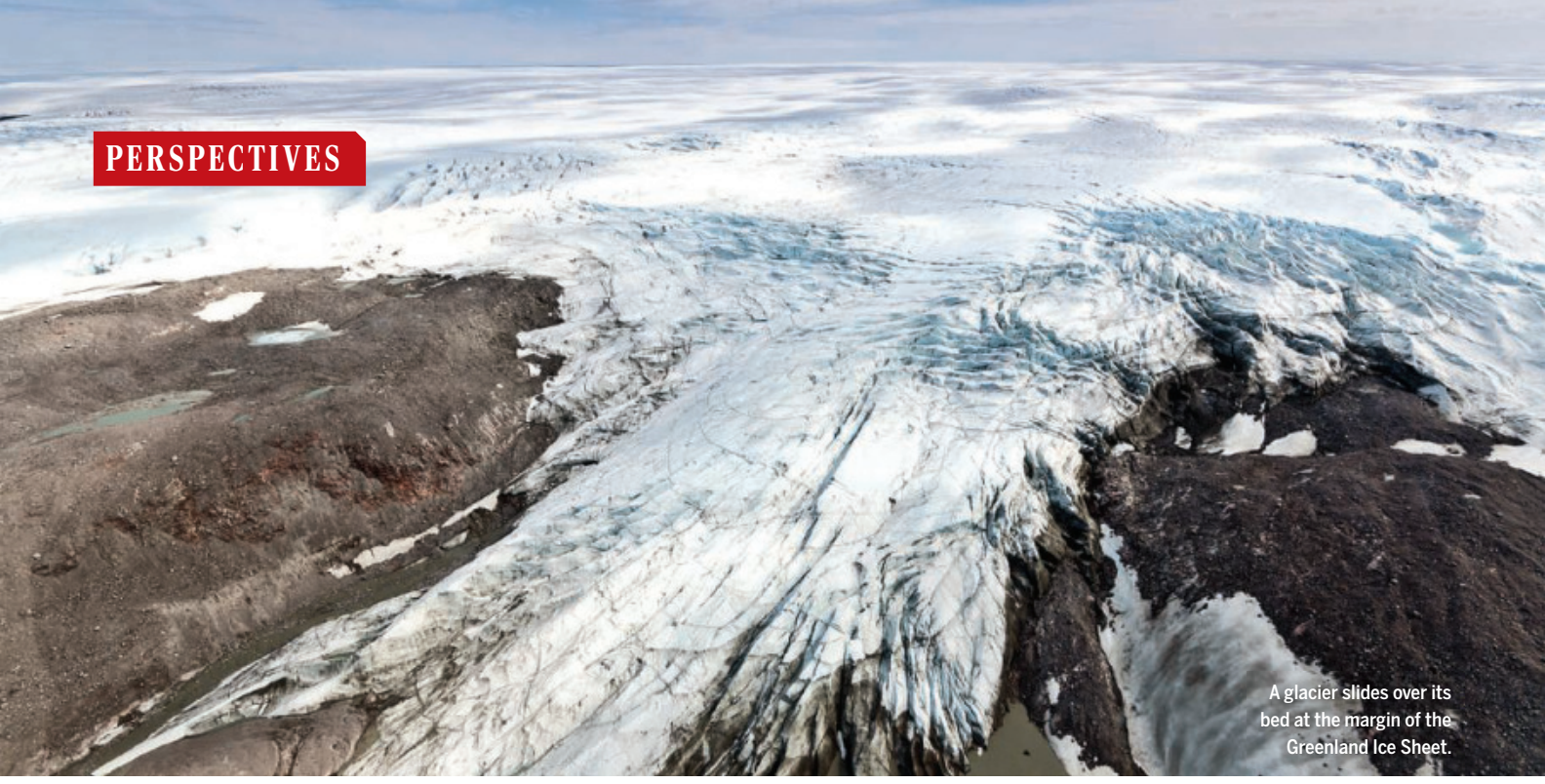

A glacier slides over its bed at the margin of the Greenland Ice Sheet.

PHOTO: IAN JOUGHIN

GEOLOGY

Toward a universal glacier slip law

A new friction rule may describe ice flow over rigid or deformable surfaces

By **Brent Minchew**[1] *and* **Ian Joughin**[2]

Glaciers and ice sheets shape Earth's surface and are important components of the climate system. Among the notable effects of glacier flow are erosion and sedimentation of Earth's surface and variations in sea level as glaciers lose or gain mass. These effects depend on the slip of glaciers along their beds, which is accompanied by drag at ice-bed interfaces. Parameterizations of drag with slip rate are called sliding or slip laws. Recent acceleration in glacier flow and rates of mass loss in Greenland and Antarctica highlight the need to better understand and parameterize glacier sliding (*1*–*4*). On page 76 of this issue, Zoet and Iverson (*5*) present a slip law for deformable sediment that is similar to laws derived for rigid beds, thereby supporting a universal slip law that could improve projections of ice sheet contributions to sea level.

Given that myriad processes act at the ice-bed interface, it is not immediately obvious that a universal slip law should exist. Glaciers slide over beds that vary from rigid bedrock to deformable sediment, with slip defined as the combination of sliding along the ice-bed interface and deformation of the bed itself (*6*). Irrespective of composition, glacier beds have roughness features that influence drag but are difficult to characterize from observations (*7*, *8*). Water at the bed acts as a lubricant. When this water is pressurized to nearly the overburden pressure (weight of ice column per unit area) of the glacier, cavities can form downstream of bumps in the bed, decoupling the ice from the bed (*8*, *9*). Thus, basal water pressure influences slip while introducing complexities as it varies spatially and temporally in response to changes in basal and surface melt rates and evolution of hydrological systems above, below, and within the glacier (*6*, *10*).

The potential for a universal form of the slip law is underpinned by the fact that total drag is the sum of skin friction and form drag. Skin friction describes the resistance to sliding along an interface, whereas form drag results from the pressure gradient associated with flow around an object. In the context of a slip law, the important distinctions between these two mechanisms are their dependencies on water pressure and the rate of slip at the bed.

Form drag strongly depends on flow speed but does not directly depend on water pressure. Conversely, skin friction strongly depends on water pressure but is essentially independent of the slip rate. Thus, a slip law that represents only skin friction may be considered perfectly plastic (rate-independent), similar to Coulomb friction, in which drag equals the product of a friction coefficient and effective normal stress (pressure), the difference between overburden and water pressure (*11*, *12*). By contrast, a slip law representing only form drag with no cavity formation is rate-strengthening (drag increases with slip rate) and can take the form of a power-law relation between drag and slip rate (*7*). Allowing for cavity formation admits rate-strengthening, rate-weakening, and perfectly plastic behavior, depending on the bed properties and slip rate (*9*).

Zoet and Iverson derive a simple slip law for sediment-covered glacier beds, wherein the total drag is governed by form drag at slow slip rates and skin friction at faster rates. Form drag dominates when the bed is rigid and ice flows around rocks (clasts) at the ice-bed interface. Skin friction dominates when the bed is deforming and friction acts on sediment grain boundaries. Thus, the transition between the two drag mechanisms is controlled by the shear strength (or yield stress) of the sediment, defined as the product of the effective pressure and the tangent of the internal friction angle (*11*, *12*) (see the figure). Zoet and Iverson benchmark their model with several laboratory experiments that examine glacier slip over glacial sediment. These experiments were conducted under constant water pressure

[1]Department of Earth, Atmospheric and Planetary Sciences, Massachusetts Institute of Technology, Cambridge, MA, USA. [2]Polar Science Center, Applied Physics Lab, University of Washington, Seattle, WA, USA. Email: minchew@mit.edu

Universal glacier slip law

New evidence suggests that a single glacier slip law can describe slip over the full spectrum of glacier bed types, from rough, rigid beds to deformable, sediment-covered beds. Such a universal slip law should improve projections of glacier and ice sheet mass loss.

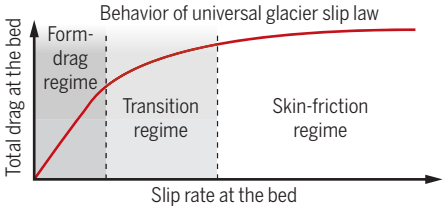

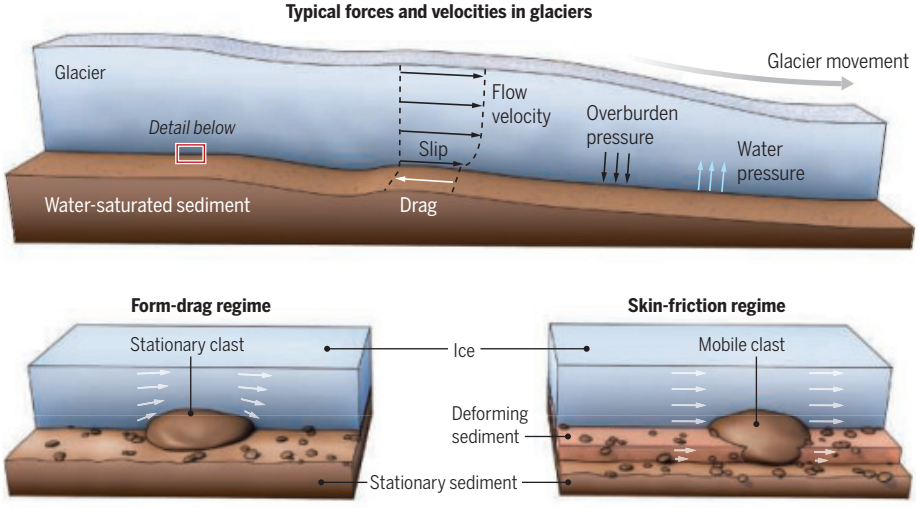

with and without centimeter-scale clasts embedded in the sediment, and at slip rates ranging from zero to moderately fast by glacier standards (~500 m/year). Overall, they found good agreement between their model and experiments.

Zoet and Iverson focus on glaciers with deformable beds, but their slip law has the same form as the so-called regularized Coulomb sliding law originally proposed for glaciers sliding over rough, rigid beds (*9*). At slow slip rates, the two laws represent form drag due to flow of ice around roughness features. The transition to plasticity at faster slip rates in the rigid-bed model, however, arises from cavity formation that reduces the ice-bed contact area and, thereby, form drag. The limit on drag at rapid sliding rates is governed by the product of effective pressure and the tangent of the maximum bed slope, known as Iken's bound (*13*), which is a different physical mechanism with the same functional form as skin friction in the Zoet and Iverson model. Despite the differences in physical mechanisms, the deformable-bed and rigid-bed models yield the same parameterization, suggesting that the form of the regularized Coulomb sliding law is universally applicable to glaciers irrespective of bed type (*1*). A major benefit of this similarity is that observationally constrained models can be used to infer the slip law parameters without prior knowledge of whether the bed is rigid or deforming.

The potential for a universal form of the slip law is encouraging but remains to be thoroughly tested with observations. The increasing availability of remote sensing datasets has enabled a few relevant studies by providing measurements of spatiotemporal variations in glacier flow velocity and surface elevation. Most of these studies support the use of the regularized Coulomb sliding law (*1*, *14*, *15*), although more work is needed to test the robustness of this slip law and to constrain the parameters. Zoet and Iverson's laboratory experiments have provided strong evidence suggesting that the regularized Coulomb sliding law works similarly well for deformable beds as theory and observation suggest for rigid beds (*1*, *9*, *15*). This is an encouraging development that should help reduce uncertainties in sea level projections. ■

REFERENCES AND NOTES

1. I. Joughin, B. E. Smith, C. G. Schoof, *Geophys. Res. Lett.* **46**, 4764 (2019).
2. The IMBIE Team, *Nature* **579**, 233 (2020).
3. C. Ritz *et al.*, *Nature* **528**, 115 (2015).
4. J. Brondex, F. Gillet-Chaulet, O. Gagliardini, *Cryosphere* **13**, 177 (2019).
5. L. K. Zoet, N. R. Iverson, *Science* **368**, 76 (2020).
6. K. M. Cuffey, W. S. B. Paterson, *The Physics of Glaciers* (Elsevier, ed. 4, 2010).
7. J. Weertman, *J. Glaciol.* **3**, 33 (1957).
8. A. C. Fowler, *J. Glaciol.* **33**, 255 (1987).
9. C. Schoof, *Proc. R. Soc. London Ser. A* **461**, 609 (2005).
10. G. E. Flowers, *Proc. R. Soc. London Ser. A* **471**, 20140907 (2015).
11. B. Kamb, *J. Geophys. Res.* **96**, 16585 (1991).
12. S. Tulaczyk, W. B. Kamb, H. F. Engelhardt, *J. Geophys. Res.* **105**, 463 (2000).
13. A. Iken, *J. Glaciol.* **27**, 407 (1981).
14. B. Minchew *et al.*, *J. Glaciol.* **62**, 147 (2016).
15. F. Gillet-Chaulet *et al.*, *Geophys. Res. Lett.* **43**, 10311 (2016).

10.1126/science.abb3566

MEDICINE

Tuning drug binding

Understanding anticancer drug binding to its target could improve drug discovery and efficacy

By **Dea Slade**[1] *and* **Sebastian Eustermann**[2]

Inhibitors of poly(ADP-ribose) polymerase 1 (PARP-1) are used to treat ovarian and breast cancer (*1*). PARP-1 is activated on binding single-stranded DNA breaks (SSBs) and released from DNA by automodification (auto-PARylation) (*2*, *3*). By preventing auto-PARylation, PARP inhibitors induce PARP-1 trapping on DNA (*4*). PARP inhibitors have similar in vitro potency in reducing PARP-1 activity, but their ability to induce cell killing differs substantially, most likely owing to differential potency in trapping PARP-1 on DNA (*5*, *6*). In addition to catalytic inhibition, PARP-1 trapping was proposed to rely on reverse allosteric changes within PARP-1 from the catalytic domain to the DNA binding domain (*5*–*7*). On page 46 of this issue, Zandarashvili *et al.* (*8*) dissect the allosteric effects of different PARP inhibitors and show how these can be harnessed for targeted design of new pro-trapping or pro-release PARP inhibitors, which may have greater efficacy and versatile application potential.

A particularly enigmatic form of allosteric regulation lies at the heart of PARP-1 activation (*2*). A cascade of structural changes is triggered when a single PARP-1 molecule encounters an SSB: The flexibly connected PARP-1 domains no longer behave like beads on a string but instead engage each other in communicating the DNA damage signal from the amino-terminal zinc fingers toward the Trp-Gly-Arg (WGR) domain and the carboxyl-terminal domain, which consists of the helical domain (HD) and the catalytic adenosine diphosphate (ADP)–ribosyltransferase domain. Partial unfolding of the HD relieves its autoinhibitory effects and allows the NAD^+ (oxidized form of nicotinamide adenine dinucleotide) cofactor to access the

[1]Max Perutz Labs, University of Vienna, Vienna Biocenter, Dr. Bohr-Gasse 9, 1030 Vienna, Austria. [2]Structural and Computational Biology Unit, European Molecular Biology Laboratory (EMBL), Heidelberg, Germany. Email: dea.slade@univie.ac.at; sebastian.eustermann@embl.de

GRAPHIC: C. BICKEL/*SCIENCE*

catalytic site. As a result, the catalytic domain is allosterically activated (*2*, *7*, *9*).

PARP inhibitors compete with NAD^+ for the PARP-1 active site. Clinically relevant PARP inhibitors were proposed to induce PARP-1 trapping through "reverse allostery" (*5*), whereby allosteric changes spread in a reverse direction from the catalytic domain onto the HD, WGR domain, and DNA binding domain (*2*, *7*). So far, reverse allostery has been demonstrated for the nonclinical PARP inhibitor benzamide adenine dinucleotide (BAD), a nonhydrolyzable NAD^+ analog (*7*). Zandarashvili *et al.* used hydrogen-deuterium exchange mass spectrometry to probe the effect of clinically relevant PARP inhibitors on allosteric changes within different PARP-1 domains. Furthermore, to assess how allosteric changes interlink with PARP-1 DNA trapping, the authors determined PARP-1 SSB affinity and dissociation rates in the presence of PARP inhibitors in vitro.

In accordance with previous results (*7*), another NAD^+ analog, EB-47, induced pronounced allosteric changes and strong PARP-1 DNA trapping in vitro, consistent with the reverse allostery model (*5*, *7*). Zandarashvili *et al.* classified this NAD^+ analog as a type I pro-retention inhibitor. Clinically relevant PARP inhibitors induced either no allosteric changes or opposite allosteric changes from those observed for the NAD^+ analog, which calls into question reverse allostery as the mechanism of PARP-1 trapping by clinical PARP inhibitors. The PARP inhibitors talazoparib and olaparib caused weak or no allosteric changes, destabilization of the HD, and weak PARP-1 DNA trapping in vitro. These were classified as type II mild or no pro-retention inhibitors. Other PARP inhibitors—veliparib, niraparib, and rucaparib—induced pronounced allosteric changes that involved stabilization of the HD and increased PARP-1 release from SSBs. Thus, these were classified as type III pro-release inhibitors. This is concordant with weak cellular PARP-1 trapping reported for these inhibitors (*5*). PARP-1 trapping is favorable in cytotoxic anticancer treatment, where pro-retention PARP inhibitors induce replication stress, mitotic catastrophe, and cancer cell death (*1*). PARP inhibitors are also indicated for stroke and heart failure, where PARP-1 overactivation causes energy depletion and cell death (*10*). In such conditions, pro-release PARP inhibitors would be the drugs of choice because they do not induce cell death (see the figure).

Cellular PARP-1 trapping by clinical PARP inhibitors is typically assessed by measuring the shift in PARP-1 distribution in the nucleus from being soluble to chromatin-bound (*4*–*6*). Although the in vitro measurements of Zandarashvili *et al.* classify talazoparib as a mild pro-retention PARP inhibitor, cellular measurements reveal its strong pro-retention properties (*6*). Adding further to the complexity of biochemical and physiological system comparisons, ovarian cancer patient mutation $Arg^{591}Cys$ in the PARP-1 WGR domain was found to reduce olaparib-mediated PARP-1 trapping in cells (*11*). This residue is critical for allosteric pro-retention effects of PARP inhibitors, suggesting that allosteric regulation could also play a role in olaparib-mediated PARP-1 trapping in cells.

The apparent disparity between PARP-1 trapping measurements in vitro and in cells suggests that additional factors determine the efficiency of cellular PARP-1 trapping. Indeed, a myriad of chromatin factors, DNA damage response proteins, and RNAs are known to interact with PARP-1. PARP-1–interacting protein histone PARylation factor 1 (HPF1) recently emerged as a fascinating example of a PARP-1 modulator that directs catalytic specificity toward serine ADP-ribosylation by forming a joint active site with PARP-1 or PARP-2. HPF1 likely also modulates cellular PARP-1 trapping by PARP inhibitors (*12*). Moreover, the dynamic nature of PARP-1 enables its activation on binding not only SSBs but also unligated Okazaki fragments during DNA replication, illustrating its engagement in different pathways: DNA repair and replication fork stability (*13*). Therefore, its allosteric multidomain cascade provides a rapid switch for activation as well as pathway-specific regulation (*2*).

On the basis of the structural insights into allosteric changes induced by type I pro-retention inhibitors, Zandarashvili *et al.* converted the type III inhibitor veliparib into a new-generation type I veliparib variant, UKTT15, which induces type I pro-retention allosteric effects and shows increased cytotoxicity compared with veliparib. Among all clinically relevant PARP inhibitors, veliparib shows the highest selectivity for PARP-1 and PARP-2 inhibition (*14*). Enhancing PARP-1 trapping while preserving high selectivity is an example of intelligent drug design that can be extended to other available PARP inhibitors for customized application in different disease settings. However, this strategy may increase cytotoxicity to normal cells, which could increase side effects (*1*, *15*). The potential of targeting allosteric changes for drug discovery is only just beginning to be harnessed. ■

Allosteric modulation

Poly(ADP-ribose) polymerase 1 (PARP-1) is allosterically activated upon binding to single-stranded DNA breaks. Pro-retention and pro-release PARP inhibitors differentially harness PARP-1 allostery to induce PARP-1 trapping or release from DNA, which can be applied in the clinic depending on whether cytotoxicity or cytoprotection is desirable.

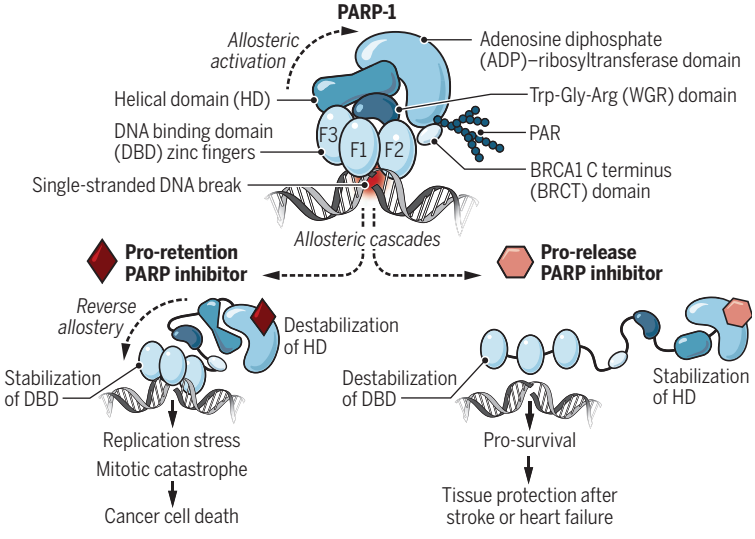

GRAPHIC: KELLIE HOLOSKI/*SCIENCE*

REFERENCES AND NOTES

1. D. Slade, *Genes Dev.* **34**, 360 (2020).
2. S. Eustermann *et al.*, *Mol. Cell* **60**, 742 (2015).
3. M. F. Langelier *et al.*, *Science* **336**, 728 (2012).
4. T. A. Hopkins *et al.*, *Mol. Cancer Res.* **13**, 1465 (2015).
5. J. Murai *et al.*, *Cancer Res.* **72**, 5588 (2012).
6. J. Murai *et al.*, *Mol. Cancer Ther.* **13**, 433 (2014).
7. M. F. Langelier *et al.*, *Nat. Commun.* **9**, 844 (2018).
8. L. Zandarashvili *et al.*, *Science* **368**, eaax6367 (2020).
9. J. M. Dawicki-McKenna *et al.*, *Mol. Cell* **60**, 755 (2015).
10. N. J. Curtin, C. Szabo, *Mol. Aspects Med.* **34**, 1217 (2013).
11. S. J. Pettitt *et al.*, *Nat. Commun.* **9**, 1849 (2018).
12. M. J. Suskiewicz *et al.*, *Nature* 10.1038/s41586-020-2013-6 (2020).
13. H. Hanzlikova, K. W. Caldecott, *Trends Genet.* **35**, 412 (2019).
14. A. G. Thorsell *et al.*, *J. Med. Chem.* **60**, 1262 (2017).
15. T. A. Hopkins *et al.*, *Mol. Cancer Res.* **17**, 409 (2019).

ACKNOWLEDGMENTS

D.S. is supported by the Austrian Science Fund (P 31112 B28).

10.1126/science.abb1462

COMPLEX OXIDES

Straining quantum materials even further

A nanoscale membrane enables exploration of large tensile strains on complex oxides

By **Christianne Beekman**

Quantum materials display strong electron-electron correlations that lead to distinctive electronic properties because charge, spin, orbital, and structural degrees of freedom are highly intertwined. Examples include unconventional superconductivity and nematicity in high–critical temperature (T_c) superconductors (*1*), charge-orbital ordered states (*2*), and exotic magnetic states (*3*). For many of these states of matter, we do not yet understand their origin (*4*), but it is clear that they form when the system is on the verge of instability—that is, near a phase boundary between competing ground states. Phase diagrams in which order parameters are plotted against external perturbations (field, composition, or strain) are important tools for recognizing patterns in complex systems. On page 71 of this issue, Hong *et al.* (*2*) made thin membranes of the perovskite manganite $La_{0.7}Ca_{0.3}MnO_3$ to apply large tensile strains and investigate previously inaccessible parts of its phase space.

Complex oxides such as perovskite manganites are highly tunable and stable materials with rich phase diagrams. For example, colossal magnetoresistance was recently observed in an oxide at room temperature (*5*), where application of a field leads to a large drop in resistance around a temperature-dependent metal-to-insulator transition. Clearly, temperature, applied magnetic fields (*1*), and structural changes (*6*, *7*) can tip the balance between competing phases. The strong entanglement of spin, charge, and orbital degrees of freedom with the lattice in particular stems from the strong electron correlations limiting the number of electrons that can reside at a specific lattice site. Furthermore, orbital hybridizations between neighboring atoms govern the macroscopic properties of materials, as they determine the pathways of electron exchange between atomic sites. Thus, the correlations, bonding properties, and orbital order within these materials play key roles in determining their functional properties.

Structural tuning of materials that affect the atomic spacing and the local structural environment around an atom within a crystal can be done in several ways. In bulk materials, application of hydrostatic pressure leads to isotropic compressive strain fields, which equally decrease the atomic spacing in all directions in the material. It has been shown that pressure and strain can greatly enhance T_c and critical current density in iron pnictide and cuprate superconductors (*8*–*10*).

For epitaxial thin films, the lattice mismatch between the substrate and the film will determine the strain field that can be imposed. Such strain can be biaxial or uniaxial and can be compressive (atomic spacing decreases in the film plane with a corresponding increase in the out-of-plane direction) as well as tensile (atomic spacing increases in the film plane with a corresponding decrease in the out-of-plane direction). Usually, only a few substrates are compatible for growing the desired film material, so relatively few discrete tensile and compressive strain states of up to a few percent can be achieved. This limitation provides piecemeal access to phase space at best. Still, such "small" strains have been shown to greatly affect the properties of complex oxides (*6*, *7*, *11*, *12*).

A disadvantage of the epitaxial strain approach is that film growth will be subject to uncontrolled defect formation that facilitates strain relaxation, which results in strain and lattice parameter gradients across any given thin-film sample. The membrane technique presented by Hong *et al.* is fundamentally different in that large and homogeneous tensile strains can be applied across the entire thin oxide membrane. This is because they grew pristine thin films in bulk-like form on a lattice-matched buffer layer. Hence, the absence of a strain gradient greatly reduces the likelihood of crystal imperfections and disorder. Through the use of carefully selected water-soluble buffer layers, the membranes were transferred onto flexible substrates. The substrate and the oxide membrane were stretched laterally by applying tensile strain, up to ~8%. Not only could unprecedented large tensile strains be reached, but any arbitrary lower tensile strain value could also be investigated. Additionally, mild heating released the strain (up to 3%), so the process was reversible for smaller strain values.

For $La_{0.7}Ca_{0.3}MnO_3$, Hong *et al.* found that at low temperatures, large strain fields transformed the ferromagnetic metal into a charge/orbital-ordered (COO) insulator (see the figure). Furthermore, the application of magnetic fields revealed that this COO state can be "melted," reverting the system back to the metallic phase. Thus, materials can be successfully strain-tuned through correlation-driven phase transitions while varying other parameters, such as temperature and magnetic field.

Strain gains

Strain can be applied to quantum materials such as complex oxides in increments by epitaxial growth on substrates with lattice mismatch. Hong *et al.* induce continuous and large strain using flexible membranes.

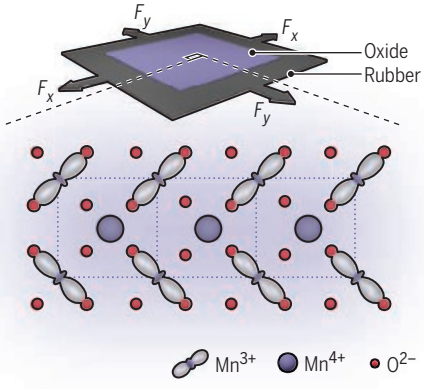

Pulling on complex oxides

Hong *et al.* transferred a pristine membrane of $La_{0.7}Ca_{0.3}MnO_3$ onto flexible substrates. They achieve uniaxial and biaxial tensile strains up to 8% by applying forces *F*. Only one layer of the oxide in the charge/orbital-ordered (COO) state is shown.

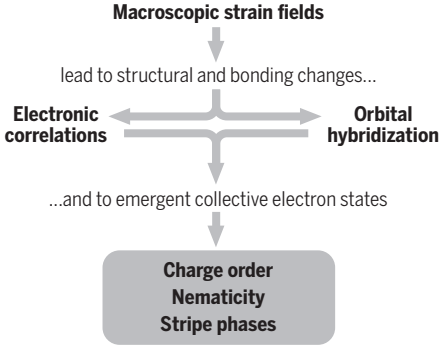

Exploring strain-induced properties

Changes in strain field alter electron correlations and bonding and create new collective electron states with distinctive magnetic and electronic properties.

GRAPHIC: A. KITTERMAN/*SCIENCE*

Department of Physics, Florida State University, and National High Magnetic Field Laboratory, Tallahassee, FL 32310, USA. Email: beekman@magnet.fsu.edu

The advancements in thin-film growth techniques and the ability to apply gradual and controlled changes to the crystal lattice using the strain technique presented by Hong *et al.* provide a new step in scientists' quest for materials by design. Furthermore, this applied strain can be biaxial and uniaxial, allowing anisotropic changes to unit cell symmetry and the orbital degrees of freedom. If interatomic distances, unit cell symmetries, and bond lengths and angles can be gradually and reversibly controlled in specific directions within a crystal, then orbital hybridizations (that is, electron-exchange pathways) and electronic correlation strengths can be manipulated (*13*) by using carefully designed coherent strain fields. The compatibility of this technique with applied magnetic fields opens up the exploration of magnetic phases. The ability to continuously synthesize and measure a wide range of high-quality materials under various (and sometimes extreme) conditions leads to a better understanding of the physics that they host.

The control of applied coherent strain fields developed by Hong *et al.* provides a platform for exploring and designing new properties in strongly correlated electron materials, as well as conventional materials. This method could be applied to nanostructures, which would provide a better understanding of microscopic behaviors associated with correlation-driven metal-insulator transitions and the often mesoscopic phase separation associated with them. One could also imagine constructing a phase diagram that shows the gradual and directional tuning of correlations in high-T_c superconductors, which could reveal how emergent collective electronic states, such as specific forms of charge order and nematicity, are linked to superconductivity (*1*, *14*, *15*). Answers to these major unsolved condensed matter physics problems are now within reach (*4*). ■

REFERENCES AND NOTES

1. F. Ronning *et al.*, *Nature* **548**, 313 (2017).
2. S. S. Hong *et al.*, *Science* **368**, 71 (2020).
3. P. Khuntia, *J. Magn. Magn. Mater.* **489**, 165435 (2019).
4. Special Issue on Strongly Correlated Electron Systems, L. H. Greene, J. Thompson, J. Schmalian, Eds., *Rep. Prog. Phys.* **80**(3) (2017).
5. S. Yamada *et al.*, *Phys. Rev. Lett.* **123**, 126602 (2019).
6. J. Hwang *et al.*, *Mater. Today* **31**, 100 (2019).
7. Y. E. Suyolcu, G. Christiani, P. A. van Aken, G. Logvenov, *J. Supercond. Novel Magn.* **33**, 107 (2019).
8. L. Gao *et al.*, *Phys. Rev. B* **50**, 4260 (1994).
9. H.-H. Kim *et al.*, *Science* **362**, 1040 (2018).
10. B. Shabbir *et al.*, *Sci. Rep.* **5**, 8213 (2015).
11. C. W. Hicks *et al.*, *Science* **344**, 283 (2014).
12. R. C. Haislmaier *et al.*, *Adv. Funct. Mater.* **26**, 7271 (2016).
13. A. Pustogow *et al.*, *Sci. Adv.* **4**, eaau9123 (2018).
14. S. Kasahara *et al.*, *Nature* **486**, 382 (2012).
15. R. M. Fernandes, A. J. Millis, *Phys. Rev. Lett.* **111**, 127001 (2013).

10.1126/science.aba6469

NEUROSCIENCE

Revealing animal emotions

Facial expressions in mice are detected and classified by machine learning

By **Benoit Girard** *and* **Camilla Bellone**

In his 1872 book, Charles Darwin established the basis for studying the expression of emotions (*1*). He described emotions as innate, universal, and endowed with communicative function. Darwin also proposed that facial expressions are the richest source of information about emotions for humans and animals. Numerous studies tried to identify and correlate facial expressions with emotions in nonhuman primates, horses, sheep, and dogs (*2*, *3*). Several of the methods to recognize emotions using facial expression in rodents are limited to a single emotion, require a long process of manual scoring, and are biased by human factors or difficult to reproduce (*4*, *5*). On page 89 of this issue, Dolensek *et al.* (*6*) used machine learning to objectively investigate stereotyped facial expressions and their neuronal correlates in mice in response to emotionally salient stimuli.

Emotions are functional brain states that usually cause external changes in behavior. Across animal species, emotions are used to communicate information about internal states and influence the way an individual makes decisions and takes actions to maximize survival (*7*). It is difficult to accurately, rapidly, and reproducibly identify emotions in animal models. Indeed, in humans, the subjective component of an emotion can be measured through self-evaluation and verbal expression. In animals, subjectivity can only be estimated with indirect measures. Homology to human behavior is currently used to recognize emotion in different animal species; identifying emotions using species-specific behavioral settings has been challenging so far (*8*, *9*).

Dolensek *et al.* report that, although it is possible for human observers to detect in animals facial movement in response to a set of sensory stimuli, it is difficult to intuitively classify the intrinsic attractiveness or aversiveness of the relative emotion. To overcome these limitations, they created an unsupervised learning algorithm to cluster and classify facial expressions of mice into different emotional events using quinine (disgust), sucrose (pleasure), lithium chloride (malaise), escape (active fear), freezing (passive fear), and tail shock

Department of Basic Neuroscience, University of Geneva, Geneve, Switzerland. Email: camilla.bellone@unige.ch

Emotions in mice

Dolensek *et al.* used a machine learning program to classify facial expressions of mice caused by various stimuli into emotions. When coupled with imaging of neuron activation, the authors identified neural circuits in the insular cortex that correlate with facial expression and could be linked to emotions.

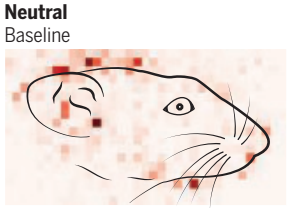

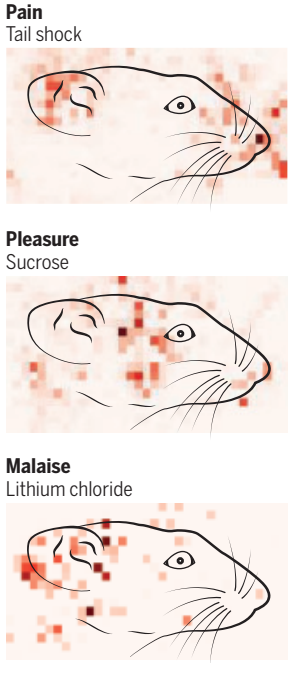

GRAPHIC: V. ALTOUNIAN/*SCIENCE* BASED ON DOLENSEK *ET AL.* (6)

(pain) (see the figure). The authors showed that changes in facial expression are not reflex-like reactions but reflected some of the properties of emotions, such as valence (positive or negative), scalability (graded nature of emotional intensity), and flexibility (ability to flexibly regulate emotions). Because facial expressions change quickly and the algorithm allows direct observation in real time, it became possible to investigate how neural circuits contribute to different emotions. By coupling the facial expression detection with in vivo calcium imaging to detect neuron activation, Dolensek *et al.* identified activation of "face-responsive" neurons in the insular cortex that correlate with facial expression but not with the stimuli per se.

The insular cortex, or insula, is part of the cerebral cortex that is important for the representation of feelings and emotions (*10*). Indeed, by integrating signals from within the body and the environment, the insula can assign the emotional valence of a specific experience. The possibility of identifying facial expression in mice will provide a tool for studying the neuronal mechanisms of insular functions.

"Facial expression may serve as a readout for emotional states associated with psychiatric disorders in rodent models."

In humans, identifying and understanding facial expression are important factors in social interaction that can be used to guide actions. Humans use constant facial expression to reveal moods and emotions to their peers. For example, a sad face could be considered an expression of mourning, but it could also be used to solicit a hug. Why do animals exhibit facial expressions, and why is it important to be able to detect them? Emotions help to prepare immediate action with minimal consciousness. For example, specific facial expression, such as disgust, modifies alertness for perception and action (*11*). The neurobiological basis for accurately responding to unexpected events by changing facial expression could be shared across species. Animals can use information provided by conspecifics (other members of the same species) to guide their own behavior. For example, rodents can change their food preference through interaction with a demonstrator or can learn spatial exploration through the observation of conspecifics. Furthermore, because rodents recognize and react to the pain of conspecifics (*12*), recognition of facial expressions will promote the investigation of empathy-associated behaviors and their neuronal correlates. Investigation of facial expression could help understanding of advanced and unexplored social behaviors such as the nature of interpersonal relationships, requests of specific social behavior, or control of behaviors in perceivers.

Not all emotions are equally expressed by humans. For example, culture and society could shape the expression of emotion such that an individual may feel fear or pleasure differently to others. Applying the approach used by Dolensek *et al.* will make it possible to study facial expression induced by a defined stimulus in different individuals and investigate whether the neuronal mechanisms underlying emotions are strongly conserved. Moreover, not only are there large individual differences in the expression of different emotions, but several psychiatric disorders such as anxiety disorders and depression are associated with emotional dysfunctions. Preclinical animal models of psychiatric disorders offer the advantage of studying the neuronal basis of behavioral deficits. Facial expression may serve as a readout for emotional states associated with psychiatric disorders in rodent models.

Dolensek *et al.* provide an objective analysis tool that is essential to be able to understand the neurobiological mechanisms of emotions, to identify species-specific emotions, and to identify their variability across individuals. However, although facial expression often reflects a genuine emotion, humans can pose expressions even in the absence of an underlying emotion. Can animals do this too? It is also interesting to consider whether using the approach proposed by Dolensek *et al.* will allow sufficient understanding of emotion to build robots that can read and react to human emotion to better interact with our society. ■

REFERENCES AND NOTES

1. C. Darwin, *The Expression of the Emotions in Man and Animals* (London, Murray, 1872).
2. C. Fureix, P. Jego, S. Henry, L. Lansade, M. Hausberger, *PLOS ONE* **7**, e39280 (2012).
3. T. Bloom, H. Friedman, *Behav. Processes* **96**, 1 (2013).
4. K. Finlayson, J. F. Lampe, S. Hintze, H. Würbel, L. Melotti, *PLOS ONE* **11**, e0166446 (2016).
5. D. J. Langford *et al.*, *Nat. Methods* **7**, 447 (2010).
6. N. Dolensek *et al.*, *Science* **368**, 89 (2020).
7. R. J. Dolan, *Science* **298**, 1191 (2002).
8. J. Panksepp, *Neurosci. Biobehav. Rev.* **35**, 1791 (2011).
9. D. J. Anderson, R. Adolphs, *Cell* **157**, 187 (2014).
10. N. Gogolla, *Curr. Biol.* **27**, 12 (2017).
11. J. M. Susskind *et al.*, *Nat. Neurosci.* **11**, 843 (2008).
12. D. J. Langford *et al.*, *Science* **312**, 1967 (2006).

ACKNOWLEDGMENTS

We thank C. Luscher and D. Jabaudon for helpful input during writing.

10.1126/science.abb2796

ANTHROPOLOGY

All who wander are not lost

New hominin cranial fossils highlight the early exploits of *Homo erectus*

By **Susan C. Antón**

Today's humans can learn a thing or two about life from *Homo erectus*, our most likely direct ancestor. Dispersed across Africa and Asia, *H. erectus* survived for more than 1.5 million years, enduring climatic, geographical, and ecosystem variability while coexisting with other closely related ancestral-human species and diverse animal populations (*1*). On page 47 of this issue, Herries *et al.* provide geochronological context for two new hominin cranial fossils (DNH 134 and DNH 152) that reveals some early habits of *H. erectus* (*2*).

Excavated in Drimolen, South Africa, DNH 134 and DNH 152 are from two different but contemporary genera, *Homo* and *Paranthropus*, respectively. The cranial fossils are the oldest known representatives of the species *Homo* aff. *erectus* and *Paranthropus robustus* and are contemporaries of a third genus, *Australopithecus* (known to take its last breaths in South Africa ~2 million years ago). Although once hotly debated, the coexistence of *Homo* and other early-human species is now broadly accepted (*3*). That *H. erectus* and *P. robustus* first appeared ~2 million years ago is more contested. Herries *et al.* provide the most precisely dated remains in South Africa, add more than 100,000 years to the first appearance dates of at least *H. erectus*, and reveal that *H. erectus* was a group of wanderers from the start.

Both Drimolen genera arose and diversified ~2.8 million to 1.5 million years ago in Africa. The earliest *Homo* was ~2.8 million years old (*4*). Right around, and just after, 2 million years ago, a variety of different morphs of *Homo* existed (see the figure) (*5*, *6*). The first *H. erectus* appeared in Kenya ~1.87 million years ago (*7*). *Paranthropus aethiopicus* and *Paranthropus boisei* arose in East Africa ~2.7 million and 2.3 million

Center for the Study of Human Origins, Department of Anthropology, New York University, New York, NY 10003, USA. Email: susan.anton@nyu.edu

years ago, respectively, and *P. robustus* existed in South Africa by ~1.8 million years ago (*8*, *9*). Thus, two or three species of *Homo* and *P. boisei* coexisted in East Africa for about a half million years, and in South Africa, *Homo* and *P. robustus* overlapped a bit longer. Only *H. erectus* persisted past this time.

The appearance and evolution of *Homo* and *Paranthropus* were influenced by challenges and opportunities that arose during a period of climatic variability and increasing aridity (*10*). Although both genera lived in increasingly open, but variable, habitats, they displayed different adaptations. Isotopic analyses suggest that they each had a relatively broad diet. But *Paranthropus* had massive teeth and jaws compared with those of *Homo* and likely built their diets around C_4 plants such as sedges and corms (*11*). This dietary habit might explain why *P. boisei* and *P. robustus* were regionally restricted in Africa.

By contrast, at least three species of *Homo* coexisted in Africa starting about 2 million years ago (see the figure). All three showed increased brain size but also had different facial structures; these included relatively primitive teeth and jaws (*H. habilis*) (*6*); distinct dental proportions, resulting in relatively flatter faces (*H. rudolfensis*) (*5*); and even larger brains and yet differently shaped faces and braincases (*H. erectus*) (*1*, *5*, *12*). Scientists have hypothesized that *Homo* as a genus relied more heavily on technological extraction of food resources (meat, marrow, and plants) and was behaviorally more flexible than *Paranthropus* or *Australopithecus* (*13*).

Even in light of the diversity among *Homo* species, *H. erectus* seems to be the beginning of something new. In the ~7-million-year history of the human lineage, *H. erectus* was the first species to leave the African continent (see the figure). In fact, almost as soon as they arose, *H. erectus* appeared outside of Africa at the site of Dmanisi in the Republic of Georgia (*14*). Over the next nearly 2 million years, *H. erectus* occupied a variety of different habitats and contexts before going extinct well after 0.5 million years ago on present-day Java (*1*). The initial moves in *H. erectus* dispersal were so quick that researchers have questioned whether *H. erectus* might instead have originated in Asia (*14*).

The Drimolen ages support an African origin by providing an even earlier age for the first African *H. erectus*. Given the strong evidence of early *Homo* species in East Africa, Herries *et al.* do not advocate for a South African origin of *H. erectus* but do reasonably conclude that their early presence at Drimolen signals an almost immediate habit of long-range dispersal.

Of course, the importance of context for fossil finds cannot be overstated, and all of these inferences hinge on the veracity of the geochronological data and species identifications. To date, the rich fossil cave assemblages of South Africa have featured less in discussions of human evolution—especially the origin and evolution of genus *Homo*—because the deposits are complex and difficult to date, fossils are fragmentary, and often, precious context has been lost to commercial mining. Unlike the East African open-air sites, with relatively straightforward stratigraphy and abundant interbedded volcanics suitable for $^{40}Ar/^{39}Ar$ dating, the karst systems of South Africa present complex sedimentary relationships and no ashes for dating.

The new study used a combination of other methods to date the flowstone and other sediments of the Drimolen quarry, identify flowstone-bounded units, decipher their lithology, assess relationships among units, and thus provide a rich context for the hominin remains. How firm are the species identifications? DNH 152 was recognized as *P. robustus* on the basis of dental morphology, but the DNH 134 assignation is less firm. The size and shape of the DNH 134 braincase (vault) merit its assignment to *Homo* and preclude its affiliation with two species of *Homo* living on the continent at the time (*H. rudolfensis* and *H. habilis*). *H. erectus* has a distinctly shaped vault compared with other early *Homo* species and one that is present even in young individuals; on this basis, the authors recognized DNH 134 as *H.* aff. *erectus*.

Yet, much of the differentiation among other early *Homo* species in East Africa is based on facial morphology (*5*, *6*). Thus, it is possible that greater species diversity is obscured by the dearth of faces from South Africa. Perhaps more species shared this brain shape but differed in facial anatomy than are visible to researchers because of the vagaries of preservation in the fossil record. This is a plausible concern across much of the Asian *H. erectus* range as well because so many assemblages lack facial remains (*1*).

For the time being, this vault shape is associated only with *H. erectus*, and the first appearance of it seems to be at ~2 million years ago in Africa. This marks the beginning of the most successful species of *Homo* ever known—present company included. ■

Temporal existence of archaic human species

Shown are the ages of fossils DNH 134 and DNH 152. Stone-tool time ranges are shown with wavy lines. The dashed part of the wavy line indicates lesser frequency of find sites.

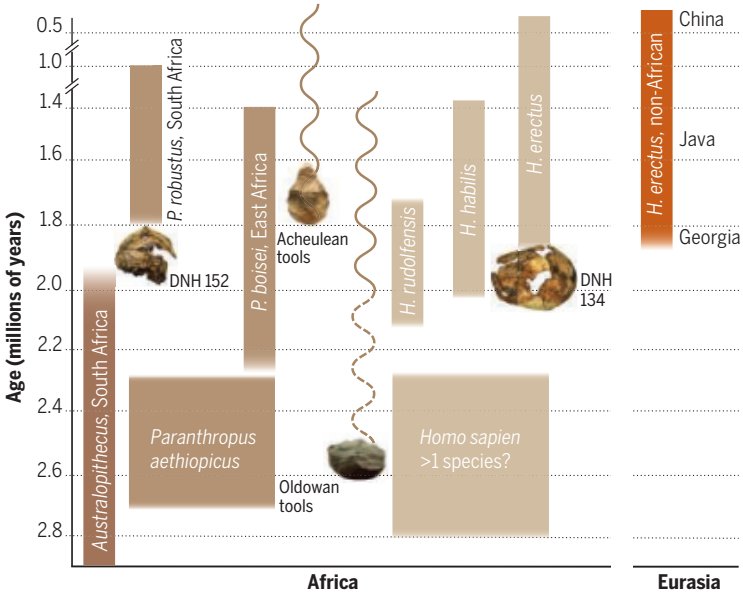

GRAPHIC: N. CARY/*SCIENCE*; (PHOTOS) ANTÓN *ET AL.* (*13*) AND HERRIES *ET AL.* (*2*)

REFERENCES AND NOTES

1. S. C. Antón, *Yearb. Phys. Anthropol.* **46**, 126 (2003).
2. A. I. R. Herries *et al.*, *Science* **368**, 47 (2020).
3. R. E. F. Leakey, A. C. Walker, *Nature* **261**, 572 (1976).
4. B. Villmoare *et al.*, *Science* **347**, 1352 (2015).
5. M. G. Leakey *et al.*, *Nature* **488**, 201 (2012).
6. F. Spoor *et al.*, *Nature* **519**, 83 (2015).
7. C. J. Lepre, D. V. Kent, *J. Hum. Evol.* **86**, 99 (2015).
8. T. Harrison, in *Paleontology and Geology of Laetoli: Human Evolution in Context*, T. Harrison, Ed. (Springer Verlag, 2011), vol. 2, pp. 141–188.
9. R. Gibbon *et al.*, *Quat. Geochronol.* **24**, 10 (2014).
10. R. Potts, *Quat. Sci. Rev.* **73**, 1 (2013).
11. G. A. Macho, *PLOS ONE* **9**, e84942 (2014).
12. F. Spoor *et al.*, *Nature* **448**, 688 (2007).
13. S. C. Antón, R. Potts, L. C. Aiello, *Science* **345**, 1236828 (2014).
14. R. Ferring *et al.*, *Proc. Natl. Acad. Sci. U.S.A.* **108**, 10432 (2011).

10.1126/science.abb4590

POLICY FORUM

ENERGY AND CLIMATE

Granular technologies to accelerate decarbonization

Smaller, modular energy technologies have advantages

By C. Wilson[1,2], A. Grubler[1], N. Bento[1,3], S. Healey[1,4,5], S. De Stercke[1,6], C. Zimm[1]

Of the 45 energy technologies deemed critical by the International Energy Agency for meeting global climate targets, 38 need to improve substantially in cost and performance while accelerating deployment over the next decades (*1*). Low-carbon technological solutions vary in scale from solar panels, e-bikes, and smart thermostats to carbon capture and storage, light rail transit, and whole-building retrofits. We make three contributions to long-standing debates on the appropriate scale of technological responses in the energy system (*2*, *3*). First, we focus on the specific needs of accelerated low-carbon transformation: rapid technology deployment, escaping lock-in, and social legitimacy. Second, we synthesize evidence on energy end-use technologies in homes, transport, and industry, as well as electricity generation and energy supply. Third, we go beyond technical and economic considerations to include innovation, investment, deployment, social, and equity criteria for assessing the relative advantage of alternative technologies as a function of their scale. We suggest numerous potential advantages of more-granular energy technologies for accelerating progress toward climate targets, as well as the conditions on which such progress depends.

We use "granularity" to describe technologies in terms of scale—physical, economic, or both. More-granular energy technologies have smaller and more variable unit sizes (MW/unit) and lower unit investment costs in absolute terms ($/unit), and are more modular or divisible, so they are more likely to scale through replication. We use "lumpiness" to describe the converse: larger units, higher unit investment costs, greater nondivisibility, and more likelihood of up-scaling in unit size. Granular-lumpy is a continuum, not a binary categorization. The figure shows bivariate relationships between measures associated with accelerated low-carbon transformation and granularity [see supplementary materials (SM) for detail and methods].

[1]International Institute for Applied Systems Analysis (IIASA), Laxenburg, Austria. [2]Tyndall Centre for Climate Change Research, University of East Anglia, Norwich, UK. [3]Instituto Universitário de Lisboa (ISCTE-IUL), DINÂMIA'CET, Lisbon, Portugal. [4]School of Resource and Environmental Management, Simon Fraser University, Burnaby, Canada. [5]Transport Canada, Ottawa, Canada. [6]Department of Civil and Environmental Engineering, Imperial College London, London, UK. Email: charlie.wilson@uea.ac.uk

RAPID TECHNOLOGY DEPLOYMENT

Rapid technology deployment depends on short diffusion time scales, attractive risk profiles for investors, and strong potential for cost and performance improvements (see the figure, red panels). These conditions are interdependent. Deployment generates experience, which feeds back into technology improvement. Improving competitiveness and reducing investment risk stimulate adoption and compress the time taken for technologies to diffuse through markets. Clear expectations for market growth attract further investment and strengthen the rationale for policy support. These dynamics are evident in recent trajectories of rapid solar photovoltaic (PV) deployment.

Short diffusion time scales

Early research on industrial process innovations found that smaller investment size and higher expected profitability predicted faster diffusion (*4*). We show that energy supply and end-use technologies with lower unit investment costs diffuse more quickly from 1 to 50% market share (see figure panel B and SM-1). Lower absolute unit costs mean that access to capital becomes less restricted or specialized, and opportunity costs decrease.

Attractive risk profiles for investors

Capital cost overruns on new energy infrastructure are a simplified measure of investment risk. Using a dataset of cost overruns in 350 electricity generation projects (*5*), we find that investment risk tends to increase for larger hydro, nuclear, and thermal plants but to decrease for larger solar and wind plants (SM-2). For more-granular renewable technologies, modular construction of standardized units means lower investment risks even at larger project sizes.

Cost and performance improvements

Learning describes how cumulative experience with each additional technological unit produced, installed, or used can lead to cost reductions and performance improvements. We show that learning is faster for more-granular energy technologies, using two different formulations of the learning rate (see figure panels F and G and SM-3). In both cases, more-granular technologies offer more opportunities for repetitive, replicative experience to drive faster improvement.

ESCAPING LOCK-IN

Useful energy services like mobility or heating are provided by hierarchical systems of technologies and infrastructures such as road networks, cars, and engines, or gas pipelines, buildings, and furnaces. Tackling climate change means overcoming "lock-in" or inertia in fossil-fuel–dependent systems (*6*) (SM-4). This depends, inter alia, on rapid renewal of capital stock, low technological complexity, and downsizing the system through end-use efficiency and demand reduction (see the figure, blue panels). Long-lived energy infrastructure and strong interdependencies between technologies increase switching costs and slow down change. Rapid innovation cycles in simpler, short-lived technologies create more opportunities to develop, test, deploy, and learn how to challenge incumbent processes. Downsizing the system by reducing aggregate demand for energy further reduces switching costs and counteracts the increasing returns to scale on which incumbent firms' dominant market positions are built.

Rapid renewal of capital stock

How long capital stock remains technically viable as well as economically attractive will determine renewal rates. More-granular technologies at the lower levels of the system hierarchy have shorter technical lifetimes (see figure panel C and SM-4). Obsolescence opens up opportunities for upgrades, substitutions, or replacements. Shorter lifetimes allow for more rapid turnover and so more rapid entry of low-carbon alternatives.

Low technological complexity

More-granular energy end-use technologies have fewer components and hence lower technological complexity (see figure panel D and SM-5). Less complex technologies present lower interoperability and coordination challenges at the component level, which in turn helps stimulate more rapid innovation cycles.

Downsizing through end-use efficiency

More-granular technologies offer larger potential efficiency gains, particularly for individual and household users for whom energy

input costs have proven less salient than for industrial users of more-lumpy technologies (see figure panel H and SM-6). Improving the efficiency of end-use technologies leverages more than proportionate improvements in overall system efficiency. Currently, one unit of energy saved through end-use efficiency avoids the need for 3.2 units of primary energy resource (SM-6).

SOCIAL LEGITIMACY

Widespread support for political leadership on climate change enables the stringent policies required to incentivize decarbonization and overcome system inertia. Social legitimacy of accelerated low-carbon transformation depends on more equitable access to technologies and infrastructures for raising living standards, on job creation benefits from low-carbon technologies, and on social returns from public resources invested in innovation (see the figure, green panels). The political feasibility of expanding public funding for low-carbon R&D is strengthened by resulting societal benefits of employment, security, health, and a more productive economy. Jobs can be created by investments in new energy facilities. However, these potential benefits of low-carbon transformation can be distant from lower-income households, particularly in developing economies. Widening affordable access to modern energy systems is critical for raising living standards.

Access to technologies and infrastructures

Unit investment costs of end-use technologies range along a granular-lumpy continuum (see figure panel A), as do the unit costs of incrementally extending service infrastructures providing electricity, broadband, clean water, and sanitation to households previously without access. More-granular technologies and infrastructure extensions are widely accessible (see figure panel E and SM-7). Lower investment barriers promote more equity in raising living standards.

Net job creation

We draw on three metastudies that synthesized evidence from over 80 discrete studies of direct (construction and operation) and indirect (supply chain) employment effects of power generation and energy-efficiency investments (*7*). We find that energy facilities for more-granular technologies create more jobs over their lifetimes (see figure panel I and SM-8). We reason that more granularity is linked to greater breadth and diversity of application, which increase labor-capital ratios relative to large technological units.

Social returns on public R&D investments

The U.S. National Research Council quantified the wider economic, environmental, and

Characteristics of accelerated low-carbon transformation on the granular-lumpy continuum

Data points in each panel represent an energy technology. Unit size and unit cost correlate strongly (panel A) and are used interchangeably as measures of granularity on log horizontal axes (B) to (J). Vertical axes show measures of rapid technology deployment (red panels), escaping lock-in (blue panels), and social legitimacy (green panels). Δt, the time period over which a technology diffuses from 1 to 50% market share. Conventional learning rate, % cost reduction per doubling of cumulative capacity, conflates two drivers of cost reduction: unit scale economies (more capacity per unit) and experience (more units). Descaled "true" learning rate, % cost reduction per doubling of cumulative numbers of units, strips out the effects of unit scale economies on cost trends. Gini coefficients measure (in)equality on a scale from 0 denoting perfect equality (every household has the same access) to 1 denoting perfect inequality (one household has all the access). R^2 and p values denoted by asterisks describe simple bivariate model fits (*$p < 0.05$, **$p < 0.01$, ***$p < 0.001$). See supplementary materials for details on data and methods.

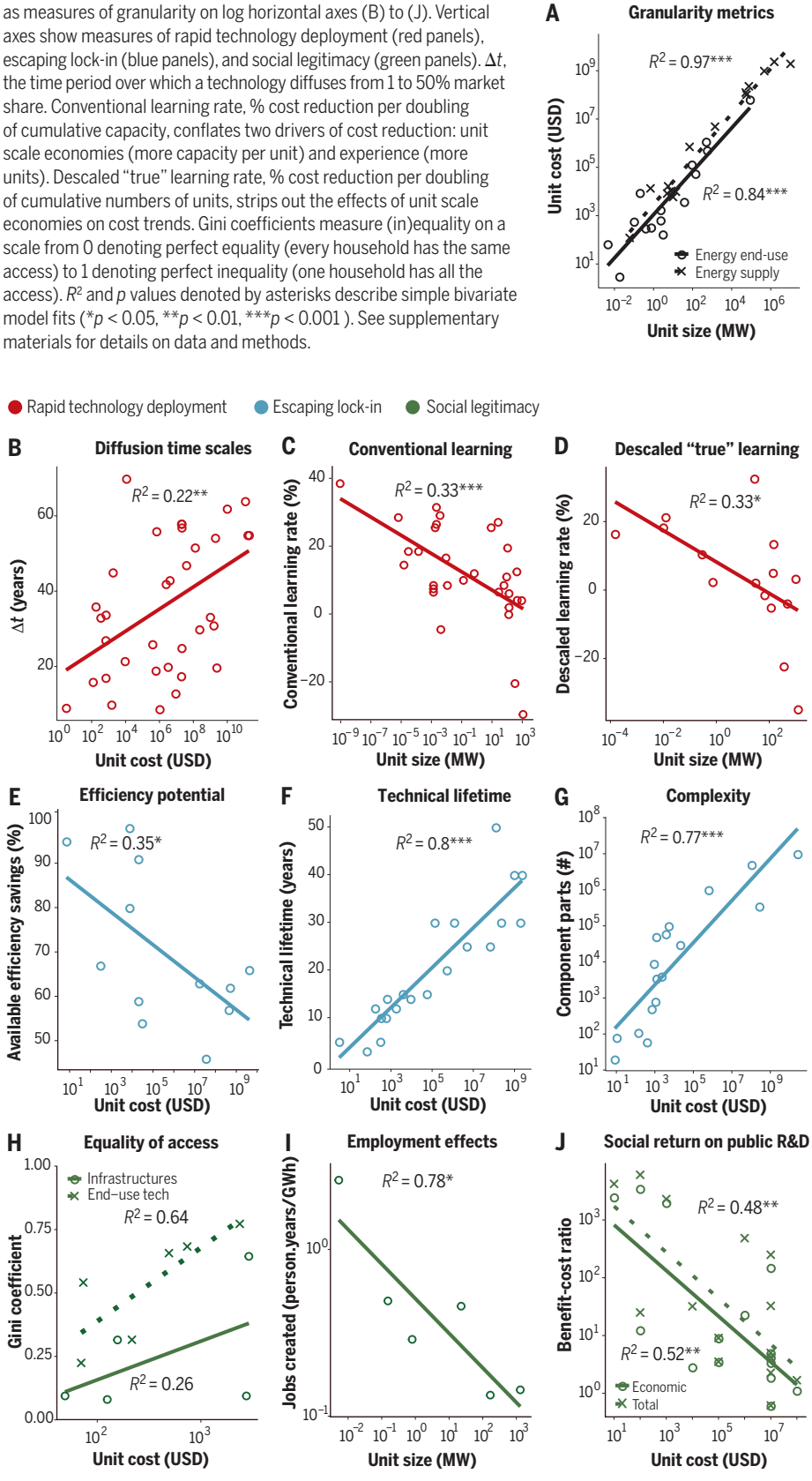

GRAPHIC: N. CARY AND X. LIU/*SCIENCE*

security benefits of the U.S. Department of Energy's public R&D portfolio from 1978 to 2000 (*8*). This study is distinct in its use of a transparent and standardized case-study methodology based on data, not model simulations. This allows for comparative analysis across nine end-use efficiency and six energy-supply technology R&D programs. R&D investments in more-granular technologies generated higher social returns (see figure panel J and SM-9). We consider this benefit of more granularity to be associated with lower market barriers to entry, and the wider scope and number of commercial applications.

DISCUSSION

Underlying mechanisms for each of the relationships shown in the figure are well substantiated in the literature (diffusion speed, investment risk, learning), have simple explanations (technical lifetime, complexity, end-use efficiency, equality of access), or can be plausibly reasoned (job creation, social returns on R&D investment). Although we have measured each relationship in isolation, their importance lies in their interaction. Under conditions for escaping lock-in, social legitimacy enables rapid technology deployment, which further destabilizes incumbent fossil-fuel–dependent regimes. Lower investment risks and shorter diffusion times grow market share, which drives greater equality of access and job creation. Lower risks and barriers to entry for more-granular technologies are important, as low-carbon and energy-efficient alternatives to incumbents tend to be more capital-intensive.

The potential for accelerated change is not just technological but institutional. More-granular technologies enable simple and rapid project planning with distributed and less complex decision-making processes. This is particularly important in markets with weaker governance institutions, where lumpy projects are beset by even greater complexities, costs, and risks (*9*).

However, the benefits of more-granular technologies are neither deterministic nor realizable in all contexts. The nine measures in the figure do not paint a complete picture of accelerated low-carbon transformation. First, there are many omitted variables such as the effect of profitability on diffusion speed (see figure panel B). Relatively weak model fits for some of the relationships are explained by the diversity of technology characteristics and adoption environments in the data (SM-0).

Second, although we intentionally construct diverse samples to identify generalizable relationships, contextual factors are important. For example, the acceptability and legitimacy of new energy infrastructure vary by place and perspective. The entwining of climate action and social justice movements highlights the importance of perceived fairness in both the process and outcome of low-carbon transformation. Communities, companies, and countries left "stranded" by rapid decarbonization can weaken political capacity to drive transformative change.

Third, there are important characteristics of rapid technology deployment, escaping lock-in, and social legitimacy that we do not measure. For example, lock-in has institutional and behavioral dimensions for which there are no standardized metrics, particularly at the systems level (*6*) (SM-4). Fourth, interactions between the relationships in the figure can dampen as well as accelerate dynamics of change. Rapid turnover of short-lived capital stock may also fail to destabilize larger systems of interdependent technologies, infrastructures, and institutions.

Outliers are also informative. For example, in panel B of the figure, the data point at the top represents cars which, although relatively granular, diffused slowly over long time scales, as they drove systemic change in transportation infrastructure and social organisation (SM-1). In panel E of the figure, the data points at the bottom left and right both measure access to electricity but from solar lanterns and grid extensions, respectively. These granular and lumpy substitutes have very different qualitative impacts on living standards and economic opportunity (SM-7). In panels F and G of the figure, the data points with high rates of negative learning are nuclear power and flue gas desulfurization, which upscaled and diffused with strong policy and institutional support. These caveats and examples highlight important conditions for realizing the advantages of granularity: substitutability, standardization, economies of scale, system integration and access to infrastructure, and political economy.

"...portfolios of more-granular technologies... outperform lumpy alternatives"

Substitutability and risks of granularity

In some cases, clear alternatives on the granular-lumpy continuum compete to serve a broadly equivalent function (e.g., nuclear and renewable power plants generating electricity). In other cases, more-granular technologies offer a similar service but with different attributes (e.g., e-bikes and cars for intra-urban mobility). But in some contexts, lumpiness may offer something qualitatively different and nonsubstitutable (e.g., long-haul flights). This limits the generalizability of the relationships shown in the figure.

Systems models, which represent both quantities and types of energy service, can test the feasibility, cost, and other conditions under which granular and lumpy alternatives are substitutable. The evidence is clearest for electricity systems in which distributed generation, storage, and demand-response technologies offer granular alternatives to historically centralized models (*3*). A recent global scenario study shows how portfolios of granular technologies throughout the energy system can limit warming to 1.5°C without relying on lumpy carbon capture and storage infrastructure (*10*). But none of these examples offer granular substitutes for long-distance air travel or steel and cement manufacturing.

The substitutability of lumpiness by portfolios of more-granular technologies introduces three potential issues: coordination and security, transaction costs, and pollution exposure and material waste. If large numbers of technological units need to interact in energy, transport, or building networks, then more granularity poses coordination problems. Digitalization enables "smart" system management but relies on high-resolution, real-time dataflows, which raise concerns about security, privacy, and data rights. If technology adoption and use take time and effort, then more granularity implies higher transaction costs. In some cases, this barrier to adoption can be reduced through aggregation (e.g., municipal shared vehicles), standardization (e.g., certified or off-the-shelf products), or third-party management (e.g., energy service companies).

If technologies are polluting, then more granularity can increase pollution exposure pathways and exacerbate adverse health impacts. End-of-pipe pollution controls can be effective if deployed in large numbers (e.g., catalytic converters, air and oil filters, heat recovery units), but highly distributed sources of pollutants such as CO_2 are hard to mitigate. Decarbonization strategies therefore rely heavily on electrifying energy end use in buildings and transport, as well as industry. Alongside air pollution risks, short-lived technologies with rapid innovation cycles can create considerable material waste unless careful attention is placed on material efficiency, life-cycle design, and product durability, modularity, and reparability (*11*).

Standardization and lock-in

Mass commercialization of more-granular technologies depends on standardization, which converges technological variety onto a dominant design, stimulates cost-reducing process innovation, enables mass production, provides quality control, and helps align user expectations with technology performance (*12*). Efficiency standards drive more rapid

learning. Standardization of balance-of-system components in PV installations enables off-site fabrication at higher production volumes, driving quality and reducing cost.

However, "standardized granularity" raises two important concerns. Dominant designs can become locked in by interdependencies with complementary technologies or infrastructures that are reinforced by standardization (e.g., railway gauges, power-network frequencies). Historically, this helped give rise to monopolistic system operators. Positive network externalities—the value of a network to all users increasing with each new user—combine with standardization to generate increasing returns to scale and winner-takes-all incumbents. Granularity can help escape carbon lock-in while also risking new forms of system inertia and regulatory capture.

Replicated uniformity also risks disregarding local context (*11*). However, standardizing design fundamentals, production processes, and system integration still allows for differentiated applications. Small-scale fabrication units can 3D print locally adapted products using standardized design data. A mass-manufactured PV module can be configured in myriad arrays, installed and used by individuals or large firms.

Unit and manufacturing economies of scale

Rapid cost reductions associated with more-granular technologies (see figure panels F and G) are partly explained by large production runs, seeking scale economies and product quality through standardization and mass manufacturing. For more lumpy energy technologies, scale economies may be available at the unit level (building larger) rather than in manufacturing (producing more). Controlling for learning effects, unit scale economies have been demonstrated for energy technologies including nuclear, wind power, and bioethanol distillation (SM-3).

Unit and manufacturing scale economies therefore offer alternative drivers of cost reduction for different energy technologies. For example, order-of-magnitude increases in production output from solar PV manufacturing facilities explain over a third of observed cost reductions in module costs from 2001 to 2012 (*13*). Conversely, up-scaling of plant sizes explains almost three-quarters of observed cost reductions in U.S. coal power production from 1908 to 1970 (*14*).

Infrastructure and system integration

Turnover times vary at the different scales of a technological system: years for boilers, engines, consumer products (technologies); decades for building envelopes, cars, capital equipment (technological clusters); centuries for buildings, roads, industrial organizations (infrastructures) (*6*). Short-lived, fast-learning, rapidly diffusing technologies at the lower levels of the hierarchy allow for rapid improvement within more slowly changing contexts. How technologies integrate into systems and access infrastructure strongly conditions the impact of granularity. Accommodating large numbers of granular technologies may require infrastructure expansion, upgrade, or replacement. Infrastructure change that is large, costly, indivisible, and system-wide requires massive centralized direction and investment and imposes high switching costs (e.g., piped H_2 through gas networks, long-distance DC electricity transmission). But infrastructure change may also be incremental and modular [e.g., electric vehicle (EV) charging stations].

Political economy

Increasing alignment between incumbent firms and regulatory frameworks is an institutional characteristic of lock-in (*6*). Lumpiness has been favored during the 20th-century development of the energy system. High upfront costs, nondivisible risks, and high consequences of failure in more lumpy technologies reinforce the rationale for public policy to underwrite returns, collectivize risks, or protect market positions. Publicly directed innovation efforts historically have been skewed toward centralized energy supply. More lumpytechnologies are also attractive politically as they demonstrate commitment and materiality (mobilization of human, financial, and physical resources) (*15*).

In comparison, heat pumps, rolls of insulation, EV charging points, smart meters, rooftop solar modules, and shared "taxi-buses" are heterogeneous and dispersed. Coalitions of actors are concentrated in particular sectors like consumer electronics, automotive manufacturing, or power generation. This weakens the political economic influence of more-granular technologies in low-carbon transformation (*15*). It also makes more-granular technologies less analytically tractable as the functions they serve vary so widely.

More recently, a confluence of factors, including market liberalization, technological innovation, and digitalization, has strengthened political economic support for granularity. More-granular energy technologies vary in scale, have more heterogeneous applications, and involve a greater diversity of firms and users through which the legitimacy of new technologies is established and resistance from incumbent actors counteracted. By enabling smaller increments of capital investment, more-granular technologies de-risk research, development, and demonstration (RD&D) portfolios and open markets to the destabilizing force of new entrants.

Conclusions

Under certain conditions, more-granular technologies are empirically associated with faster diffusion, lower investment risk, faster learning, more opportunities to escape lock-in, more equitable access, more job creation, and higher social returns on innovation investment. In combination, these advantages enable rapid change. Unit scale in physical or cost terms is a readily available criterion for helping evaluate whether net-zero emission pathways, clean energy R&D portfolios, industrial strategies, and technology demonstration programs can deliver near-term decarbonization. Governments, firms, investors, and civil society organizations seeking to accelerate progress on decarbonization should include granularity as a criterion for designing mitigation strategies, targeting policy support, funding R&D investments, and supporting low-carbon innovation. More-granular technologies could then be assessed against emission-reduction objectives. Scientists also need to explicitly account for granularity in scenarios and assessments, which often prominently feature large-scale solutions, and in modeling tools and analysis, which are often scale-free. Diverse portfolios of more-granular technologies are not a universal solution, but in many contexts, they outperform lumpy alternatives as a means of accelerating low-carbon transformation to meet global climate targets. ■

REFERENCES AND NOTES

1. IEA, *World Energy Outlook* (International Energy Agency, Paris, 2019).
2. A. Lovins *et al.*, *Small Is Profitable: The Hidden Economic Benefits of Making Electrical Resources the Right Size* (Rocky Mountain Institute, Snowmass, CO, 2003).
3. R. K. Jain *et al.*, *Nat. Energy* **2**, 17112 (2017).
4. E. Mansfield, *Industrial Research and Technological Innovation* (Norton, 1968).
5. B. K. Sovacool *et al.*, *Energy Res. Soc. Sci.* **3**, 152 (2014).
6. K. C. Seto *et al.*, *Annu. Rev. Environ. Resour.* **41**, 425 (2016).
7. W. Blyth *et al.*, Low carbon jobs: The evidence for net job creation from policy support for energy efficiency and renewable energy (UK Energy Research Centre London, 2014).
8. NRC, Energy Research at DoE: Was it Worth It? Energy Efficiency and Fossil Energy Research 1978-2000. Committee on Benefits of DoE R&D on Energy Efficiency and Fossil Energy, National Research Council (NRC), Washington, DC, 2001.
9. P. Alstone *et al.*, *Nat. Clim. Chang.* **5**, 305 (2015).
10. A. Grubler *et al.*, *Nat. Energy* **3**, 515 (2018).
11. J. M. Allwood *et al.*, *Philos. Trans. A Math. Phys. Eng. Sci.* **375**, 20160361 (2017).
12. K. Blind, The Impact of Standardization and Standards on Innovation (NESTA Working Paper Series, Manchester, 2013).
13. G. Kavlak *et al.*, *Energy Policy* **123**, 700 (2018).
14. J. McNerney *et al.*, *Energy Policy* **39**, 3042 (2011).
15. E. Moe, *Renewable Energy Transformation or Fossil Fuel Backlash: Vested Interests in the Political Economy* (Springer, 2016).

ACKNOWLEDGMENTS

This research was supported by the Research Institute of Innovative Technology for the Earth (RITE), Kyoto, Japan. C.W. was also supported by ERC Starting grant 678799.

SUPPLEMENTARY MATERIALS

science.sciencemag.org/content/368/6486/36/suppl/DC1

10.1126/science.aaz8060

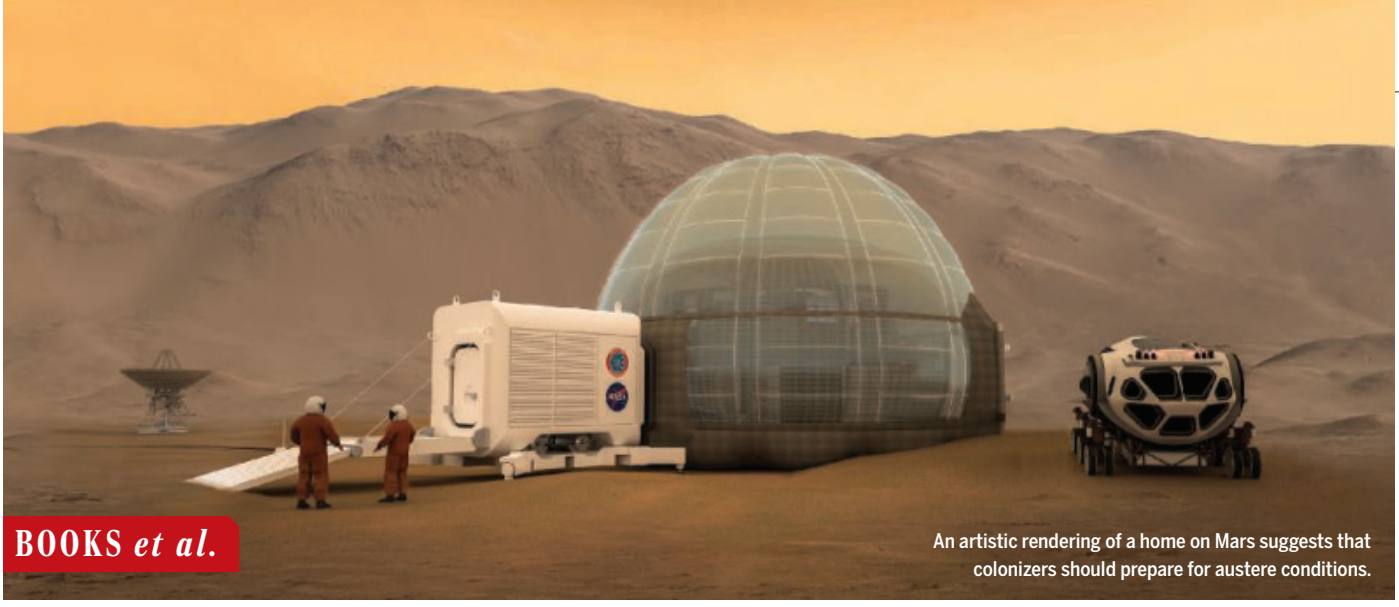

An artistic rendering of a home on Mars suggests that colonizers should prepare for austere conditions.

ENGINEERING

Colonizing the final frontier

Commercial interest in space is high, and the technology to get us there is nearly ready

By **David P. D. Munns**

"To go boldly, if prudently" would be a terrible tagline for a *Star Trek* spin-off, but it is the most sensible way to colonize space. Space settlements, Moon bases, and Mars colonies—no matter how futuristic—all require a business plan, explains science journalist Christopher Wanjek in his new book, *Spacefarers*.

Wanjek's book is an optimistic treatise on commercial endeavors that seek to increase the number of people in space by employing more efficient and cheaper launch vehicles and systems. "The market is there; the technology is almost there," he writes.

There is plenty of interest and investment in novel space launch systems, but the firms involved are not necessarily driven by scientific curiosity, the wish to inspire, or a desire to tackle a daunting challenge. And while a military mandate or the fear that plagues or large-scale ecological disasters could render Earth uninhabitable drives some to work toward a space-based refuge, a Moon, Mars, or asteroid base will require more than these motivators to keep us there. "A war might get us to the Moon or Mars; economic sustainability will keep us there," writes Wanjek.

Spacefarers: How Humans Will Settle the Moon, Mars, and Beyond
Christopher Wanjek
Harvard University Press, 2020. 400 pp.

Many private companies have mining in mind. Others are focused on space tourism. A Kevlar inflatable shelter manufactured by Bigelow Aerospace was placed on the International Space Station (ISS) in 2016. It is not too much of a leap to imagine that the first space tourists might live in such a shelter for a week or so. Similarly, both Elon Musk's Space X and Richard Branson's Virgin Galactic SpaceShipTwo are methodically clearing developmental and regulatory hurdles. If all continues to go well, they might start delivering tourists to space sometime soon.

As Wanjek sees it, companies such as Space X are attempting "to avoid the sins of the NASA shuttle program by applying basic business savvy." His argument hinges on a comparable phenomenon that occurred in the auto industry in the 1970s, when General Motors was caught off guard by the lean management of Toyota. Space X, he maintains, could be the Toyota of space.

As with any business plan, however, the devil is in the fine print. Underpinning a new era of space colonization will be the need to ensure life support and the safe return of early adventurers. And although our future in space might be led more by private than public imperatives, it is government space programs that have invested in tackling many of the initial medical studies, engineering projects, and habitability issues. Plants are now regularly grown in space, and NASA has learned about muscle and bone loss by studying the effects of microgravity and radiation on astronauts.

Analogous earthbound missions, from Antarctic expeditions to nuclear submarine deployments, offer some useful insights. "Meals are morale boosters" to people living in confined quarters for long periods of time, Wanjek notes, as is a view outside. Among the most promising of these studies are the ones being conducted in the Eden ISS greenhouse, a 20-foot-long shipping container in which researchers are currently growing crops at Germany's Neumayer III Antarctic base. This endeavor demonstrates that it is possible to grow vegetables while it is dark and freezing outside, as will have to be done in a space hotel. (The plants also generate oxygen, a welcome by-product for any space inhabitant.)

But if space travel is going to be a commercial activity, then it may make more sense to conceive of such journeys as akin to those undertaken by the first European adventurers, many of whom sacrificed their lives to the cause. As William Dalrymple reminds readers in *The Anarchy*, the young and adventurous often risked a 50 to 60% chance of death in exchange for the possibility of receiving a share of an eye-watering profit during the early days of the East India Company's trading expeditions (*1*).

Readers should consult *Spacefarers* alongside Mary Roach's *Packing for Mars*, which documents the current public efforts to return humans to the Moon and to get them to Mars. But Wanjek's analysis of the commercial approach to space exploration adds an important perspective to the conversation about our future in space. ■

The reviewer is at the Department of History, John Jay College of Criminal Justice, New York, NY 10019, USA. Email: dmunns@jjay.cuny.edu

REFERENCES AND NOTES

1. W. Dalrymple, *The Anarchy: The Relentless Rise of the East India Company* (Bloomsbury, 2019).

10.1126/science.abb1992

IMAGE: NASA/CLOUDS AO/SEARCH

MATERIALS SCIENCE

The things we make that make us who we are

Our cultural values get baked into the materials we create, changing humanity along the way

By **Mark Miodownik**

Humans spend a lot of time and effort making stuff. At last count, humanity has created more than 100,000 different materials from which we build our cities, our clothing, our smartphones, our world. Without our stuff, we would be naked, vulnerable, and, arguably, not very human. The question of how much of our humanity is due to this material wealth and how our cultural values are baked into the materials we create is the subject of Ainissa Ramirez's fascinating new treatise, *The Alchemy of Us*.

The book is structured according to broad themes—e.g., "convey," "capture," "discover"—which provide a satisfying way to explore how new materials have influenced culture throughout history. The book's central thesis is that we make materials and materials make us. The desire to articulate the relationship between materials and culture is not new, but the book brings a fresh perspective, in some ways taking up where Cyril Stanley Smith—who championed the role of aesthetics and the arts in the development of materials technologies—left off (*1*).

Ramirez's meditation on the materials that have facilitated community ("share") is particularly illuminating. Here, she writes about the phonograph's impact on how music was enjoyed. The ability to record music meant that the experience of listening to it no longer had to be a communal one. This spelled the end of much homemade folk music defined by materials such as brass, wind, or strings—"cellos, violins, and guitars produced tones too soft for the early phonograph to pick up, so louder instruments like pianos, banjoes, xylophones, tubas, trumpets, and trombones became preferred for recordings of music"—but it also opened up uncharted horizons. The recordings allowed a cross-fertilization of musical culture between jazz, blues, and rock and roll, even as the musicians themselves remained segregated by race politics.

On the subject of race and racial discrimination, Ramirez argues that a society that is racist will reflect racism in the substances that it makes. For example, photographic film, she writes, was largely developed by white people for white people. Because dark skin absorbs more light than white skin, early photographs of black people were often underexposed, rendering images that were barely recognizable. Ramirez describes how Kodak, the major producer of color film in the early 20th century, was aware of this problem but failed to reformulate its product until furniture makers and confectioners started to complain that it was impossible for customers to discern the difference between wood species and chocolate varieties, respectively. And although the cultural bias embedded in color film was corrected through chemical reformulations, it reemerged decades later in digital photography's automatic facial recognition, which frequently fails to detect darker skin tones.

Some of the book's chapters are less dramatic than others, but only because Ramirez is not prepared to sacrifice the fruits of detailed research to render a simplified narrative. Instead, the book recounts the twists and turns of how materials evolved, describing how some people made huge contributions and received little credit, while others were rewarded with fame and money. One such story is that of Reverend Hannibal Goodwin, an Episcopalian pastor who experimented for 10 years in his attic to invent a method to make photographic film. After filing for a patent, he discussed his efforts with George Eastman, a camera manufacturer, who promptly patented his own version and made a fortune. In the end, Goodwin's descendants did get financial redress, but Goodwin himself died a broken man.

Ramirez is particularly keen to debunk the idea that materials arise from flashes of insight experienced by extraordinary individuals, instead painting a picture of a diverse range of people from all walks of life driven by love, passion, and intellect. The culture of innovation, she maintains, does not belong only to privileged elites, it can be found in all those who care enough to reinvent the material world and, as a result, themselves. ■

The reviewer is at the Department of Mechanical Engineering, University College London, London WC1E 7JE, UK.
Email: m.miodownik@ucl.ac.uk

The Alchemy of Us: How Humans and Matter Transformed One Another
Ainissa Ramirez
MIT Press, 2020. 328 pp.

PHOTO: LIBRARY OF CONGRESS, PRINTS & PHOTOGRAPHS DIVISION, LC-B2- 2215-5

Package-laden postal workers had steel rails to blame for the boom in Christmas shopping in the early 1900s.

REFERENCES AND NOTES

1. C. S. Smith, *A Search for Structure: Selected Essays on Science, Art, and History* (MIT Press, 1981).

10.1126/science.aba8965

RESEARCH

Strained oxide membranes

Hong et al., *p. 71*

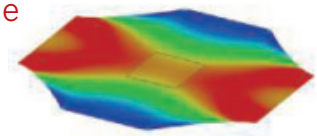

IN *SCIENCE* JOURNALS

Edited by **Michael Funk**

Mice respond to emotionally salient events with specific facial expressions.

NEUROSCIENCE

How to read the face of a mouse

The neuroscientific investigation of emotions is hindered by a lack of rapid and precise readouts of emotion states in model organisms. Dolensek *et al*. identified facial expressions as innate and sensitive reflections of the internal emotion state in mice (see the Perspective by Girard and Bellone). Mouse facial expressions evoked by diverse stimuli could be classified into emotion-like categories, similar to basic emotions in humans. Machine-learning algorithms categorized mouse facial expressions objectively and quantitatively at millisecond time scales. Intensity, value, and persistence of subjective emotion states could thus be decoded in individual animals. Combining facial expression analysis with two-photon calcium imaging allowed the identification of single neurons whose activity closely correlated with specific facial expressions in the insular cortex, a brain region implicated in affective experiences in humans. —PRS

Science, this issue p. 89; see also p. 33

NANOMATERIALS

Seeing subtle nanoparticle differences

A challenge in the fabrication of nanoparticles is that even for particles of uniform size, there will still be a distribution in the atomic arrangements and surface capping ligands from one particle to the next. Using liquid-cell transmission electron microscopy, Kim *et al*. reconstructed the structure of individual nanocrystals synthesized in one batch while they were still in solution. A comparison of multiple particles showed structural heterogeneity and differences between the interior and the outer shell of the individual nanoparticles, as well as nanoparticles containing extended defects and thus differences in internal strain, all of which can affect the physical and chemical properties of each particle. —MSL

Science, this issue p. 60

CANCER

New ideas about neoantigens

Tumors with a low mutational burden are thought to have fewer neoantigens available for T cells to respond to and thus are not necessarily considered for checkpoint blockade therapy. Subudhi *et al*. treated patients with metastatic, castration-resistant prostate cancer, which has a relatively low mutation burden, with the cancer drug ipilimumab. Patients that responded to the treatment had a T cell response signature and detectable neoantigen immunity. Checkpoint blockade therapy with ipilimumab can thus instigate T cell responses to tumor neoantigens, despite the low tumor mutational burden status. —YN

Sci. Transl. Med. **12**, eaaz3577 (2020).

ICE SHEETS

Slipping on till

How do glaciers flow over the ground underlying them? We know that friction, ice stream velocity, and water pressure at the ice bed all matter, but we still do not know how to represent the process over both hard beds (which are solid rock) and soft ones (composed of unconsolidated erosion products called till). Zoet and Iverson present experimental results describing how glacial ice moves over water-saturated till (see the Perspective by Minchew and Joughin). These observations should help to solve the long-standing problem of constructing a generalized slip law that combines the processes of hard-bedded sliding and bed deformation. —HJS

Science, this issue p. 76; see also p. 29

CREDITS (FROM TOP): HONG *ET AL.*; MARC PERKINS

IMMUNE CELLS

Airway-hugging macrophages

Effective immune defense in the lungs relies on myeloid cells that phagocytose, process, and present foreign substances that enter the airways, including pathogens. Ural *et al*. studied a subset of pulmonary interstitial macrophages predominantly found within the lungs that serve an immunoregulatory role during responses to lung inflammation. These findings provide a deeper insight into the specialized myeloid subsets that contribute to maintaining pulmonary homeostasis. —IRW

Sci. Immunol. **5**, eaax8756 (2020).

ASTEROIDS

Blowing a crater in asteroid Ryugu

The Hayabusa2 spacecraft was designed to collect samples from the nearby asteroid (162173) Ryugu and return them to Earth for laboratory analysis. Arakawa *et al*. describe how the spacecraft's Small Carry-on Impactor was fired into the asteroid's surface, producing an artificial impact crater. Analysis of the resulting plume of ejecta, recorded by a remote camera, sets an upper limit on the strength of the rubble-pile surface. The crater has a semicircular shape, probably due to a large boulder buried close to the impact location. The crater exposed material from Ryugu's subsurface, which has not been subjected to space weathering, that is suitable for collection by Hayabusa2. —KTS

Science, this issue p. 67

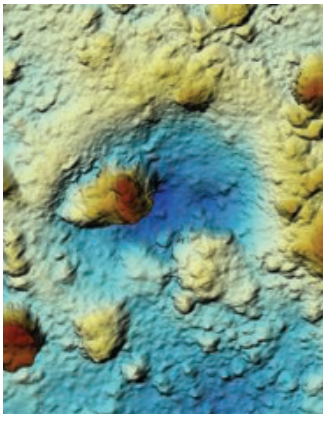

Digital elevation map of the artificial impact crater on Ryugu

CREDITS (FROM LEFT): ARAKAWA *ET AL.*; D. HURST/ALAMY STOCK PHOTO

PROTEIN DESIGN

Designer gates

Signaling in cells can occur through protein-protein interactions. Chen *et al*. describe the design of logic gates that can regulate protein association. The gates were built from small, designed proteins that all have a similar structure but where one module can be designed to interact specifically with another module. Using monomers and covalently connected monomers as inputs and encoding specificity through designed hydrogen-bond networks allowed the construction of two-input or three-input gates based on competitive binding. The modular control elements were used to regulate the association of elements of transcription machinery and split enzymes in vitro and in yeast cells. —VV

Science, this issue p. 78

CELL BIOLOGY

Organelle cross-talk

Endoplasmic reticulum (ER)–associated degradation (ERAD) is a quality control mechanism that allows for targeted degradation of proteins in the ER. Zhou *et al*. found that a particular protein complex in ERAD, Sel1L-Hrd1, regulates the dynamics of another organelle, the mitochondrion, by altering ER-mitochondria contacts. Three-dimensional high-resolution imaging in brown adipocytes from cold-challenged mice revealed that defective ERAD led to the formation of enlarged and abnormally shaped mitochondria with perforating ER tubules. The authors explored the consequences of ERAD deficiency on mitochondrial function and thermogenesis, which provides insights into ERAD-mediated ER-mitochondrial cross-talk and advances our understanding of the physiological importance of interorganelle contact. —SMH

Science, this issue p. 54

IN OTHER JOURNALS

Edited by **Caroline Ash** *and* **Jesse Smith**

NUTRITION

Perils of nighttime dining

There's a lot of debate in the health media not just about what to eat but also about when to eat whatever is decided is best to eat. Humans, like all mammals, have day-night metabolic rhythms (circadian cycles), approximately tuned to a 24-hour day-night period. Kelly *et al*. put individuals between 51 and 63 years of age separately into a room calorimeter that contained facilities for daily life, such that minute-by-minute energy expenditure of the room's occupant was measured very precisely. Each individual was given three meals a day, with nutritionally equivalent meals in the morning and late evening. The authors discovered that the late evening snack resulted in less lipid oxidation than breakfast and was more likely to be stored as adipose tissue. —CA

PLOS Biol. **18**, e3000622 (2020).

Nighttime snacking means less lipid oxidation and more fat tissue.

PHYSIOLOGY

Maternal obesity affects offspring

Alterations in cellular homeostasis can cause endoplasmic reticulum (ER) stress and activation of the stress pathway—the unfolded protein response. Obesity in mice induces ER stress in tissues and the hypothalamus, a brain region that plays a role in many important functions, including controlling food intake and energy expenditure. Park *et al*. found that diet-induced obesity in pregnant mice resulted in postnatal ER stress in the

Some bacteria can degrade toxins produced by blue-green algae, such as these on the highly polluted and eutrophic Lake Taihu.

BIODEGRADATION

Microbes against microbial toxins

Algal blooms in polluted lakes are often associated with high levels of microbial toxins, including a class of cyclic peptides known as microcystins. Although these molecules are resistant to normal peptidases, some bacteria have developed specialized enzymes and pathways to metabolize them. Prospecting in the notoriously polluted and eutrophic Lake Taihu in China, Yang *et al*. isolated a bacterium capable of completely degrading microcystins. A multi-omics analysis confirmed many previously known steps of the pathway and suggested that genes involved in phenylacetic acid metabolism contribute to the breakdown of one of the unusual amino acid components. —MAF

Water Res. **174**, 115638 (2020).

pancreas and hypothalamus of offspring. These mice had increased food intake, adiposity, and body weight and showed disrupted development of specific hypothalamic neurons associated with energy homeostasis. Treatment of offspring with an ER stress–relieving drug reversed these effects. This suggests that in mice, maternal physiology has important nutritional programming effects on offspring. —GKA

PLOS Biol. **18**, e3000296 (2020).

IMMUNOLOGY

Fetal stress affects adult immune function

Exposure to stress in the womb not only has acute effects on the fetus but also influences physiological function later in adult life. Hong *et al*. propose a mechanism by which perinatal exposure to dexamethasone, a drug resembling corticosteroid stress hormone, causes problems with CD8 T cell function in adulthood. Adult offspring of mice treated with dexamethasone when pregnant had CD8 T cells with blunted production of interferon-γ, decreased response to cancer cells, and impaired antibacterial function. The problems may, in part, reflect a long-term decrease in production of corticosterone by the adrenal gland and, consequently, decreased glucocorticoid receptor signaling in the T cells. —LBR

Cell **180**, 847 (2020).

POPULATIONS

Human movements in the United States

North America has a long history of migration, movement, and admixture. However, how indigenous people and the continuous waves of global migration shaped the modern United States is poorly understood. Dai *et al*. analyzed genetic data from more than 32,000 individuals registered with the National Geographic Genographic Project. The authors linked population structure to the genetics of individuals, location of birth, and geography of the United States, including previously underrepresented populations of Asian and Middle Eastern ancestry. From this analysis, the authors show how population substructure reflects historical events, such as the slave trade with Africa. Locales of high genetic similarity were found, and, interestingly, Latinos showed a range of differing geographical and genetic histories. This fine map of U.S. population structure can aid in personalized medicine by providing relevant population-specific information from underrepresented groups within the United States. —LMZ

Am. J. Hum. Genet. **106**, 371 (2020).

ELECTROCATALYSIS

Details of cobalt's ups and downs

Breaking carbon-hydrogen bonds to make complex molecules has often required copious quantities of toxic oxidants. Electrochemistry offers a cleaner approach that has recently been showing great promise. Meyer *et al.* report a close look at how cobalt catalysis in conjunction with anodic oxidation can add methoxy groups to aryl rings. They isolated and structurally characterized a cobalt(III) complex that has cleaved the aryl carbon-hydrogen bond. Cyclic voltammetry then provided evidence for further oxidation to cobalt(IV), which accelerates formation of the carbon-oxygen bond through reductive elimination back down to cobalt(II). —JSY

Angew. Chem. Int. Ed. 10.1002/anie.202002258 (2020).

DWARF GALAXIES

Merging dwarfs distribute globular clusters

The Fornax Dwarf Spheroidal (dSph) is a satellite galaxy of the Milky Way. It contains unexpectedly numerous globular star clusters on wide orbits, which may indicate an unusual distribution of dark matter. Leung *et al*. constructed a semi-analytic model to explain the number and distribution of the globular clusters. They propose that the Fornax dSph is the result of a merger between two smaller dwarf galaxies about 10 billion years ago, which caused some globular clusters to be lifted to higher orbits and triggered the formation of others. The results are consistent with compositional data and constrain the Fornax dSph's dark matter profile. —KTS

Mon. Not. R. Astron. Soc. **493**, 320 (2020).

PHOTO: IMAGINE CHINA/NEWSCOM

REVIEW SUMMARY

PLANT SCIENCE

A plant's diet, surviving in a variable nutrient environment

Giles E. D. Oldroyd* and Ottoline Leyser

BACKGROUND: Although plants are dependent on the capture of a number of elemental nutrients from the soil, the principal nutrients that limit plant productivity are nitrogen (N) and phosphorus (P). Acquisition of these nutrients is essential for crop performance, but levels of these nutrients in most agricultural soils limit productivity. Therefore, these nutrients are typically applied at high concentrations in the form of inorganic fertilizers to support food production. However, overuse of fertilizers allows environmental nutrient release, which reduces biodiversity and contributes to climate change. Many farmers around the world lack the financial resources to access fertilizers, and their crop productivity suffers as a consequence. A more sustainable and equitable agriculture will be one that is less dependent on inorganic fertilizers.

ADVANCES: Accessibility of N and P in the soil is affected by many factors that create a variable spatiotemporal landscape of their availability, both at the local and global scale. Plants optimize uptake of the N and P available by modifications to their growth and development and through engagement with microorganisms that facilitate their capture. Where N and P are ample, the ratio of root:shoot biomass allocation can be low, with minimal root systems capturing sufficient nutrients. Typically, vegetative growth is extended, allowing resource accumulation and investment in seed production. In environments where these nutrients are limiting, overall growth is reduced but root systems are expanded and colonization by microorganisms is encouraged to facilitate nutrient capture. Plants can recognize a patchwork of nutrient availability and activate root growth within this patchwork to optimize nutrient capture.

ON OUR WEBSITE

Read the full article at http://dx.doi.org/10.1126/science.aba0196

Plants are able to measure multiple facets of nutrient availability: local sensing of nutrients in the soil, roots experiencing nutrient deprivation, roots experiencing high nutrient availability, and the total nutrient requirements of the plant. Such sensing involves an integration of root and shoot signaling, with a variety of hormones moving between the root and the shoot to both signal nutrient availability and coordinate plant development. Such root-shoot-root signaling is essential to allow plants to make use of local nutrient patches, but to do so only when there is sufficient need for that nutrient.

Some microorganisms have capabilities for the capture of N and P from the environment. For instance, N-fixing bacteria can access nitrogen from the atmosphere, something that plants are unable to do. Arbuscular mycorrhizal fungi can access insoluble forms of phosphate in the soil that are mostly inaccessible to plants. Under situations where plants are unable to access N and P from their immediate environment, they turn to these microorganisms to find new sources of these limiting nutrients. Many of the processes that coordinate the plants' developmental response to nutrient availability also regulate the plants' interaction with microorganisms. These processes regulate the plants' receptiveness to their microbial communities, promoting symbiotic associations and restricting immunogenic processes.

OUTLOOK: Although our understanding of how plants engage with nutrients has advanced, there are few examples of how such knowledge has affected plant performance, perhaps because much of our understanding derives from studies in model, not crop, plants. Years of breeding crops for success under high-nutrient environments have left us with some crop varieties that are poor at optimizing use of limited nutrients. Nonetheless, many processes exist in plants to ensure productivity under poor nutrient conditions, some of which are already accessible in the diversity of crop species and wild near-relatives. We are poised to use the knowledge generated in model systems to optimize the performance of crop plants under nutrient limitation. ■

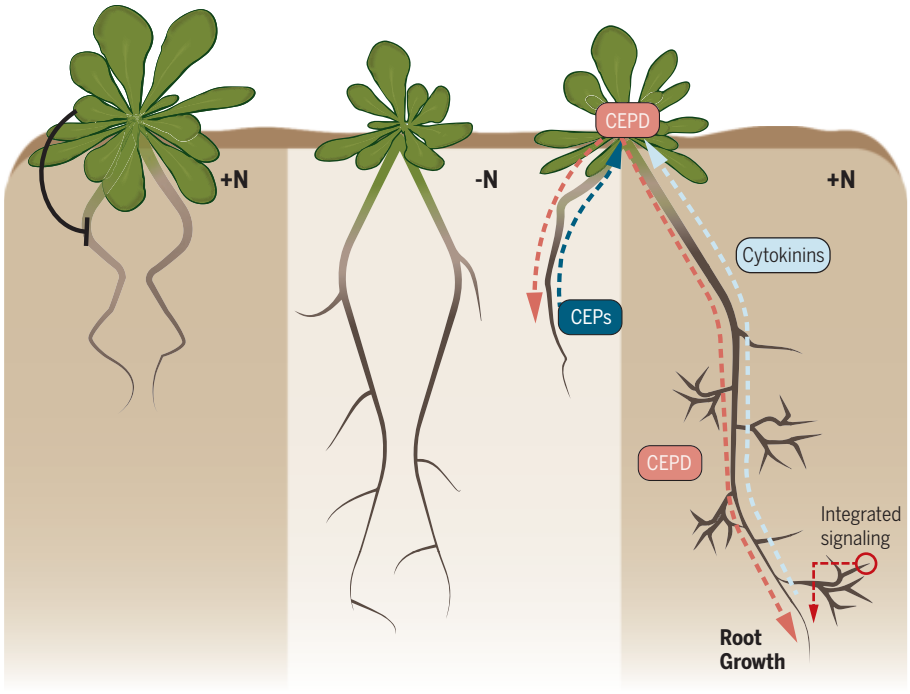

N response and signaling. Root responses of *Arabidopsis* plants grown in uniform high N (NO_3^-; dark gray, left), uniform low N (light gray, middle), and differential treatments of high and low N (right). Note how the root responses are opposite to the local treatments in uniform versus differential treatments. Underpinning these responses are C-terminally encoded peptides (CEPs) produced in roots experiencing low N, cytokinins produced in roots experiencing high N, and an N-sufficiency signal in the shoot. All regulate shoot-to-root signaling, which involves CEP DOWNSTREAM 1 (CEPD) peptides. Systemic signaling is integrated with local signaling (indicated by red) that is induced by local perception of NO_3^-.

The list of author affiliations is available in the full article online.
*Corresponding author. Email: gedo2@cam.ac.uk
Cite this article as G. E. D. Oldroyd and O. Leyser, *Science* **368**, eaba0196 (2020). DOI: 10.1126/science.aba0196

RESEARCH ARTICLE SUMMARY

MOLECULAR BIOLOGY

Structural basis for allosteric PARP-1 retention on DNA breaks

Levani Zandarashvili*, Marie-France Langelier*, Uday Kiran Velagapudi, Mark A. Hancock, Jamin D. Steffen, Ramya Billur, Zain M. Hannan, Andrew J. Wicks, Dragomir B. Krastev, Stephen J. Pettitt, Christopher J. Lord, Tanaji T. Talele, John M. Pascal†, Ben E. Black†

INTRODUCTION: Poly(ADP-ribose) polymerase–1 (PARP-1) is an abundant enzyme in the cell nucleus that regulates genome repair by binding to DNA damage sites and creating the poly(ADP-ribose) posttranslational modification. PARP-1 hyperactivity leads to cell stress or death associated with many prominent diseases (e.g., cardiovascular disease and several common neurodegenerative disorders). PARP-1 has notably emerged as an effective clinical target for a growing list of cancers. Clinical PARP-1 inhibitor (PARPi) compounds all bind at the same location at the catalytic center of the enzyme to block the binding of substrate nicotinamide adenine dinucleotide (NAD^+) and prevent poly(ADP-ribose) production, yet they exhibit vastly different outcomes in tumor cell killing and efficacy in the clinic—a paradox that has confounded the development of PARPi. The resolution of this paradox likely lies in the realization that the most effective PARPi compounds trap PARP-1 at the site of a DNA break, generating a lesion that becomes cytotoxic, especially in tumor cells with deficiencies in the repair of DNA strand breaks.

RATIONALE: The molecular roots of PARP-1 trapping on DNA remain poorly understood. We focused on the retention of PARP-1 on damaged DNA, examining a panel of PARPi that included those currently approved for clinical use. Solution biophysical approaches, especially hydrogen/deuterium exchange mass spectrometry (HXMS), combined with x-ray structures and a battery of biochemical assays, were used to interrogate the molecular impact of PARPi binding to PARP-1 engaged on sites of DNA damage. Structure-guided modification of PARPi through medicinal chemistry was combined with chromatin fractionation to monitor trapped PARP-1 and with cell survival assays to assess PARPi efficacy, so as to probe the molecular underpinnings of the variable outcomes between clinical PARPi.

RESULTS: HXMS experiments revealed that a critical allosteric regulatory domain of PARP-1, the helical domain (HD), is affected in distinct ways depending on the particular PARPi engaged in the NAD^+-binding site adjacent to the HD. Certain PARPi destabilized specific HD regions, some had no effect on the HD, and others actually stabilized regions of the HD. PARPi that destabilized the HD increased PARP-1 affinity for DNA and retained PARP-1 on DNA breaks. Conversely, PARPi that stabilized the HD decreased PARP-1 affinity for DNA breaks. PARPi molecules were thus classified into three types: type I, allosteric pro-retention on DNA; type II, non-allosteric; and type III, allosteric pro-release from DNA. X-ray structure analysis identified PARPi contacts with the HD structural element helix αF, which was established to be the discriminating factor between the types of PARPi. We found that type I PARPi contact helix αF to initiate an allosteric chain reaction that travels ~40 Å through the multidomain PARP-1 molecule and culminates in increased DNA binding affinity. Structure-guided mutagenesis of helix αF disrupted PARPi contacts and abrogated the allosteric effects of a type I inhibitor, transforming it into a non-allosteric type II inhibitor. Other mutations that disrupted PARP-1 allostery, including one identified in a de novo PARPi-resistant patient with ovarian cancer, also prevented type I PARPi from retaining PARP-1 on a DNA break. Type III PARPi influenced PARP-1 allostery in a manner that reduced DNA binding and favored DNA release. Structure-inspired modification of a pro-release (type III) inhibitor converted it to a pro-retention (type I) inhibitor that conferred potent PARP-1 trapping within the cellular context and increased its ability to kill cancer cells.

ON OUR WEBSITE

Read the full article at http://dx.doi.org/10.1126/science.aax6367

CONCLUSION: Our findings establish the impact of clinical PARPi on PARP-1 allostery and demonstrate that allostery plays a critical role in cellular PARP-1 trapping and can increase potency toward cancer cell killing. The results illuminate the molecular basis for the fine-tuning of PARPi to achieve allosteric effects and to influence PARP-1 retention on DNA damage and trapping on chromatin in cells. In contrast to cancer, other diseases would seem to benefit from PARP-1 inhibition but not cell death (e.g., cardiovascular disease, neurodegenerative diseases, and inflammation). Our studies provide the molecular understanding and the appropriate toolset to create and evaluate tunable PARPi for clinical applications where PARP-1 trapping and associated cytotoxicity are either desirable or undesirable in specific patients. ■

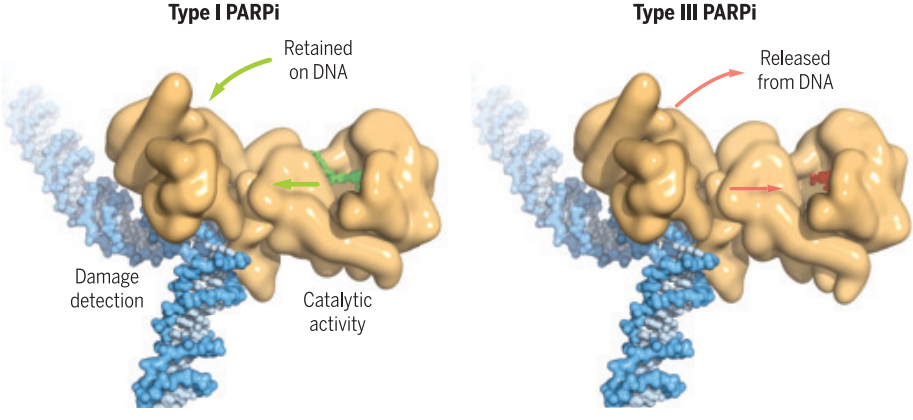

PARPi impact on PARP-1 allostery. PARP-1 (tan) uses multiple domains to detect DNA breaks, and DNA damage detection is allosterically coupled to poly(ADP-ribose) production. PARPi bind to the catalytic domain to inhibit PARP-1 activity. Type I PARPi influence PARP-1 allostery and retain PARP-1 on DNA (left, UKTT15 in green), whereas type III PARPi perturb PARP-1 allostery and release PARP-1 from DNA (right, veliparib in red). Type II PARPi do not influence PARP-1 allostery.

The list of author affiliations is available in the full article online.
*These authors contributed equally to this work.
†Corresponding author. Email: john.pascal@umontreal.ca (J.M.P.); blackbe@pennmedicine.upenn.edu (B.E.B.)
Cite this article as L. Zandarashvili *et al.*, *Science* **368**, eaax6367 (2020). DOI: 10.1126/science.aax6367

RESEARCH ARTICLE SUMMARY

PALEOANTHROPOLOGY

Contemporaneity of *Australopithecus*, *Paranthropus*, and early *Homo erectus* in South Africa

Andy I. R. Herries*†, Jesse M. Martin†, A. B. Leece†, Justin W. Adams†, Giovanni Boschian†, Renaud Joannes-Boyau, Tara R. Edwards, Tom Mallett, Jason Massey, Ashleigh Murszewski, Simon Neubauer, Robyn Pickering, David S. Strait, Brian J. Armstrong, Stephanie Baker, Matthew V. Caruana, Tim Denham, John Hellstrom, Jacopo Moggi-Cecchi, Simon Mokobane, Paul Penzo-Kajewski, Douglass S. Rovinsky, Gary T. Schwartz, Rhiannon C. Stammers, Coen Wilson, Jon Woodhead, Colin Menter

INTRODUCTION: Drimolen is one of several ancient caves located in the Hominid Caves of South Africa United Nations Educational, Scientific, and Cultural Organization (UNESCO) World Heritage Area in South Africa. Between ~2.3 million and ~1.8 million years ago, there were major climactic changes and faunal turnovers in the region, including the last occurrence of the genus *Australopithecus* and the first occurrence of *Paranthropus* and *Homo*, as well as the first occurrence of stone and bone tools. However, the exact nature of these changes has been hard to elucidate because of past difficulties in dating caves of this age and their perceived geological complexity. Unlike in eastern Africa, where volcanic material is available for dating, the South African caves have been dated with a variety of evolving methods that have often given conflicting age estimates. This means that South Africa's early human record and its relationship to east African hominin species have been difficult to determine. This is especially problematic given that each record is distinct in terms of hominin species until perhaps the origin and early evolution of the genus *Homo*. Although many fragmentary fossil specimens in South Africa have been attributed to early *Homo*, there is no consensus regarding species attribution.

RATIONALE: Drimolen Main Quarry has yielded one of the richest records of early human fossils in South Africa, including examples of *Homo* and the most complete female skull (DNH 7) of *Paranthropus robustus*. Excavations between 2015 and 2018 yielded the first new hominin calvaria (DNH 134 and DNH 152) from the site in 20 years. A combination of uranium-lead dating on flowstones, uranium-series electron spin resonance (US-ESR) dating on teeth, and palaeomagnetism on sediments was undertaken to establish the age of the site and its early human fossils.

RESULTS: The DNH 134 cranium shares clear affinities with *Homo erectus*, whereas the DNH 152 cranium represents *P. robustus*. Stratigraphic analysis of the Drimolen Main Quarry deposits indicates that unlike many other South African sites, there was only one major phase of relatively short deposition between ~2.04 million years ago and ~1.95 million years ago. This age has been constrained by the identification of the ~1.95-million-year-old magnetic field reversal at the base of the Olduvai SubChron within the sediments and by the direct uranium-lead dating of a flowstone that formed during the reversal. This has been augmented by direct dating on fossils by means of US-ESR that suggests that the DNH 134 and DNH 152 crania were deposited just before this reversal, with the DNH 134 crania deposited at ~2.04 million years ago. The DNH 134 cranium shares affinities with *H. erectus* and predates all known specimens in that species. The age range of Drimolen Main Quarry overlaps with that of *Australopithecus sediba* from the nearby site of Malapa and indicates that *Homo*, *Paranthropus*, and *Australopithecus* were contemporaneous in South Africa between 2.04 million and 1.95 million years ago. It is the first time that dating has conclusively demonstrated that these three taxa shared the same landscape during the same time range, making it less likely that a population of *A. sediba* is ancestral to *Homo*, as has been previously suggested. Analysis of fauna preserved at Drimolen documents a period of ecological change, with earlier South African species going extinct and new species moving into the region from other parts of Africa, including early representatives of *H. erectus*.

ON OUR WEBSITE

Read the full article at http://dx.doi.org/10.1126/science.aaw7293

CONCLUSION: Drimolen is the best dated early hominin site in South Africa. DNH 134 is the oldest and best preserved Early Pleistocene *Homo* cranium from South Africa. The DNH 134 *Homo* cranium has affinities with *H. erectus* and extends the species' temporal range by ~200,000 to 150,000 years. DNH 134 being older than *A. sediba* complicates the likelihood of this species being ancestral to *Homo* in South Africa, as previously suggested. With the oldest occurrence of *H. erectus* at the southern tip of Africa, this argues against a suggested Asian origin for *H. erectus*. DNH 152 represents the oldest *P. robustus* cranium in South Africa. The Drimolen stone and bone tools are also the oldest from the region.

The faunal community from Drimolen as a whole indicates substantial changes in South African ecosystems, with many first and last appearance dates of species that are related to the extinction of some indigenous South African species and the migration of others into the region ~2 million years ago, likely including *Homo erectus*. ■

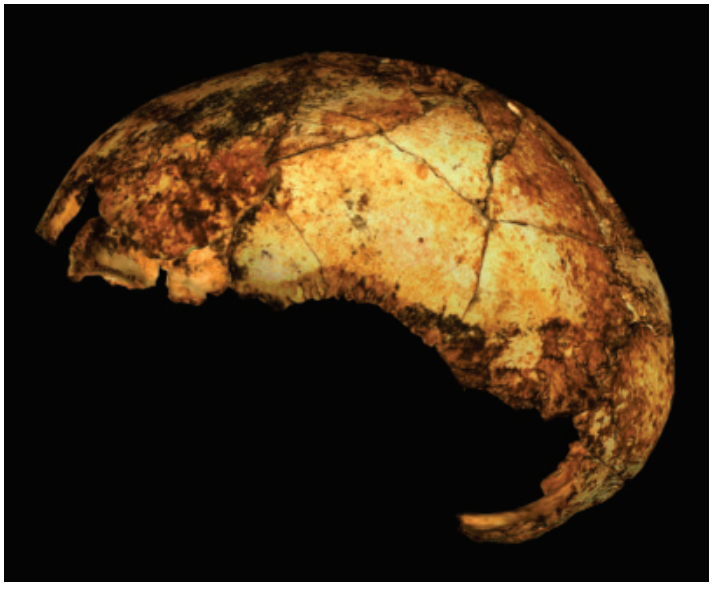

The DNH 134 *H. erectus* cranium from South Africa.

PHOTO: JESSE MARTIN, REANUD JOANNES-BOYAU, ANDY I. R. HERRIES

The list of author affiliations is available in the full article online.
*Corresponding author. Email: a.herries@latrobe.edu.au
†These authors contributed equally to this work.
Cite this article as A. I. R. Herries *et al.*, *Science* **368**, eaaw7293 (2020). DOI: 10.1126/science.aaw7293

RESEARCH ARTICLES

NEURODEVELOPMENT

Maintenance of neural stem cell positional identity by *mixed-lineage leukemia 1*

Ryan N. Delgado[1,2,3,4]*, Benjamin Mansky[1,2,5]*, Sajad Hamid Ahanger[1,2,6], Changqing Lu[7], Rebecca E. Andersen[1,2,8], Yali Dou[9], Arturo Alvarez-Buylla[1,2], Daniel A. Lim[1,2,6]†

Neural stem cells (NSCs) in the developing and postnatal brain have distinct positional identities that dictate the types of neurons they generate. Although morphogens initially establish NSC positional identity in the neural tube, it is unclear how such regional differences are maintained as the forebrain grows much larger and more anatomically complex. We found that the maintenance of NSC positional identity in the murine brain requires a *mixed-lineage leukemia 1* (*Mll1*)–dependent epigenetic memory system. After establishment by sonic hedgehog, ventral NSC identity became independent of this morphogen. Even transient MLL1 inhibition caused a durable loss of ventral identity, resulting in the generation of neurons with the characteristics of dorsal NSCs in vivo. Thus, spatial information provided by morphogens can be transitioned to epigenetic mechanisms that maintain regionally distinct developmental programs in the forebrain.

Early in embryonic development, morphogens provide positional information to NSCs, inducing the expression of region-specific transcription factors (*1*–*3*). The morphogen sonic hedgehog (SHH) drives ventral NSC identity across the neural tube, including the telencephalon, where it induces the expression of ventral transcription factors such as *NK homeobox 2* (*Nkx2-1*) (*4*). NSCs of the postnatal ventricular-subventricular zone (V-SVZ) also have distinct positional identities along the dorsal-ventral axis (*5*) and arise from embryonic NSCs before embryonic day 13.5 (E13.5) (*6*, *7*). V-SVZ NSCs maintain the positional information of their embryonic precursors, including the expression of region-specific transcription factors, throughout adulthood (*6*), making them a well-suited model system in which to study the mechanisms underlying long-term maintenance of positional identity. In particular, embryonic NSCs in the ventrally located medial ganglionic eminence (MGE) express *Nkx2-1* and give rise to the population of *Nkx2-1*$^+$ NSCs in the postnatal ventral V-SVZ (*8*, *9*) (Fig. 1A).

Mll1, not SHH, maintains *NKX2-1 expression* in NSCs in vivo

Although it has been hypothesized that ongoing morphogen signaling is required to maintain the positional identity of NSCs (*2*, *10*), other studies have suggested that NSC positional identity is maintained in a cell-autonomous fashion (*5*). Around E8.0, SHH signaling induces the expression of *Nkx2-1* in the ventral neural tube (*11*), and deletion of *Shh* at ~E10 reduces NKX2-1 expression in the dorsal aspect of the E12.5 MGE (*12*). To determine whether ongoing SHH signaling was required to maintain *Nkx2-1* expression in V-SVZ NSCs, we used the *Nkx2-1*-Cre driver to delete conditional alleles of the SHH receptor *Smoothened* (*Smo*^{F}) and followed the fate of recombined cells with a tdTomato transgenic Cre reporter (Ai14).

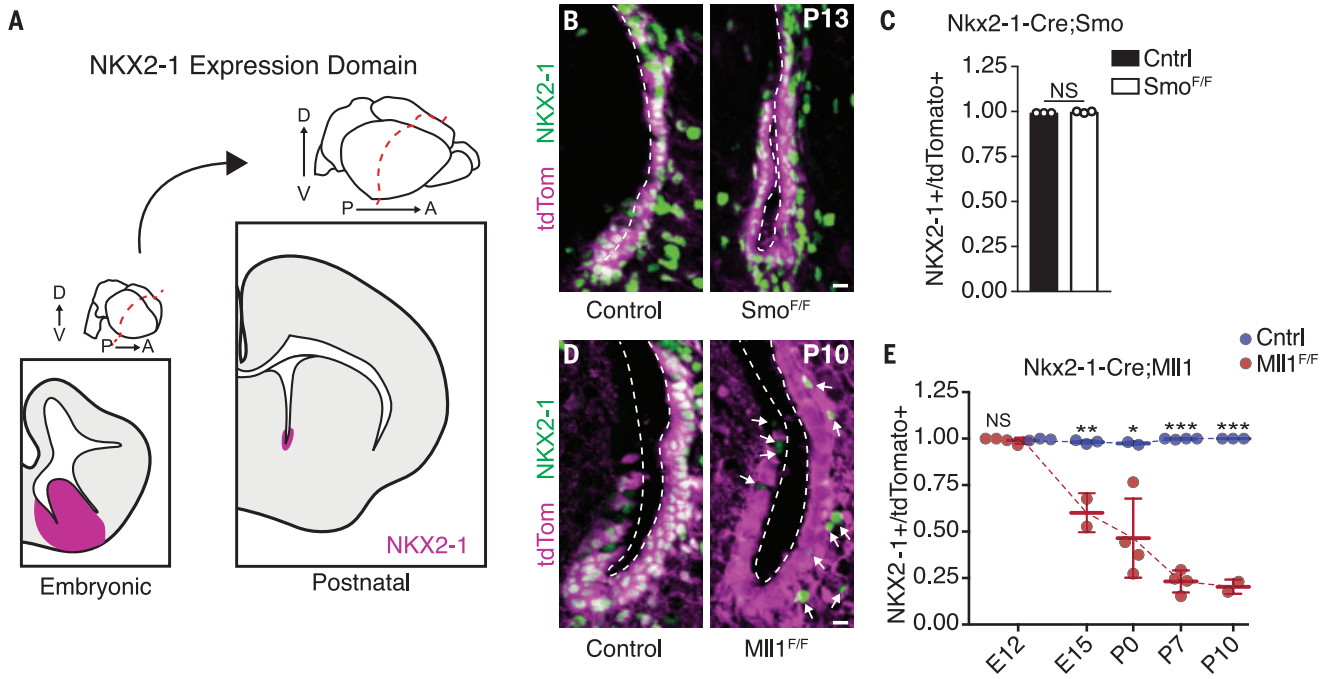

Fig. 1. *Mll1*, but not SHH signaling, is required to maintain NKX2-1 expression in postnatal V-SVZ. (**A**) NKX2-1 expression in the germinal zones of embryonic forebrain and postnatal V-SVZ. NKX2-1 domain shown in magenta. D, dorsal; V, ventral; P, posterior; A, anterior. (**B**) Representative images of NKX2-1 (green) and tdTomato (magenta) expression in P13 coronal sections from ventral V-SVZ of *Nkx2-1*-Cre;*Smo*$^{F/+}$ and *Nkx2-1*-Cre;*Smo*$^{F/F}$ mice. Ventricular walls are demarcated by a dashed line. (**C**) Quantification of NKX2-1$^+$;tdTomato$^+$ double-positive V-SVZ cells in *Nkx2-1*-Cre:*Smo*$^{F/+}$ (control) and *Nkx2-1*-Cre:*Smo*$^{F/F}$ animals at P13 (mean ± SD; NS, not significant; two-tailed student's *t* test). (**D**) Representative images of NKX2-1 (green) and tdTomato (magenta) expression in ventral V-SVZ of P10 *Nkx2-1*-Cre;*Mll1*$^{F/+}$ and *Nkx2-1*-Cre;*Mll1*$^{F/F}$ mice. Ventricular walls are demarcated by a dashed line. Arrows indicate tdTomato$^-$;NKX2-1$^+$ cells. (**E**) Quantification of NKX2-1$^+$;tdTomato$^+$ double-positive V-SVZ cells from *Nkx2-1*-Cre:*Mll1*$^{F/+}$ (control) and *Nkx2-1*-Cre:*Mll1*$^{F/F}$ mice over the course of development (mean ± SD, *P < 0.05, **P < 0.01, ***P < 0.001, two-tailed student's *t* test). Scale bars, 10 μm [(B) and (D)].

Although deletion of *Smo* at ~E8.25 has been shown to abolish the initiation of *Nkx2-1* expression in ventral NSCs (*13*), the majority (99.7 ± 0.45%, $n = 3$ animals) of tdTomato$^+$ cells in the postnatal V-SVZ of *Nkx2-1*-Cre; *Smo$^{F/F}$*;Ai14 mutant mice remained NKX2-1$^+$ (Fig. 1, B and C), as did *Nkx2-1*-Cre:*Smo$^{F/+}$* controls (99.2 ± 0.01%, $n = 3$ animals, $P = 0.10$). These data indicate that once *Nkx2-1* is expressed, canonical SHH signaling is no longer required to maintain the *Nkx2-1*$^+$ population of ventral V-SVZ precursors, and instead they are maintained by another mechanism.

Mixed-lineage leukemia 1 (*Mll1*) is the mammalian homolog of the *Drosophila* gene *trithorax*, and these genes are required to maintain—but not induce—the proper regional expression of *Hox* cluster genes that determine the anterior-posterior body plan during early embryogenesis (*14*–*16*). The vertebrate telencephalon develops from the most anterior aspect of the neural tube, and telencephalic NSCs remain regionally distinct throughout development and into postnatal life (*9*, *17*, *18*). To investigate whether *Mll1* is required to maintain *Nkx2-1* in ventral NSCs through embryonic and postnatal development, we used the *Nkx2-1*-Cre driver to delete conditional alleles of *Mll1* (*Mll1^F*) (*19*). *Nkx2-1*-Cre;*Mll1$^{F/F}$*;Ai14 animals were born at expected Mendelian frequencies but died by postnatal day 13 (P13). *Nkx2-1*-Cre;*Mll1$^{F/F}$*; Ai14 mutants exhibited a progressive loss of NKX2-1 in tdTomato$^+$ cells as compared with *Nkx2-1*-Cre;*Mll1$^{F/+}$* controls beginning at E15.5 and reached an 80% reduction by P10 (Fig. 1, D and E, and fig. S1A)—the decrease occurring in a posterior-to-anterior gradient over this developmental period (fig. S1, B and C). In *Nkx2-1*-Cre;*Mll1$^{F/F}$*;Ai14 mutants, the expression of the cell cycle marker Ki67 in tdTomato$^+$ cells was not different from that in controls (fig. S1, D and E), indicating that changes in NSC proliferation do not account for the decrease in NKX2-1$^+$/tdTomato$^+$ cells. Mice with germline null mutation of *Mll1* at E10 had normal expression of NKX2-1 in ventral NSCs (fig. S1F), indicating that *Mll1* is not required for the initial expression of *Nkx2-1*. Thus, *Mll1* is required for the maintenance, but not the initial induction, of *Nkx2-1* in vivo.

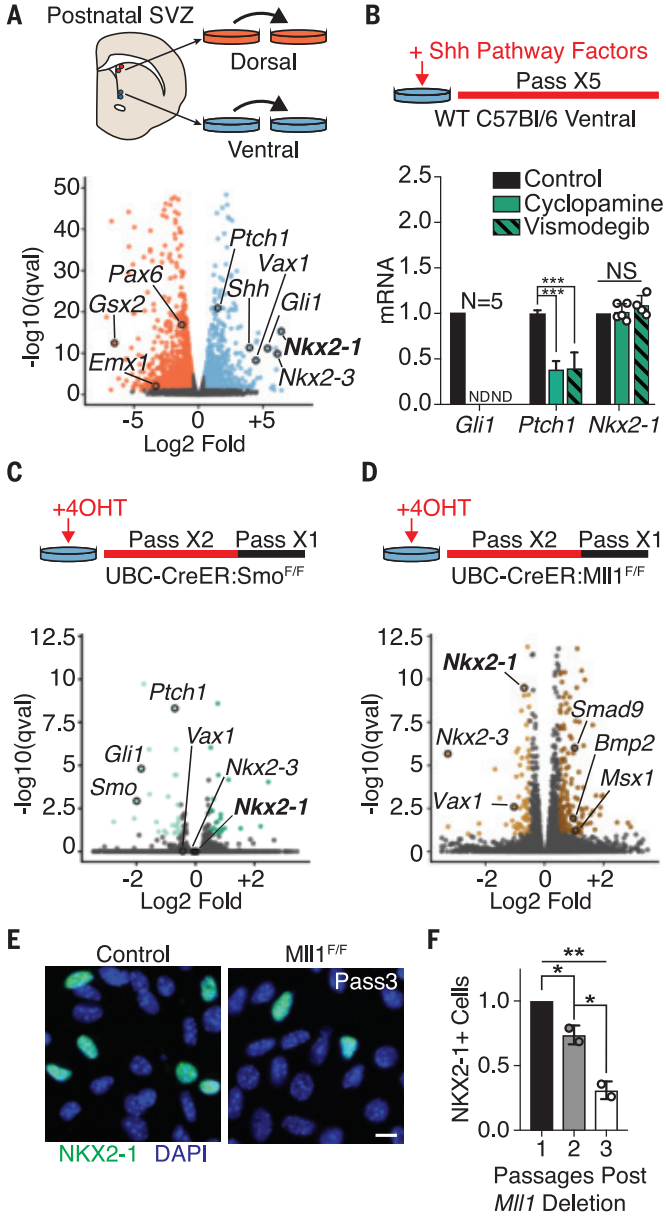

Fig. 2. *Mll1*-dependent NSC transcriptional identity does not require SHH signaling. (**A**) Derivation of region-specific NSC cultures from the dorsal and ventral P7 mouse V-SVZ (top panel). Volcano plot of differential gene expression by RNA-seq in dorsal and ventral NSC cultures. Dorsal-enriched genes, orange; ventral-enriched genes, light blue. (**B**) Pharmacological SHH pathway inhibition assay timeline (top panel). qPCR from ventral V-SVZ NSC cultures exposed to SHH pathway inhibitors (mean ± SD, ***$P < 0.001$, two-tailed student's *t* test; ND, not detected). *Gli1* and *Nkx2-1* analysis from 4 to 5 biological replicates, *Ptch1* in technical triplicate. (**C**) Schematic of ubiquitous *Smo* deletion from ventral NSC cultures by 4-OHT administration (top). Volcano plot of differential gene expression by RNA-seq in ventral *UBC*-CreER; *Smo$^{F/+}$* and *UBC*-CreER; *Smo$^{F/F}$* NSC cultures. Genes up-regulated, dark green; down-regulated, light green; not significantly changed, gray. (**D**) Schematic of ubiquitous *Mll1* deletion from ventral NSC cultures by 4-OHT administration (top). Volcano plot of differential gene expression by RNA-seq in ventral *UBC*-CreER;*Mll1$^{F/+}$* and *UBC*-CreER; *Mll1$^{F/F}$* NSC cultures. Genes up-regulated, dark brown; down-regulated, light brown; not significantly changed, gray. (**E**) Representative image of NKX2-1$^+$ cells in ventral *UBC*-CreER;*Mll1$^{F/+}$* and *UBC*-CreER;*Mll1$^{F/F}$* NSC cultures. Scale bar, 10 μm. (**F**) Quantification of NKX2-1$^+$ cells after in vitro deletion of *Mll1* by *UBC*-CreER relative to baseline at first passage (mean ± SD, *$P < 0.05$, **$P < 0.01$, one-way analysis of variance with Tukey's multiple comparison test).

Mll1$^{-/-}$ NSCs adopt a dorsal-like transcriptional profile

To further investigate the mechanisms that maintain NSC positional identity, we used postnatal V-SVZ NSC cultures that maintain their positional identity through serial passage in vitro (*5*, *20*) (Fig. 2A). Dorsally derived NSC cultures had higher expression of transcription factors found in the dorsal V-SVZ in vivo—e.g., *paired box 6* (*Pax6*), *empty spiracles homeobox 1* (*Emx1*), and *GS homeobox 2* (*Gsx2*)—and ventral NSC cultures were enriched for factors such as *Nkx2-1*, *ventral anterior homeobox 1* (*Vax1*), and *NK2 homeobox 3* (*Nkx2-3*) (Fig. 2A and data S1). Ventral NSCs expressed *Shh* as well as *patched 1* (*Ptch1*) and *GLI-kruppel family member GLI1* (*Gli1*) (Fig. 2A), two genes that are downstream transcriptional readouts of SHH signaling. While the addition of Smo pharmacological inhibitors cyclopamine or vismodegib reduced

[1]Department of Neurological Surgery, University of California, San Francisco, San Francisco, CA 94143, USA. [2]Eli and Edythe Broad Center of Regeneration Medicine and Stem Cell Research, University of California, San Francisco, San Francisco, CA 94143, USA. [3]Medical Scientist Training Program, University of California, San Francisco, San Francisco, CA 94143, USA. [4]Biomedical Sciences Graduate Program, University of California, San Francisco, San Francisco, CA 94143, USA. [5]Neuroscience Graduate Program, University of California, San Francisco, San Francisco, CA 94143, USA. [6]San Francisco Veterans Affairs Medical Center, San Francisco, CA 94121, USA. [7]Department of Human Anatomy, West China School of Basic Medical Sciences and Forensic Medicine, Sichuan University, Chengdu 610041, Sichuan, P.R. China. [8]Developmental and Stem Cell Biology Graduate Program, University of California, San Francisco, San Francisco, CA 94143, USA. [9]Department of Pathology, University of Michigan, Ann Arbor, MI 48109, USA.
*These authors contributed equally to this work.
†Corresponding author. Email: daniel.lim@ucsf.edu

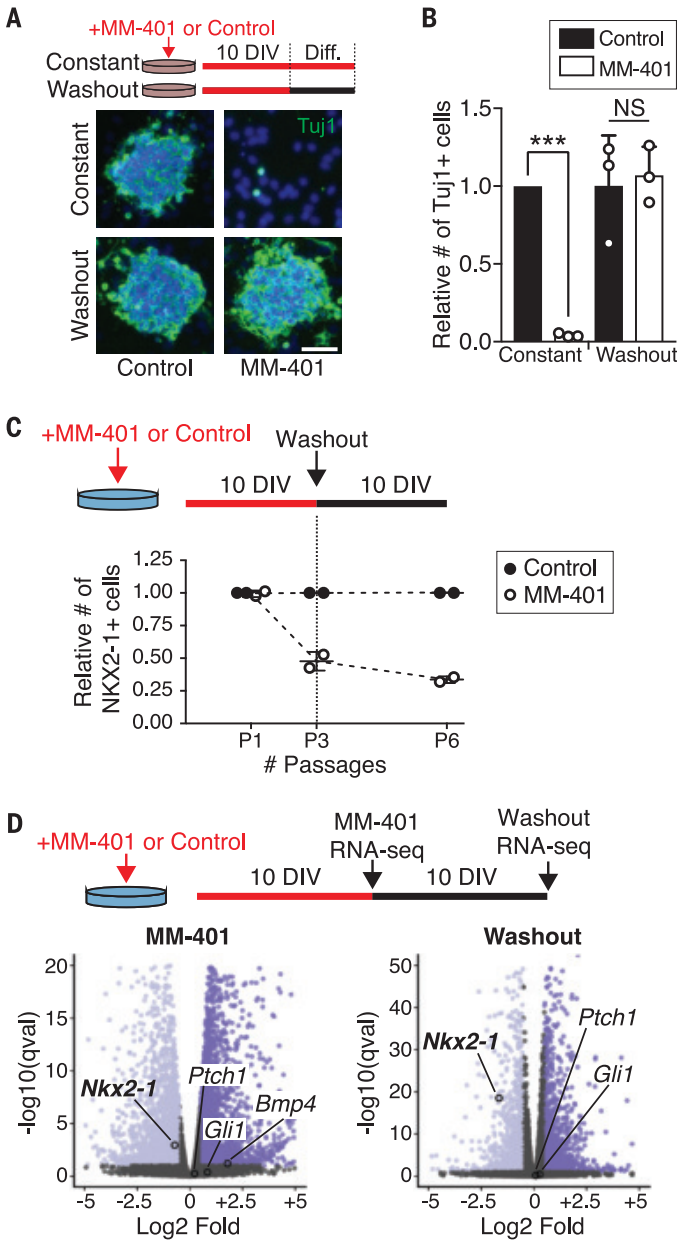

Fig. 3. Ventral NSC transcriptional identity requires continuous MLL1 function.
(**A**) Treatment timeline of V-SVZ NSCs with the MLL1-specific inhibitor MM-401 (or vehicle control) under proliferative conditions for 10 days in vitro (DIV), followed by differentiation (Diff.) with or without drug washout (top). Representative images of Tuj1 (green) and DAPI (4′,6-diamidino-2-phenylindole, blue) after differentiation. Scale bar, 50 μm. (**B**) Quantification of Tuj1$^+$ cells after differentiation of MM-401–treated NSCs (mean ± SD, ***$P < 0.001$, two-tailed student's t test). (**C**) Treatment timeline of ventral V-SVZ NSCs with MM-401 and subsequent washout under proliferative conditions (top). Quantification of NKX2-1$^+$ cells normalized to control-treated group at each time point. (**D**) Volcano plot of differential gene expression by RNA-seq in ventral NSCs treated with MM-401 (left) and then after washout (right) under proliferative conditions. Genes up-regulated, dark purple; down-regulated, light purple; not significantly changed, gray.

Gli1 and *Ptch1* mRNA levels, the expression of *Nkx2-1* remained unchanged, as assessed by quantitative polymerase chain reaction (qPCR) (Fig. 2B) and immunocytochemistry (fig. S2, A and B). Sequestration of SHH ligand by the 5E1 antibody resulted in decreased expression of *Ptch1* and *Gli1* but did not affect *Nkx2-1* expression (fig. S2, C to E). We also genetically disrupted SHH signaling by deriving ventral V-SVZ cultures from *Smo*$^{F/F}$ mice carrying the *UBC*-Cre-ERT2 transgene (*21*) and adding 4-hydroxytamoxifen (4-OHT) to induce recombination. RNA sequencing (RNA-seq) analysis of *Smo*-deleted cultures identified 59 differentially expressed genes (27 down-regulated, 32 up-regulated) as compared with *UBC*-CreERT2;*Smo*$^{F/+}$ controls (Fig. 2C, fig. S2F, and data S2). With *Smo* deletion, *Smo*, *Gli1*, and *Ptch1* were all significantly down-regulated, but the expression of *Nkx2-1*, *Vax1*, *and Nkx2-3* remained unchanged. Thus, neither pharmacological nor genetic disruption of SHH signaling reduces the expression of transcriptional markers of ventral V-SVZ NSCs.

To study *Mll1* deletion in ventral V-SVZ NSCs, we derived cultures from *UBC*-CreERT2;*Mll1*$^{F/F}$ mice. After 4-OHT–induced deletion of *Mll1* (fig. S2G), we performed RNA-seq, identifying 272 differentially expressed genes (81 down-regulated, 191 up-regulated) as compared with *UBC*-CreERT2;*Mll1*$^{F/+}$ controls (Fig. 2D and data S3). Genes down-regulated in *Mll1*-deleted cultures were almost entirely distinct from those down-regulated in *Smo*-deleted cultures (fig. S2H). Whereas neither *Gli1* nor *Ptch1* was decreased by *Mll1*-deletion (fig. S2I), the expression of ventral genes including *Nkx2-1*, *Vax1*, and *Nkx2-3* was down-regulated (Fig. 2D and fig. S2J). Similar to the progressive loss of NKX2-1 observed in vivo (Fig. 1E), the proportion of NKX2-1$^+$ cells in *Mll1*-deleted cultures decreased with serial passage (Fig. 2, E and F) without differences in cell proliferation, as measured by incorporation of the thymidine analog 5-ethynyl-2'-deoxyuridine (fig. S2K) or cell death (fig. S2L). SHH pathway inhibition did not increase the rate or magnitude of *Nkx2-1* loss after *Mll1*-deletion (fig. S3, A to D), indicating that the gradual nature of *Nkx2-1* loss was not due to persistent SHH signaling. Instead, inhibition of cell proliferation with either mitomycin C or colchicine (fig. S3, E and F) attenuated *Nkx2-1* loss in *Mll1*-deleted cells over time (fig. S3, G to I), suggesting that the progressive loss of *Nkx2-1* relates to serial cell division. In *Mll1*-deleted ventral NSCs, we also observed increased levels of dorsally enriched genes including *limb and CNS expressed 1* (*Lix1*) as well as bone morphogenetic protein (BMP) pathway genes such as *bone morphogenic protein 2* (*Bmp2*), *SMAD family member 9* (*Smad9*), and *inhibitor of DNA binding 3* (*Id3*) (Fig. 2D and data S3). BMP signaling has multiple developmental functions including the dorsalization of the telencephalon (*22*), leading to the expression of the dorsal marker *Msx1* (*23*), which was also up-regulated in *Mll1*-deleted NSCs (Fig. 2D). However, inhibition of BMP signaling with LDN-193189 (*24*, *25*) in *Mll1*-deleted cells did not prevent the loss of *Nkx2-1* expression (fig. S3, J to M), suggesting that the loss of this aspect of ventral identity is not secondary to increased BMP signaling. Together, these results indicate that, in addition to losing the expression of ventral markers, ventral NSCs also gain some transcriptional characteristics of dorsal NSCs after the deletion of *Mll1*.

Ventral NSC transcriptional identity requires continuous MLL1 function

MM-401 is a small-molecule drug that specifically blocks MLL1 function and is reversible upon drug removal (*26*) (hereafter referred to as washout). Deletion of *Mll1* inhibits neurogenesis from V-SVZ NSCs (*27*), and consistent with these prior results, the presence of MM-401 in ventral V-SVZ cultures abolished the production of new neurons in culture (Fig. 3A). After MM-401 washout, NSCs produce the same number of new neurons as control-treated cells (Fig. 3B and fig. S4A) with no difference in cell death or proliferation (fig. S4, B and C).

Although transient MLL1 inhibition did not impair the ability of V-SVZ NSCs to differentiate into neurons in vitro, we considered the possibility that NSC positional identity might

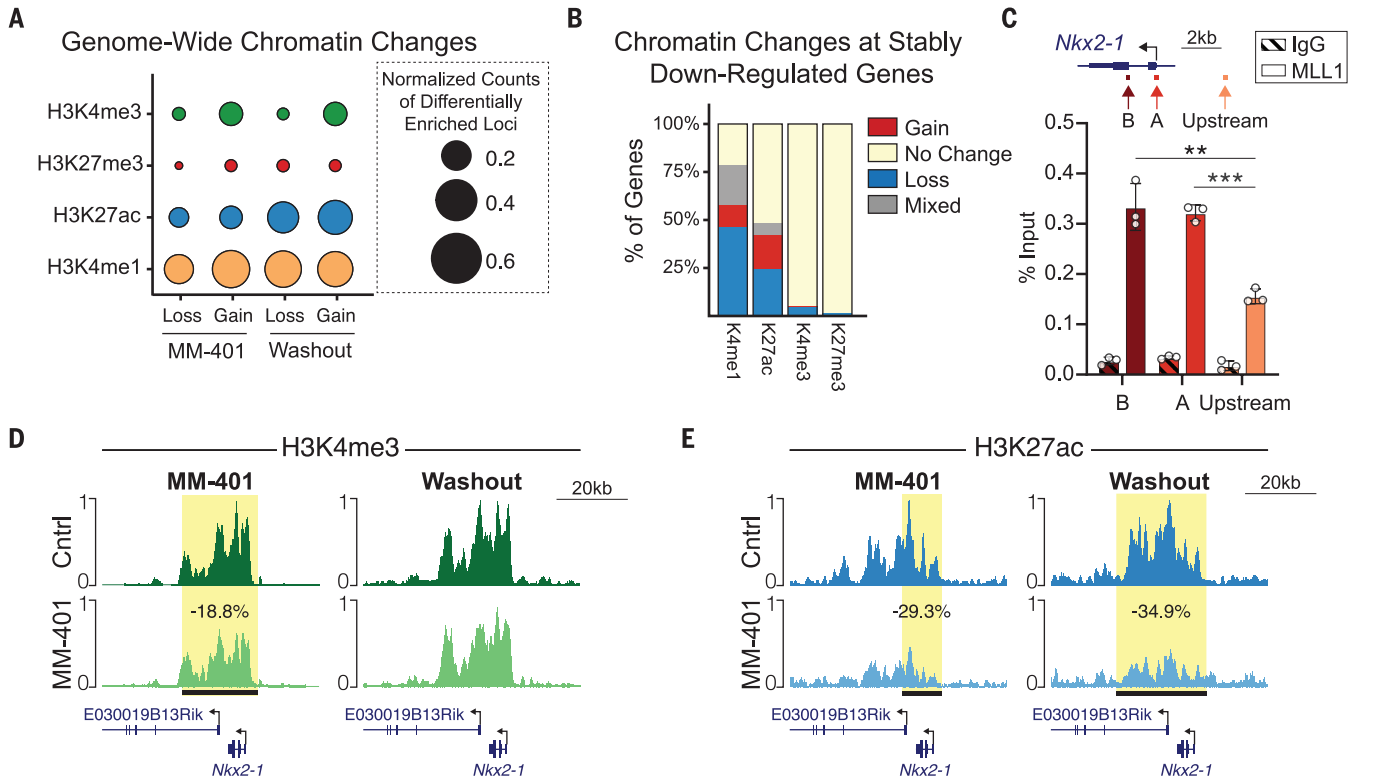

Fig. 4. Chromatin state changes to ventral NSCs after transient MLL1 inhibition. (**A**) Genome-wide quantification of chromatin changes in MM-401–treated and MM-401–washout ventral NSC cultures. Circle size represents the number of sites that have either a gain or loss of a chromatin mark in the treatment group compared with control, normalized to the size of genome covered by statistically called peaks for that chromatin mark (×10,000). (**B**) Quantification of chromatin changes within stably down-regulated genes after MM-401 washout. (**C**) Locations of qPCR primers at the *Nkx2-1* locus (top). ChIP-qPCR analysis of MLL1 enrichment at *Nkx2-1* (mean ± SD, $^{**}P < 0.01$, $^{***}P < 0.001$, two-tailed student's *t* test, in technical triplicate). IgG, immunoglobulin G; kb, kilobases. (**D** and **E**) CUT&RUN traces of (D) H3K4me3 and (E) H3K27ac enrichment over the *Nkx2-1* locus in control- and MM-401–treated cultures (left) and after 10 days of washout (right). Horizontal black bar with yellow highlight depicts genomic region with statistically significant differential chromatin enrichment.

have been durably affected. Consistent with *Mll1* deletion in ventral NSCs (Figs. 1, D and E, and 2, D to F), including those from adult mice (fig. S4, D and E), the presence of MM-401 reduced the proportion of NKX2-1^{+} cells as compared with control-treated cultures (Fig. 3C), without changes to the expression levels of *Gli1* and *Ptch1* (fig. S4C). Even after 10 days of MM-401 washout (five serial passages), the expression of *Nkx2-1* did not recover (Fig. 3D and fig. S4, F and G). Similarly, transient inhibition of MLL1 in ventral NSCs from adult (P60) mice also resulted in stable loss of *Nkx2-1* expression (fig. S4, D and H), suggesting that MLL1 activity is required for NSC positional identity throughout life. In addition to *Nkx2-1*, ~28% of the genes down-regulated in the presence of MM-401 remained down-regulated after drug washout, as revealed by RNA-seq (data S4 and S5). Among the genes that were down-regulated in the presence of MM-401, *Nkx2-1* was the most down-regulated after washout of MM-401 (fig. S4G). Although it has been suggested that NKX2-1 protein can autoregulate its own expression (*28*, *29*) (fig. S5A), in ventral NSCs in vivo, active transcription of the *Nkx2-1* locus did not require NKX2-1 protein (fig. S5, B to D). Thus, continuous MLL1 function is required for the transcriptional memory of markers of ventral identity in proliferating NSC cultures.

MLL1 can regulate chromatin via its methyltransferase domain, recruitment of acetyltransferases, and antagonism of polycomb repressive factors (*30*–*36*). We therefore performed genome-wide analysis of modifications related to histone methylation (H3K4me3 and H3K4me1), acetylation (H3K27ac), and polycomb factor repression (H3K27me3) using Cleavage Under Targets and Release Using Nuclease (CUT&RUN) (*37*). In ventral V-SVZ cultures, H3K4me1, a mark associated with transcriptional enhancers, and H3K27ac, a mark associated with active enhancers and promoters, were the most commonly decreased chromatin marks during MM-401 treatment (Fig. 4A). These changes corresponded to the differential gene expression observed with this ongoing inhibition of MLL1 activity (fig. S6A). Ten days after MM-401 washout, the genome-wide landscape of NSCs remained enriched for changes of H3K4me1 and H3K27ac levels (Fig. 4A). Fifty-three percent of loci with decreased H3K4me1 and 51% of loci with decreased H3K27ac under MLL1 inhibition remained decreased after MM-401 washout (fig. S6B). This "stable" loss of H3K4me1 at putative enhancer sequences correlated significantly with stably down-regulated gene expression (fig. S6C). Within gene bodies, the stable loss of H3K27ac also corresponded to stably down-regulated gene expression (fig. S6D). Focusing on genes that remained down-regulated after MM-401 washout, we found that decreases in H3K4me1 and/or H3K27ac enrichment were the most common chromatin changes (Fig. 4B).

At the *Nkx2-1* locus, MLL1 protein was enriched near the transcriptional start site, as indicated by chromatin immunoprecipitation (ChIP) analysis (Fig. 4C). Treatment with MM-401 resulted in a small but statistically significant decrease (18.8%, $P_{adj} = 0.009$) in H3K4me3 enrichment across the *Nkx2-1* gene body (Fig. 4D, left, and fig. S6D). However, this decrease in H3K4me3 was transient as there was no difference in H3K4me3 enrichment detected after the washout of MM-401 (Fig. 4D, right, and fig. S6D). In contrast, we observed a durable loss of H3K27ac enrichment across the *Nkx2-1* gene body both during MM-401 treatment (Fig. 4E, left, and fig. S6E) and

after washout of the inhibitor (Fig. 4E, right, and fig. S6E). Together, these results indicate that transient MLL1 inhibition leads to persistent changes to the chromatin landscape that relate to stable differential gene expression.

Transient MLL1 inhibition alters developmental fate of ventral NSCs

To investigate whether transient inhibition of MLL1 activity affected the developmental potential of ventral NSCs, we studied the fate of their daughter cells after transplantation back to the V-SVZ. Throughout life, the V-SVZ produces new neurons for the olfactory bulb, and NSC positional identity underlies which olfactory bulb neuronal subtypes are generated

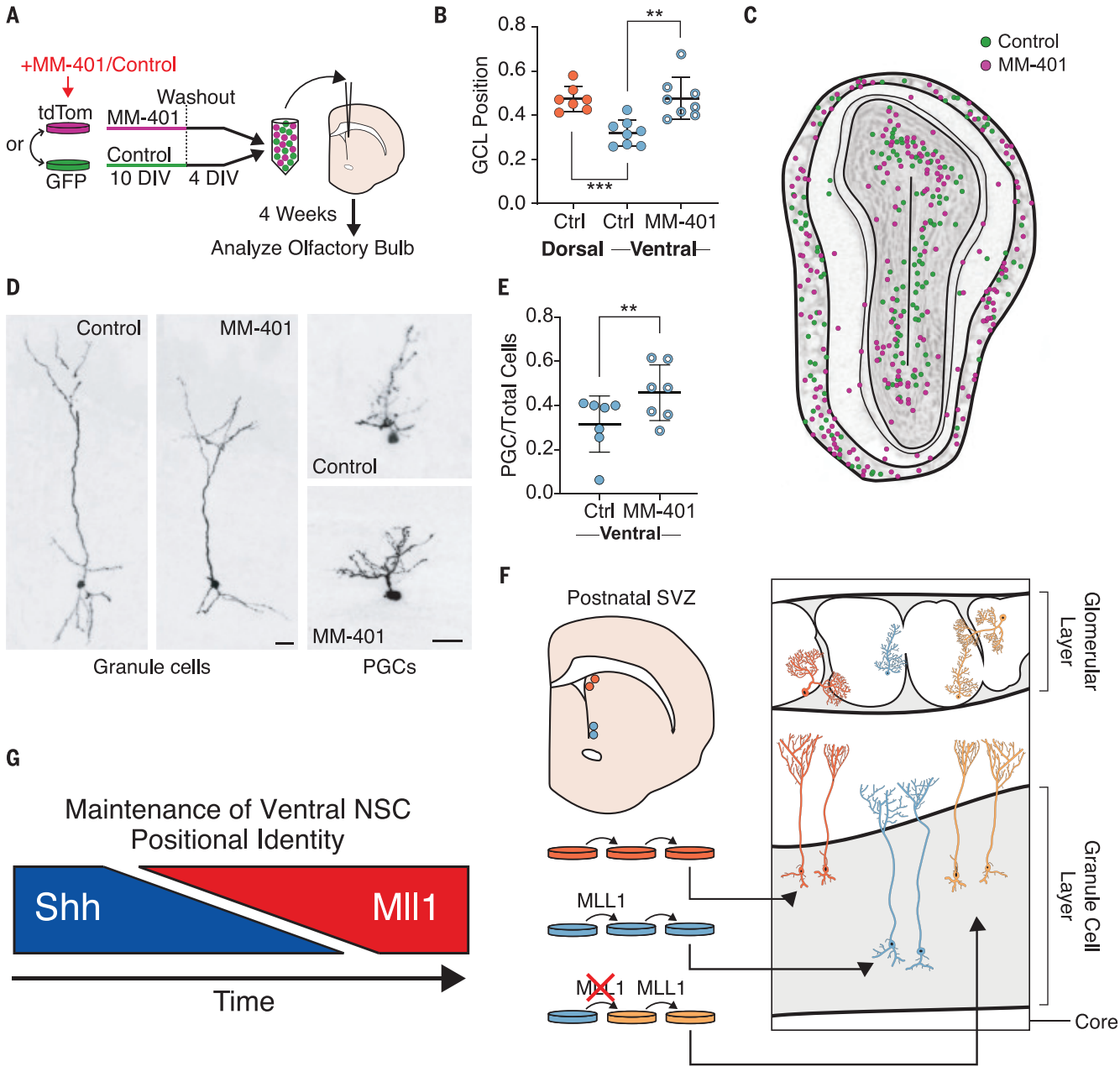

Fig. 5. Transient MLL1 inhibition alters NSC positional identity. (**A**) Derivation and treatment of NSC cultures labeled with GFP or tdTomato for transplantation into adult V-SVZ. (**B**) Granule cell layer (GCL) position of transplant-derived olfactory bulb (OB) GC interneurons per animal (mean ± SD, $^{**}P < 0.01$, $^{***}P < 0.001$, two-tailed student's *t* test, three separate rounds of transplantation). Dorsal-derived cells, orange; ventral-derived cells, light blue; control-treated cells, solid circles; MM-401–treated cells, rings. (**C**) Map of ventral NSC transplant-derived neurons within OB, pooled from two animals. MM-401–treated cells (magenta) and control cells (green). (**D**) Representative GC and periglomerular (PGC) OB interneurons generated by transplanted ventral NSCs. Scale bars, 20 μm. (**E**) Relative proportion of transplant-derived PGCs produced by control and MM-401–treated ventral NSCs (mean ± SD, $^{**}P < 0.01$, two-tailed student's *t* test). (**F**) Schematized results of MM-401–mediated MLL1 inhibition followed by washout and transplantation. GC interneurons derived from transplanted NSCs are color coded to indicate positional identity: dorsal, orange; ventral, light blue; "dorsal-like," yellow. (**G**) Generalized model of the regulation of ventral NSC positional identity over the course of development, where SHH signaling is initially required but later shifts to a state of MLL1-dependence.

(*5*). In vivo, dorsal NSCs generate superficial granule cells, whereas ventral NSCs generate deep granule cells (*5*, *9*), and such differences in developmental potential are maintained in vitro even after transplantation to ectopic V-SVZ locations (*5*) (e.g., ventral NSCs still generate deep granule cells when grafted to the dorsal V-SVZ). Thus, deep and superficial granule cells are distinct neuronal subtypes that arise from different populations of NSCs with distinct positional identities related to their location in the walls of the V-SVZ. We treated ventral NSC cultures with MM-401 or vehicle control for 10 days, after which the cells were cultured under washout conditions for 4 days before transplantation to the V-SVZ of adult mice (Fig. 5A). MM-401-washout and control NSCs were labeled with either tdTomato or green fluorescent protein (GFP) and mixed together in equal numbers before being cotransplanted into the V-SVZ. In experiments performed in parallel, consistent with previous findings (*5*), control NSCs from the dorsal V-SVZ generated granule cell neurons more superficial than those generated from ventral V-SVZ NSCs (Fig. 5B). Four weeks post-transplantation, the number of olfactory bulb neurons derived from MM-401-washout and control NSCs was similar (fig. S7A), again indicating that transient MLL1 inhibition does not impair the ability of NSCs to differentiate into neurons (Fig. 3, A and B). Furthermore, graft-derived neurons had normal morphologies and were dispersed throughout the olfactory bulb (Fig. 5, C and D, and fig. S7, B and C). However, instead of producing deep granule cells, MM-401-washout ventral NSCs produced granule cells whose location was similar to those born from dorsal NSC controls (Fig. 5B). MM-401-washout cells also generated a greater number of periglomerular cells (Fig. 5E), an olfactory bulb neuron subtype preferentially born from the anterior V-SVZ (*5*). Thus, after transient MLL1 inhibition, the normal developmental potential of ventral V-SVZ NSCs is altered, producing neuronal subtypes more typical of an anterior-dorsal NSC identity (Fig. 5F).

Outlook

Our results support a model in which MLL1 functions as part of a transcriptional memory system in telencephalic NSCs, retaining key aspects of NSC positional identity that underlie the generation of proper neuronal diversity. After ventral NSC identity is established by SHH in the early forebrain, MLL1 is required to maintain this positional information (Fig. 5G). As key aspects of ventral NSC identity are not lost by inhibition of SHH signaling, we propose that the maintenance of regional differences in NSCs during telencephalic development can become independent of the morphogen gradients that initially pattern the neural tube. MLL1 can remain localized to target genes through mitosis, allowing for the rapid reestablishment of transcription after cell cycle exit (*38*, *39*). In ventral NSCs, MLL1 may be targeted to loci by SHH-induced transcription factors, with MLL1 remaining localized over serial cell divisions, resulting in persistent chromatin-state changes even after SHH withdrawal.

The mechanism(s) by which chromatin regulators maintain specific patterns of gene expression over serial cell division remain poorly understood. We found persistent, genome-wide changes in H3K4me1 and H3K27ac after transient inhibition of MLL1 (Fig. 4A). MM-401 blocks the interaction between MLL1 and WD repeat-containing protein 5 (WDR5), which disrupts the localization of MLL1 to chromatin (*27*). A lack of proper MLL1 localization may lead to both the local loss of H3K4me1, which is one of the histone modifications catalyzed by MLL1 (*34*), and loss of H3K27ac, which is catalyzed by CREB (cAMP response element–binding protein) binding protein (CBP), a histone acetyltransferase that interacts directly with MLL1 (*35*, *36*). Whereas many loci exhibited persistent changes of H3K4me1 and H3K27ac after MM-401 washout, losses of H3K4me3 enrichment were relatively few and mostly transient, suggesting that other histone methyltransferases can compensate for loss of MLL1 activity. Rather than acting solely through its methyltransferase function, localized MLL1 protein may serve as a genomic "bookmark" for the reestablishment of gene expression after mitosis (*38*, *39*).

This model provides an alternative understanding of how the boundaries for populations of regionally distinct NSCs are maintained as the cells continue to proliferate—expanding the germinal zones by many orders of magnitude—and while the brain undergoes complex morphological changes. Our finding that MLL1 plays a role in the positional identity of NSCs may inform future methods for producing specific neuronal subtypes from NSCs in vitro for clinical or research purposes or provide additional insights into the neurodevelopmental defects of Wiedemann-Steiner syndrome, which is caused by mutations in *MLL1* (*40*).

REFERENCES AND NOTES

1. J. Ericson, J. Briscoe, P. Rashbass, V. van Heyningen, T. M. Jessell, *Cold Spring Harb. Symp. Quant. Biol.* **62**, 451–466 (1997).
2. M. Fuccillo, A. L. Joyner, G. Fishell, *Nat. Rev. Neurosci.* **7**, 772–783 (2006).
3. M. Sur, J. L. Rubenstein, *Science* **310**, 805–810 (2005).
4. J. Ericson *et al.*, *Cell* **81**, 747–756 (1995).
5. F. T. Merkle, Z. Mirzadeh, A. Alvarez-Buylla, *Science* **317**, 381–384 (2007).
6. L. C. Fuentealba *et al.*, *Cell* **161**, 1644–1655 (2015).
7. F. T. Merkle, A. D. Tramontin, J. M. García-Verdugo, A. Alvarez-Buylla, *Proc. Natl. Acad. Sci. U.S.A.* **101**, 17528–17532 (2004).
8. R. N. Delgado, D. A. Lim, *Dev. Biol.* **407**, 265–274 (2015).
9. K. M. Young, M. Fogarty, N. Kessaris, W. D. Richardson, *J. Neurosci.* **27**, 8286–8296 (2007).
10. R. A. Ihrie *et al.*, *Neuron* **71**, 250–262 (2011).
11. K. Shimamura, D. J. Hartigan, S. Martinez, L. Puelles, J. L. Rubenstein, *Development* **121**, 3923–3933 (1995).
12. Q. Xu, C. P. Wonders, S. A. Anderson, *Development* **132**, 4987–4998 (2005).
13. M. Fuccillo, M. Rallu, A. P. McMahon, G. Fishell, *Development* **131**, 5031–5040 (2004).
14. S. J. Geisler, R. Paro, *Development* **142**, 2876–2887 (2015).
15. B. Schuettengruber, D. Chourrout, M. Vervoort, B. Leblanc, G. Cavalli, *Cell* **128**, 735–745 (2007).
16. B. D. Yu, J. L. Hess, S. E. Horning, G. A. Brown, S. J. Korsmeyer, *Nature* **378**, 505–508 (1995).
17. A. Alvarez-Buylla, M. Kohwi, T. M. Nguyen, F. T. Merkle, *Cold Spring Harb. Symp. Quant. Biol.* **73**, 357–365 (2008).
18. R. N. Delgado, D. A. Lim, *Front. Mol. Neurosci.* **10**, 373 (2017).
19. C. D. Jude *et al.*, *Cell Stem Cell* **1**, 324–337 (2007).
20. R. N. Delgado, C. Lu, D. A. Lim, *Neurogenesis* **3**, e1187321 (2016).
21. Y. Ruzankina *et al.*, *Cell Stem Cell* **1**, 113–126 (2007).
22. A. M. Bond, O. G. Bhalala, J. A. Kessler, *Dev. Neurobiol.* **72**, 1068–1084 (2012).
23. Y. Furuta, D. W. Piston, B. L. Hogan, *Development* **124**, 2203–2212 (1997).
24. G. D. Cuny *et al.*, *Bioorg. Med. Chem. Lett.* **18**, 4388–4392 (2008).
25. S. M. Chambers *et al.*, *Nat. Biotechnol.* **30**, 715–720 (2012).
26. F. Cao *et al.*, *Mol. Cell* **53**, 247–261 (2014).
27. D. A. Lim *et al.*, *Nature* **458**, 529–533 (2009).
28. A. Das *et al.*, *Am. J. Physiol. Lung Cell. Mol. Physiol.* **301**, L427–L440 (2011).
29. H. Oguchi, S. Kimura, *Endocrinology* **139**, 1999–2006 (1998).
30. B. Schuettengruber, H. M. Bourbon, L. Di Croce, G. Cavalli, *Cell* **171**, 34–57 (2017).
31. P. Ernst, J. Wang, M. Huang, R. H. Goodman, S. J. Korsmeyer, *Mol. Cell. Biol.* **21**, 2249–2258 (2001).
32. T. A. Milne *et al.*, *Mol. Cell* **10**, 1107–1117 (2002).
33. Y. Dou *et al.*, *Nat. Struct. Mol. Biol.* **13**, 713–719 (2006).
34. A. Patel, V. Dharmarajan, V. E. Vought, M. S. Cosgrove, *J. Biol. Chem.* **284**, 24242–24256 (2009).
35. R. N. De Guzman, N. K. Goto, H. J. Dyson, P. E. Wright, *J. Mol. Biol.* **355**, 1005–1013 (2006).
36. M. S. Cosgrove, A. Patel, *FEBS J.* **277**, 1832–1842 (2010).
37. P. J. Skene, S. Henikoff, *eLife* **6**, e21856 (2017).
38. G. A. Blobel *et al.*, *Mol. Cell* **36**, 970–983 (2009).
39. M. Bina *et al.*, *BMC Genomics* **14**, 927 (2013).
40. W. D. Jones *et al.*, *Am. J. Hum. Genet.* **91**, 358–364 (2012).

ACKNOWLEDGMENTS

We thank C. Guinto for providing expertise and help with transplantation experiments. **Funding:** Supported by NIH grant 1R01NS091544; VA grant 5I01 BX000252; the Program for Breakthrough Biomedical Research, which is partially funded by the Sandler Foundation; the Shurl and Kay Curci Foundation; the LoGlio Foundation; and the Sontag Foundation (D.A.L.). Work in the Alvarez-Buylla laboratory is supported by NIH grants R01 NS028478 and a generous gift from the John G. Bowes Research Fund. A.A.-B. is the Heather and Melanie Muss Endowed Chair and Professor of Neurological Surgery at the University of California, San Francisco. **Author contributions:** R.N.D. conceived of, designed, and performed experiments; interpreted data; and wrote the manuscript. B.M. performed experiments, interpreted data, and helped write the manuscript. C.L. assisted in performing histological work and in data quantification. R.E.A. performed transplantation experiments. S.H.A. performed biochemical experiments. Y.D. contributed the MM-401 compound. A.A.-B. supervised research. D.A.L. conceived of and supervised research and helped write the manuscript. **Competing interests:** The authors declare no competing interests. **Data and materials availability:** All datasets generated from this study are available in the GEO repository under accession number GSE145871.

SUPPLEMENTARY MATERIALS

science.sciencemag.org/content/368/6486/48/suppl/DC1
Materials and Methods
Figs. S1 to S7
Table S1
References (*41*–*56*)
MDAR Reproducibility Checklist
Data S1 to S5

16 December 2019; accepted 9 March 2020
10.1126/science.aba5960

CELL BIOLOGY

Endoplasmic reticulum–associated degradation regulates mitochondrial dynamics in brown adipocytes

Zhangsen Zhou[1]*, Mauricio Torres[1]*, Haibo Sha[2]†, Christopher J. Halbrook[1], Françoise Van den Bergh[1], Rachel B. Reinert[3], Tatsuya Yamada[4], Siwen Wang[1], Yingying Luo[1], Allen H. Hunter[5], Chunqing Wang[6], Thomas H. Sanderson[1,7], Meilian Liu[6], Aaron Taylor[8], Hiromi Sesaki[4], Costas A. Lyssiotis[1,9,10], Jun Wu[1,11], Sander Kersten[12], Daniel A. Beard[1], Ling Qi[1,3]‡

The endoplasmic reticulum (ER) engages mitochondria at specialized ER domains known as mitochondria-associated membranes (MAMs). Here, we used three-dimensional high-resolution imaging to investigate the formation of pleomorphic "megamitochondria" with altered MAMs in brown adipocytes lacking the Sel1L-Hrd1 protein complex of ER-associated protein degradation (ERAD). Mice with ERAD deficiency in brown adipocytes were cold sensitive and exhibited mitochondrial dysfunction. ERAD deficiency affected ER-mitochondria contacts and mitochondrial dynamics, at least in part, by regulating the turnover of the MAM protein, sigma receptor 1 (SigmaR1). Thus, our study provides molecular insights into ER-mitochondrial cross-talk and expands our understanding of the physiological importance of Sel1L-Hrd1 ERAD.

Membrane contact sites mediate interorganellar communication and are key to organelle homeostasis and organismal health (*1*–*3*). Endoplasmic reticulum (ER)–derived mitochondria-associated membranes (MAMs) are indispensable for mitochondrial dynamics and function. MAMs, characterized by intimate contact between the ER and mitochondria (~10 to 25 nm apart) (*4*), mark sites for mitochondrial DNA synthesis and fission (*5*–*7*) and for calcium exchange and lipid biosynthesis (*1*, *8*, *9*). During mitochondrial fission, ER tubules envelop and constrict mitochondria, and the activated dynamin-related guanosine triphosphatase (GTPase) protein (Drp1) aggregates to cleave the organelle (*5*, *10*–*13*). The mechanism underlying interorganellar communication and the physiological consequences of miscommunication remain largely unclear.

[1]Department of Molecular and Integrative Physiology, University of Michigan Medical School, Ann Arbor, MI 48105, USA. [2]Division of Nutritional Sciences, Cornell University, Ithaca, NY 14850, USA. [3]Department of Internal Medicine, Division of Metabolism, Endocrinology and Diabetes, University of Michigan Medical School, Ann Arbor, MI 48105, USA. [4]Department of Cell Biology, Johns Hopkins University School of Medicine, Baltimore, MD 21205, USA. [5]College of Engineering and Michigan Center for Materials Characterization, University of Michigan, Ann Arbor, MI 48109, USA. [6]Department of Biochemistry and Molecular Biology and Autophagy, Inflammation and Metabolism Center for Biomedical Research Excellence, University of New Mexico Health Sciences Center, Albuquerque, NM 87131, USA. [7]Department of Emergency Medicine, University of Michigan Medical School, Ann Arbor, MI 48105, USA. [8]Biomedical Research Core Facilities, University of Michigan, Ann Arbor, MI 48109, USA. [9]Department of Internal Medicine, Division of Gastroenterology and Hepatology, University of Michigan Medical School, Ann Arbor, MI 48109, USA. [10]Rogel Cancer Center, University of Michigan Medical School, Ann Arbor, MI 48109, USA. [11]Life Sciences Institute, University of Michigan, Ann Arbor, MI 48109, USA. [12]Nutrition, Metabolism and Genomics group, Wageningen University, Wageningen, Netherlands.
*These authors contributed equally to this work.
†Present address: In Vivo Pharmacology, Cardiovascular and Metabolic Diseases, Novartis Institutes for BioMedical Research, Inc., Cambridge, MA 02139, USA.
‡Corresponding author. Email: lingq@med.umich.edu

ER-associated degradation (ERAD) is a conserved quality control mechanism to recruit ER proteins for cytosolic proteasomal degradation (*14*–*19*). The Sel1L-Hrd1 protein complex constitutes the most conserved form of ERAD from yeast to humans. Sel1L resides on the ER membrane and controls the stability of the E3 ligase Hrd1 (*16*–*18*, *20*–*22*). Sel1L-Hrd1 ERAD is indispensable for fundamental physiological processes in vivo such as lipid metabolism, water balance, food intake, and systemic energy homeostasis (*15*, *19*, *23*–*31*).

Formation of megamitochondria in *Sel1L*$^{-/-}$ brown adipocytes

Serendipitously, we observed elongated mitochondria in *Sel1L*$^{-/-}$ primary brown preadipocytes, resembling those in *Drp1*$^{-/-}$ preadipocytes but distinct from those in profusion *Opa1*$^{-/-}$ cells (fig. S1, A and B). These findings prompted us to explore a possible role of Sel1L in mitochondria-rich brown adipose tissue (BAT), a potential therapeutic target for obesity (*32*). Acute cold challenge induces mitochondrial fission in BAT to enhance respiration and maintain body temperature (*33*), while having no impact on the expression of ERAD genes (fig. S2, A and B).

We generated adipocyte-specific *Sel1L*-deficient mice (*Sel1L*^{AdipCre}) by crossing *Sel1L*$^{f/f}$ mice to the adiponectin promoter–driven Cre mice (*25*). Sel1L was deleted specifically in both white adipose tissue (WAT) and BAT, resulting in lower Hrd1 expression (fig. S2C). We next performed transmission electron microscopy (TEM) to visualize mitochondria in BAT from mice housed at room temperature (22°C), or 4°C for 6 hours. There was no difference in mitochondrial morphology between *Sel1L*$^{f/f}$ and *Sel1L*^{AdipCre} BAT at 22°C (Fig. 1, A and B). Acute cold challenge led to smaller mitochondria in *Sel1L*$^{f/f}$ BAT owing to increased fission (Fig. 1, A and C). By contrast, most mitochondria in *Sel1L*^{AdipCre} brown adipocytes were enlarged and pleomorphic, with abnormal cristae architecture (yellow arrows, Fig. 1, B and C, and fig. S3, A and B). Consequently, mitochondrial density per cell was reduced in cold-stimulated *Sel1L*^{AdipCre} mice compared to littermate controls (fig. S3C).

To exclude a possible contribution from WAT, we generated brown adipocyte–specific *Sel1L*-deficient mice (*Sel1L*^{Ucp1Cre}) using Ucp1 promoter–driven Cre mice (fig. S2D). Consistent with *Sel1L*^{AdipCre} mice, mitochondria in *Sel1L*^{Ucp1Cre} BAT were markedly enlarged and pleomorphic upon acute cold exposure (yellow arrows, Fig. 1, D and E, and fig. S3D). This observation was confirmed using confocal microscopy, with BAT immunolabeled for translocase of outer mitochondrial membrane 20 (Tomm20) and matrix protein pyruvate dehydrogenase (PDH) (fig. S3E).

To gain further insight into mitochondrial morphology at the three-dimensional (3D) level, we performed serial block-face scanning electron microscopy (SBF-SEM) (fig. S4A), which allows imaging of a large field (>10 cells) at 3D planes with nanometer resolution (fig. S4, B and C) (*34*). In cold-exposed *Sel1L*$^{f/f}$ BAT, mitochondria were predominantly spherical or ovoid, with an average volume of ~1.7 μm^3 (fig. S4B and Fig. 1, F to H). Mitochondrial volume was increased fivefold in *Sel1L*$^{-/-}$ BAT (Fig. 1, F to H, and fig. S4C). Moreover, 3D reconstruction analyses revealed pleomorphic megamitochondria, e.g., branched, or chair- or cup-shaped (Fig. 1G and movies S1 and 2). Thus, Sel1L deficiency in brown adipocytes triggers the formation of pleomorphic megamitochondria within hours of cold exposure.

Sel1L controls ER-mitochondria contacts

We next explored whether Sel1L deficiency affected MAMs. In *Sel1L*$^{f/f}$ BAT, MAMs were identified as thin sheets aligned with mitochondria, with the distance between the two organelles averaging 10 to 20 nm (cyan arrows, Fig. 2, A, C, and D, and fig. S5A). By contrast, MAMs of *Sel1L*$^{-/-}$ BAT formed tubules located closer to mitochondria, with an average distance of 5 to 10 nm (Fig. 2, B to D, and fig. S5B). Moreover, the number of MAMs per mitochondrion was increased in *Sel1L*$^{-/-}$ BAT after cold exposure (Fig. 2E). These perimitochondrial tubular structures were verified as ER by binding-immunoglobulin protein (BiP)-specific immunoelectron microscopy (Fig. 2F): Pleomorphic megamitochondria appeared to "grow" around ER tubules in cold-stimulated *Sel1L*$^{-/-}$ BAT.

We next performed focused ion-beam SEM (FIB-SEM) to reconstruct mitochondria with MAMs at the 3D level. In comparison to SBF-SEM, FIB-SEM offers higher resolution at the *z* plane (*35*) with a resolution of 5-nm isotropic voxels (fig. S6). Three-dimensional reconstruction

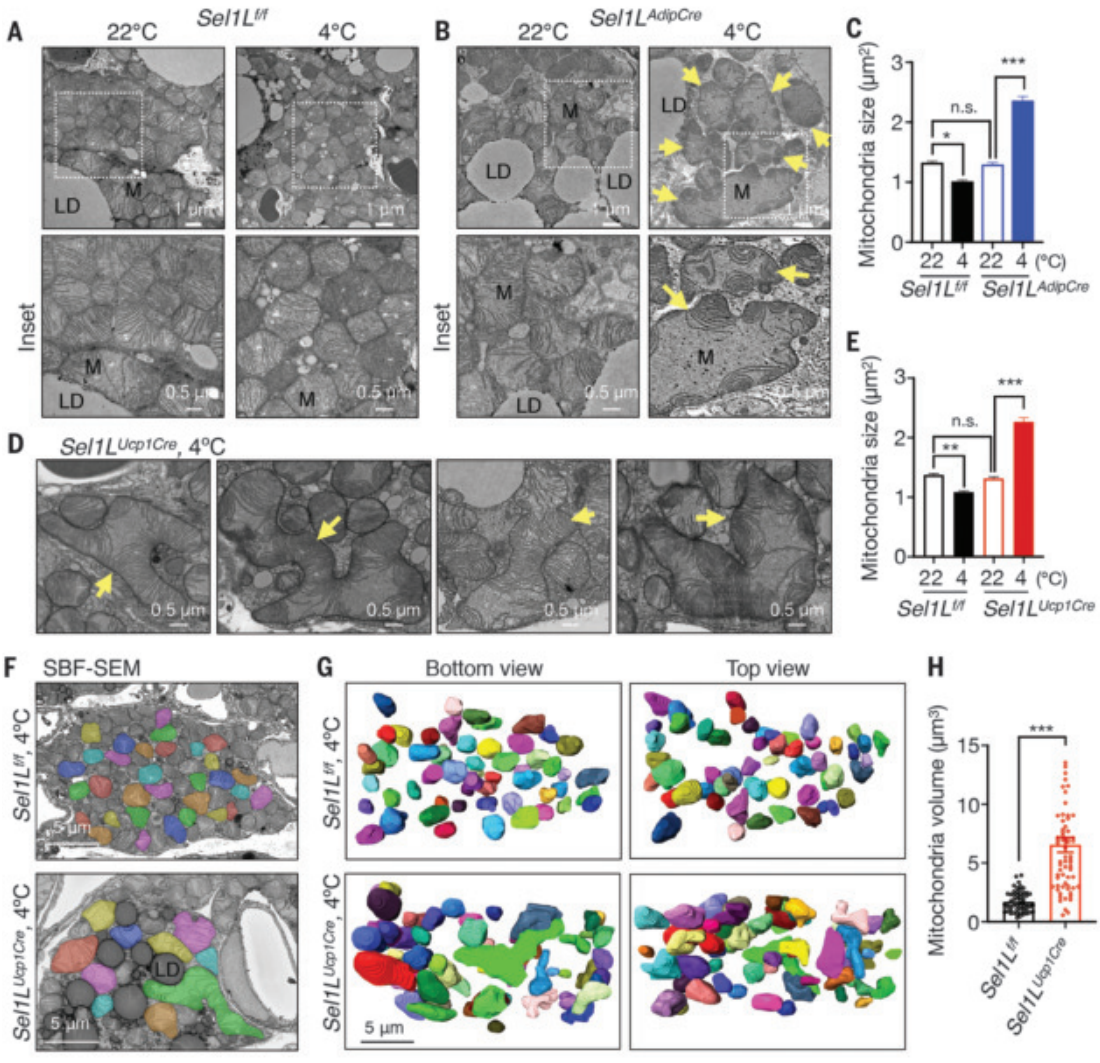

Fig. 1. Sel1L regulates mitochondrial morphology in BAT during cold exposure. (**A** to **C**) Representative TEM images of BAT from *Sel1L*$^{f/f}$ (A) and *Sel1L*^{AdipCre} mice (B) at 22°C (left) or 4°C (right) for 6 hours, with quantitation of mitochondrial size shown in (C) (n = 870, 601 mitochondria from three *Sel1L*$^{f/f}$ mice each at 22°C and 4°C; 624, 821 from three *Sel1L*^{AdipCre} mice each at 22°C and 4°C, one-way analysis of variance (ANOVA). Yellow arrows, megamitochondria. M, mitochondrion; LD, lipid droplet. (**D** and **E**) Representative TEM images of BAT from *Sel1L*^{Ucp1Cre} mice at 4°C for 6 hours, with quantitation of mitochondrial size shown in (E) (n = 676, 618 mitochondria for three *Sel1L*$^{f/f}$ mice each at 22°C and 4°C; 582, 674 for three *Sel1L*^{Ucp1Cre} mice each at 22°C and 4°C, one-way ANOVA). (**F** to **H**) Representative SBF-SEM images (F) and 3D reconstruction (G) of mitochondria from BAT of *Sel1L*$^{f/f}$ and *Sel1L*^{Ucp1Cre} mice at 4°C for 6 hours. Mitochondria in pseudocolors were reconstructed from a set of 150 SBF-SEM image stacks (65 nm/slice). (H) Quantitation of 3D volume of mitochondria (n = 61 and 63, *Sel1L*$^{f/f}$ and *Sel1L*^{Ucp1Cre} mice, Student's t test). All experiments were repeated three times. Data are mean ± SEM. *p < 0.05; **p < 0.01; ***p < 0.001; n.s., not significant.

revealed more intimate interactions between the ER (green) and mitochondria (purple) in *Sel1L*^{Ucp1Cre} BAT versus a *Sel1L*$^{f/f}$ mitochondria (pink) (Fig. 2G). In many U-shaped mitochondria, several ER tubules were found along the entire concavity of the organelle (orange arrows, Fig. 2G and movie S3).

Formation of mitochondria-perforating ER tubules in the absence of Sel1L

In many U- or dumbbell-shaped megamitochondria, the outer membrane folded back on itself, with less than 10 nm between membranes (green arrows, Fig. 3A and fig. S7A), which we speculated may fuse to embed ER tubules within the mitochondria. Indeed, there were many tubular structures embedded within mitochondrial profiles in *Sel1L*$^{-/-}$ BAT (red arrows, Fig. 3, B and C, and fig. S7, B and C). In some, double- or triple- membrane structures were noted. Moreover, these tubular structures served as a "hub" from which cristae folds radiated (Fig. 3, B and C, and fig. S7, B to D). To determine whether these peculiar structures inside mitochondria were ER, we performed BiP-specific immunoelectron microscopy. Clusters of BiP-positive signal were detected both perimitochondrially (cyan arrows) and within mitochondrial profiles (red arrows, Fig. 3D and fig. S7E). We then performed SBF- and FIB-SEM to reconstruct whole mitochondria with perforating ER tubules. For example, we present 12 consecutive images of one megamitochondrion with two parallel penetrating ER tubules (fig. S8 and Fig. 3, E and F). Two ER tubules (arrows) perforated the mitochondrial profiles in parallel, at a distance of 1 to 1.3 μm apart, with radiating and interconnecting cristae folds, resembling wagon wheel spokes. Similarly, independent FIB-SEM analyses showed two parallel ER tubules (0.7 to 1 μm apart) penetrating another megamitochondrion in *Sel1L*^{Ucp1Cre} BAT upon cold exposure (fig. S9 and movie S4). Thus, Sel1L deficiency leads to the formation of pleomorphic megamitochondria with perforating ER tubule(s) in brown adipocytes upon cold challenge.

Impaired mitochondrial function and thermogenic response in *Sel1L*$^{-/-}$ mice

Next, we asked how Sel1L deficiency affected mitochondrial function and thermogenesis. Purified mitochondria from cold-exposed *Sel1L*^{AdipCre} mice had a reduced oxygen consumption rate (OCR) from oxidation of pyruvate and malate compared to those from *Sel1L*$^{f/f}$ mice (Fig. 4A). In addition, differentiated *Sel1L*$^{-/-}$ brown adipocytes showed defective respiration in response to adrenergic receptor agonist norepinephrine (NE) stimulation (Fig. 4B). Mitochondrial functional defects were further confirmed using a targeted metabolomics

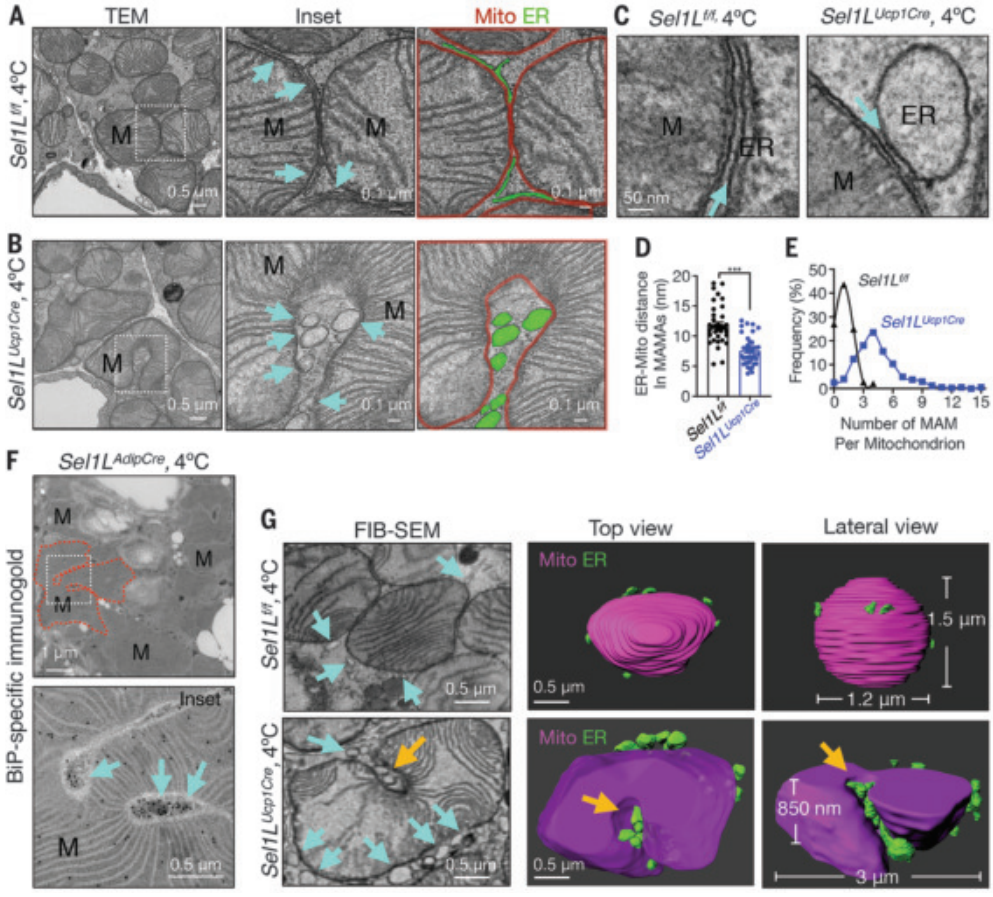

Fig. 2. Sel1L controls ER-mitochondria contacts in cold-stimulated brown adipocytes. (**A** and **B**) Representative TEM images of BAT from *Sel1L*$^{f/f}$ (A) and *Sel1L*^{Ucp1Cre} (B) mice at 4°C for 6 hours. M, mitochondrion; cyan arrows, MAMs; red lines, mitochondrial membranes; green, ER. The area shown by white dotted lines is enlarged in the inset. (**C** to **E**) Representative TEM images of the MAMs in BAT from *Sel1L*$^{f/f}$ and *Sel1L*^{Ucp1Cre} mice at 4°C for 6 hours, with quantitation of ER-mitochondrion distance (D) and abundance of MAM per mitochondrion (E). n = 35 and 40 MAMs (D) and n = 450 and 572 mitochondria (E) for *Sel1L*$^{f/f}$ and *Sel1L*^{Ucp1Cre}. (**F**) Representative TEM images of BiP-specific immunogold labeling in BAT from *Sel1L*^{AdipCre} mice at 4°C for 6 hours. Red dotted line outlines one megamitochondrion; cyan arrows, BiP-positive ER tubule(s). (**G**) Representative FIB-SEM (left) and the 3D tomography images (300 and 170 slices, 5 nm/slice) of mitochondria in BAT from *Sel1L*$^{f/f}$ and *Sel1L*^{Ucp1Cre} mice at 4°C for 6 hours. Magenta, mitochondria; green, ER. Cyan arrows, MAMs; orange arrows, MAMs going through the concave surface of a mitochondrion. All experiments were repeated two to three times. Data are mean ± SEM. ***p < 0.001 by Student's t test.

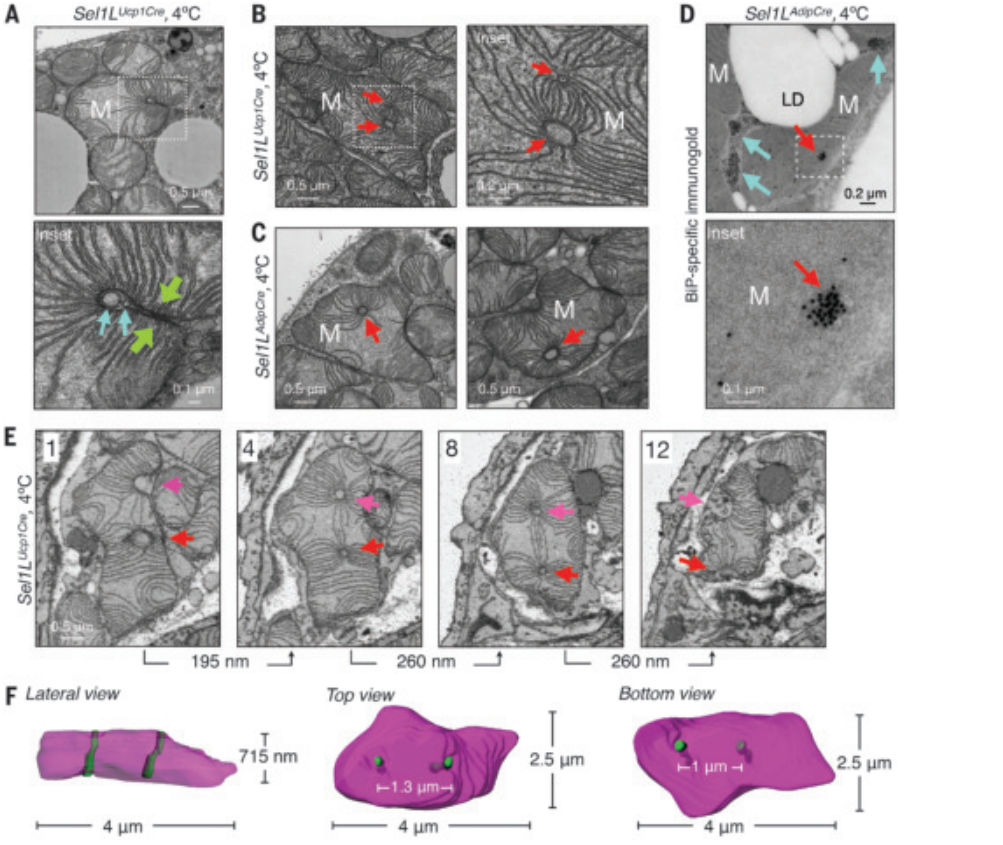

Fig. 3. Sel1L deficiency leads to the formation of megamitochondria with perforating ER tubules. (**A**) Representative TEM images of BAT in *Sel1L*^{Ucp1Cre} mice housed at 4°C for 6 hours, showing a megamitochondrion wrapping around the tubular structures (cyan arrows). Green arrows, two opposite sides of a mitochondrion. (**B** and **C**) Representative TEM images of BAT from *Sel1L*^{Ucp1Cre} (B) and *Sel1L*^{AdipCre} (C) mice at 4°C for 6 hours, showing megamitochondria with tubular structures (red arrows). (**D**) Representative BiP-immunogold TEM images of BAT in *Sel1L*^{AdipCre} mice at 4°C for 6 hours. Red and cyan arrows, mitochondria-perforating ER tubules and perimitochondria ER tubules. (**E** and **F**) Representative SBF-SEM images (E) and 3D reconstruction (F) in BAT of *Sel1L*^{Ucp1Cre} mice at 4°C for 6 hours, showing four different slices of a megamitochondrion with two parallel perforating ER tubules (red and magenta arrows). All 12 slices (65 nm/slice) are shown in fig. S8. All experiments were repeated two to three times.

analysis of 119 intracellular metabolites in NE-treated differentiated *Sel1L*$^{f/f}$ versus *Sel1L*$^{-/-}$ brown adipocytes (fig. S10). Pathway analysis of the 30 significantly altered metabolites revealed three main pathways altered in *Sel1L*$^{-/-}$ adipocytes: tricarboxylic acid (TCA) cycle, and pyrimidine and purine metabolism (Fig. 4C), all of which are associated with mitochondrial function.

Both *Sel1L*^{AdipCre} and *Sel1L*^{Ucp1Cre} mice appeared normal and grew at a rate comparable to that of their *Sel1L*$^{f/f}$ littermates up to 22 weeks on a low-fat diet at room temperature (fig. S11A). Although core body temperatures (~37°C) were similar between cohorts when housed at room temperature, *Sel1L*^{AdipCre} mice were cold sensitive and dropped core body temperature to 26°C within 6 hours of cold exposure (Fig. 4D, versus 33°C in *Sel1L*$^{f/f}$). Histological examination of BAT revealed that, although largely indistinguishable at room temperature, *Sel1L*^{AdipCre} BAT exhibited larger lipid droplets upon cold exposure compared to *Sel1L*$^{f/f}$ mice (Fig. 4E), pointing to defects in lipid mobilization. This was confirmed using immunostaining of lipid droplet binding protein Perilipin 1 (Fig. 4F). Similar observations were made with *Sel1L*^{Ucp1Cre} mice (Fig. 4D and fig. S11, B and C). Phosphorylation of hormone-sensitive lipase (HSL) was not affected in response to β_3-adrenergic receptor agonists (fig. S11, D and E), thereby uncoupling β-adrenergic signaling from the thermogenic defect of *Sel1L*$^{-/-}$ mice.

Sel1L effect on mitochondria is mediated through Hrd1 ERAD

Sel1L may have an Hrd1-independent function, and vice versa (*25*, *36*, *37*). To determine

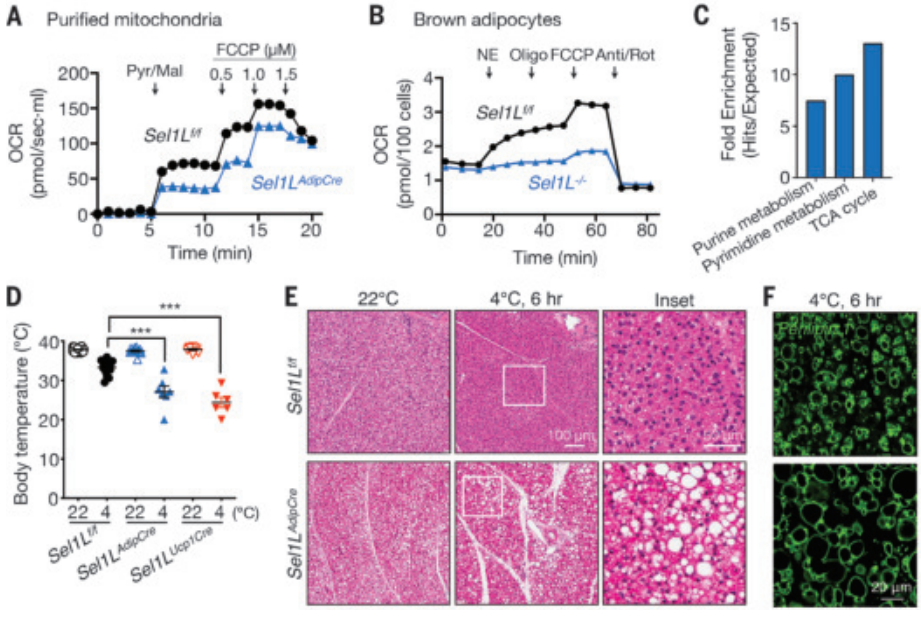

Fig. 4. Sel1L in brown adipocytes regulates mitochondrial function and cold-induced thermogenesis. (**A** and **B**) Oxygen consumption rate (OCR) of purified mitochondria from BAT of cold-exposed mice (A) and differentiated brown adipocytes (B) with the addition of various stimuli as indicated. NE, norepinephrine; Oligo, oligomycin; Pyr/Mal, pyruvate/malate; FCCP, carbonyl cyanide *p*-trifluoromethoxyphenylhydrazone; Anti, antimycin; Rot, Rotenone. (**C**) Metaboanalyst pathway enrichment analysis for the metabolites in *Sel1L*$^{f/f}$ and *Sel1L*$^{-/-}$ brown adipocytes treated with 1 μM NE for 1 hour (n = 3 per group). (**D**) Rectal temperature of 8- to 10- week-old mice housed at 22°C or 4°C for 6 hours (n = 7 to 10 mice each, one-way ANOVA). (**E** and **F**) Representative H&E (hematoxylin and eosin) (E) and Perilipin1 (F) staining of BAT from *Sel1L*$^{f/f}$ and *Sel1L*^{AdipCre} mice housed at 22°C or 4°C for 6 hours. All experiments were repeated three times except panel (C) (three samples per group). Data are mean ± SEM. ***p < 0.001.

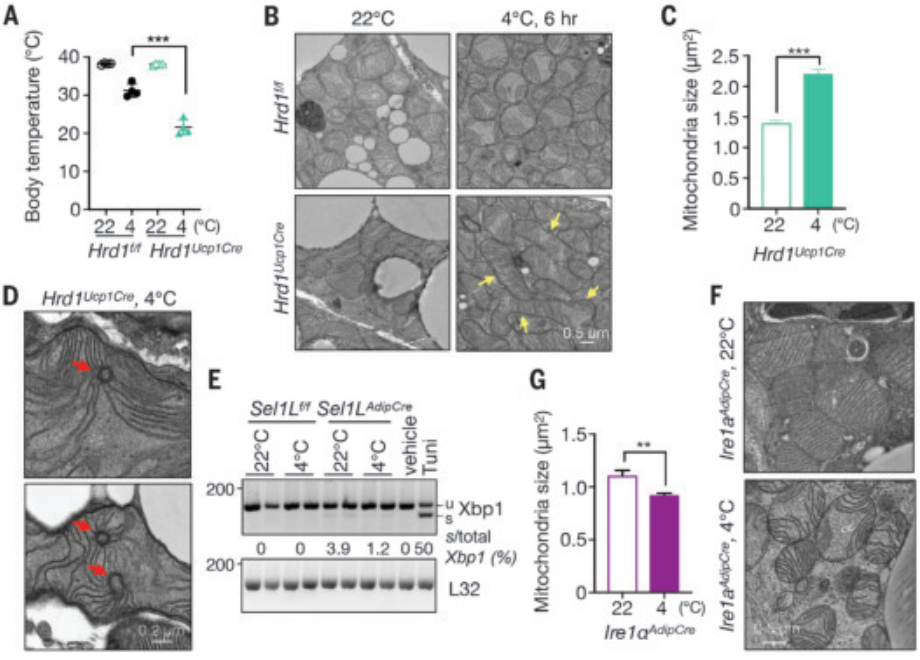

Fig. 5. Hrd1, but not Ire1α of UPR, controls mitochondrial morphology and thermogenesis in brown adipocytes. (**A**) Rectal temperature of 8- to 10- week-old *Hrd1*$^{f/f}$ and *Hrd1*^{Ucp1Cre} mice housed at 22°C or 4°C for 6 hours, n = 4 per group (one-way ANOVA). (**B** to **D**) Representative TEM images of BAT from *Hrd1*$^{f/f}$ and *Hrd1*^{Ucp1Cre} mice housed at 22°C or 4°C for 6 hours with quantitation shown in (C). n = 543, 581 mitochondria for 22°C and 4°C, Student's t test. Yellow arrows, mega-mitochondria; red arrows, ER tubules within mitochondrial profiles. (**E**) Reverse transcription–polymerase chain reaction analysis of *Xbp1* mRNA splicing in BAT at 22°C or 4°C for 6 hours with quantitation of the ratio of spliced Xbp1 (s) to total Xbp1 [spliced + unspliced (u)] shown below the gel (n = 6 mice per group). BAT from wild-type mice injected with vehicle or tunicamycin (Tuni, 1 mg/kg) included as controls. (**F** and **G**) Representative TEM images of BAT from *Ire1a*^{AdipCre} mice at 4°C for 6 hours with quantitation shown in (G) (n = 500, 665 from two mice each, Student's t test). All experiments were repeated two to three times. Data are mean ± SEM. **p < 0.01; ***p < 0.001.

whether Sel1L and Hrd1 act similarly to regulate mitochondria in BAT, we generated brown adipocyte–specific *Hrd1*-deficient (*Hrd1*^{Ucp1Cre}) mice (fig. S12A). Deletion of Hrd1 stabilized Sel1L protein (fig. S12A), in line with the notion that Sel1L is a substrate of Hrd1. *Hrd1*^{Ucp1Cre} mice grew normally (fig. S12B) but were cold sensitive (Fig. 5A), with more lipid droplets in cold-challenged BAT compared to *Hrd1*$^{f/f}$ mice (fig. S12C). Moreover, *Hrd1*^{Ucp1Cre} BAT demonstrated enlarged mitochondria, some with penetrating ER tubule(s), upon cold stimulation (Fig. 5, B to D, and fig. S12D).

Because ER stress has been linked to mild mitochondrial elongation (*38*, *39*), we next asked whether the effect of ERAD deficiency on mitochondria was mediated through ER stress. Basal *Xbp1* mRNA splicing was slightly higher in *Sel1L*^{AdipCre} BAT compared to *Sel1L*$^{f/f}$ BAT at room temperature; however, cold exposure reduced *Xbp1* mRNA splicing in *Sel1L*^{AdipCre} BAT (Fig. 5E). There was no detectable cell death in *Sel1L*^{AdipCre} BAT (fig. S13A). To study

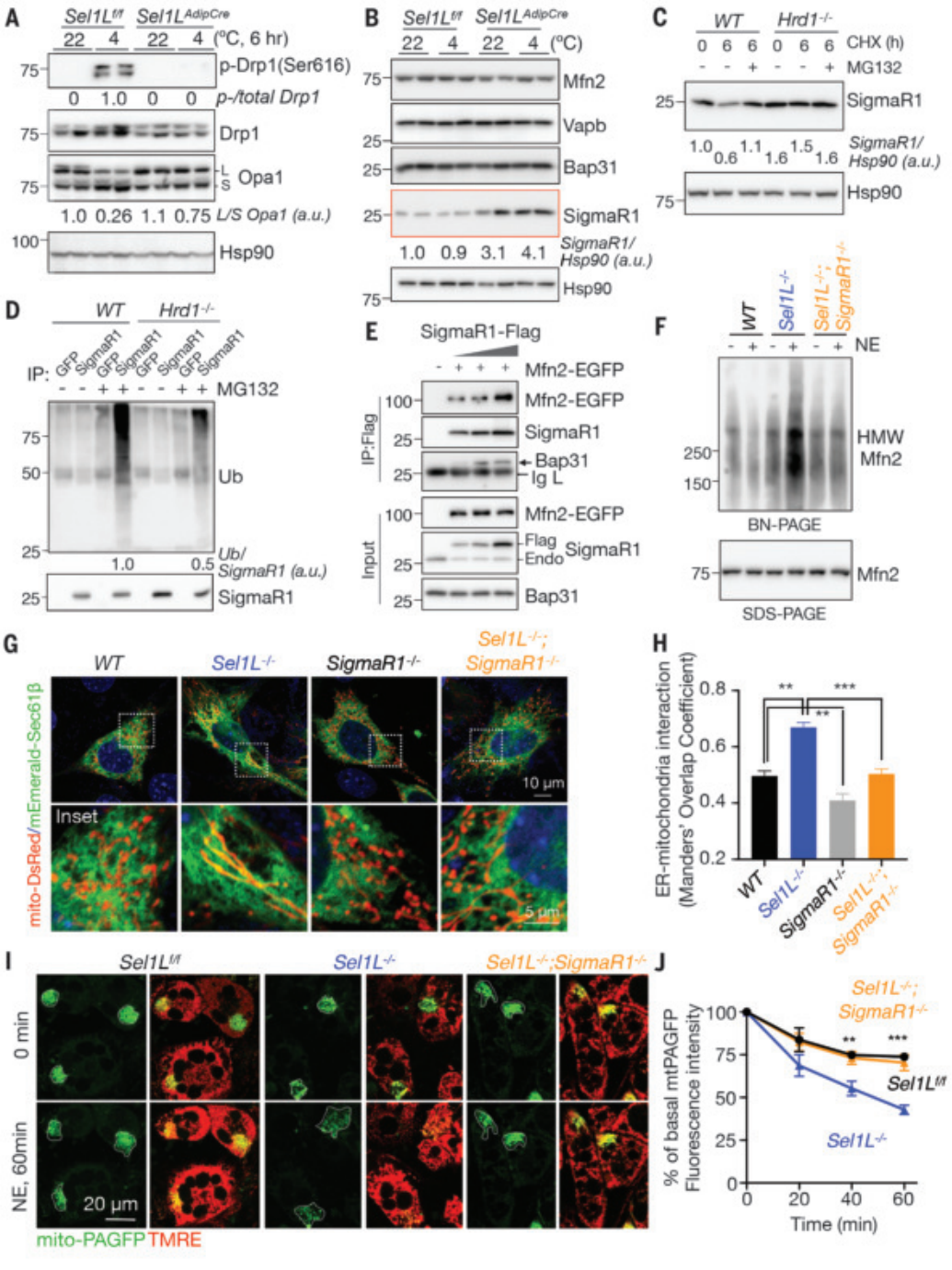

Fig. 6. Sel1L-Hrd1 ERAD regulates MAM and mitochondrial dynamics through SigmaR1. (**A**) Immunoblot analysis of mitochondrial dynamic proteins in BAT from *Sel1L*$^{f/f}$ and *Sel1L*^{AdipCre} mice at 22°C or 4°C for 6 hours with quantitation of phos-/total Drp1 and large (L)-/small (S)-Opa1 shown below the gel (n = 7 mice per group). (**B**) Immunoblot analysis of MAM proteins in BAT of *Sel1L*$^{f/f}$ and *Sel1L*^{AdipCre} mice with quantitation of SigmaR1/Hsp90 shown below the gel (n = 7 mice per group). (**C**) Immunoblot analysis of endogenous SigmaR1 in *WT* and *Hrd1*-deficient (*Hrd1*$^{-/-}$) HEK293T cells with or without cycloheximide (CHX) and MG132 treatment. (**D**) Immunoblot analysis of GFP or endogenous SigmaR1 immunoprecipitates in HEK293T (with or without MG132 treatment), showing Hrd1-mediated SigmaR1 ubiquitination. (**E**) Immunoblot analysis of Flag immunoprecipitates in HEK293T cells transfected with a combination of plasmids, showing a dose-dependent interaction between SigmaR1-Flag and Mfn2-EGFP (enhanced GFP). (**F**) Immunoblot analysis of Mfn2 oligomers or Mfn2-containing high molecular weight (HMW) complexes in brown adipocytes treated with or without NE (1 μM, 1 hour) in blue native (BN)–polyacrylamide gel electrophoresis (PAGE) and regular SDS-PAGE. (**G** and **H**) Representative images of mito-DsRed– and mEmerald-Sec61b–expressing pre-adipocytes. DAPI (4′,6-diamidino-2-phenylindole) (blue) with quantitation of ER-mitochondrial colocalization using Manders' overlap coefficient (50 cells each) shown in (H), one-way ANOVA. (**I** and **J**) Confocal images showing the spread and decay of mitochondria-targeted photoactivated GFP (mito-PAGFP) in brown adipocytes 60 min after NE stimulation and photoactivation. Active mitochondrial were stained with tetramethylrhodamine ethyl ester perchlorate (TMRE) (red). Quantitation of changes of GFP signal intensity over time shown in (J). (n = 13, 15, and 10 cells for *Sel1L*$^{f/f}$, *Sel1L*$^{-/-}$, and *Sel1L*$^{-/-}$;*SigmaR1*$^{-/-}$, one-way ANOVA). All experiments were repeated two to three times. Data are mean ± SEM. **p < 0.01; ***p < 0.001.

a possible impact of ER stress signaling on mitochondria in vivo, we generated mice lacking Ire1α, a key sensor of the unfolded protein response (UPR), specifically in adipocytes ($Ire1a^{AdipCre}$). These knockout mice grew normally and were not cold sensitive (fig. S13, B to D). Mitochondria from $Ire1a^{AdipCre}$ exhibited normal morphology, with reduced size at 4°C (Fig. 5, F and G). Thus, the effect of Sel1L on mitochondria is mediated by ERAD, independent of ER stress or cell death.

Sel1L-Hrd1 ERAD regulates ER-mitochondria contacts and dynamics through SigmaR1

We next explored how mitochondrial dynamics were affected by ERAD dysfunction. Whereas total protein amounts of mitochondrial respiratory proteins and Ucp1 were largely comparable between the cohorts (fig. S14A), cold-induced phosphorylation of Drp1 at Ser^{616}, a key activating event in mitochondrial division (*11*, *40*), was reduced in $Sel1L^{AdipCre}$ BAT compared to $Sel1L^{f/f}$ BAT (Fig. 6A). Opa1 processing to its shorter form upon cold exposure did not occur in $Sel1L^{AdipCre}$ BAT (Fig. 6A). Protein amounts of outer mitochondrial membrane Drp1 receptors Fis1 and Mff were unchanged (fig. S14A). Similar observations were obtained in $Hrd1^{-/-}$ BAT (fig. S14B), but not in $Ire1a^{-/-}$ BAT (fig. S13E). Furthermore, in $Sel1L^{-/-}$ BAT, cold exposure increased oligomerization of key fusion factor Mfn2 into high molecular weight (HMW) complexes as revealed by blue-native gels and sucrose gradient fractionation (fig. S14, C and D). Indeed, the Mfn2 HMW complex promotes mitochondrial fusion (*41*–*43*). We then tested the protein abundances of several known MAM proteins, including Mfn2, Vapb, Bap31, and SigmaR1. Only SigmaR1 amounts were increased in *Sel1L*- and *Hrd1*-deficient BAT (Fig. 6B and fig. S15, A and B), but not in $Ire1a^{-/-}$ BAT (fig. S13E). However, *SigmaR1* mRNA abundance was comparable in $Sel1L^{-/-}$ versus *WT* BAT in response to cold (fig. S15C), pointing to a posttranscriptional regulation of SigmaR1 protein.

SigmaR1 is a single-span ER-resident protein residing at the MAMs, where it may regulate ER-mitochondria contacts and mitochondrial dynamics (*44*, *45*), although a detailed mechanism remains vague. SigmaR1 protein was degraded by the proteasome with a half-life of ~6 hours (Fig. 6C), interacted with the E3 ligase Hrd1 (fig. S15, D and E), and was ubiquitinated in a largely Hrd1-dependent manner (Fig. 6D). In the absence of Sel1L or Hrd1, SigmaR1 protein was stabilized (Fig. 6C) and accumulated in the ER (fig. S15F). SigmaR1 interacted with Mfn2 as well as other MAM proteins Bap31 and Vapb, but not Ip3r (Fig. 6E and fig. S15G), and was localized at very close proximity to mitochondria in $Sel1L^{-/-}$ cells (fig. S15H). Genetic deletion of *SigmaR1* reduced cold-induced Mfn2 HMW complexes in $Sel1L^{-/-}$ brown adipocytes (Fig. 6F and fig. S16A). Deletion of *SigmaR1* reversed mitochondrial elongation (fig. S16, B and C) and reduced ER-mitochondrial contacts in $Sel1L^{-/-}$ cells (Fig. 6, G and H). In a mitochondrial fusion assay (*33*) using mitochondria-targeted photoactivated green fluorescent protein (mito-PAGFP), deletion of *SigmaR1* attenuated the spread and decay of GFP intensity seen in $Sel1L^{-/-}$ brown adipocytes upon NE treatment (Fig. 6, I and J). Thus, SigmaR1 mediates mitochondrial hyperfusion in *Sel1L*-deficient cells, thereby linking ERAD to ER-mitochondrial contacts and mitochondrial dynamics in brown adipocytes.

Discussion

Here, we found a critical role for Sel1L-Hrd1 ERAD in regulating ER-mitochondria contacts and mitochondrial function. We observed profound changes in mitochondrial morphology, beyond mere elongation or swelling that is commonly associated with mitochondrial dysfunction or ER stress. Using 3D imaging techniques, we reconstructed these pleomorphic mitochondria and their associated MAMs. We speculate that the ER tubules embedded within profiles of pleomorphic megamitochondria represent halted fission and/or accelerated fusion intermediates. Our mechanistic studies identified MAM protein SigmaR1 as an ERAD substrate, which, when deleted, reduced ER-mitochondria contacts and rescued abnormal mitochondrial dynamics and morphology in $Sel1L^{-/-}$ cells. SigmaR1 may regulate mitochondrial dynamics by interacting with Mfn2 as well as other MAM proteins and promoting Mfn2 oligomerization in an unknown manner.

MAMs are disturbed in many diseases such as obesity (*46*), cardiac disease (*47*), and neurodegeneration (*48*); however, to date, the nature of this disruption in disease pathogenesis remains vague. Our data suggest that Sel1L-Hrd1 ERAD may regulate the dynamics of ER-mitochondria interactions through modulation of MAMs. Indeed, an inverse correlation between Sel1L and SigmaR1 expression levels has been reported in patients with neurodegeneration (*49*–*51*). Considering the recent identification of Sel1L mutants in progressive early-onset cerebellar ataxia in canines (*52*) and various cancers (*53*, *54*), this study may have implications not only for interorganelle communication but also for the pathophysiological role of Sel1L-Hrd1 ERAD.

REFERENCES AND NOTES

1. H. Wu, P. Carvalho, G. K. Voeltz, *Science* **361**, eaan5835(2018).
2. A. A. Rowland, G. K. Voeltz, *Nat. Rev. Mol. Cell Biol.* **13**, 607–625 (2012).
3. B. Kornmann *et al.*, *Science* **325**, 477–481 (2009).
4. G. Csordás *et al.*, *J. Cell Biol.* **174**, 915–921 (2006).
5. J. R. Friedman *et al.*, *Science* **334**, 358–362 (2011).
6. A. Murley *et al.*, *eLife* **2**, e00422 (2013).
7. S. C. Lewis, L. F. Uchiyama, J. Nunnari, *Science* **353**, aaf5549 (2016).
8. R. Salvador-Gallego, M. J. Hoyer, G. K. Voeltz, *Cell* **171**, 1224–1224.e1 (2017).
9. K. S. Lee *et al.*, *Proc. Natl. Acad. Sci. U.S.A.* **115**, E8844–E8853 (2018).
10. W. K. Ji *et al.*, *J. Cell Biol.* **216**, 4123–4139 (2017).
11. E. Smirnova, L. Griparic, D. L. Shurland, A. M. van der Bliek, *Mol. Biol. Cell* **12**, 2245–2256 (2001).
12. A. M. Labrousse, M. D. Zappaterra, D. A. Rube, A. M. van der Bliek, *Mol. Cell* **4**, 815–826 (1999).
13. W. Bleazard *et al.*, *Nat. Cell Biol.* **1**, 298–304 (1999).
14. J. Hwang, L. Qi, *Trends Biochem. Sci.* **43**, 593–605 (2018).
15. L. Qi, B. Tsai, P. Arvan, *Trends Cell Biol.* **27**, 430–440 (2017).
16. P. Carvalho, V. Goder, T. A. Rapoport, *Cell* **126**, 361–373 (2006).
17. R. G. Gardner *et al.*, *J. Cell Biol.* **151**, 69–82 (2000).
18. R. Y. Hampton, R. G. Gardner, J. Rine, *Mol. Biol. Cell* **7**, 2029–2044 (1996).
19. A. Bhattacharya, L. Qi, *J. Cell Sci.* **132**, jcs232850 (2019).
20. N. Vashistha, S. E. Neal, A. Singh, S. M. Carroll, R. Y. Hampton, *Proc. Natl. Acad. Sci. U.S.A.* **113**, 5934–5939 (2016).
21. X. Wu, T. A. Rapoport, *Curr. Opin. Cell Biol.* **53**, 22–28 (2018).
22. S. Schoebel *et al.*, *Nature* **548**, 352–355 (2017).
23. G. H. Kim *et al.*, *J. Clin. Invest.* **128**, 1125–1140 (2018).
24. G. Shi *et al.*, *J. Clin. Invest.* **127**, 3897–3912 (2017).
25. H. Sha *et al.*, *Cell Metab.* **20**, 458–470 (2014).
26. S. Sun *et al.*, *Proc. Natl. Acad. Sci. U.S.A.* **111**, E582–E591 (2014).
27. A. Bhattacharya *et al.*, *EMBO J.* **37**, e99277 (2018).
28. Y. Ji *et al.*, *Cell Rep.* **16**, 2630–2640 (2016).
29. Y. Yang *et al.*, *J. Biol. Chem.* **293**, 12934–12944 (2018).
30. J. Wei *et al.*, *EMBO J.* **37**, e98942 (2018).
31. S. Sun *et al.*, *Mol. Biol. Cell* **27**, 483–490 (2016).
32. A. M. Cypess, C. R. Kahn, *Curr. Opin. Endocrinol. Diabetes Obes.* **17**, 143–149 (2010).
33. J. D. Wikstrom *et al.*, *EMBO J.* **33**, 418–436 (2014).
34. W. Denk, H. Horstmann, *PLOS Biol.* **2**, e329 (2004).
35. G. Knott, H. Marchman, D. Wall, B. Lich, *J. Neurosci.* **28**, 2959–2964 (2008).
36. J. Schulz *et al.*, *J. Cell Sci.* **130**, 3322–3335 (2017).
37. J. C. Christianson *et al.*, *Nat. Cell Biol.* **14**, 93–105 (2011).
38. E. Balsa *et al.*, *Mol. Cell* **74**, 877–890.e6 (2019).
39. J. Lebeau *et al.*, *Cell Rep.* **22**, 2827–2836 (2018).
40. E. Smirnova, D. L. Shurland, S. N. Ryazantsev, A. M. van der Bliek, *J. Cell Biol.* **143**, 351–358 (1998).
41. J. Steffen *et al.*, *Mol. Biol. Cell* **28**, 600–612 (2017).
42. G. L. McLelland *et al.*, *eLife* **7**, e32866 (2018).
43. A. Sugiura *et al.*, *Mol. Cell* **51**, 20–34 (2013).
44. E. Gregianin *et al.*, *Hum. Mol. Genet.* **25**, 3741–3753 (2016).
45. N. Bernard-Marissal, J. J. Médard, H. Azzedine, R. Chrast, *Brain* **138**, 875–890 (2015).
46. A. P. Arruda *et al.*, *Nat. Med.* **20**, 1427–1435 (2014).
47. H. Zhou, S. Wang, S. Hu, Y. Chen, J. Ren, *Front. Physiol.* **9**, 755 (2018).
48. S. Paillusson *et al.*, *Trends Neurosci.* **39**, 146–157 (2016).
49. L. Montibeller, J. de Belleroche, *Cell Stress Chaperones* **23**, 897–912 (2018).
50. J. Prause *et al.*, *Hum. Mol. Genet.* **22**, 1581–1600 (2013).
51. T. Mori, T. Hayashi, T. P. Su, *J. Pharmacol. Exp. Ther.* **341**, 663–671 (2012).
52. K. Kyöstilä *et al.*, *PLOS Genet.* **8**, e1002759 (2012).
53. H. Kim, A. Bhattacharya, L. Qi, *Semin. Cancer Biol.* **33**, 25–33 (2015).
54. M. Mellai *et al.*, *Oncotarget* **6**, 12452–12467 (2015).

ACKNOWLEDGMENTS

We thank D. Fang, L. M. Hendershot, D. Lombard, J. Lin, S. Soleimanpour, T.-P. Su, and R. Wojcikiewicz for providing reagents; F. Mao for data analysis; P. Arvan, L. Rui, Y. Shi, S. Sun, and O. MacDougald for constructive comments on the manuscript; and other members in the Arvan and Qi laboratories for technical assistance and insightful discussions. **Funding:** This work is supported by 1R01GM123266 and R01GM130695 (H.Se.); HL144657 (D.A.B.); 1R01DK107583 (J.W.); R01DK110439 and P20GM121176 (M.L.); R01NS086819 and R01NS091242 (T.H.S.); UL1TR000433, F32CA228328, and P30DK034933 (C.J.H.); and 1R01GM113188, 1R01DK105393, 1R01DK120047, and 1R35GM130292 (L.Q.). Metabolomics studies performed at the University of Michigan were supported by NIH grant DK097153. Z.Z. is supported by ADA Postdoctoral Fellowship (1-19-PDF-093). M.T. was supported in part by the Pew Latin American Postdoctoral

Fellowship. R.B.R. is supported by the Training Program in Endocrinology and Metabolism (5T32DK007245). C.A.L. was supported by a 2017 AACR NextGen Grant for Transformative Cancer Research (17-20-01-LYSS) and an ACS Research Scholar Grant (RSG-18-186-01). **Author contributions:** Z.Z. and M.T. designed and performed most of the experiments; H.Sh., S.K., C.J.H., F.V.d.B., C.A.L., T.Y., S.W., Y.L., C.W., M.L., H.Se., and A.H.H. performed the experiments; A.T., J.W., T.H.S., and D.A.B. provided reagents and insightful discussion; R.B.R. edited the manuscript and provided insightful discussion; L.Q. directed the study and wrote the manuscript; Z.Z. and M.T. wrote the methods and figure legends; all authors commented on and approved the manuscript. **Competing interests:** The authors declare no conflicts of interest. **Data and materials availability:** The microarray data have been deposited in Gene Expression Omnibus with accession number GSE145895.

SUPPLEMENTARY MATERIALS

science.sciencemag.org/content/368/6486/54/suppl/DC1
Materials and Methods
Figs. S1 to S16
References (*55*–*64*)
Movies S1 to S4

5 June 2019; resubmitted 19 January 2020
Accepted 4 March 2020
Published online 19 March 2020
10.1126/science.aay2494

NANOMATERIALS

Critical differences in 3D atomic structure of individual ligand-protected nanocrystals in solution

Byung Hyo Kim[1,2]*, Junyoung Heo[1,2]*, Sungin Kim[1,2], Cyril F. Reboul[3,4], Hoje Chun[5], Dohun Kang[1,2], Hyeonhu Bae[6], Hyejeong Hyun[7], Jongwoo Lim[7], Hoonkyung Lee[6], Byungchan Han[5], Taeghwan Hyeon[1,2], A. Paul Alivisatos[8,9,10], Peter Ercius[11]†, Hans Elmlund[3,4]†, Jungwon Park[1,2]†

Precise three-dimensional (3D) atomic structure determination of individual nanocrystals is a prerequisite for understanding and predicting their physical properties. Nanocrystals from the same synthesis batch display what are often presumed to be small but possibly important differences in size, lattice distortions, and defects, which can only be understood by structural characterization with high spatial 3D resolution. We solved the structures of individual colloidal platinum nanocrystals by developing atomic-resolution 3D liquid-cell electron microscopy to reveal critical intrinsic heterogeneity of ligand-protected platinum nanocrystals in solution, including structural degeneracies, lattice parameter deviations, internal defects, and strain. These differences in structure lead to substantial contributions to free energies, consequential enough that they must be considered in any discussion of fundamental nanocrystal properties or applications.

The three-dimensional (3D) atomic arrangement of materials determines their physical and catalytic properties (*1*, *2*). The 3D structures of nanocrystals typically deviate from the periodic atomic arrangement of their bulk counterparts owing to the dominance of surface dangling bonds, defects, and dislocations, as well as intrinsic quantum effects due to finite size (*3*–*5*). Such deviations are more pronounced in small nanocrystals that have diameters less than 4 nm. For example, interatomic distances near the surface of Au nanocrystals are shortened compared with the perfect face-centered cubic (fcc) structure of bulk Au (*6*), whereas cerium oxide nanocrystals show extended interatomic distances near the surface (*7*). Au nanoparticles below a critical size can have an icosahedral structure that is thermodynamically unfavored in the bulk counterpart (*8*). These distinctive physical properties make nanocrystals attractive as heterogeneous catalysts (*9*). Populations of synthesized nanocrystals tend to have heterogeneous atomic structures because uniform control at the level of individual nanocrystals is extremely difficult to accomplish (*10*, *11*). The organic ligands and solvents used in a typical colloidal synthesis coordinate surface atoms and further affect the crystal and electronic structures of nanocrystals (*12*–*16*). Thus, understanding their distinctive properties requires precise and reproducible determination of the positions of the individual atoms at the level of a single nanocrystal directly from the solution phase, in which most of the catalytic and chemical reactions occur.

The 3D atomic structures of nanocrystals can be determined by electron tomography, whereby the structures are reconstructed from a tilt series of transmission electron microscopy (TEM) images (*17*–*20*). However, this method relies on image acquisition under vacuum and on a substrate, which can cause structural deformation of the nanocrystals. Furthermore, the spatial resolution is frequently nonuniform in 3D space owing to missing projection directions (*21*). Single-particle reconstruction based on cryo-TEM, as an alternative approach, is also not appropriate for studying heterogeneous nanocrystal populations because the analysis relies on 2D images collected from a large number of different particles assumed to have the same structure (*22*). We previously introduced 3D SINGLE (structure identification of nanoparticles by graphene liquid cell electron microscopy) as a direct method to resolve 3D structures of nanocrystals in solution, but the resolution obtained was only sufficient to determine overall morphologies in 3D (*23*) and the understanding of how to analyze such information to extract key structure factors was still limited.

We developed a "Brownian one-particle reconstruction" method—atomic-resolution 3D SINGLE—and applied it to analyze the 3D atomic arrangements of individual Pt nanocrystals in solution. Our high-resolution 3D density maps of eight individual Pt nanocrystals from the same synthesis batch and fitted atomic models show fcc structures with structural heterogeneity, including single-crystallinity, distortion, and dislocation. The precise assignment (±19 pm) of the 3D atomic positions allowed direct investigation of lattice expansion, internal defects, strain near the surfaces and dislocation planes, and their contribution to the free energy. The resulting information shows that structural information obtained in a realistic solution based on the SINGLE method can provide a vital new guide for future improved synthesis and for understanding the properties of the current materials.

3D reconstruction from electron microscopy images of Pt nanocrystals in liquid

Atomic-resolution 3D SINGLE of nanocrystals in solution was achieved through aberration-corrected TEM imaging, by using a direct electron detector with high temporal (2.5 ms) resolution (fig. S1). The high temporal resolution allowed us to capture projection images of the nanocrystals in different views as they were tumbling in solution. The individual particles were tracked throughout the time series, and the extracted trajectories of 2D images were reconstructed to obtain Coulomb charge 3D density maps of the individual particles (see

[1]Center for Nanoparticle Research, Institute for Basic Science (IBS), Seoul 08826, Republic of Korea. [2]School of Chemical and Biological Engineering, and Institute of Chemical Processes, Seoul National University, Seoul 08826, Republic of Korea. [3]Department of Biochemistry and Molecular Biology, Biomedicine Discovery Institute, Monash University, Clayton, VIC 3800, Australia. [4]ARC Centre of Excellence for Advanced Molecular Imaging, Clayton, VIC 3800, Australia. [5]Department of Chemical and Biomolecular Engineering, Yonsei University, Seoul 03722, Republic of Korea. [6]Department of Physics, Konkuk University, Seoul 05029, Republic of Korea. [7]Department of Chemistry, Seoul National University, Seoul 08826, Republic of Korea. [8]Department of Chemistry, University of California, Berkeley, CA 94720, USA. [9]Material Sciences Division, Lawrence Berkeley National Laboratory, Berkeley, CA 94720, USA. [10]Kavli Energy NanoScience Institute, Berkeley, CA 94720, USA. [11]National Center for Electron Microscopy, Molecular Foundry, Lawrence Berkeley National Laboratory, Berkeley, CA 94720, USA.
*These authors contributed equally to this work.
†Corresponding author. Email: percius@lbl.gov (P.E.); hans.elmlund@monosh.edu (H.E.); jungwonpark@snu.ac.kr (J.P.)

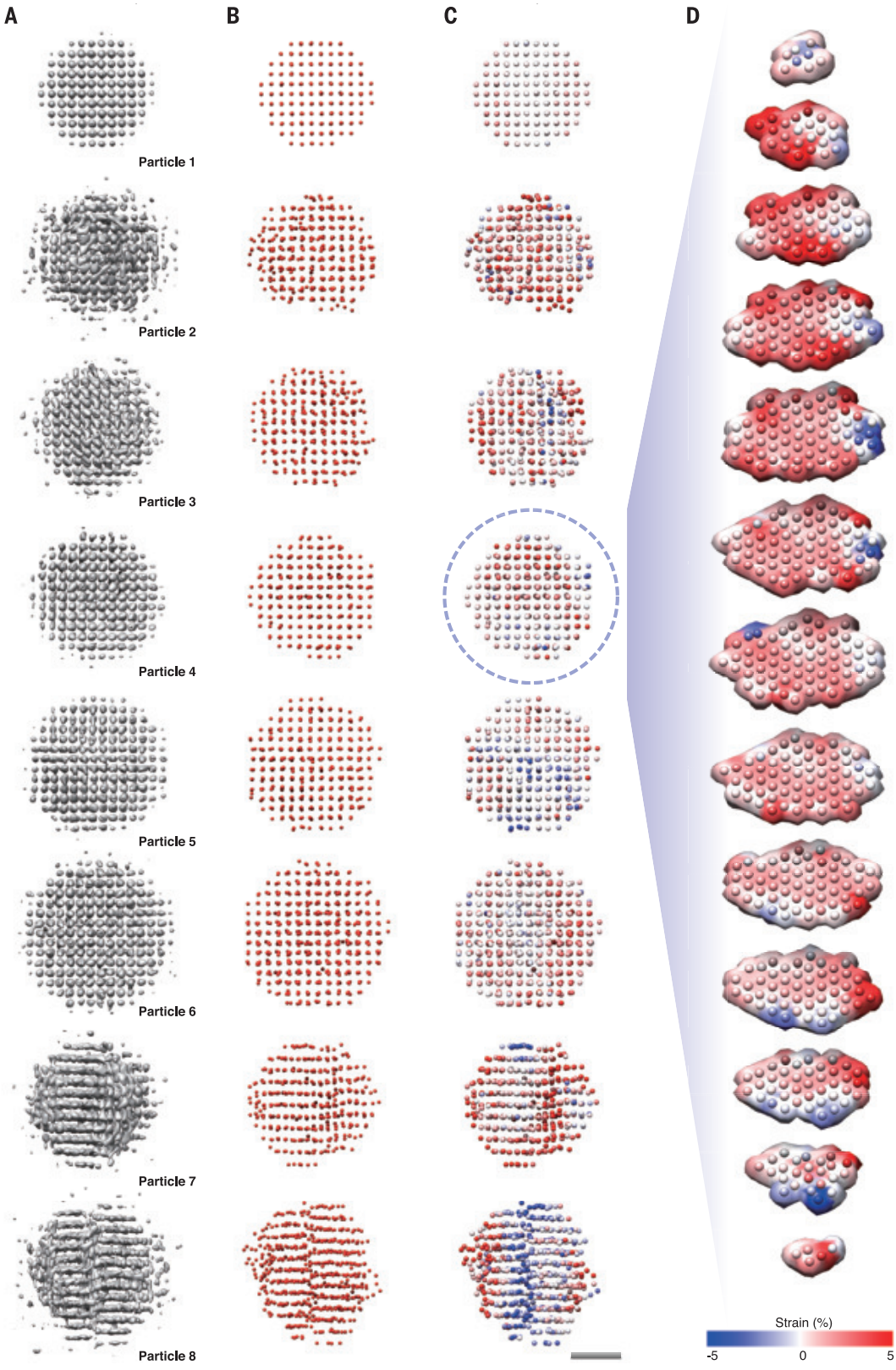

Fig. 1. Atomic-resolution 3D SINGLE for Pt nanocrystals in solution phase. (**A** to **C**) Isosurfaces of high-resolution 3D density maps (A), atomic position maps (B), and strain (ε_{xx}) maps (C) of eight individual nanocrystals (particles 1 to 8). (**D**) Sliced images of the strain (ε_{xx}) map of particle 4. Strain is indicated by the color scale. Scale bar, 1 nm.

supplementary materials and movie S1). Obtaining thousands of high-resolution images within a few seconds allowed complete coverage of the projection angles, which is required for accurate 3D reconstruction. The 3D orientations of the projections of the randomly rotating nanocrystals were determined using an iterative Fourier 3D reconstruction algorithm based on stochastic hill climbing (*24*). To overcome uncertainties originating from the random movement and innate noise in the TEM images, we developed algorithms for motion correction and subtraction of the background introduced by the liquid cell (see supplementary materials). These are key steps in the

advanced 3D reconstruction algorithm to obtain high-resolution 3D density maps.

Representative Pt nanocrystal density maps are depicted in Fig. 1A and movie S2. The reconstructed 3D density maps of the nanocrystals have resolutions better than 0.72 Å, according to the 0.143 Fourier shell correlation criterion (fig. S2) (*25*), allowing assignment of the positions of all constituent atoms in 3D space within the domain of each nanocrystal (Fig. 1B and figs. S3 to S5). The assigned atomic coordinates can further be used to calculate the formation energy of individual nanocrystals (table S1). We obtained strain maps from the atomic position information,

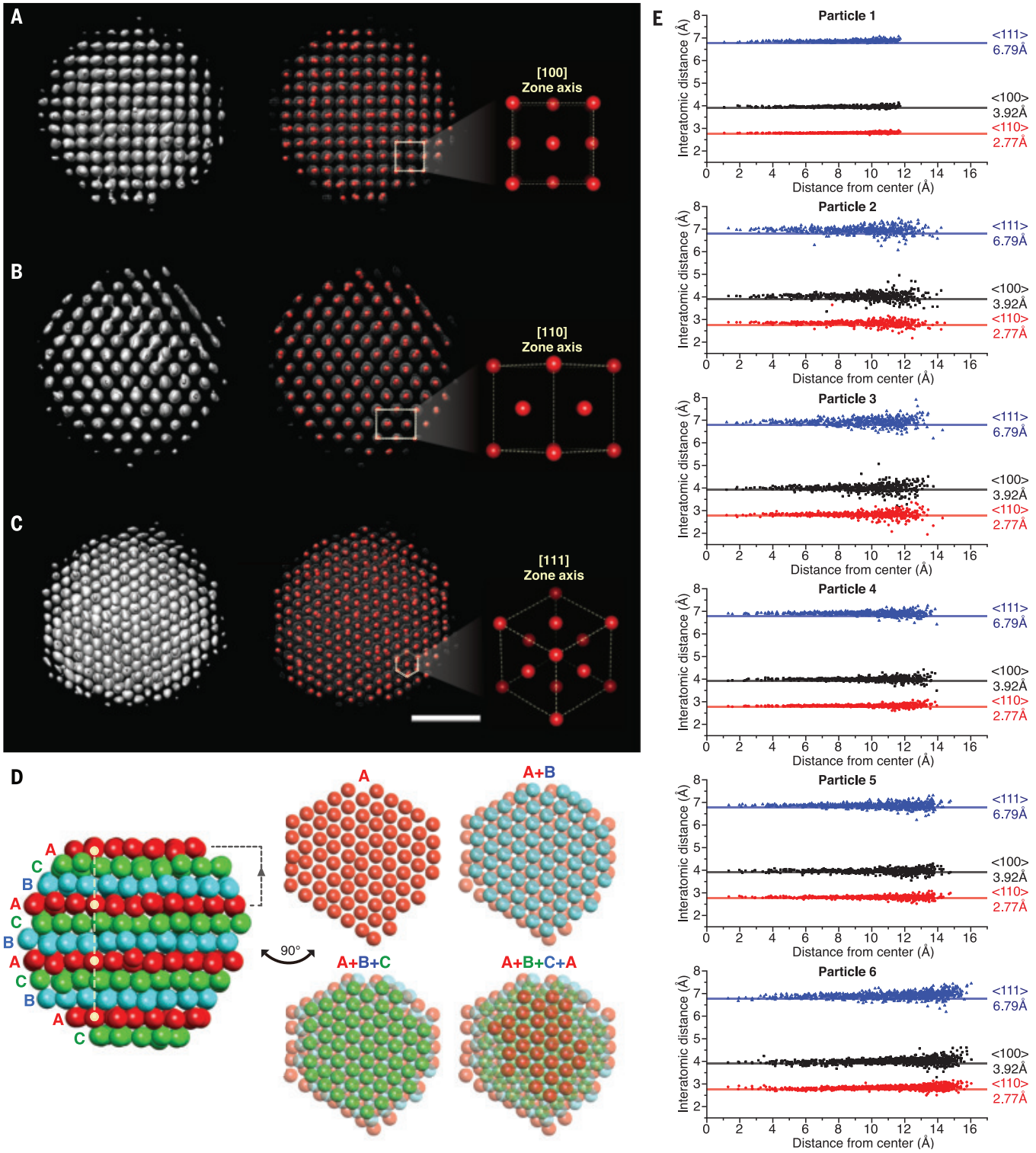

Fig. 2. Atomic-structure analysis of single-crystalline Pt nanocrystals reveals progressive disorder close to the surface. (**A** to **C**) 3D density maps and atomic positions of particle 4 along the [100] (A), [110] (B), and [111] (C) zone axes. Scale bar, 1 nm. (**D**) Packing structure of the nanocrystal. A, B, and C represent repeating lattice planes in fcc crystal structure along the [111] zone axis. (**E**) Interatomic distances in the directions of <110> (red), <100> (black), and <111> (blue) for nanocrystals with six different sizes (particles 1 to 6).

which indicate the lattice distortion (Fig. 1C and fig. S6). Sliced 3D maps provide detailed structural information and strain tensors (an example for one Pt nanocrystal is shown in Fig. 1D).

The reconstruction method and resulting 3D maps were validated in several ways (see supplementary materials). First, the algorithm was verified by reconstructing multislice simulated TEM images of model fcc nanocrystals with 2.5- and 4.0-nm diameters with varying parameters, including different pixel resolutions and binning processes, to mimic the imaging mechanism in TEM (figs. S7 to S9) (*26*). To confirm the robustness of the reconstruction method in the presence of the substantial random noise that originates from TEM imaging of liquid, multislice simulated TEM images, including model nanocrystals and water molecules that continuously change orientation and geometry, were generated by using molecular dynamics simulation and used for successful verification of 3D reconstruction (see supplementary materials and figs. S10 and S11). Second, to validate the experimental 3D structures, we confirmed that reprojected images of the obtained 3D electron density maps were in good agreement with the original projections (figs. S12 and S13). Third, we repeated the reconstruction process by using simulated images obtained by multislice simulation of the atomic position map and measured the similarity between the 3D atomic structures from the original TEM images and the simulated images (fig. S14). The average root mean square difference is 9.9 to 19 pm (fig. S14). In addition, the projection directions of the rotating nanocrystals show wide coverage (fig. S15), indicating that the 3D maps include ample crystallographic information obtained from numerous zone axes. Experiments on simulated data show that vertical movement of the

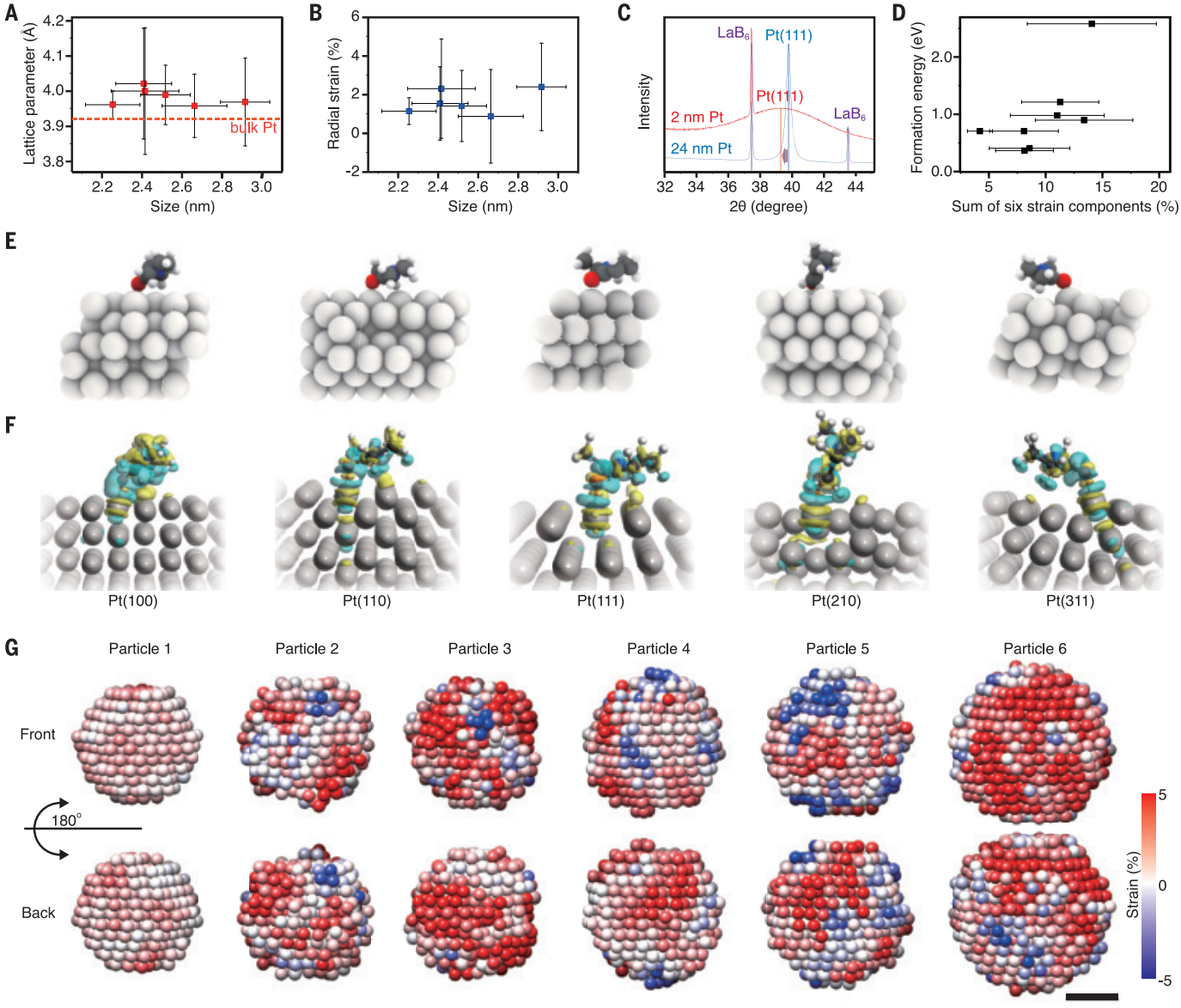

Fig. 3. Size-dependent properties of Pt nanocrystals inferred from their 3D atomic maps. (**A** and **B**) Fitted lattice parameters (A) and averaged radial strain values (B) of single-crystalline nanocrystals with six different sizes. Error bars of *x* axes represent standard deviations of sizes measured in different orientations of individual nanocrystals. Error bars of *y* axes represent standard deviations of averaged interatomic distances along the <100> directions (A) and radial strains (B) of individual atoms. (**C**) XRD patterns of 2-nm-diameter PVP-protected Pt nanocrystals and 24-nm-sized Pt nanocrystals as a reference. (**D**) Formation energy of the reconstructed Pt nanocrystals calculated using their atomic coordinates in a vacuum environment. Error bar represents standard deviation of the sum of six strain components. (**E** and **F**) Binding mode of a PVP ligand onto Pt surfaces with five different planes (E) and its charge density distributions (F). Blue color indicates the electron-deficient region. (**G**) Radial strain maps of the six single-crystalline particles. Strain is indicated by the color scale. Scale bar, 1 nm.

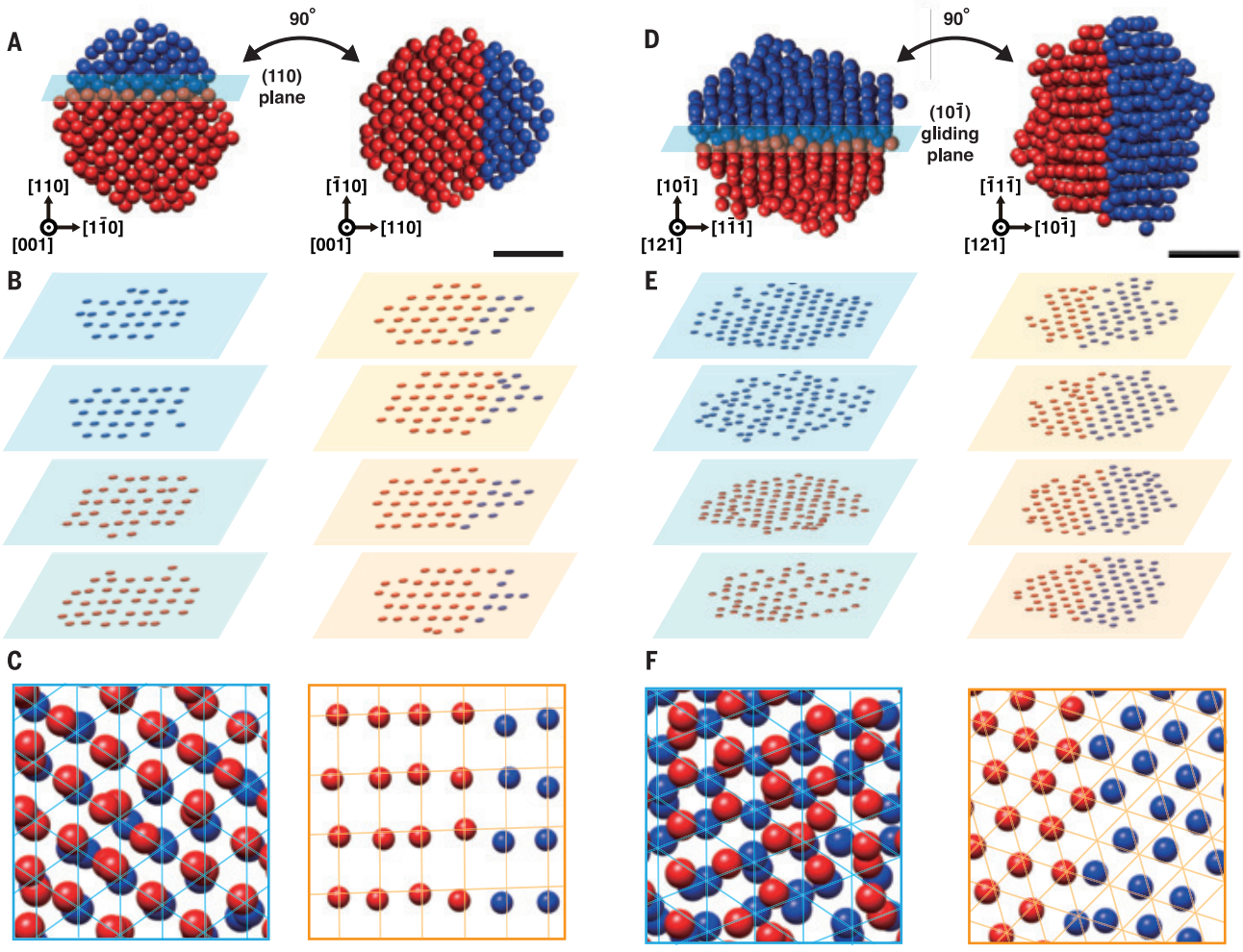

Fig. 4. 3D structure analysis of nanocrystals that have complicated structures. (**A** to **C**) 3D structure analysis of a distorted nanocrystal (particle 7). The overall atomic position map shown along the [001] zone axis appears in (A). Red and blue spheres represent atoms of each domain. Sliced planes of (110) (left) and ($\bar{1}$10) (right) are shown in (B). Superimposed atomic positions of two layers of each domain are shown in (C). (**D** to **F**) 3D structure analysis of a nanocrystal with a dislocation (particle 8). Overall atomic position map shown along the [121] zone axis appears in (D). Sliced planes of (10$\bar{1}$) (left) and ($\bar{1}$1$\bar{1}$) (right) planes are shown in (E). Superimposed atomic positions of two layers of each domain are shown in (F). Scale bars, 1 nm.

nanocrystals has a negligible effect on the final atomic structure (fig. S16).

Effects of surface ligands on the 3D atomic structures of Pt nanocrystals

The Pt nanocrystals were prepared by a typical optimized synthesis to make the final population homogeneous in terms of size and shape distribution, but it is widely known that the individual crystal structures do not have identical atomic arrangements owing to the complexity of their growth trajectories (*27*). Our reconstructed 3D density maps (Fig. 1A and fig. S3A) and corresponding atomic coordinate maps (Fig. 1B and fig. S3B) show this expected structural heterogeneity. Many of the nanocrystals from the same synthesis batch are single crystalline with fcc atomic arrangements, with the exception of heterogeneity due to slight variations in diameter of 2.25, 2.41, 2.42, 2.52, 2.66, and 2.92 nm for particles 1 to 6, respectively, as shown in Fig. 1. Some of the nanocrystals incorporate more diversity in their structures. Shear distortions (particle 7 in Fig. 1) and dislocations (particle 8 in Fig. 1) are frequently observed in the reconstructed 3D density and atomic position maps.

Our 3D density and atomic position maps match the expected fcc atomic structure. Projections along the [100] zone axis of the 2.52-nm-diameter nanocrystal (particle 4) show that the atoms are positioned with fourfold symmetry at a lattice spacing of 2.0 Å, which corresponds to the Pt (200) plane distance (Fig. 2A). A 45° rotation around [001] (Fig. 2A) reveals a typical lattice projection along the [110] axis with lattice spacing of 2.2-Å {111} and 2.0-Å {200} planes (Fig. 2B). In addition, in a view along the [111] zone axis, the 3D structure exhibits the hexagonal close-packed arrays of atoms (Fig. 2C). The fcc structure can also be identified by an ABC packing sequence along the [111] direction, where every third layer is in the same position (Fig. 2D). Owing to this close-packed structure, the nanocrystals have a coordination number of 12, with the exception of surface atoms (fig. S17).

As nanocrystals become smaller, the fraction of surface atoms becomes substantial. Because they have dangling bonds with surface organic ligands, which is different from the perfect symmetric coordination in a bulk crystal, surface atoms contribute asymmetric atomic orbital overlaps with inner atoms (*28*). In addition, the electronic structure of small nanocrystals can be notably affected by atomic defects (*29*). To understand microscopic structural details of nanocrystals and the extent to which the bulk crystal motif is maintained at the nanoscale level, we measured all interatomic distances along the <111>, <100>, and <110> directions (see the supplementary materials) and plotted them according to

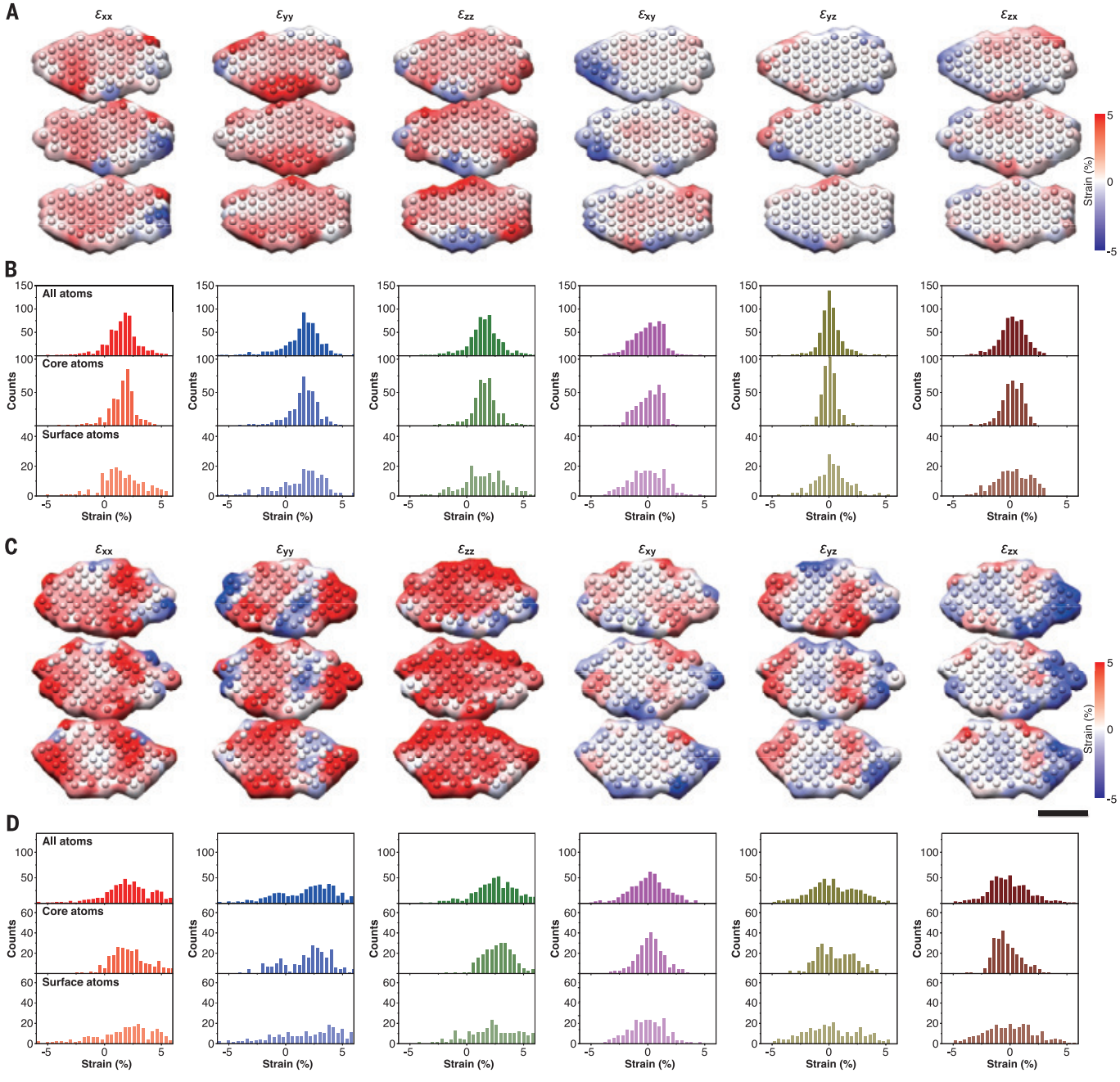

Fig. 5. 3D strain tensor analysis of Pt nanocrystals. (**A**) Sliced maps of the six components of the strain tensors for a single-crystalline particle (particle 4). (**B**) Histograms of the strain tensors of all atoms (top), core atoms (middle), and surface atoms (bottom) of particle 4. (**C**) Sliced maps of the six components of the strain tensors for a particle with a distorted lattice (particle 7). Scale bar, 1 nm. (**D**) Histograms of the strain tensors of all atoms (top), core atoms (middle), and surface atoms (bottom) of particle 7. In (A) and (C), strain is indicated by the color scale.

the distance from the center (Fig. 2E). Although the interatomic distances are almost constant near the core, they deviate gradually toward the surface, indicating a noticeable deviation of surface atoms from their periodic positions.

By fitting the atomic coordinates, we found an overall expansion of the fcc lattice structure. For example, the lattice parameters of particle 4 are a = 3.990 Å, b = 3.985 Å, c = 3.990 Å, α = 89.96°, β = 89.70°, and γ = 89.75°. Interestingly, such lattice expansion is consistently observed in other nanoparticles (*30*, *31*). The averaged fcc unit-cell lattice constants of the 2.25-, 2.41-, 2.42-, 2.52-, 2.66-, and 2.92-nm-diameter nanocrystals are 3.96, 4.02, 4.00, 3.99, 3.96, and 3.97 Å, respectively, which are 1.02, 2.56, 2.02, 1.74, 0.95, and 1.22% larger than the bulk values, respectively (Fig. 3A). The lattice expansion can be effectively described by the radial strain (ε_{rr}), which is defined as $\varepsilon_{rr} = \frac{\partial u_r}{\partial r}$, where r is the distance between an atom and the center of mass of a particle and u_r is radial displacement (fig. S18). Consistent with our observed deviations of lattice parameters, the arithmetic mean (averaged over all atom positions) radial strain is

positive for particles 1 through 6 (Fig. 3B). We revisited previous x-ray diffraction (XRD) studies of ligand-protected nanocrystals and found that such lattice expansion, which was unrecognized because the peak shift was very small, is observed consistently in polyvinylpyrrolidone (PVP)–protected metal nanocrystals (*30*, *31*). We also checked our PVP-protected Pt nanocrystals using synchrotron XRD experiments. XRD patterns exhibit a slightly enlarged lattice parameter (3.976 Å) compared with that of bulk Pt (Fig. 3C). These observations imply that crystal structures of Pt nanocrystals tend to expand slightly when protected by PVP surface ligands in the native solution phase. These results are in contrast to lattice compressions theoretically observed for metal nanocrystals without protecting ligands, which is explained by the effect of surface tension and strong bonding of surface atoms with low coordination numbers (*6*). Our results indicate that such effects can be weakened and even reversed when surface ligands are adsorbed on the metal nanocrystals in the solution phase. We performed density functional theory (DFT) calculations and show that the adsorption of PVP ligands can induce localization of electron density around surface Pt atoms. As a result, the inward metallic bonds are weakened as the atomic distance increases (Fig. 3, E and F). Because the PVP ligands are long polymers decorated with multiple binding functional groups, the coverage of polymeric binding may not be uniform across the surface. This is likely to induce local deviation of the atomic lattice and the resulting surface strain. Particular surface regions of a Pt nanocrystal, where binding of pyrrolidone groups are more dominant, are presumably expanded. Our radial strain measurements show such a localization on specific surface regions of the particle (see Fig. 3G).

The observed lattice fluctuations and the expansion of the fcc crystal structure are difficult to measure in conventional high-resolution TEM images of nanocrystals because the interatomic distances are averaged over each atomic column along the projection direction. Further, motion in the liquid makes it difficult to capture the correct zone axis with the high precision that is required. Our atomic-resolution 3D SINGLE method overcomes these limitations and allows measurement of the interatomic distances between all constituent atoms in 3D space, enabling detailed structural characterization. We confirmed that the lattice fluctuations are not due to inaccuracy of the reconstruction method. Accurate interatomic distances were measured in the 3D atomic position map generated from reconstructing simulated noisy TEM images of a model nanocrystal with a perfect fcc structure. The interatomic distances consistently follow bulk fcc parameters with a very marginal deviation throughout the volume of the nanocrystal (fig. S7C). Thus, the observed deviation of the lattice parameter is inherent to these small ligand-protected Pt nanocrystals.

By using the experimentally determined atomic positions, the formation energy of each nanocrystal can be directly evaluated using DFT calculation without relaxation processes. Overall, the higher-strained particles require a higher formation energy, as shown in Fig. 3D (see supplementary materials). Highly strained nanocrystals, such as distorted particles, show high formation energies attributed to the strain field (Fig. 3D). It is possible that the energetically metastable structures, including the dislocations, are kinetically trapped during complicated synthetic reactions that incorporate particle coalescence (*23*). The DFT calculation considered bare surfaces for reliable comparison between nanocrystals without uncertainty originating from the complexity of ligand passivation (table S1). By considering the stabilization effect of surface binding groups, the formation energy of nanocrystals with PVP ligands can be substantially reduced (fig. S19 and table S2).

Structural heterogeneity of Pt nanocrystals

Our 3D density and atomic position maps reveal that Pt nanocrystals have more complicated crystal structures than the single-crystalline fcc structure. The atomic arrangement of the distorted nanocrystal (particle 7) is slightly bent around a (110) plane (Fig. 4, A to C). Overlaying different atomic planes from each domain as red and blue reveals that the lattice points of the two domains are slightly mismatched (Fig. 4C). In addition, several vacancies are observed near the boundary (Fig. 4B).

Particle 8 has a $(1\bar{1}1)$ partial edge dislocation, as viewed along a [121] zone axis in Fig. 4D. This is a Shockley partial dislocation with the Burger's vector of $a/2$<111> and a gliding plane of $(10\bar{1})$. The atoms near the dislocation are highly disordered (Fig. 4E), whereas other atoms conform to an fcc lattice. A magnified image of a $(1\bar{1}1)$ plane (Fig. 4F), which is perpendicular to the gliding plane, shows a hexagonal array within each domain and breakage of periodicity near the boundary between the two domains. The origin of the disordered structure of the nanocrystal can be explained by coalescence events during the formation of the nanocrystals (*23*, *32*). Recent liquid-phase TEM studies have revealed that Pt nanocrystals frequently coalesce along low-index surfaces and become multidomain structures when they grow by an aggregative pathway (*23*, *27*, *33*, *34*).

Strain analysis of individual Pt nanocrystals from the 3D atomic maps

Strain imposed on the constituent atoms determines catalytic activities of metal nanocrystals because the strain modifies the local binding energy with adsorbates by changing the bandwidth of d orbitals (*35*). Engineering tensile strain is indeed successfully applied in tuning reactivity of Pt nanocrystals in many important catalytic reactions, including the methanol oxidation reaction and the oxygen reduction reaction (*36*, *37*). Strain analysis at high resolution will be an important asset in understanding catalytic performance of heterogeneous catalysts and tuning their performance. Using the fcc structure with a best-fit lattice parameter as a reference, we obtained 3D strain maps by calculating the atomic displacement field, convolving it with a 2-Å-wide 3D Gaussian kernel, and differentiating it (Fig. 5 and figs. S20 and S21) (*17*). We also used geometric phase analysis (*38*) for comparison. Both methods showed similar results (fig. S22). The full six-element strain tensor of particle 4 is mapped for each atomic position in 3D space (Fig. 5A). The strain maps clearly show that the surface of the nanocrystals has larger strain compared with the core atoms (Figs. 1D and 5B). The strain distributions of the surface atoms—defined as $r > R - d_{111}$, where r is the distance of an atom from the center of mass, R is the radius of the nanocrystal, and d_{111} is the bulk Pt(111) plane distance—are 1.89, 2.27, 1.92, 1.54, 1.49, and 1.52%, whereas those of core atoms are 1.14, 1.28, 1.15, 1.07, 0.66, and 0.93% for ε_{xx}, ε_{yy}, ε_{zz}, ε_{xy}, ε_{yz}, and ε_{zx}, respectively (Fig. 5B and fig. S23). The broader strain distribution of the surface atoms is due to the disorder of the surface atoms, presumed to be accommodated by surface ligand protection. Tensile strain occurs throughout the nanocrystal for both surface and core atoms. The average strains of ε_{xx}, ε_{yy}, and ε_{zz} (parallel to the <100> directions) for particle 4 are 1.54, 1.49, and 1.58%, respectively, consistent with the expanded lattice parameters obtained by fitting of the atomic coordinates.

The distorted Pt nanocrystal (particle 7) also shows tensile strain throughout the nanocrystal and large strain distribution on the surface. Owing to its structural deformation, the strain distribution of the distorted particle is 2.23%, which is 1.7 times broader than that of the single crystal (particle 4; 1.31%). In addition, the bent structure leads to high shear strain of atoms at the domain boundary (Fig. 5C), resulting in a bimodal shear strain distribution with two distribution centers (Fig. 5D). The nanocrystal with the dislocation also shows large strains at the domain boundary (particle 8 in Fig. 1C), which is known to enhance catalytic activities (*39*).

Conclusion

We show that high-resolution 3D atomic arrangements of Pt nanocrystals synthesized from a single batch have critical structural differences. This was made possible by the

development of atomic-resolution 3D SINGLE for solving the structure of nanocrystals in solution phase. Our results can be understood by the nature of typical colloidal synthesis of nanocrystals, which thermodynamically deviates from expectations based on bulk crystallography. Structure and strain analysis enabled by assignment of precise atomic positions reveals lattice expansions of ligand-protected metal nanocrystals in solution and the existence of large strain near domain boundaries, dislocation edges, and surfaces. The detailed structural information we introduce is strongly linked to the origin of the catalytic performance of Pt nanocrystals. We also demonstrate that the precise atomic structures obtained by our approach can be utilized in computational chemistry to improve the accuracy of property predictions of nanocrystals. Atomic-resolution 3D SINGLE can be applied to nanocrystals with various composition (fig. S24) and atomic structural integrity. It will find applications in other systems, including colloidal nanomaterials and biological macromolecules, where structural information in solution is required.

REFERENCES AND NOTES

1. M. A. Pfeifer, G. J. Williams, I. A. Vartanyants, R. Harder, I. K. Robinson, *Nature* **442**, 63–66 (2006).
2. M. Cargnello *et al*., *Science* **341**, 771–773 (2013).
3. L. Hultman *et al*., *Phys. Rev. Lett.* **87**, 225503 (2001).
4. M. Azubel *et al*., *Science* **345**, 909–912 (2014).
5. T. Nilsson Pingel, M. Jørgensen, A. B. Yankovich, H. Grönbeck, E. Olsson, *Nat. Commun.* **9**, 2722 (2018).
6. Z. Huang, P. Thomson, S. Di, *J. Phys. Chem. Solids* **68**, 530–535 (2007).
7. L. Chen, P. Fleming, V. Morris, J. D. Holmes, M. A. Morris, *J. Phys. Chem. C* **114**, 12909–12919 (2010).
8. Y. Negishi *et al*., *J. Am. Chem. Soc.* **137**, 1206–1212 (2015).
9. W. Zhu *et al*., *J. Am. Chem. Soc.* **136**, 16132–16135 (2014).
10. S. G. Kwon, T. Hyeon, *Small* **7**, 2685–2702 (2011).
11. W. Gao *et al*., *Sci. Adv.* **5**, eaau9590 (2019).
12. Z. Fan *et al*., *Nat. Commun.* **6**, 6571 (2015).
13. W. Wu, E. V. Shevchenko, *J. Nanopart. Res.* **20**, 255 (2018).
14. K. Yang *et al*., *J. Mater. Chem. A Mater. Energy Sustain.* **7**, 3863–3873 (2019).
15. F. Bertolotti *et al*., *Nat. Mater.* **15**, 987–994 (2016).
16. T. Altantzis *et al*., *Nano Lett.* **19**, 477–481 (2019).
17. R. Xu *et al*., *Nat. Mater.* **14**, 1099–1103 (2015).
18. Y. Yang *et al*., *Nature* **542**, 75–79 (2017).
19. B. Goris *et al*., *Nat. Mater.* **11**, 930–935 (2012).
20. J. Miao, P. Ercius, S. J. L. Billinge, *Science* **353**, aaf2157 (2016).
21. A. Bartesaghi *et al*., *J. Struct. Biol.* **162**, 436–450 (2008).
22. Y. Cheng, *Cell* **161**, 450–457 (2015).
23. J. Park *et al*., *Science* **349**, 290–295 (2015).
24. C. F. Reboul, M. Eager, D. Elmlund, H. Elmlund, *Protein Sci.* **27**, 51–61 (2018).
25. M. van Heel, M. Schatz, *J. Struct. Biol.* **151**, 250–262 (2005).
26. E. J. Kirkland, *Advanced Computing in Electron Microscopy* (Springer, 2010).
27. J. M. Yuk *et al*., *Science* **336**, 61–64 (2012).
28. S. Baumann *et al*., *Science* **350**, 417–420 (2015).
29. A. D. P. Leach *et al*., *J. Phys. Chem. C* **120**, 5207–5212 (2016).
30. T. Teranishi, M. Hosoe, T. Tanaka, M. Miyake, *J. Phys. Chem. B* **103**, 3818–3827 (1999).
31. C. Song *et al*., *Sci. Rep.* **6**, 31400 (2016).
32. J. C. Ondry, M. R. Hauwiller, A. P. Alivisatos, *ACS Nano* **12**, 3178–3189 (2018).
33. D. Li *et al*., *Science* **336**, 1014–1018 (2012).
34. B. Luo *et al*., *ACS Nano* **11**, 7626–7633 (2017).
35. M. Mavrikakis, B. Hammer, J. K. Nørskov, *Phys. Rev. Lett.* **81**, 2819–2822 (1998).
36. P. Strasser *et al*., *Nat. Chem.* **2**, 454–460 (2010).
37. X. Huang *et al*., *Science* **348**, 1230–1234 (2015).
38. M. J. Hÿtch, E. Snoeck, R. Kilaas, *Ultramicroscopy* **74**, 131–146 (1998).
39. R. G. Mariano, K. McKelvey, H. S. White, M. W. Kanan, *Science* **358**, 1187–1192 (2017).

ACKNOWLEDGMENTS

The experiments performed at the Molecular Foundry, Lawrence Berkeley National Laboratory, were supported by the U.S. Department of Energy (DOE) under contract no. DE-AC02-05CH11231. **Funding:** J.P. and T.H. acknowledge the Institutes for Basic Science (IBS-R006-D1). J.P. acknowledges National Research Foundation of Korea (NRF) grants funded by the Korean government (MSIT) (nos. NRF-2017R1C1B2010434, NRF-2017R1A5A1015365, and NRF-2019M3E6A1064877); the Ministry of Trade, Industry, and Energy (MOTIE); and the Korea Semiconductor Research Consortium (KRSC) support program for the development of future semiconductor devices (no. 10080657). B.H.K., J.H., S.K., and J.P. acknowledge support from the Samsung Science and Technology Foundation under project number SSTF-BA1802-08 for the development of the reconstruction algorithm. H.E. acknowledges Australian Research Council (ARC) grant DP170101850 and National Health and Medical Research Council, Australia, grant APP1125909. C.F.R. acknowledges an Early Career Fellowship (APP1122769). P.E. acknowledges the DOE, Office of Basic Energy Sciences, Materials Sciences and Engineering Division, under contract no. KC22ZH. A.P.A. acknowledges support from the DOE, Office of Science, Office of Basic Energy Sciences, Materials Sciences and Engineering Division, under contract no. DE-AC02-05-CH11231 within the Physical Chemistry of Inorganic Nanostructures Program (KC3103). H.C. and B.H. were supported by the Creative Materials Discovery Program through the NRF funded by the Ministry of Science and ICT (NRF-2017M3D1A1039287) and the Global Frontier Program through the Global Frontier Hybrid Interface Materials (GFHIM) of the NRF funded by the Ministry of Science and ICT (project no. 2013M3A6B1078882). **Author contributions:** B.H.K. and J.H. contributed equally to this work. B.H.K., J.H., P.E., H.E., and J.P. planned the research. B.H.K., P.E., and J.P. discussed and/or acquired the data. B.H.K., J.H., S.K., C.F.R., and H.E. conducted the image reconstruction. B.H.K., J.H., S.K., A.P.A., T.H., P.E., H.E., and J.P. analyzed and interpreted the results. H.C., D.K., H.B., H.L., and B.H. performed the DFT calculations and molecular dynamics simulations. B.H.K., H.H., and J.L. obtained the XRD pattern. B.H.K., J.H., P.E., H.E., and J.P. wrote the manuscript. P.E., H.E., and J.P. supervised the research. All authors contributed to the discussion of results. **Competing interests:** The authors declare no competing financial interests. **Data and materials availability:** All data are available in the main text or the supplementary materials.

SUPPLEMENTARY MATERIALS

science.sciencemag.org/content/368/6486/60/suppl/DC1
Materials and Methods
Figs. S1 to S24
Tables S1 and S2
References (*40*–*42*)
Movies S1 and S2

13 March 2019; accepted 20 February 2020
10.1126/science.aax3233

REPORTS

ASTEROIDS

An artificial impact on the asteroid (162173) Ryugu formed a crater in the gravity-dominated regime

M. Arakawa[1]*, T. Saiki[2], K. Wada[3], K. Ogawa[1,4], T. Kadono[5], K. Shirai[1,2], H. Sawada[2], K. Ishibashi[3], R. Honda[6], N. Sakatani[2], Y. Iijima[2]†, C. Okamoto[1]†, H. Yano[2], Y. Takagi[7], M. Hayakawa[2], P. Michel[8], M. Jutzi[9], Y. Shimaki[2], S. Kimura[10], Y. Mimasu[2], T. Toda[2], H. Imamura[2], S. Nakazawa[2], H. Hayakawa[2], S. Sugita[3,11], T. Morota[11], S. Kameda[12], E. Tatsumi[11,13], Y. Cho[11], K. Yoshioka[14], Y. Yokota[2,6], M. Matsuoka[2], M. Yamada[3], T. Kouyama[15], C. Honda[16], Y. Tsuda[2], S. Watanabe[2,17], M. Yoshikawa[2,18], S. Tanaka[2,18], F. Terui[2], S. Kikuchi[2], T. Yamaguchi[2]‡, N. Ogawa[2], G. Ono[19], K. Yoshikawa[19], T. Takahashi[2]§, Y. Takei[2,19], A. Fujii[2], H. Takeuchi[2,18], Y. Yamamoto[2,18], T. Okada[2,20], C. Hirose[19], S. Hosoda[2], O. Mori[2], T. Shimada[2], S. Soldini[21], R. Tsukizaki[2], T. Iwata[2,18], M. Ozaki[2,18], M. Abe[2,18], N. Namiki[22,23], K. Kitazato[16], S. Tachibana[11], H. Ikeda[19], N. Hirata[16], N. Hirata[1], R. Noguchi[2], A. Miura[2,18]

The Hayabusa2 spacecraft investigated the small asteroid Ryugu, which has a rubble-pile structure. We describe an impact experiment on Ryugu using Hayabusa2's Small Carry-on Impactor. The impact produced an artificial crater with a diameter >10 meters, which has a semicircular shape, an elevated rim, and a central pit. Images of the impact and resulting ejecta were recorded by the Deployable CAMera 3 for >8 minutes, showing the growth of an ejecta curtain (the outer edge of the ejecta) and deposition of ejecta onto the surface. The ejecta curtain was asymmetric and heterogeneous and it never fully detached from the surface. The crater formed in the gravity-dominated regime; in other words, crater growth was limited by gravity not surface strength. We discuss implications for Ryugu's surface age.

The Hayabusa2 spacecraft reached the near-Earth asteroid (162173) Ryugu in June 2018 and found that this small asteroid is covered with boulders with sizes (diameters) up to ~160 m (*1*, *2*). The surface is covered with a regolith layer composed of boulders and granules under microgravity conditions (gravitational acceleration ~1×10^{-4} m s^{-2}), and the surface is expected to have strength originating from cohesion forces between regolith grains, with the maximum theoretical strength of the surface layer predicted to be 1 kPa (*3*). Impact craters that are formed under those conditions should be limited in size by this surface strength, which reduces the expected crater diameter compared with a strengthless surface (*4*). Crater sizes produced by hypervelocity impacts on

small bodies can be predicted using a variety of crater scaling laws. The number and sizes of craters on asteroids (including Ryugu) can be used to date their surfaces, but different crater scaling laws give ages that differ by more than an order of magnitude (*1*).

Hayabusa2 was equipped with a Small Carry-on Impactor (SCI) designed to launch a 2-kg copper projectile at a velocity of 2 km s^{-1} to form an artificial impact crater (referred to hereafter as the SCI crater) on the surface of Ryugu. The SCI crater was intended to expose the asteroid subsurface for remote sensing and sample collection (*5*, *6*). The Deep Impact spacecraft previously performed an impact experiment on a small body and formed an artificial impact crater on the nucleus of the comet 9P/Tempel 1 (*7*–*9*). The SCI impact can be used to test crater scaling laws for the crater size and ejecta velocity distribution, which were constructed using laboratory experiments (*10*–*12*), and can be compared with numerical simulations of the impact cratering processes in a microgravity environment (*13*).

The SCI impact operation was carried out on 5 April 2019 (*14*). The impact and evolution of impact ejecta were simultaneously observed by Hayabusa2's Deployable CAMera 3 (DCAM3) (*14*). About 3 weeks after the SCI impact, Hayabusa2 searched for evidence of the impact crater using its Optical Navigation Camera-Telescopic (ONC-T) from an altitude of 1.7 km with a resolution of ~18 cm per pixel. The fresh crater was identified at latitude 7.9°N and longitude 301.3°E (Fig. 1, A and B), ~20 m from the aiming point (which was latitude 6.00°N, longitude 303.00°E). This location is in a northern part of Ryugu's equatorial ridge (*2*). The impact angle was estimated to be ~60° from the local horizontal surface (*14*).

A comparison of ONC-T images taken from the same altitude before and after the impact (Fig. 1, A and B, and movie S1) shows the formation of an artificial impact crater. A dozen boulders with sizes of at least tens of centimeters were driven away from the surface, and a large block with a size of 5 m [which we refer to as the mobile block (MB)] was excavated and moved ~3 m northwest and >1 m above the initial surface by the impact. Before the impact, MB was adjacent to another large block, stable block (SB) (Fig. 1A), but SB was hardly moved by the SCI impact. SB might be part of a larger block buried below the crater floor. We speculate that SB and its subsurface extension halted the crater growth toward the southeast. Alternatively, SCI may have impacted closer to MB than SB, allowing the higher pressure to move MB but not SB.

To investigate the crater morphology profile, we generated a digital elevation map (DEM) (Fig. 2A) from the ONC-T images (*14*). This shows an elevated rim with a height of ~40 cm surrounding the SCI crater (Fig. 2B). The elevated rim could be composed of ejecta deposits and/or structural uplifts. We used the DEM to produce an ortho-corrected (geometrically accurate) image on which we traced the top of the rim to determine the crater shape (Fig. 1C). The SCI crater is semicircular with a rim-to-rim diameter D_{rim} of 17.6 ± 0.7 m. This shape is not due to the oblique impact but rather is the effect of a large block (possibly

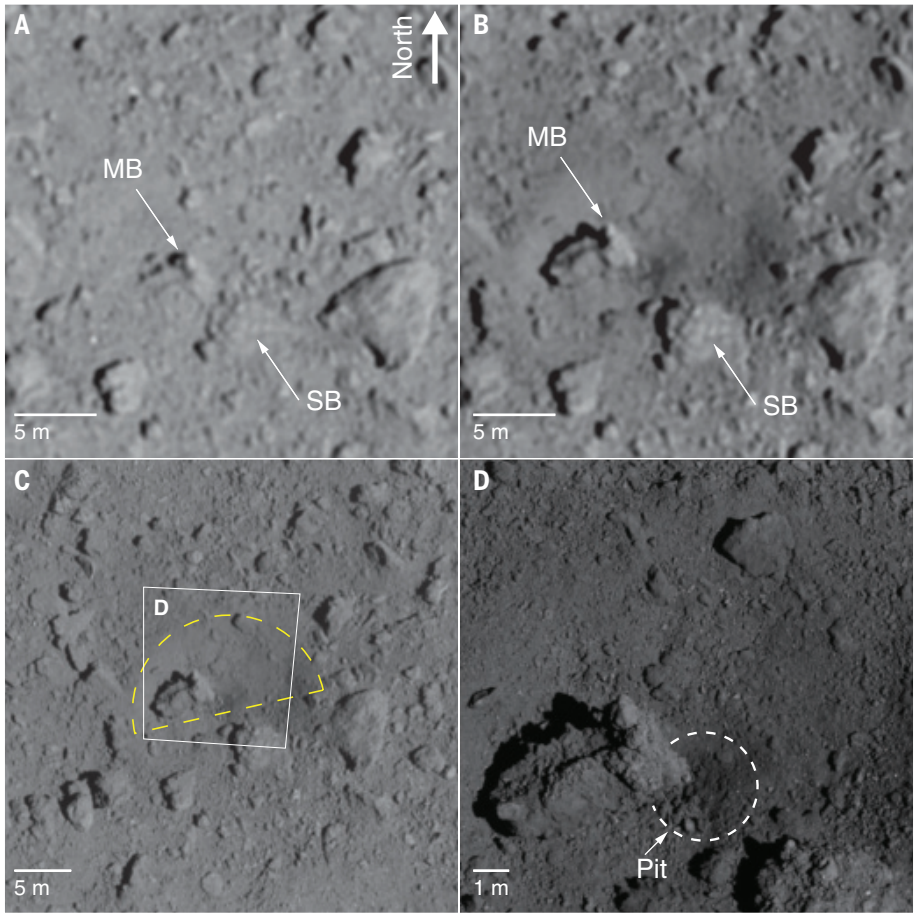

Fig. 1. ONC-T images of the SCI crater. (**A**) The area around the SCI aiming point before the impact, taken from an altitude of 1.72 km (image hyb2_onc_20190321_192706_tvf_l2b). The MB and SB are indicated with arrows. (**B**) The same location after the impact, observed from the same altitude (hyb2_onc_20190425_031226_tvf_l2b). (**C**) Ortho-corrected context image of the impact location (hyb2_onc_20190516_023615_tvf_l2c) with the SCI crater shown by a yellow dashed semicircle. The white box indicates the region in (D). (**D**) Close up image of the SCI crater taken from an altitude of 115 m (hyb2_onc_20190613_020217_tvf_l2c). A small pit is shown by the dashed curve. For (A) and (B), the spatial resolution has been enhanced by a factor of four through deconvolution; the original images are shown in fig. S2. Movie S1 shows a blink comparison between (A) and (B).

[1]Department of Planetology, Kobe University, Kobe 657-8501, Japan. [2]Institute of Space and Astronautical Science, Japan Aerospace Exploration Agency, Sagamihara 252-5210, Japan. [3]Planetary Exploration Research Center, Chiba Institute of Technology, Narashino 275-0016, Japan. [4]JAXA Space Exploration Center, Japan Aerospace Exploration Agency, Sagamihara 252-5210, Japan. [5]Department of Basic Sciences, University of Occupational and Environmental Health, Kitakyusyu 807-8555, Japan. [6]Department of Information Science, Kochi University, Kochi 780-8520, Japan. [7]Department of Regional Business, Aichi Toho University, Nagoya 465-8515, Japan. [8]Observatoire de la Côte d'Azur, Université Côte d'Azur, CNRS, Laboratoire Lagrange, CS34229, 06304 Nice Cedex 4, France. [9]Physics Institute, University of Bern, National Centre of Competence in Research PlanetS, Gesellschaftsstrasse 6, 3012, Bern, Switzerland. [10]Department of Electrical Engineering, Tokyo University of Science, Noda 278-8510, Japan. [11]Department of Earth and Planetary Science, The University of Tokyo, Tokyo 113-0033, Japan. [12]Department of Physics, Rikkyo University, Tokyo 171-8501, Japan. [13]Instituto de Astrofísica de Canarias, University of La Laguna, 38205 San Cristóbal de La Laguna, Spain. [14]Department of Complexity Science and Engineering, The University of Tokyo, Kashiwa 277-8561, Japan. [15]National Institute of Advanced Industrial Science and Technology, Tokyo 135-0064, Japan. [16]School of Computer Science and Engineering, The University of Aizu, Aizu-Wakamatsu 965-8580, Japan. [17]Department of Earth and Environmental Sciences, Nagoya University, Nagoya 464-8601, Japan. [18]Department of Space and Astronautical Science, The Graduate University for Advanced Studies, SOKENDAI, Hayama 240-0193, Japan. [19]Research and Development Directorate, Japan Aerospace Exploration Agency, Sagamihara 252-5210, Japan. [20]Department of Chemistry, The University of Tokyo, Tokyo 113-0033, Japan. [21]Department of Mechanical, Materials and Aerospace Engineering, University of Liverpool, Liverpool L3 5TQ, UK. [22]National Astronomical Observatory of Japan, Mitaka 181-8588, Japan. [23]Department of Astronomical Science, The Graduate University for Advanced Studies, SOKENDAI, Hayama 240-0193, Japan.
***Corresponding author. Email: masahiko.arakawa@penguin.kobe-u.ac.jp** †Deceased. ‡Present address: Mitsubishi Electric Corporation, Kamakura 247-8520, Japan. §Present address: NEC Corporation, 1-10 Nisshin-cho, Fuchu, Tokyo 183-0036, Japan.

SB) southeast of the impact point (Fig. 1B) (*14*). Impact craters are usually symmetrical at this impact angle, so we assume that the SCI impact point is the center of the semicircular crater rim. A crater's apparent diameter D is conventionally measured at an initial surface elevation. Using the DEM, we determine the SCI crater to have D = 14.5 ± 0.8 m (Fig. 2A).

There is a small pit close to the impact point on the crater floor. The pit entrance is at a depth of 1.7 m from the initial surface (Fig. 2B); the diameter of the pit is ~3 m and its depth is 0.6 m. The pit has a conical shape that is similar to those of the simple craters formed in laboratory experiments (*10*, *15*). On the Moon, central pits are commonly observed in craters smaller than a few hundred meters because the lunar subsurface has a layered structure that consists of a relatively hard layer covered with a softer cohesionless regolith (*16*). Therefore, the pit could be explained if the SCI impact occurred above a subsurface layer with cohesive strength. Some small natural craters on Ryugu also have pit features (fig. S4). The cohesive strength of this putative subsurface layer would be between 140 and 670 Pa (*14*). Alternatively, a central pit could be formed on compressive material if the projectile density is larger than that of the targets (*7*, *8*). Because the pit depth is 2.7 m from the rim top, the depth-to-rim diameter ratio of the SCI crater is 0.15 ± 0.01. This value is consistent with ratios for natural craters found on Ryugu, which range from 0.14 to 0.20 (*1*).

Several boulders with sizes of 0.6 to 1.9 m are present within the crater. The crater wall appears to be smooth (Fig. 1D) because the boulders are buried inside the wall. They could have been exposed by the excavation flow of subsurface materials during the crater growth. The size-frequency distribution (fig. S5A) of boulders embedded in the wall is about one-third of that on a nearby area of undisturbed surface (the C01-C region at 10°N, 300°E, about 20 m northwest of the impact point; fig. S5B), where the size-frequency distribution in the undisturbed area could be similar to that of the impact point before the SCI impact in submeter range. The SCI crater wall must be composed primarily of regolith with rock sizes smaller than 20 cm. Assuming that the crater wall represents the subsurface structure, we conclude that the subsurface layer is dominated by regolith with rock sizes smaller than 20 cm.

DCAM3 observed the impact ejecta from the moment of impact until >8 min later. Figure 3, A to F, and movie S2 show the images taken by DCAM3 from 5 to 498 s after the impact. The image at 5 s shows the impact ejecta curtain growing northwards from the surface at an angle of 40° (Fig. 3A and fig. S6A). Subsequent images show that the impact ejecta curtain was asymmetric and contained multiple rays

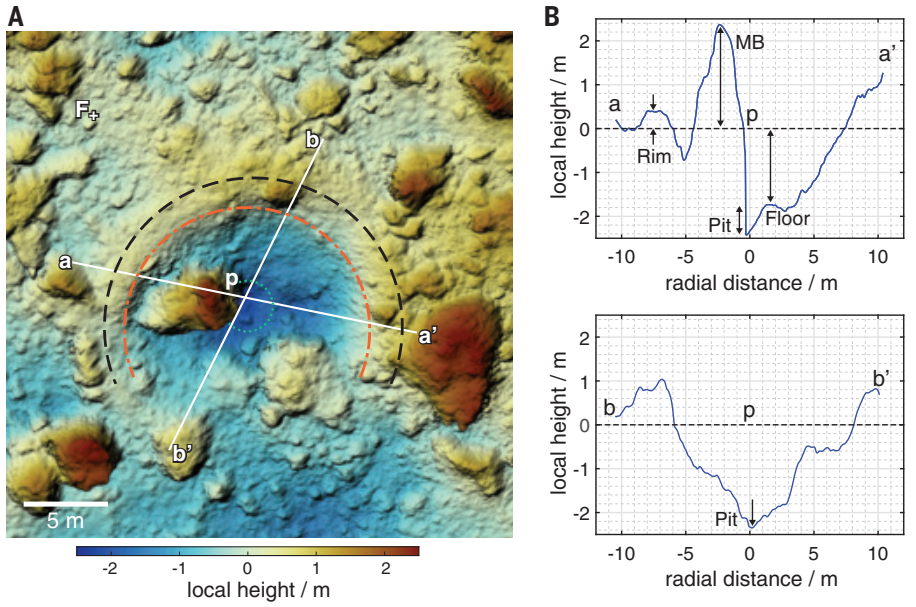

Fig. 2. Topography of the SCI crater. (**A**) DEM of the SCI impact area. The black dashed semicircle shows the crater rim with diameter 17.6 m, and the red dashed-dotted semicircle shows the crater wall with diameter 14.5 m. The green dotted circle shows the central pit. The local height is measured relative to point F, which is labeled northwest of the crater. The white lines show the locations plotted in (B). Figure S3 shows a contour map of this area. (**B**) Cross sections of the SCI crater. Radial distances are measured from the point p. The rim, pit, crater floor, and MB are labeled.

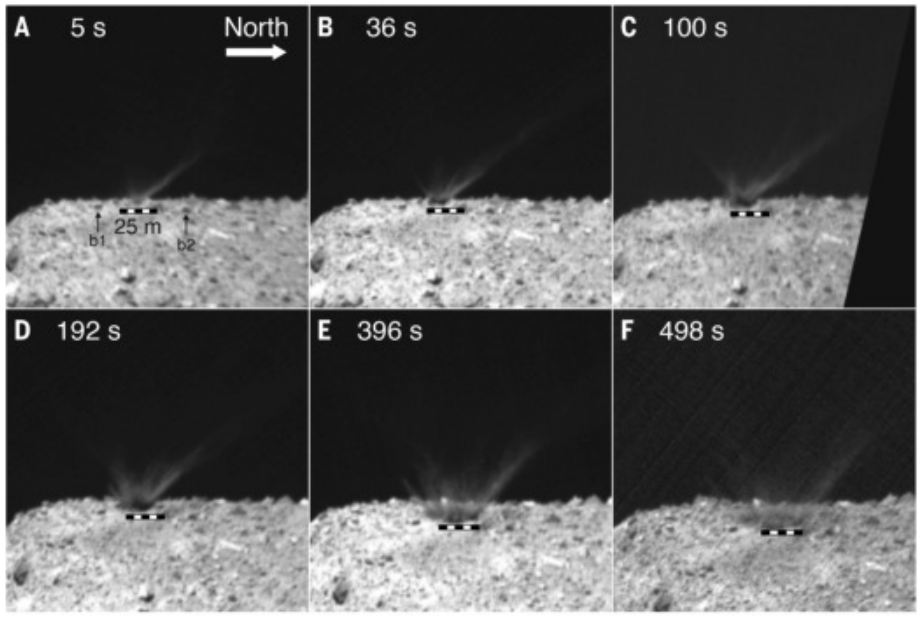

Fig. 3. DCAM3 images of the SCI impact. (**A** to **F**) The images were taken at elapsed time after the impact of 5 s (hyb2_dcam3d_img-f_01309_l2a) (A), 36 s (hyb2_dcam3d_img-f_01340_l2a) (B), 100 s (hyb2_dcam3-d_img-f_01404_l2a) (C), 192 s (hyb2_dcam3d_img-f_01496_l2a) (D), 396 s (hyb2_dcam3d_img-f_01700_l2a) (E), and 498 s (hyb2_dcam3d_img-f_01802_l2a) (F). The scale bars of 25 m were calibrated using the distance between the boulders labeled b1 and b2. Three visible rays are seen in a (B) and they are marked as 2, 3, and 4 in fig. S6B. The impact point moved toward DCAM3 during the observations because of the rotation of Ryugu. Movie S2 shows an animated version of this figure.

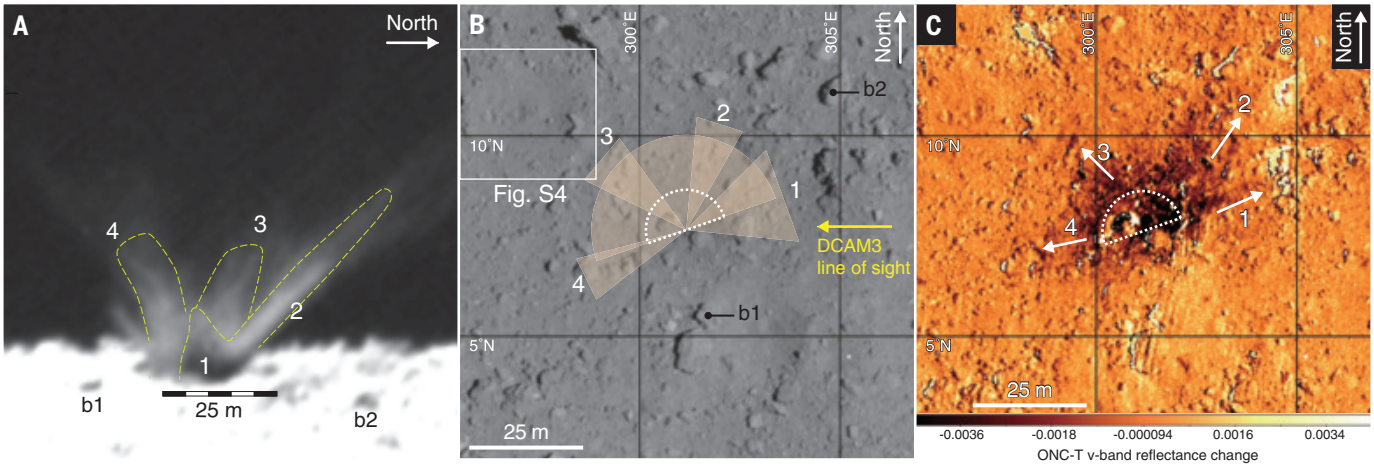

Fig. 4. Distribution of the SCI ejecta. (**A**) DCAM3 image taken at 192 s, extracted from Fig. 3D with increased contrast. Four ejecta rays are identified, enclosed with dashed lines, and numbered from 1 to 4 on the image. The scale bar and labeled boulder are the same as in Fig. 3. (**B**) ONC-T *v*-band image map. The line of sight of DCAM3 at the time of Fig. 4A is shown with the yellow arrow. Numbered sectors correspond to the separate ejecta rays, and a semicircle corresponds to the continuous ejecta curtain, both of which are projected onto the ONC-T image and colored light orange. The white box indicates a natural pit crater northwest of the SCI crater, shown in detail in fig. S4. (**C**) Difference in ONC-T *v*-band reflectance before and after the SCI impact. The typical reflectance factor of this area is about 0.018, thus the darkest regions in this map have decreased in reflectance by about 20% after the impact. Four discrete extended darkened areas correspond with the ejecta rays and are numbered 1 to 4. The same pre-impact shape model is used for both pre- and post-impact reflectance calculations (*14*) to emphasize weak reflectance changes caused by ejecta deposit outside of the crater.

in the early stages. Ejecta growth toward the south is not observed, but low-speed ejecta at the base of the ejecta curtain are visible in faint scattered light.

At 36 s, the northward ejecta ray becomes clearer and more extensive. Two more ejecta rays appear at this time (Fig. 3B and fig. S6B). Multiple rays of ejecta were previously observed in the Deep Impact experiments (*7*). A continuous portion of ejecta curtain, which appears as a shadow at the base of the ejecta curtain, begins to grow vertically and horizontally. This growth could originate from the expanding crater because of ongoing excavation of the subsurface material.

These three ejecta rays continue to grow in both size and thickness, becoming more visible at 100 and 192 s (Fig. 3, C and D, and fig. S6, C and D), which indicates that the crater growth is continuing at these times. An additional ejecta ray appears as a dark shadow in these images at the center of the ejected region, which we interpret as moving toward the line of sight of DCAM3, but there is no visible ejecta curtain in the southeast area. The surface of Ryugu is covered with many large boulders with a power law size distribution (*1*), which we presume also applies to boulders buried in the subsurface. The SCI impact area was covered with boulders >0.6 m, some of which had most of their volume buried in the ground (Fig. 1A). These boulders could cause a heterogeneous ejecta growth, which would then result in ejecta rays; in other words, the boulders on or under the surface might stop the excavation flow, separating the ejecta curtain into several rays. The ejecta curtain formed by the Deep Impact collision exhibited an up-range zone of avoidance (ZoA) (*7*). We see a similar ZoA for the SCI impact, which may be caused by the oblique nature of the impact, as in Deep Impact. However, the resulting semicircular shape of the SCI crater demonstrates the influence of large boulders.

We analyzed the distribution of ejecta rays around the SCI crater using the image at 192 s (Fig. 4A) with ONC-T images of the SCI crater area that were obtained after the impact. The direction and covered surface area of each ejecta ray were identified on the images taken by ONC-T with reference to the DCAM3 line of sight. Figure 4B shows the distribution of the main ejecta rays mapped on an ONC-T surface image; each numbered sector on the map corresponds to the numbered, separated ejecta ray in Fig. 4A, whereas the continuous ejecta curtain corresponds with a semicircle at the center. The whole ejecta, including the rays and the continuous curtain, was only distributed on the northwest side. This distribution map can be compared with an ONC-T v-band (0.55 μm) reflectance difference map shown in Fig. 4C (*14*). We interpret regions with a larger decrease of the reflectance factor as being covered with a thicker ejecta deposit. These regions are arranged asymmetrically around the crater: There are four discrete extended areas but none (or only a very faint one) to the southeast of the crater. These features in the reflectance difference map are consistent with those in the ejecta distribution map, so we are convinced that these maps represent the spatial distribution of the ejecta deposit and that the ejected subsurface material has a lower reflectance than the average Ryugu surface.

At 396 and 498 s, the surface of Ryugu is visible through the ejecta curtain (Fig. 3, E and F, and fig. S6, E and F), which indicates that the optical thickness of the ejecta curtain was lower than at 192 s. A deep gray elliptical area appears, surrounded by the ejecta rays. We interpret this as the intrinsic color of the surface and suggest that it represents the excavated area and/or the ejecta deposit area. Because crater growth is expected to have halted after 250 s (*14*), the ejecta curtain observed in these images must have been falling toward the surface on a ballistic trajectory. The major axis of the ellipse at 498 s was determined to be 36 m (*14*).

Detachment of the whole ejecta curtain from the ground is generally expected during crater formation in the strength-dominated regime but not in the gravity-dominated regime (*5*). No detachment of the ejecta curtain was observed for the SCI crater formation, including in the final observation at 498 s (Fig. 3, A to F). In Fig. 3 and movie S2, the ejecta curtain appears to be deposited at the crater rim. This is further supported by the ONC-T reflectance difference map in Fig. 4C, so the elevated rim surrounding the SCI crater could be (at least partially) composed of the ejecta deposits. This is expected for crater formation in the gravity-dominated regime (*15*, *17*). We conclude that the structures of the SCI crater and the ejecta curtain indicate that they formed in the gravity-dominated regime.

For the crater formation to be dominated by gravity, the effective strength of the target must be <1.3 Pa (*14*). Cohesionless materials such as sand can satisfy that small strength at a depth shallower than 10 m, because the

subsurface shear strength originates from the frictional stress exerted on cohesionless materials, and this stress is proportional to the surface gravity. We calculate the expected SCI crater radius using the conventional scaling law in the gravity-dominated regime $\pi_R = k_1 \times {\pi_2}^{-\mu/(2+\mu)} {\pi_4}^{(2+\mu-6\nu)/[3(2+\mu)]}$ (*18*), where $\pi_R = R(\rho/m)^{1/3}$, $\pi_2 = (ga/u^2)$, $\pi_4 = (\rho/\delta)$, R is the apparent crater radius, ρ the target density, m the projectile mass, a the projectile radius, u the impact velocity, and δ the projectile density. The parameters k_1, μ, and ν are empirical parameters determined by laboratory experiments, which apply to typical cohesionless surfaces such as coarse or loose sand (*14*). The calculated expected radius is from 6.9 to 7.7 m, which is close to the apparent radius of the observed SCI crater of 7.3 ± 0.4 m. We conclude that the SCI crater formed on a cohesionless surface and that the broader surface of Ryugu must be composed of sand-like cohesionless material. According to the conventional scaling law, we can estimate the optimal $k_1$value applicable to the surface of Ryugu from the SCI crater radius R = 7.3 m (*14*). We obtain k_1 = 0.62 if we assume that other parameters have typical values for sand and can be extrapolated to cohesionless targets at high impact velocities: μ = 0.41 and ν = 0.4 (*14*, *18*). We derive the crater size scaling law for the surface of Ryugu $\pi_R = 0.62 \times {\pi_2}^{-0.17} {\pi_4}^{0.0014}$.

Our results affect the interpretation of the crater chronology on Ryugu. On the basis of the collision frequency models for the asteroid Main Belt (*19*, *20*), two estimates of the surface age of Ryugu have been obtained: (1.58 ± 0.47) × 10^8 years for a surface composed of dry-soils with cohesion or (8.9 ± 2.5) × 10^6 years for a cohesionless surface (*1*). Our conclusion that the SCI crater was formed in the gravity-dominated regime on a cohesionless surface supports the younger age estimate. It also suggests that the crater retention age of the top 1 m of Ryugu's surface is ~1 × 10^5 years or younger, assuming crater production functions for near-Earth orbits (*14*, *19*, *20*).

REFERENCES AND NOTES

1. S. Sugita *et al*., *Science* **364**, eaaw0422 (2019).
2. S. Watanabe *et al*., *Science* **364**, 268–272 (2019).
3. K. Wada *et al*., *Prog. Earth Planet. Sci.* **5**, 82 (2018).
4. K. Holsapple, I. Giblin, K. Housen, A. Nakamura, E. Ryan, in *Asteroids III*, W. F. Bottke, A. Cellino, P. Paolicchi, R. P. Binzel, Eds. (Univ. of Arizona Press, 2002), pp. 443–462.
5. M. Arakawa *et al*., *Space Sci. Rev.* **208**, 187–212 (2017).
6. S. Tachibana *et al*., *Geochem. J.* **48**, 571–587 (2014).
7. P. H. Schultz *et al*., *Icarus* **191**, 84–122 (2007).
8. P. H. Schultz, C. M. Ernst, J. L. Anderson, *Space Sci. Rev.* **117**, 207–239 (2005).
9. M. F. A'Hearn *et al*., *Science* **310**, 258–264 (2005).
10. K. Matsue, M. Yasui, M. Arakawa, S. Hasegawa, *Icarus* **338**, 113520 (2020).
11. E. Tatsumi, S. Sugita, *Icarus* **300**, 227–248 (2018).
12. M. J. Cintala, L. Berthoud, F. Hörz, *Meteorit. Planet. Sci.* **34**, 605–623 (1999).
13. M. Jutzi, K. A. Holsapple, K. Wünneman, P. Michel, in *Asteroids IV*, P. Michel, F. E. DeMeo, W. F. Bottke, Eds. (Univ. of Arizona Press, 2015), pp. 679–699.
14. Materials and methods are available as supplementary materials.
15. H. J. Melosh, *Impact Cratering: A Geologic Process* (Oxford Univ. Press, 1989).
16. Z. Yue *et al*., *Icarus* **329**, 46–54 (2019).
17. K. R. Housen, R. M. Schmidt, K. A. Holsapple, *J. Geophys. Res.* **88**, 2485–2499 (1983).
18. K. R. Housen, K. A. Holsapple, *Icarus* **211**, 856–875 (2011).
19. W. F. Bottke Jr. *et al*., *Icarus* **175**, 111–140 (2005).
20. D. P. O'Brien, R. Greenberg, *Icarus* **178**, 179–212 (2005).

ACKNOWLEDGMENTS

Hayabusa2 was developed and built under the leadership of Japan Aerospace Exploration Agency (JAXA), with contributions from the German Aerospace Center (DLR) and the Centre National d'Études Spatiales (CNES), and in collaboration with NASA and other universities, institutes, and companies in Japan. SCI was developed by JAXA, Kobe University, Chiba Institute of Technology, University of Occupational and Environmental Health, Aichi Toho University, Kyushu Institute of Technology, Hosei University, and other universities, institutes, and companies in Japan. DCAM3 was developed by JAXA, Kobe University, Kochi University, Chiba Institute of Technology, Tokyo University of Science, University of Occupational and Environmental Health, and other universities, institutes, and companies in Japan. M.Ar. thanks M. Yasui for help in conducting laboratory impact experiments. K.W. is grateful to H. Kimura for discussions on the observational possibility of ejecta curtains. **Funding:** M.Ar., T.O., T.M., S.W., N.N., K.W., T.M., K.O., M.Ab., S.Ka., A.M., S.Su., K.Yoshio., and Y.C. were supported by KAKENHI from the Japanese Society for Promotion of Science (JSPS) (grant nos. JP16H04041, JP17H06459, JP15K05273, JP19H01951, JP19H00719, JP16H04044, JP19K03955, JP19H00727, JP17KK0097, JP18K11610, JP17H01175, and JP19K14778). This study was supported by JSPS Core-to-Core program "International Network of Planetary Sciences." P.M. acknowledges funding support from the French space agency CNES and from Academies of Excellence: Complex systems and Space, environment, risk, and resilience, part of the IDEX JEDI of the Université Côte d'Azur. **Author contributions:** M.Ar. coordinated coauthor contributions; led the SCI and DCAM3 data acquisition, analyses, and interpretations; and wrote the paper, with contributions from K.W., K.O., T.Ka., K.S., K.I., R.H., N.S., P.M., M.J., and Y.S. SCI operations: T.Sa., K.W., T.Ka., K.S., Y.I., C.O., H.Y., Y.Taka., M.H., H.Im., and N.H. (Aizu). DCAM3 data acquisitions and reductions: K.W., K.O., K.S., H.S., K.I., R.H., N.S., Y.I., S.Kim., Y.M., T.To., S.N., and H.H. ONC-T data acquisitions and reductions: H.S., R.H., N.S., M.H., S.Su., T.M., S.Ka., E.T., Y.C., K.Yoshio., Y.Yo., M.M., M.Ya., T.Ko., and C.Ho. Image analysis: K.W., K.O., T.Ka., K.S., K.I., R.H., N.S., and Y.S. Spacecraft operations: T.Sa., K.O., K.S., H.S., R.H., N.S., H.Y., M.H., Y.M., S.N., Y.Ts., S.W., M.Yo., S.Tan., F.T., S.Kik., T.Y., N.O., G.O., K.Yoshiz., T.Ta., Y.Take., A.F., H.T., Y.Ya., T.O., C.Hi., S.H., O.M., T.Sh., S.So., R.T., T.I., M.O., M.Ab., N.N., K.K., S.Tac., and H.Ik. Shape modeling: K.S., Y.S., N.H. (Aizu), N.H. (Kobe), R.N., and A.M. **Competing interests:** Y.Ya. is also affiliated with Tokyo Metropolitan University. **Data and materials availability:** All images, input data, and the DEM used in this study are available on the JAXA Data Archives and Transmission System (DARTS) at www.darts.isas.jaxa.jp/pub/hayabusa2/paper/Arakawa_2020/. Additional data from Hayabusa2 ONC-T and DCAM3 will be made available through DARTS at www.darts.isas.jaxa.jp/planet/project/hayabusa2/.

SUPPLEMENTARY MATERIALS

science.sciencemag.org/content/368/6486/67/suppl/DC1
Materials and Methods
Figs. S1 to S11
Table S1
References (*21*–*35*)
Movies S1 and S2

22 August 2019; accepted 4 March 2020
Published online 19 March 2020
10.1126/science.aaz1701

COMPLEX OXIDES

Extreme tensile strain states in $La_{0.7}Ca_{0.3}MnO_3$ membranes

Seung Sae Hong[1,2,3]*, Mingqiang Gu[4,5], Manish Verma[6], Varun Harbola[2,7], Bai Yang Wang[2,7], Di Lu[2,4,7], Arturas Vailionis[8,9], Yasuyuki Hikita[2], Rossitza Pentcheva[6], James M. Rondinelli[4], Harold Y. Hwang[1,2]

A defining feature of emergent phenomena in complex oxides is the competition and cooperation between ground states. In manganites, the balance between metallic and insulating phases can be tuned by the lattice; extending the range of lattice control would enhance the ability to access other phases. We stabilized uniform extreme tensile strain in nanoscale $La_{0.7}Ca_{0.3}MnO_3$ membranes, exceeding 8% uniaxially and 5% biaxially. Uniaxial and biaxial strain suppresses the ferromagnetic metal at distinctly different strain values, inducing an insulator that can be extinguished by a magnetic field. Electronic structure calculations indicate that the insulator consists of charge-ordered Mn^{4+} and Mn^{3+} with staggered strain-enhanced Jahn-Teller distortions within the plane. This highly tunable strained membrane approach provides a broad opportunity to design and manipulate correlated electron states.

Externally driven changes in atomic spacing offer access to distinct phases and functionalities of materials. In complex oxides (*1*–*3*), strain can be used to manipulate quantum states of matter (*4*–*8*) because the electrons in these materials and their correlated interactions are tightly coupled to the lattice. However, bulk oxide crystals are typically brittle and crack under relatively small tensile strain; larger strain states are usually only accessible under compression (*9*). Although epitaxial strain imparted by lattice mismatch between a thin film and the underlying

[1]Department of Applied Physics, Stanford University, Stanford, CA 94305, USA. [2]Stanford Institute for Materials and Energy Sciences, SLAC National Accelerator Laboratory, Menlo Park, CA 94025, USA. [3]Department of Materials Science and Engineering, University of California, Davis, CA 95616, USA. [4]Department of Materials Science and Engineering, Northwestern University, Evanston, IL 60208, USA. [5]Department of Physics, Southern University of Science and Technology, Shenzhen 518055, China. [6]Department of Physics and Center for Nanointegration (CENIDE), University of Duisburg-Essen, 47053 Duisburg, Germany. [7]Department of Physics, Stanford University, Stanford, CA 94305, USA. [8]Stanford Nano Shared Facilities, Stanford University, Stanford, CA 94305, USA. [9]Department of Physics, Kaunas University of Technology, LT-51368 Kaunas, Lithuania.
***Corresponding author. Email: sshong@ucdavis.edu**

substrate can modulate the properties of thin films (*5*, *6*, *10*, *11*), the discrete lattice parameters of available substrates (*10*), combined with strain-driven defect formation during high-temperature synthesis (*12*, *13*), present fundamental limitations to exploring how extreme and coherent strain fields affect correlated states in oxides. The recent development of free-standing complex oxide membranes (*14*) both circumvents these challenges and provides unique opportunities to realize previously unobserved strain-induced responses. Oxide membranes can be mechanically coupled to an external platform without an epitaxial relationship, for which strain states of different

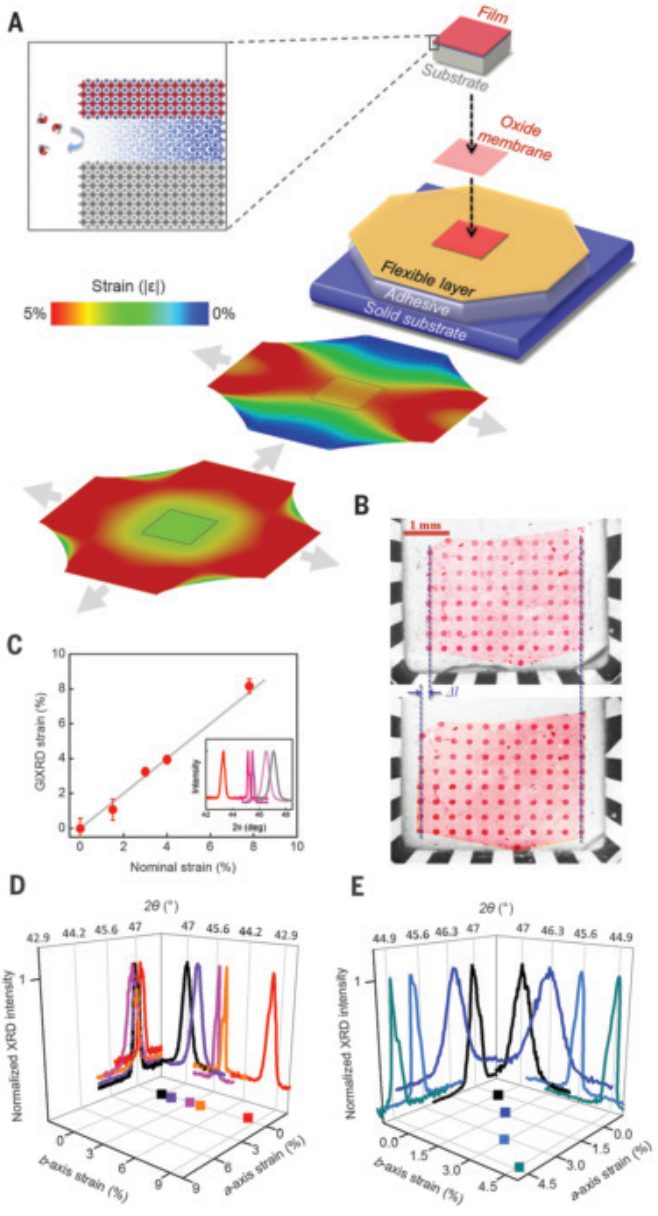

Fig. 1. Designer strain in 2D oxide membranes. (**A**) Schematic platform for straining oxide membranes. The lower maps plot finite-element analysis strain profiles of the polyimide/oxide bilayer under uniaxial and biaxial stress (*21*). The gray square in the strain maps indicates the boundary of the oxide membrane, beyond which only the polyimide remains. Inset: Lifting off a membrane from the substrate by etching a water-soluble layer in oxide heterostructures. (**B**) Optical microscope images of a 6-nm-thick LCMO membrane before (top) and after (bottom) stretching uniaxially. The ceramic chip carrier is used as a reference frame to optically characterize the strain state. (**C**) GIXRD strain as a function of the nominal strain observed optically. Error bars denote SD. Inset: GIXRD data of the LCMO (200) peak shifted by strain. (**D** and **E**) In-plane lattice changes and corresponding 2θ peaks of LCMO membranes characterized by GIXRD, for uniaxial (D) and biaxial (E) strain.

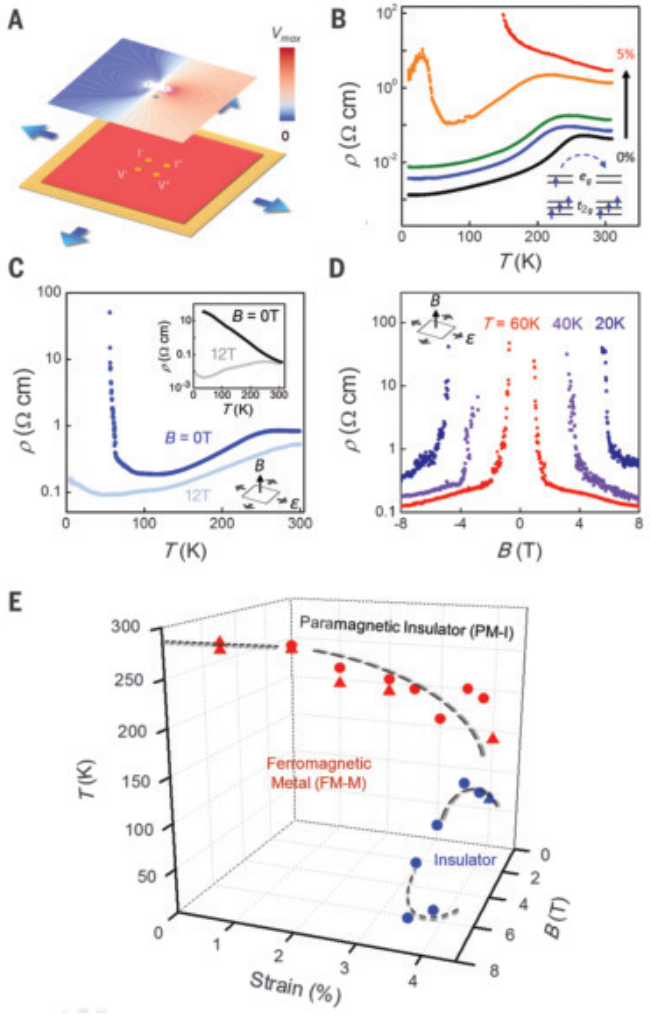

Fig. 2. Magnetotransport and phase diagram of biaxially strained $La_{0.7}Ca_{0.3}MnO_3$ membranes. (**A**) Electric potential mapping of the central vdP geometry in membranes. The boundary conditions were current nonpermeability at the edges; I^+ and I^- represent the current source and current sink. The voltage at V^- is held at $V = 0$, and V_{max} is calculated at V^+. (**B**) Evolution of the temperature-dependent resistivity of an 8-nm-thick LCMO membrane as a function of strain: 0% (black), 1% (blue), 2% (green), 4% (orange), and 5% (red) biaxial strain. No thickness dependence was observed between membranes of $d = 4$ nm and $d = 8$ nm (fig. S6). Inset: Double exchange interaction between two Mn sites. (**C**) Resistivity-temperature curves of a strained LCMO membrane ($d = 4$ nm, $\varepsilon = 3.5\%$) under perpendicular magnetic field. Inset: Resistivity-temperature curves of a LCMO film ($d = 4$ nm) grown on an $SrTiO_3$ (001) substrate under perpendicular magnetic field. (**D**) Magnetoresistance of the 4-nm-thick LCMO membrane shown in (C) at different temperatures. (**E**) Phase diagram of biaxially strained LCMO membranes. The phase boundaries are determined by resistive transitions during cooling curves ($B = 0$ T or $B = 5$ T with zero strain) and magnetoresistance data during increasing field sweeps ($T = 5$ K), acquired from membranes of two different thicknesses (circles, $d = 4$ nm; triangles, $d = 8$ nm).

symmetries can be freely chosen by design. Moreover, the critical fracture strain is often greatly enhanced for small materials length scales (*15*, *16*), enabling a viable route to impart large tensile strain states well beyond the typical values that ceramics can withstand.

Rare-earth perovskite manganites are correlated electron systems with multiple phases coupled to the lattice (*17*). A number of stable electronic and magnetic ground states arise at different carrier concentrations, as structural Jahn-Teller distortions to the MnO_6 octahedra generate different bond network configurations, which therefore change the magnetic exchange interactions between 3d electrons on neighboring sites. Here, we focused on $La_{0.7}Ca_{0.3}MnO_3$ (LCMO), a representative colossal magnetoresistance (CMR) material (*17*) with a transition between a low-temperature ferromagnetic metal (FM-M) and a high-temperature paramagnetic insulator (PM-I) at a Curie temperature T_C ~ 250 K. The metallic ground state of LCMO is closely adjacent to many other phases, such as charge/orbital ordering (COO), a ferromagnetic insulating state, and antiferromagnetic states, thereby offering an ideal testbed to understand electronic correlations controlled by elastic lattice strain.

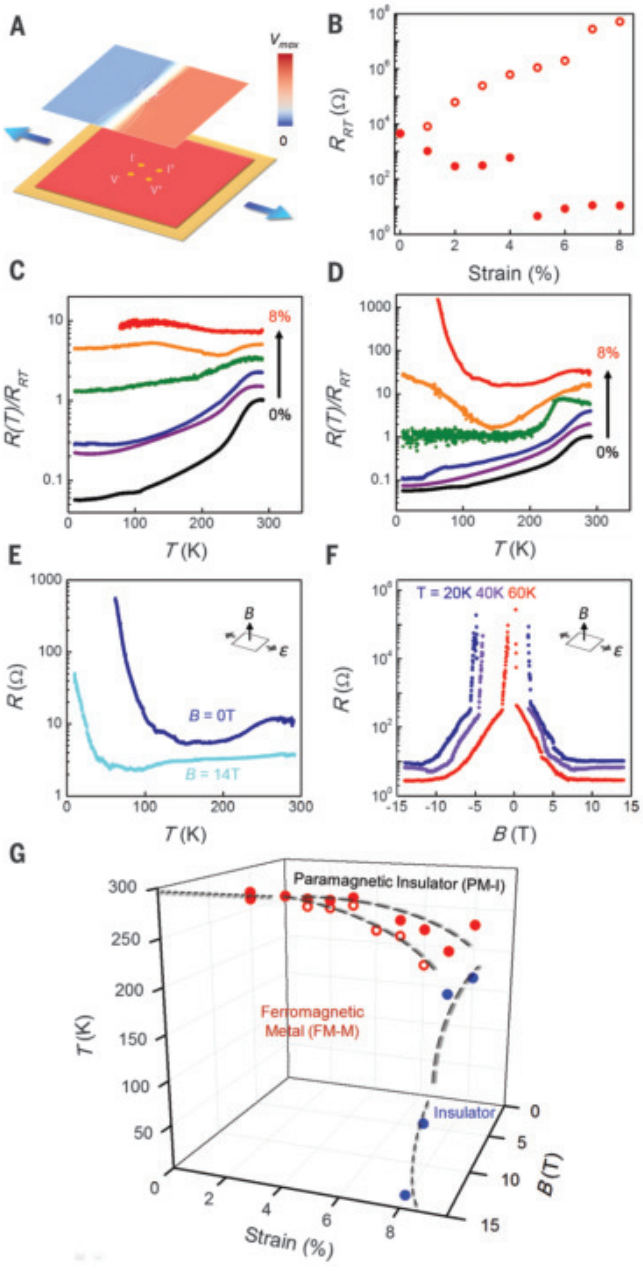

Fig. 3. Magnetotransport and phase diagram of uniaxially strained $La_{0.7}Ca_{0.3}MnO_3$ membranes. (**A**) Electric potential mapping of the central vdP geometry in membranes under a uniaxial strain, with 1:100 resistivity anisotropy. The boundary conditions were current nonpermeability at the edges; I^+ and I^- represent the current source and current sink. The voltage at V^- is held at V = 0, and V_{max} is calculated at V^+. (**B**) Room-temperature resistances R_{RT} (T = 290 K) in the central vdP geometry with different uniaxial strains. Open circles are resistances parallel to the strain direction; solid circles are resistances perpendicular to the strain direction. (**C** and **D**) Evolution of the temperature-dependent resistance of an 8-nm-thick LCMO membrane, parallel (C) and perpendicular (D) to the uniaxial strain of 0% (black), 1% (purple), 3% (blue), 5% (green), 7% (orange), and 8% (red). Each resistance-temperature curve is normalized by R_{RT} and is shifted vertically for visual clarity. (**E**) Resistance-temperature curves of the strained LCMO membrane (vdP resistance perpendicular to the strain ε = 8%) under perpendicular magnetic field. (**F**) Magnetoresistance of the LCMO membrane under perpendicular magnetic field at different temperatures. (**G**) Phase diagram of uniaxially strained LCMO membranes. The phase boundaries are determined by resistive transitions during cooling curves (B = 0 T or B = 5 T with zero strain) and magnetoresistance data during increasing field sweeps (T = 10 K), acquired from vdP resistances parallel (open circles) and perpendicular (solid circles) to the strain direction.

Using pulsed laser deposition (PLD), we synthesized multilayer heterostructures consisting of $SrCa_2Al_2O_6$ (used as a sacrificial layer), $SrTiO_3$, and LCMO (fig. S1) to release freestanding LCMO nanomembranes. The solid-solution family of $(Ba,Sr,Ca)_3Al_2O_6$ enables the continuous tuning of the sacrificial layer lattice constant from 0.382 nm (Ca 100%) to 0.413 nm (Ba 100%), covering the lattice constant range of the vast majority of perovskite and related oxides (*18*, *19*). $SrCa_2Al_2O_6$, a particular composition for the sacrificial layer developed for this experiment instead of $Sr_3Al_2O_6$ used previously (*14*), is nearly perfectly lattice-matched (<0.1%) to the LCMO lattice constant (a = 0.386 nm). We found that minimizing lattice mismatch is a critical factor to avoid crack formation in the released membranes (fig. S2) and is therefore essential to achieve homogeneous tensile strain states over large areas. The LCMO layer was kept at a minimum of 10 unit cells to avoid the Berezinskii-Kosterlitz-Thouless crystalline melting transition previously observed in the ultrathin limit (*20*). All heterostructures were grown epitaxially and monitored by in situ reflection high-energy electron diffraction (RHEED). By selectively dissolving the sacrificial layer in water, the top oxide film was detached from the substrate and transferred onto a polyimide sheet, which we used as a stretchable substrate (*21*).

The strain state of the oxide membrane can be controlled by external forces (Fig. 1A). The four sides of the polymer layer were clamped and stretched by micromanipulators with ~0.1% precision. The strong adhesion between the oxide membrane and the polymer layer provides efficient strain transfer to the oxide membrane without any observable slippage. The macroscopic size of the membrane (area > 10 mm^2) provides a uniform interior distribution of strain ε upon stretching and minimizes the edge effects observed in microflakes of exfoliated crystals (*22*). Finite-element analysis of the strained membrane/polyimide bilayer (Fig. 1A) indicated that the membrane area experiences a strain gradient near the membrane edges, whereas the majority of the membrane area at the center is homogeneously strained ($\Delta\varepsilon$ < 0.2%). The strained oxide/polymer bilayer was then glued onto a solid substrate such that the strain field was fixed even after the external force was removed (fig. S3) (*21*).

The adhesive (polycaprolactone) used here can be reversibly melted by gentle heating (T < 100°C) on the sample assembly stage. Thus, it is possible to set and probe multiple strain states of the same membrane sample. Smaller strains less than 3% could be reset to the zero strain state by melting and releasing the adhesive, whereas higher strain states could only be stretched further in an irreversible manner thanks to the plastic deformation of the outer polymer layer (Fig. 1A). We found that the strain remains fixed for at least a week, down to cryogenic temperatures (T = 2 K) and under x-ray exposure, providing a versatile platform for multiple experiments.

We first optically characterized the strained membrane and found that the membrane reaches extreme macroscopic strain states. Two optical images, taken before and after establishing uniaxial tensile strain, are compared in Fig. 1B to estimate the strain. (Note here that a small tensile stress is also applied in the perpendicular direction to prevent compression by the finite Poisson ratio.) Because the oxide membrane is nearly transparent on the polyimide layer, we measured the strain by tracking the spacing of evaporated metal (Au) markers. By stretching oxide membranes of different thickness d, we found that thicker membranes (d > 20 nm) undergo mechanical fracture under relatively small uniaxial tensile strains (<2%), as seen in optical images showing periodic crack formation (fig. S4). In contrast, ultrathin oxide membranes (d < 10 nm) could be stretched much more (>2%) without fracture.

Although the macroscopic strain state was visibly evident, we next assessed whether such large strains in the oxide membrane induce elastic or plastic deformation. We used grazing incident x-ray diffraction (GIXRD) to measure the change of the in-plane lattice constants. In an unstretched LCMO membrane, the perovskite (200) peak in a 2θ-ω scan corresponded to that of the bulk LCMO crystal. With increasing tensile strain, the GIXRD peak shifted to lower angles (Fig. 1C, inset), tracking the increase of the in-plane lattice constant. The strain values measured by the GIXRD scans closely matched the macroscopic strain observed in the optical images (Fig. 1C). The maximum tensile strain in the uniaxial geometry was 8.2% (a = 0.417 nm), far beyond typical tensile strains accessible in crystalline oxides [such as typical piezoelectrically induced strains up to ~1% (*7*)] and epitaxial strains in canonical oxide thin films up to ~3% (*23*). [It is again worth noting that for high-temperature synthesis, defect densities in such ionic materials often vary with strain (*12*, *13*).] In addition, the symmetry of the strain field can be directly controlled. In Fig. 1, D and E, we present two examples for which the strain is independently tuned along different directions: asymmetric uniaxial strain states and symmetric biaxial strain states, respectively. The ability to design both the magnitude and symmetry of the strain field—for example, through linear combinations of the two aforementioned states—opens up avenues for the manipulation of complex oxide membranes hosting electrons sensitive to orbital symmetry and filling.

We next leveraged access to these extreme strain states to both modulate the transport properties of LCMO and stabilize a nonequilibrium phase of the LCMO membranes under biaxial strain. First, we measured the membrane resistivity using van der Pauw (vdP) electrodes near the center of the membrane (Fig. 2A). In the central vdP configuration, the distribution of electric current is quite insensitive to the geometry and strain gradient of the membrane edge (fig. S5) (*21*). This requires that the membranes are large with respect to the vdP dimensions, which is easily achieved here with millimeter-scale membranes. Therefore, the electronic transport measurements accurately reflect the intrinsic response of the central area with homogeneous strain. The temperature-dependent resistivity ρ(T) in the zero strain state exhibited T_C ~ 250 K, defined by the peak in d[log(ρ)]/d(T), consistent with prior studies. Next, by repeatedly stretching the membrane in a symmetric (biaxial) manner, we acquired the full evolution of ρ(T) from the same oxide membrane at different strain states (Fig. 2B). We found that 5% biaxial tensile strain led to an increase in ρ(300 K) by more than two orders of magnitude. Moreover, T_C of the FM-M/PM-I phase transition shifted to lower temperatures. These observations are consistent with the reduction of the in-plane orbital overlap between Mn d orbitals and O p orbitals under tensile strain, which is supported by our electronic structure calculations. The marked resistivity increase at room temperature evidences the reduced bandwidth and smaller hopping integral for itinerant electrons. In double exchange, the hopping e_g electron is forced to align with the other core t_{2g} electrons by a large Hund's-rule coupling (Fig. 2B, inset). Thus, the electronic bandwidth is modulated by the spin orientation between Mn sites and gives an effective ferromagnetic interaction mediated by the electronic conduction. The smaller electronic hopping integral directly suppresses the double-exchange interaction, moving the phase boundary to substantially lower temperatures (*24*).

In addition to the large shift in T_C, we found an unexpected insulating phase emerging at high biaxial strain states (>3%) at low temperatures. The insulating state below T = 70 K can be quenched by magnetic fields with a large negative magnetoresistance (Fig. 2, C and D) and magnetic field hysteresis (fig. S7). This insulator-to-metal transition upon the application of magnetic field qualitatively resembles the field-induced melting of COO in competition with the FM-M. Similar behavior has been observed in low-bandwidth manganites (*25*). However, here the phase arises in a very different physical parameter space (temperature, strain, and resistivity) from prior reports of bulk crystals and epitaxially strained thin films of similar doping (see also Fig. 2C,

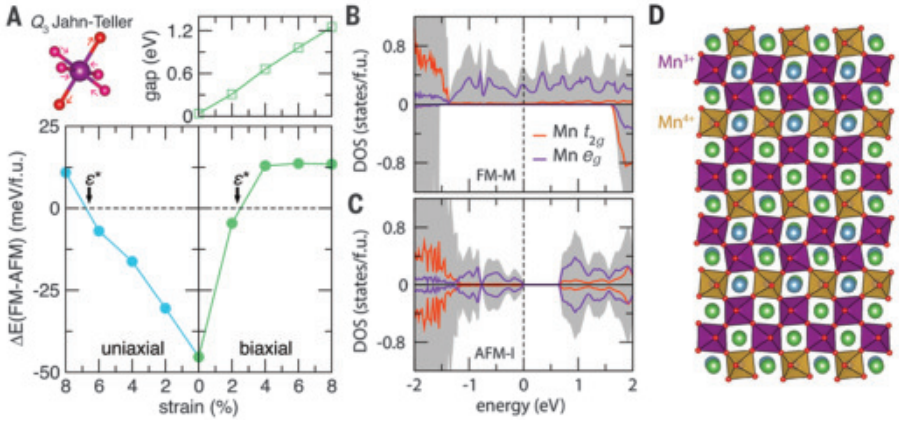

Fig. 4. Strain stabilization of insulating LCMO. (**A**) DFT total energy difference between the ferromagnetic metallic (FM-M) and antiferromagnetic insulating (AFM-I) phases with respect to uniaxial and biaxial strain in $La_{2/3}Ca_{1/3}MnO_3$. Schematic (top left) shows that Q_3 Jahn-Teller distortion of the MnO_6 octahedra active in the AFM-I phase drives the FM-M to AFM-I transition at the critical strain value ε* indicated by the bold vertical arrows. Increasing biaxial strain increases the bandgap of the insulating phase. (**B** and **C**) Electronic density of states for LCMO at 4% biaxial strain in the FM-M (B) and AFM-I (C) phases. (**D**) The AFM-I state displays charge-ordered Jahn-Teller–distorted $Mn^{3+}O_6$ (purple) and $Mn^{4+}O_6$ (orange) octahedra (see also fig. S10).

inset) (*26*). On the basis of these structural and electrical studies, we constructed a phase diagram of LCMO as a function of biaxial strain and magnetic field (Fig. 2E).

In addition to the biaxial strain states, we investigated electronic transport of the LCMO membrane under different uniaxial strains from 1% to 8% (Fig. 3A and fig. S8). We first observed that the vdP resistances of two directions, parallel and perpendicular to the uniaxial strain direction, are substantially different with large resistance anisotropy up to 10^7 (Fig. 3B). Electrostatic simulations on the finite-size vdP geometry (fig. S9) can be used to convert the maximum resistance anisotropy to a resistivity anisotropy (~10^3). For such large anisotropies, the measurement is much more sensitive to the finite-size boundary conditions than the biaxial case. Therefore, we report the directly measured resistance, from which the resistivities can be deduced (*21*). The temperature-dependent resistances $R(T)$ of the two different directions were measured for a series of uniaxial strain states (Fig. 3, C and D), showing the reduction of T_C by increasing strain. Nonmetallic temperature dependence in resistance-temperature curves first appears in the resistance parallel to the strain (ε = 6 to 8%) and is observed in the perpendicular direction at larger strains (ε = 7 to 8%). The insulating states for high uniaxial strains (T < 150 K, ε = 7 to 8%) are largely suppressed upon the application of magnetic field and show very large magnetoresistance (Fig. 3, E and F), similar to the biaxial strain states above 3%. The phase diagram of uniaxially strained LCMO membranes based on these electrical studies (Fig. 3G) qualitatively resembles the biaxial phase diagram (Fig. 2E) with the addition of a bifurcation of the resistively measured transition along the two different directions with respect to the strain direction.

We next performed density functional theory (DFT) calculations to consider the microscopic origin of the strain-induced insulating state. We first modeled LCMO using a model with ordered La^{3+} and Ca^{2+} cations (rather than a solid-solution configuration) in a ratio of 2:1 on the perovskite A-cation site to find the ground state (*27*). We applied both uniaxial and biaxial tensile strain up to 8%. A strain condition was not imposed for the out-of-plane lattice direction, and it was allowed to computationally relax. We then compared the ground-state energies of two phases—the FM-M phase and an antiferromagnetic insulator (AFM-I) phase with A-type ordering—at different strain states (Fig. 4A). The bulk DFT-relaxed FM-M phase was ~45 meV per formula unit (f.u.) lower in energy than the AFM-I phase, consistent with the experimental bulk phase diagram. The half-metallic behavior held for the FM-M phase throughout the examined strain level, as seen from the electronic density of states (Fig. 4B). We found that the energy difference between the two states decreases with increasing tensile strain until reaching a critical value $\varepsilon^* \approx 7\%$ (uniaxial), 3% (biaxial), at which point a FM-M to AFM-I transition occurs, in good agreement with the experimental results. Beyond this point, the AFM-I phase is stabilized and characterized by a COO insulating state (Fig. 4C) for both uniaxial and biaxial strain configurations. In the AFM-I state, ordering of $Mn^{4+}O_6$ and Jahn-Teller–distorted $Mn^{3+}O_6$ octahedra is found (Fig. 4D). By modeling various configurations for the A-site to simulate solid solutions with random La/Ca site occupancy, we found that the stripe-type COO (fig. S10) is robust to the A-site chemical distribution (*21*) (fig. S11). The DFT calculations confirm that the experimentally observed insulating phase under high strain is the A-type AFM-I phase with a stripe COO. For the one-third–doped LCMO, such a stripe COO was predicted with a two-dimensional model Hamiltonian that includes double-exchange and Jahn-Teller phonons (*28*), but different ground states were observed in epitaxial films (*29*, *30*). Although the detailed microscopic structure remains to be investigated, it is striking that such an anisotropic state is stabilized for both uniaxial and biaxial strain.

The FM-M phase is stable at low-strain states because the smaller in-plane lattice constants favor reduced Q_3 Jahn-Teller distortions of the MnO_6 octahedra (four short and two long Mn-O bonds, shown schematically in Fig. 4A) and more uniform Mn-O-Mn bond angles (*31*). In contrast, the COO AFM-I exhibits inequivalent Mn^{4+}/Mn^{3+} sites, forming an ordered structure controlled by the long Mn-O bond from the Q_3 Jahn-Teller distortion (fig. S10). The long Mn-O bond network is staggered in an alternating manner along $\langle 110 \rangle$ with respect to the orthorhombic lattice vectors, in which the longer Mn-O bond is elastically favored by larger in-plane lattice constants achieved through large tensile strains in the LCMO membranes. Furthermore, under extreme strain, superexchange interactions and electron localization (from weakened orbital overlap) dominate over metallic double exchange and stabilize the AFM-I ground state, which is consistent with the observed magnetic field–induced insulator-to-metal transitions (Figs. 2C and 3E).

The ability to achieve tensile strains in a continuous manner, complementing compressive strain states set by hydrostatic pressure (*9*), offers a vast unexplored phase space to control atomic spacing in correlated electron systems. The example of LCMO membranes demonstrates that a macroscopic, crack-free oxide membrane can be synthesized using a lattice tunable sacrificial layer, and is applicable to a large set of complex oxide materials to which large and uniform tensile strains can be applied. The access to such extreme tensile strain states, available in nanoscale oxide membranes, offers great opportunities to vary fundamental parameters and energy scales wherever competing orders exist, which may enable theory-based design and experimental exploration of phases beyond those in bulk equilibrium materials. Beyond complex oxides, the strain approach demonstrated here can be broadly applied to strain engineering of free-standing 2D layers, including 2D van der Waals materials (*32*) and compound semiconductor membranes (*33*).

REFERENCES AND NOTES

1. M. Imada, A. Fujimori, Y. Tokura, *Rev. Mod. Phys.* **70**, 1039–1263 (1998).
2. B. Keimer, S. A. Kivelson, M. R. Norman, S. Uchida, J. Zaanen, *Nature* **518**, 179–186 (2015).
3. H. Y. Hwang *et al.*, *Nat. Mater.* **11**, 103–113 (2012).
4. L. Gao *et al.*, *Phys. Rev. B* **50**, 4260–4263 (1994).
5. J. P. Locquet *et al.*, *Nature* **394**, 453–456 (1998).
6. I. Bozovic, G. Logvenov, I. Belca, B. Narimbetov, I. Sveklo, *Phys. Rev. Lett.* **89**, 107001 (2002).
7. C. W. Hicks *et al.*, *Science* **344**, 283–285 (2014).
8. H.-H. Kim *et al.*, *Science* **362**, 1040–1044 (2018).
9. A. Jayaraman, *Rev. Mod. Phys.* **55**, 65–108 (1983).
10. D. G. Schlom *et al.*, *MRS Bull.* **39**, 118–130 (2014).
11. Q. Gan, R. A. Rao, C. B. Eom, J. L. Garrett, M. Lee, *Appl. Phys. Lett.* **72**, 978–980 (1998).
12. C. Thiele, K. Dörr, O. Bilani, J. Rödel, L. Schultz, *Phys. Rev. B* **75**, 054408 (2007).
13. U. Aschauer, R. Pfenninger, S. M. Selbach, T. Grande, N. A. Spaldin, *Phys. Rev. B* **88**, 054111 (2013).
14. D. Lu *et al.*, *Nat. Mater.* **15**, 1255–1260 (2016).
15. M. D. Uchic, D. M. Dimiduk, J. N. Florando, W. D. Nix, *Science* **305**, 986–989 (2004).
16. A. Banerjee *et al.*, *Science* **360**, 300–302 (2018).
17. Y. Tokura, *Rep. Prog. Phys.* **69**, 797–851 (2006).
18. A. K. Prodjosantoso, B. J. Kennedy, B. A. Hunter, *Aust. J. Chem.* **53**, 195–202 (2000).
19. P. Singh *et al.*, *ACS Appl. Electron. Mater.* **1**, 1269–1274 (2019).
20. S. S. Hong *et al.*, *Sci. Adv.* **3**, eaao5173 (2017).
21. See supplementary materials.
22. Z. Liu *et al.*, *Nat. Commun.* **5**, 5246 (2014).
23. C. Adamo *et al.*, *Appl. Phys. Lett.* **95**, 112504 (2009).
24. H. Y. Hwang, T. T. M. Palstra, S.-W. Cheong, B. Batlogg, *Phys. Rev. B* **52**, 15046–15049 (1995).
25. Y. Tomioka, A. Asamitsu, H. Kuwahara, Y. Moritomo, Y. Tokura, *Phys. Rev. B* **53**, R1689–R1692 (1996).
26. J. Zhang *et al.*, *Nat. Mater.* **15**, 956–960 (2016).
27. S. Mori, C. H. Chen, S. W. Cheong, *Nature* **392**, 473–476 (1998).
28. T. Hotta, A. Feiguin, E. Dagotto, *Phys. Rev. Lett.* **86**, 4922–4925 (2001).
29. J. Klein *et al.*, *Phys. Rev. B* **66**, 052414 (2002).
30. M. Ziese, H. C. Semmelhack, K. H. Han, *Phys. Rev. B* **68**, 134444 (2003).
31. F. Rivadulla, M. A. López-Quintela, J. Mira, J. Rivas, *Phys. Rev. B* **64**, 052403 (2001).
32. K. S. Novoselov, A. Mishchenko, A. Carvalho, A. H. Castro Neto, *Science* **353**, aac9439 (2016).
33. J. A. Rogers, M. G. Lagally, R. G. Nuzzo, *Nature* **477**, 45–53 (2011).
34. Data and computational codes are available at Zenodo (doi:10.5281/zenodo.3653340).
35. Computational codes are available at Zenodo (doi:10.5281/zenodo.3647659).
36. Computational codes are available at Zenodo (doi:10.5281/zenodo.3648630).

ACKNOWLEDGMENTS

We thank A. P. Mackenzie, A. Millis, and A. Pasupathy for helpful discussions. **Funding:** Supported by the U.S. Department of Energy, Office of Basic Energy Sciences (DOE-BES), Division of Materials Sciences and Engineering, under contract DE-AC02-76SF00515 (synthesis and measurements) and the Gordon and Betty Moore Foundation's Emergent Phenomena in Quantum Systems Initiative through grant GBMF4415 (development

of strain platform). Also supported by the Air Force Office of Scientific Research (AFOSR) Hybrid Materials MURI under award FA9550-18-1-0480 (V.H.); DOE grant DE-SC0012375 (M.G.); Army Research Office (ARO) grant W911NF-15-1-0017 (J.M.R.); and the German Science Foundation (DFG) within CRC TRR80 (project G03 and G08) (M.V. and R.P.). Calculations were performed using the Extreme Science and Engineering Discovery Environment (XSEDE), which is supported by NSF grant ACI-1548562 and the CARBON Cluster at Argonne National Laboratory (DOE-BES, contract DE-AC02-06CH11357), and the MagnitUDE supercomputer at the University of Duisburg-Essen (DFG grants INST 20876/209-1 FUGG, INST20876/243-1 FUGG). Part of this work was performed at the Stanford Nano Shared Facilities (SNSF), supported by NSF award ECCS-1542152. **Author contributions:** S.S.H., Y.H., and H.Y.H. designed the experiment. S.S.H., B.Y.W., and D.L. synthesized materials and fabricated the devices. S.S.H. and A.V. carried out GIXRD measurements. V.H. and S.S.H. carried out mechanical and electrical simulations. M.G., M.V., R.P., and J.M.R. performed the DFT calculations and analysis of the electronic structure. S.S.H. wrote the paper with input from all co-authors. **Competing interests:** The authors declare no competing interests. **Data and materials availability:** All data presented in this paper and a finite-element calculation code are deposited at Zenodo (*34*). Atomic structure models used for the electronic structure calculations are available at Github and Zenodo (*35*, *36*); additional output files are available upon request. The Vienna Ab Initio Simulation Package (VASP) is proprietary software available for purchase at www.vasp.at/.

SUPPLEMENTARY MATERIALS

science.sciencemag.org/content/368/6486/71/suppl/DC1
Materials and Methods
Supplementary Text
Figs. S1 to S11
References (*37*–*44*)

8 May 2019; accepted 9 March 2020
10.1126/science.aax9753

ICE SHEETS

A slip law for glaciers on deformable beds

Lucas K. Zoet[1,2]* and Neal R. Iverson[2]

Slip of marine-terminating ice streams over beds of deformable till is responsible for most of the contribution of the West Antarctic Ice Sheet to sea level rise. Flow models of the ice sheet and till-bedded glaciers elsewhere require a law that relates slip resistance, slip velocity, and water pressure at the bed. We present results of experiments in which pressurized ice at its melting temperature is slid over a water-saturated till bed. Steady-state slip resistance increases with slip velocity owing to sliding of ice across the bed, but above a threshold velocity, till shears at its rate-independent Coulomb strength. These results motivate a generalized slip law for glacier-flow models that combines processes of hard-bedded sliding and bed deformation.

The potential collapse of the West Antarctic Ice Sheet is the single largest source of uncertainty in estimations of future sea level rise (*1*, *2*), and this uncertainty results, in part, from imperfectly modeled ice sheet processes (*3*–*5*). Among these processes is the rapid slip of marine-terminating ice streams over their beds, which transfers most of the ice sheet's discharge to the ocean (*6*). This rapid slip usually occurs where ice at its pressure-melting temperature rests on unlithified, water-saturated till—a mixture of mud, sand, and larger particles that can shear beneath the ice if it is weakened sufficiently by high pore-water pressure (*7*). Therefore, it is of central importance in glacier-flow models to accurately relate slip resistance to slip velocity and water pressure where ice rests on deformable till (i.e., soft bed) (*3*–*5*)—a condition met not only in West Antarctica but beneath many fast-flowing, marine-terminating glaciers elsewhere that contribute substantially to sea level rise (*8*).

The slip relation most widely applied in glacier-flow models is derived from considering ice resting on an irregular rock surface (i.e., hard bed). In this scenario, movement of ice past rock bumps by regelation and by creeping flow causes slip resistance to increase with slip velocity—the equivalent of viscous drag at the bed (*9*). Although viscous drag is usually assumed in glacier-flow models even where glaciers rest on deformable till, this is at odds with experiments with till that indicate its shear resistance is either independent of its deformation rate or highly insensitive to it (*10*). This observation, together with till shear resistance that increases linearly with effective stress (total-bed normal stress less pore-water pressure), has helped motivate use of Coulomb slip laws in some glacier-flow models (*11*, *12*). In modeling studies in which effects of both viscous and Coulomb slip laws are compared, ice-loss and sea level–rise projections are acutely sensitive to the form of the slip law, with viscous and Coulomb relations yielding distinct glacier responses (*3*–*5*).

This study is motivated by the hypothesis that physical processes at the interface between ice and deformable till contribute to the form of the slip relation, such that experiments with ice on hard beds or with till alone provide an incomplete description of slip behavior on soft beds. We present results of the first experiments that address coupled ice-bed mechanics where ice, under pressure and at its melting temperature, moves steadily over water-saturated till. These results provide a slip relation for soft-bedded glaciers that merges processes of hard-bedded sliding and till deformation.

Experiments are conducted with a ring-shear device designed to study glacier slip over hard (*13*) or soft (*14*) beds. This device rotates a horizontal ring of ice (0.9 m in outside diameter, 0.2 m wide, and ~0.2 m thick) at a steady velocity and under a prescribed effective stress of the order expected in natural glaciers across a till bed, while the resultant shear stress is measured (fig. S1). The ice is kept at its pressure-melting temperature by dilute ethylene glycol, regulated to 0.01°C, which circulates around the chamber that holds the ice. Calibrated thermistors measure ice temperature to the nearest 0.01°C. The bed is a 60-mm-thick layer of water-saturated, sandy till. Vertical columns of beads positioned within the till and ice allow the vertical distribution of horizontal displacement in both materials to be measured at the ends of experiments. In one kind of experiment, all grains larger than one-tenth of the till thickness (>6 mm) are removed from the till. In a second kind of experiment, designed to increase bed surface roughness, 11 isolated oblate clasts (axial lengths of ca. 40 mm by 30 mm by 30 mm) are embedded partway in the till surface (see supplementary materials for more methodological details).

Most shear deformation of the till occurs in a zone close to the ice-bed interface. Bead columns indicate that deformation in experiments without clasts occurs only in a narrow zone (7.5 mm) immediately adjacent to the sole of the ice ring (Fig. 1). Approximately

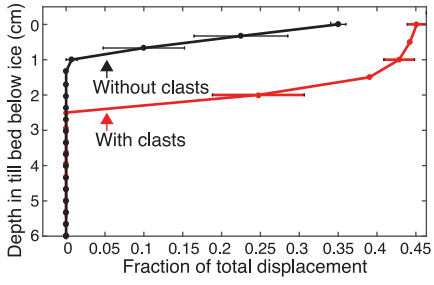

Fig. 1. Till deformation. Horizontal displacement of beads inserted in initially vertical columns in the till bed from the experiments without (black) and with clasts (red) at the bed surface. Error bars indicate ±1 standard deviation of measurements from four bead columns.

[1]Department of Geoscience, University of Wisconsin–Madison, Madison, WI 53706, USA. [2]Department of Geological and Atmospheric Sciences, Iowa State University, Ames, IA 50011, USA.
*Corresponding author. Email: lzoet@wisc.edu

35% of ice motion is caused by till deformation, whereas markers in the ice reveal no discernible strain in the nonboundary ice, indicating that ~65% of total motion results from slip at the ice-till interface. Till deformation in the experiment with clasts results in a concave-up deformation profile and is deeper, extending to a depth of ~25 mm (Fig. 1). Again, no discernible strain is observed in the nonboundary ice, indicating that ~45% of the total motion is accommodated by till deformation and ~55% results from slip at the ice-till interface (Fig. 1). The deformed bed thicknesses are ~125 and ~85% of the maximum grain diameter in the experiments without and with clasts, respectively. When clasts are present, ~25% of their radius protrudes above the interface, and they produce prow-like ridges at their downstream edges, indicating that clasts were dragged by the sliding ice through the yielding till surface (so-called plowing; see fig. S2).

In both types of experiments, steady-state resistance to slip increases with slip velocity (rate strengthening) until a transition speed, u_t, at which the shear stress equals the Coulomb shear strength of the till, the stress at which it deforms permanently, as measured independently in tests with a direct-shear device (*14*). Thus, at higher slip velocities, shear stress is limited by the shear strength of the till, and shear stress is independent of slip velocity. The value of u_t is lower with clasts at the bed surface (Fig. 2).

The motion at the ice-till interface and shear of till near the bed surface, together with the rate-strengthening and Coulomb drag responses, indicate that processes of both sliding and till deformation are needed to describe slip on a soft bed. This observation agrees with most measurements beneath modern glaciers, which indicate that basal motion occurs primarily at the surfaces of till beds or by till shear to only shallow depths (*7*). Thus, to develop accurate slip laws for ice streams and other glaciers on till beds, both types of movement must be considered.

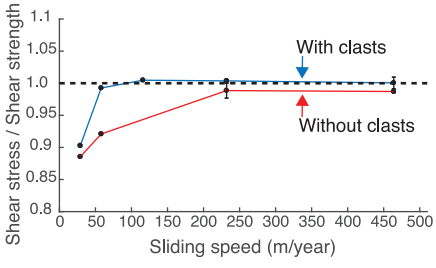

Fig. 2. Slip resistance. Steady-state shear stress supported by the till bed divided by its Coulomb shear strength for the two kinds of experiments. Slip velocity is abruptly increased, and, subsequently, the shear stress requires hours to days to attain a steady-state condition when stress fluctuates around a mean value that remains approximately steady with time. The stress values reported are the mean values, and the error bars indicate ±1 standard deviation of the fluctuations.

Our results indicate that the transition to bed deformation occurs if the drag from ice flow exerted on particles at the bed surface causes them to plow, mobilizing the bed at its failure strength (Fig. 2). At slip velocities below u_t, ice viscously deforms and regelates around static particles at the bed surface, giving rise to a rate-strengthening slip relation. At slip velocities above u_t, these processes cause sufficient drag on large particles—those closest to the controlling obstacle size of sliding theory (*9*)—to cause them to plow at a stress limited by the till's Coulomb strength, thereby shearing the bed. This hypothesis is supported by plowing structures at the ice-bed interface, deformation depths that are comparable to the largest particle diameters at the bed surface, and the dependence of u_t on the largest particle sizes at the bed surface. Smaller particles require higher slip velocities to cause drag sufficient to deform the bed by plowing (Fig. 2).

We propose a traditional rate-strengthening sliding rule [i.e., (*9*)] for slip velocities below u_t and, for higher slip velocities, Coulomb resistance similar to that measured in deformation experiments with till alone (*10*). A form of slip law that describes both processes and corresponds to our experimental observations is

$$\tau_b = \min[N\tan(\phi), (Cu_b)^{1/m}] \qquad (1)$$

where N is the effective stress; ϕ is the friction angle of the till, such that tan ϕ is a friction coefficient; u_b is the slip velocity; m is a sliding exponent; and C is a constant that depends on u_t and the bed roughness, as controlled by the sizes of particles at the bed surface. The magnitude of C can be estimated from the velocity, u_t, at which plowing deforms the bed: $C = \frac{(N\tan(\phi))^m}{u_t}$. Equation 1 has the same form as sliding rules of some numerical models (*4*) but has a different physical basis, as u_t is here explicitly estimated from plowing mechanics and then used to parametrize C, unlike previous implementations that used a viscous slip law with an assumed C to estimate u_t. Low speeds and high effective stresses result in viscous Weertman-style sliding; high sliding speeds and low effective stresses—conditions commonly present at the bases of ice streams—promote shallow deformation of the bed at its Coulomb strength.

The value of u_t can be estimated independently. The shear stress needed to cause a partially buried clast to plow, τ_p, is independent of sliding velocity, whereas the stress that sliding ice exerts on a static clast, τ_c, increases with

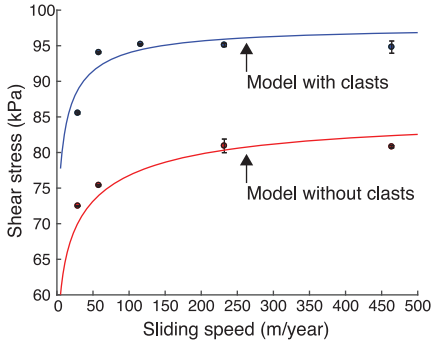

Fig. 3. Generalized model. Measured steady-state shear stresses compared with the approximate model of Eqs. 2 and 3, with R = 15 and 3 mm for till beds with and without clasts, respectively, at the bed surface. Wall drag was removed according to (*14*). Other parameter values for the model are listed in table S1.

sliding velocity. If $\tau_p = \tau_c$, plowing will occur. By modeling the upper surfaces of clasts partly buried in the bed as sinusoids, the transition speed, u_t, can be estimated by setting the shear stress exerted by sliding ice (*15*) equal to that required for clasts of radius R to plow (*16*)

$$u_t = \frac{\left(\frac{1}{\eta(Ra)^2 k_0^3} + \frac{4C_1}{(Ra)^2 k_0}\right)(N_F N)}{(2 + N_F k)} \qquad (2)$$

where η is the effective ice viscosity, $k_0 = \frac{2\pi}{4R}$, C_1 is a regelation parameter dependent on thermal properties of the ice and rock, a is the fraction of a clast radius that protrudes from the bed surface, N_F is a bearing-capacity factor for the till related to its strength, and k accounts for the till-strength reduction resulting from the ice-pressure shadow in the lee of clasts (see supplementary materials). With an estimate of u_t from Eq. 2, τ_b of Eq. 1 can be estimated for different sliding speeds and clast sizes (fig. S3). For a single clast size, τ_b has a sharp inflection at u_t, at which the slip behavior changes. More realistically, when slip is considered over a range of clast sizes (e.g., R = 15 to 30 mm), clasts begin to plow over a range of velocity (40 to 80 m/year) (fig. S3), so the average value of τ_b transitions smoothly to Coulomb behavior (fig. S3).

The viscous and Coulomb behavior of Eq. 1 can be approximated with a sliding rule of the form

$$\tau_b = N\tan(\phi)\left(\frac{u_b}{u_b + u_t}\right)^{1/p} \qquad (3)$$

where p is the slip exponent. In experiments both with and without clasts at the bed surface, $p \sim 5$ (Fig. 3), indicating insensitivity of this parameter to the detailed geometry of

the bed surface. The form of this function approximates the Coulomb behavior expected at high slip velocity ($u_b > u_t$) and low effective pressure, which causes u_t in Eq. 2 to approach zero. This sliding relationship is not only consistent with our experimental results (Fig. 3) but, through Eq. 3, is based unambiguously on physical processes at the ice-bed interface and the properties of tills. Estimating the clast radius R for calculating u_t in Eq. 3 requires noting that plowing clasts larger than a threshold size will occupy a sufficient fraction of the bed surface to cause pervasive deformation of the bed at its Coulomb strength. This threshold value of R could thus be estimated from a till grain-size distribution and by noting that plowing clasts deform adjacent till across distances comparable to clast diameters (*17*). The form of Eq. 3 is similar to that estimated for sliding over a hard bed with cavity formation (*18*), so a slip law of this form may be generally applicable without knowledge of the bed type.

The proposed slip law agrees with some observations of glacier surface velocity and affects their interpretations. Surface velocities and numerical modeling of flow at Hofsjökull ice cap, Iceland, indicate that, at velocities below a few tens of meters per year, basal drag increases with velocity but that faster-moving ice obeys a Coulomb slip relation (*19*), in agreement with our observations. Observations of glaciers in Greenland (with velocities >1000 m/year), which indicate that basal drag is highly insensitive to velocity, also agree with our observations but were interpreted to reflect no effect of basal friction on glacier flow (*20*). For low effective pressures commonly observed beneath ice streams, the transition velocity will be low, causing the frictional, velocity-independent slip resistance that characterizes Coulomb behavior to dominate.

These results demonstrate that classical mechanisms of glacier sliding over rigid beds and till deformation mechanics collectively act to shape the basal-slip relation where glaciers rest on deformable sediment. By distilling these processes that are usually considered separately, Eqs. 2 and 3 provide a slip relation for sediment-floored parts of ice sheets and other glaciers that is empirically justifiable and grounded, with minimal parameterization, on relevant processes.

REFERENCES AND NOTES

1. J. Feldmann, A. Levermann, *Proc. Natl. Acad. Sci. U.S.A.* **112**, 14191–14196 (2015).
2. A. A. Robel, H. Seroussi, G. H. Roe, *Proc. Natl. Acad. Sci. U.S.A.* **116**, 14887–14892 (2019).
3. C. Ritz *et al.*, *Nature* **528**, 115–118 (2015).
4. V. C. Tsai, A. L. Stewart, A. F. Thompson, *J. Glaciol.* **61**, 205–215 (2015).
5. J. Brondex, O. Gagliardini, F. Gillet-Chaulet, G. Durand, *J. Glaciol.* **63**, 854–866 (2017).
6. E. Rignot, J. Mouginot, B. Scheuchl, *Science* **333**, 1427–1430 (2011).
7. K. Cuffey, W. S. B. Paterson, *The Physics of Glaciers* (Butterworth-Heinemann, ed. 4, 2010).
8. E. Berthier, E. Schiefer, G. K. C. Clarke, B. Menounos, F. Remy, *Nat. Geosci.* **3**, 92–95 (2010).
9. J. Weertman, *J. Glaciol.* **3**, 33–38 (1957).
10. N. R. Iverson, *J. Glaciol.* **56**, 1104–1114 (2010).
11. M. Bougamont, S. Price, P. Christoffersen, A. J. Payne, *J. Geophys. Res. Earth Surf.* **116**, F04018 (2011).
12. F. Pattyn, *Cryosphere* **11**, 1851–1878 (2017).
13. L. K. Zoet, N. R. Iverson, *J. Geophys. Res. Earth Surf.* **121**, 1206–1217 (2016).
14. L. K. Zoet, N. R. Iverson, *Geology* **46**, 807–810 (2018).
15. J. F. Nye, *Proc. R. Soc. London Ser. A* **311**, 445–467 (1969).
16. N. R. Iverson, *J. Glaciol.* **45**, 41–53 (1999).
17. J. F. Thomason, N. R. Iverson, *J. Glaciol.* **54**, 169–181 (2008).
18. C. Schoof, *Proc. R. Soc. London Ser. A* **461**, 609–627 (2005).
19. B. Minchew *et al.*, *J. Glaciol.* **62**, 147–158 (2016).
20. L. A. Stearns, C. J. van der Veen, *Science* **361**, 273–277 (2018).

ACKNOWLEDGMENTS

Funding: Construction and use of the device for the ice-till experiments were made possible by the U.S. National Science Foundation (grants OPP-0618747 and EAR-1023586 to N.R.I.). **Author contributions:** L.K.Z. ran the experiments and analyzed the data, L.K.Z. and N.R.I. wrote the paper, and N.R.I. built the apparatus. **Competing interests:** The authors have no competing interests. **Data and materials availability:** The data from these experiments are archived at the University of Wisconsin–Madison and can be obtained at https://uwmadison.box.com/s/a3t60exvoeoo5378aab88y8ohp44gsra.

SUPPLEMENTARY MATERIALS

science.sciencemag.org/content/368/6486/76/suppl/DC1
Materials and Methods
Figs. S1 to S3
Table S1
References (*21*–*25*)

14 August 2019; accepted 12 February 2020
10.1126/science.aaz1183

PROTEIN DESIGN

De novo design of protein logic gates

Zibo Chen[1,2]*, Ryan D. Kibler[1,2]†, Andrew Hunt[3]†, Florian Busch[4,5]†, Jocelynn Pearl[6]†‡, Mengxuan Jia[4,5], Zachary L. VanAernum[4,5], Basile I. M. Wicky[1,2], Galen Dods[7], Hanna Liao[6]‡, Matthew S. Wilken[6], Christie Ciarlo[6], Shon Green[6], Hana El-Samad[7,8], John Stamatoyannopoulos[6,9,10], Vicki H. Wysocki[4,5], Michael C. Jewett[3,11,12], Scott E. Boyken[1,2]‡, David Baker[1,2,13]§

The design of modular protein logic for regulating protein function at the posttranscriptional level is a challenge for synthetic biology. Here, we describe the design of two-input AND, OR, NAND, NOR, XNOR, and NOT gates built from de novo–designed proteins. These gates regulate the association of arbitrary protein units ranging from split enzymes to transcriptional machinery in vitro, in yeast and in primary human T cells, where they control the expression of the *TIM3* gene related to T cell exhaustion. Designed binding interaction cooperativity, confirmed by native mass spectrometry, makes the gates largely insensitive to stoichiometric imbalances in the inputs, and the modularity of the approach enables ready extension to three-input OR, AND, and disjunctive normal form gates. The modularity and cooperativity of the control elements, coupled with the ability to de novo design an essentially unlimited number of protein components, should enable the design of sophisticated posttranslational control logic over a wide range of biological functions.

Protein-protein interactions are ubiquitous in cellular decision-making and controlling them will be increasingly important in synthetic biology (*1*–*4*). Although protein interactions are central to natural biological circuits, efforts to create new logic circuits have focused on control at the level of DNA (*5*, *6*), transcription (*7*–*18*), or RNA (*13*, *19*–*22*). Recently, protein-based circuits have been generated by rewiring native signaling pathways (*23*–*28*), bringing proteins together with coiled coils (*29*), or creating protease cascades (*30*, *31*); however, these circuits were constructed from a limited pool of building blocks, which hinders their scalability. The ability to de novo design protein-based logic gates modulating arbitrary protein-protein interactions could open the door to new protein-based control systems in and out of cells.

In principle, it should be possible to design a wide range of logic gates de novo using a set of heterodimeric molecules. For example, given

[1]Department of Biochemistry, University of Washington, Seattle, WA 98195, USA. [2]Institute for Protein Design, University of Washington, Seattle, WA 98195, USA. [3]Department of Chemical and Biological Engineering, Northwestern University, Evanston, IL 60208, USA. [4]Department of Chemistry and Biochemistry, The Ohio State University, Columbus, OH 43210, USA. [5]Resource for Native Mass Spectrometry Guided Structural Biology, The Ohio State University, Columbus, OH 43210, USA. [6]Altius Institute for Biomedical Sciences, Seattle, WA 98195, USA. [7]Department of Biochemistry and Biophysics, University of California, San Francisco, San Francisco, CA 94158, USA. [8]Chan-Zuckerberg Biohub, San Francisco, CA 94158, USA. [9]Department of Genome Sciences, University of Washington, Seattle, WA 98195, USA. [10]Department of Medicine, Division of Oncology, University of Washington, Seattle, WA 98109, USA. [11]Chemistry of Life Processes Institute, Northwestern University, Evanston, IL 60208, USA. [12]Center for Synthetic Biology, Northwestern University, Evanston, IL 60208, USA. [13]Howard Hughes Medical Institute, University of Washington, Seattle, WA 98195, USA.
*Present address: Division of Biology and Biological Engineering, California Institute of Technology, Pasadena, CA 91125, USA. †These authors contributed equally to this work. ‡Present address: Lyell Immunopharma, Inc., Seattle, WA 98109, USA.
§Corresponding author. Email: dabaker@uw.edu

hypothetical heterodimer pairs ***A:A′***, ***B:B′***, and ***C:C′***, an AND gate modulating the association of ***A*** with ***C′*** can be constructed by genetically fusing ***A′*** and ***B***, and ***B′*** and ***C***: association occurs only in the presence of both ***A′-B***, and ***B′-C*** (here and below "***:***" denotes noncovalent interaction and "-" a genetic fusion through flexible linkers). Several building block properties are desirable for constructing such associative logic gates. First, there should be many mutually orthogonal heterodimeric pairs so that gate complexity is not limited by the number of individual elements. Second, the building blocks should be modular and similar in structure so that differences in building block shape and

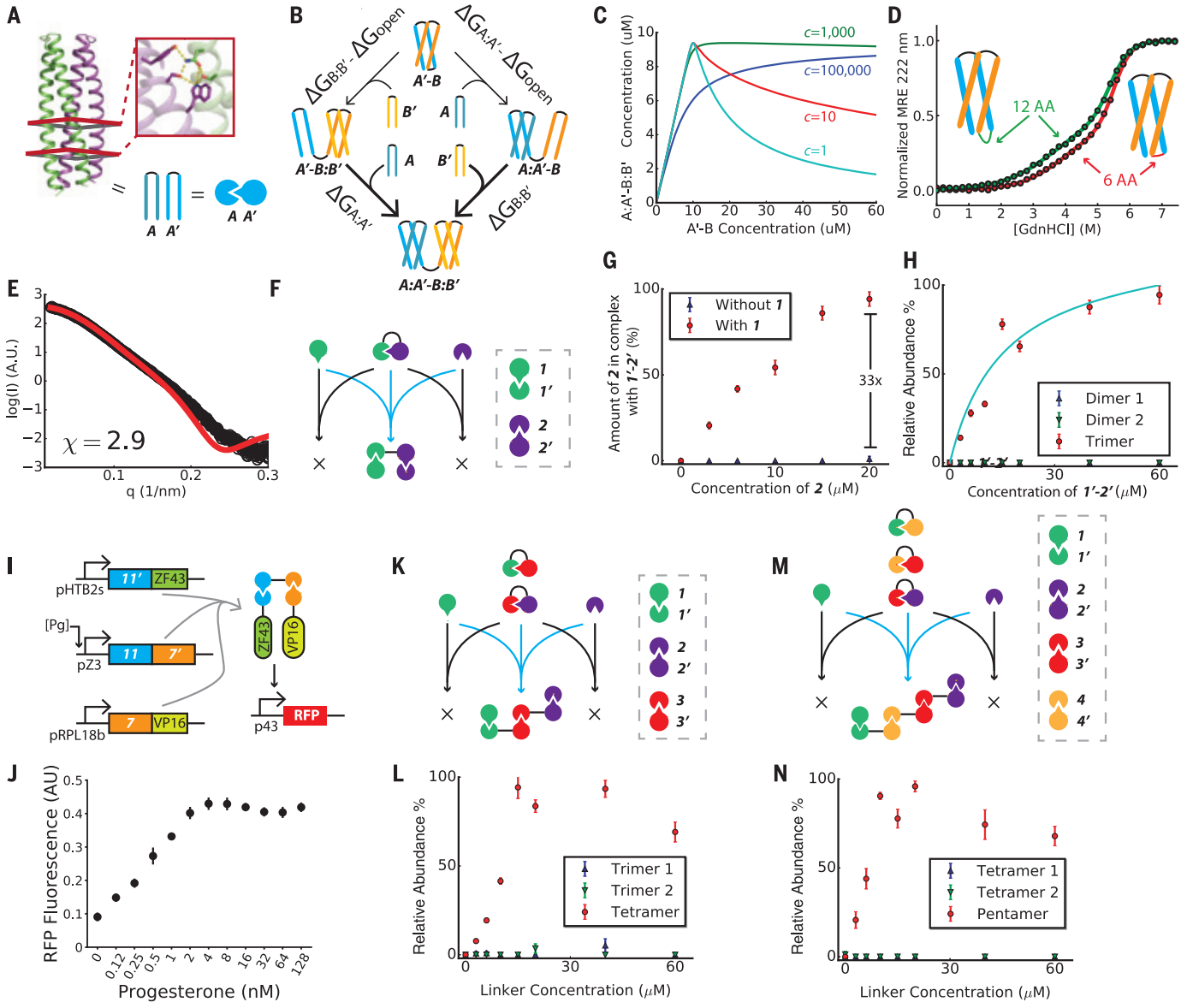

Fig. 1. Cooperativity of CIPHR logic gates. (**A**) Left: Backbone structure of ***A:A′*** heterodimer building block, with its hydrogen bond network shown in the inset. Bottom: Shorthand representations used throughout figures. (**B**) Thermodynamic cycle describing the induced dimerization system. (**C**) Simulation of the induced dimerization system under thermodynamic equilibrium. ***A*** and ***B′*** monomers were held constant at 10 μM each while titrating in various initial amounts of the ***A′-B*** dimerizer proteins. If binding is not cooperative (small *c*), then the final amount of trimeric complexes decreases when the dimerizer protein is in excess. (**D**) Equilibrium denaturation experiments monitored by CD for designs with 6- and 12-amino acid (AA) linkers. Circles represent experimental data, and lines are fits to the three-state unimolecular unfolding model. (**E**) Experimental SAXS profile of ***1′-2′*** with a six-residue linker (in black) fitted to the calculated profile of ***1:1′*** heterodimer (in red). (**F**) Schematic of induced dimerization system (with a six-residue linker); experimental results in (G) and (H). (**G**) nMS titration of ***2*** against 10 μM of ***1′-2′*** in the presence (red) or absence (blue) of 10 μM of ***1***. (**H**) nMS titration of ***1′-2′*** against 10 μM each of ***1*** and ***2***. Dimer 1 and 2 refer to partial dimeric complexes consisting of the dimerizer binding to either of the monomers. For comparison, the thermodynamic model result with *c* = 991,000 is shown in cyan. (**I**) Schematic of testing of the induced dimerization system in yeast, with in vivo results shown in (**J**). Pg, progesterone. (**K**) Two-input AND gate schematic, with nMS titration results shown in (**L**). Trimer 1 and 2 refer to partial trimeric complexes of the two dimerizer proteins binding to either one of the monomers. (**M**) A three-input AND gate, with nMS titration results shown in (**N**). Tetramer 1 and 2 refer to partial tetrameric complexes of the three dimerizer proteins binding to either one of the monomers. All error bars are standard deviations of *n* = 3 independent replicates.

other properties do not have to be considered when constructing the gates. Third, single building blocks should be able to bind to multiple partners with different and tunable affinities, allowing inputs to perform negation operations by disrupting preexisting lower-affinity interactions. Fourth, the interactions should be cooperative so that gate activation is not sensitive to stoichiometric imbalances in the inputs. In the above AND gate, for example, if the interactions are not cooperative, then a large excess of ***A′-B*** will pull the equilibrium toward partially assembled complexes (***A′-B*** with either ***A*** or ***B′-C*** but not both), which will limit gate activation.

Here, we explored the possibility of designing logic gates satisfying all four of the above criteria using de novo–designed protein heterodimers with hydrogen bond network–mediated specificity (*32*). Sets of mutually orthogonal designed heterodimers (DHDs, hereafter referred to by numbers, e.g., ***1*** and ***1′*** form one cognate pair; table S1) with hydrogen bond network–mediated specificity (e.g., see Fig. 1A, inset) are available for logic gate construction, satisfying condition 1 (orthogonality). The heterodimeric interfaces all share the same four helix bundle topology (Fig. 1A), satisfying condition 2 (modularity). The shared interaction interface allows a limited amount of cross-talk between pairs, leading to a hierarchy of binding affinities, satisfying condition 3 (multiple binding specificities). Inspired by cooperative systems in

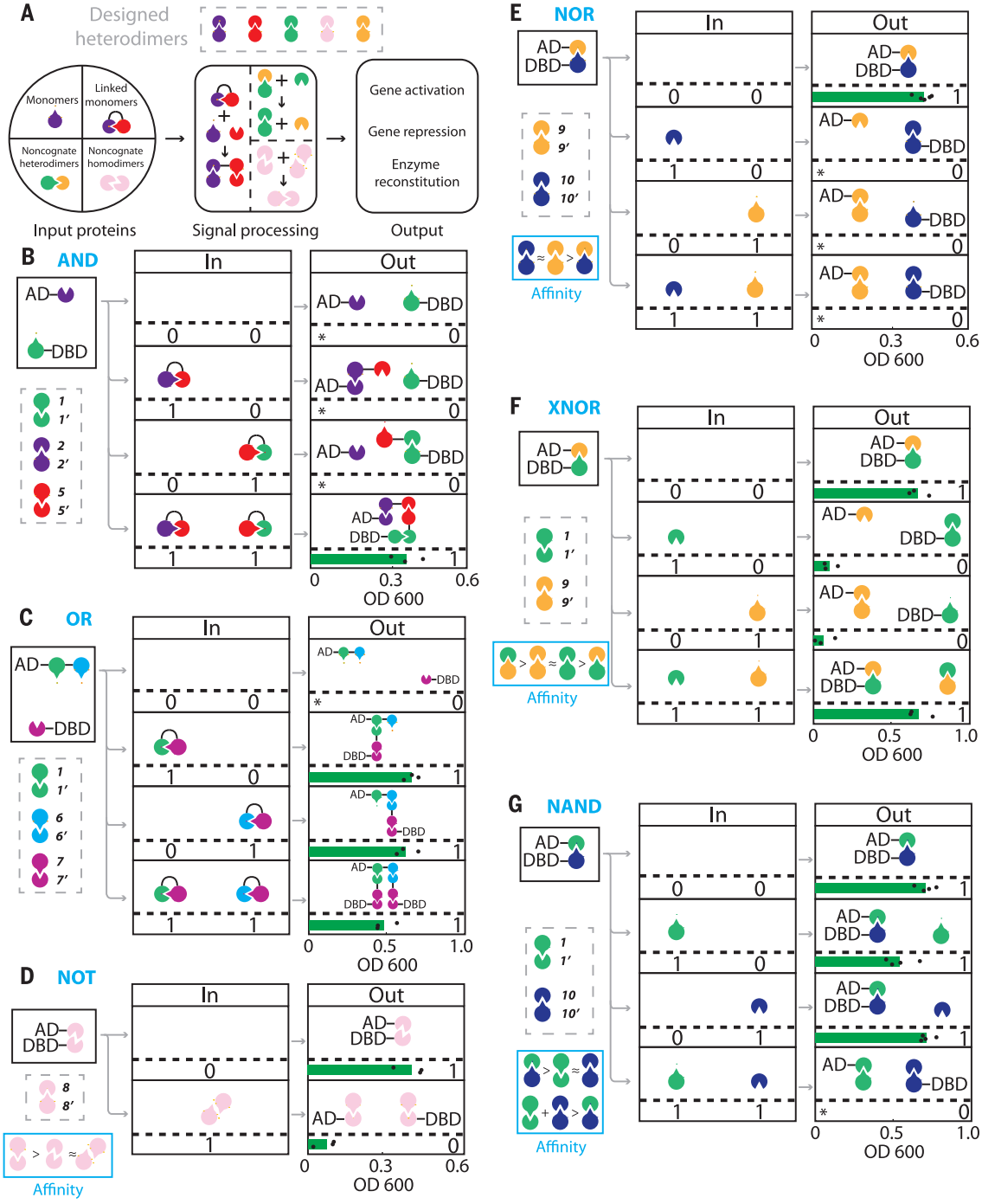

Fig. 2. CIPHR two-input logic gates. (**A**) CIPHR gates are built from DHDs (top) with monomers or covalently connected monomers as inputs (left); some gates use only the designed cognate interactions (left side of middle panel), whereas others take advantage of observed binding affinity hierarchies (right side of middle panel). (**B** and **C**) Two-input AND (B) and OR (C) CIPHR logic gates based on orthogonal DHD interactions. (**D** to **G**) NOT (D), NOR (E), XNOR (F), and NAND (G) CIPHR logic gates made from multispecific and competitive protein binding. For each gate, black dots represent individual Y2H growth measurement corrected over background growth, with their average values shown in green bars. Components in gray boxes indicate the DHD pairs used. Blue boxes indicate affinity gradients. *No yeast growth over background. "0" and "1" in the middle and right blocks represent different input states and expected outputs, respectively.

nature (*33*, *34*), we sought to achieve condition 4 (cooperativity) by constructing the monomer fusions (***A′-B*** and ***B′-C*** in the above example) in such a way that the interaction surfaces (with ***A*** and ***C***′) are buried within the fusions. The free energy required to expose these buried interfaces would oppose gate activation, and we reasoned that the system could be tuned so that the sum of the binding energies of the two partners, but not either one alone, would be sufficient to overcome this barrier, ensuring cooperative gate activation. If condition 2 (modularity) holds, then a single scheme for ensuring cooperativity could in principle work for a wide range of gate configurations.

To explore the design of cooperative building blocks, we focused on the simple system ***A*** + ***A′-B*** + ***B′*** (we refer to this as induced dimerization below, ***A*** and ***B′*** as the monomers, and ***A′-B*** as the dimerizer). If binding is not cooperative, then the amount of the trimeric complex decreases when ***A′-B*** is in stoichiometric excess relative to ***A*** and ***B′***: the formation of intermediate dimeric species of the dimerizer binding to either of the monomers competes with formation of trimeric complexes. On the contrary, if binding is cooperative such that no binding to either monomer occurs in the absence of the other, then the amount of trimeric complex formed becomes insensitive to an excess of the dimerizer. A simple thermodynamic model of the effect of binding cooperativity on the stoichiometry dependence of such induced dimerization systems (Fig. 1B and see modeling section in the supplementary materials) shows that, as the binding cooperativity decreases, there is a corresponding decrease in the population of full trimeric complexes at high dimerizer concentrations (Fig. 1C).

We hypothesized that a folded four-helix bundle–like state of the ***A′-B*** dimerizer could oppose binding to either ***A*** or ***B′*** because the relatively hydrophobic interacting surfaces would likely be sequestered within the folded structure (fig. S1A). We tested different flexible linker lengths connecting ***A′*** with ***B*** using heterodimers ***1:1′*** and ***2:2′*** as a model system. At all linker lengths tested (between 0 and 24 residues), constructs were folded and stable in circular dichroism (CD) guanidine hydrochloride denaturation experiments, with unfolding free energies >13 kcal/mol (Fig. 1D, fig. S2, and table S3). Although ***1′-2′*** dimerizer constructs with short linkers of 0 and 2 residues, or with a very long 24-residue linker, could be purified as monomers (fig. S1B), they were prone to aggregation, perhaps due to domain swapping. By contrast, designs with 6 and 12 residue linkers remained largely monomeric (table S4). Small-angle x-ray scattering (SAXS) experiments (*35*) indicated that their hydrodynamic radii are close to those of folded four-helix bundle DHDs (Fig. 1E and table S2). Linkers in this length range likely allow the two monomers (***1′*** and ***2′***) to fold back on each other such that the largely hydrophobic interaction surfaces are buried against each other; such a structure would have to partially unfold for ***1′-2′*** to interact with either ***1*** or ***2***. The magnitude of the unfolding energy (ΔG_{open} in Fig. 1B) determines the extent of cooperativity for the gate. We selected linker lengths of 6, 10, or 12 residues for all of the following experiments.

We studied the cooperativity of the induced dimerizer system in vitro using native mass spectrometry (nMS, *36*, *37*), which can directly measure the populations of different oligomeric species in a sample (tables S5 to S8; for calibration curve, see fig. S3). We first measured the extent to which ***1*** activates the binding of ***2*** to ***1′-2′*** (Fig. 1F). ***1***, ***2***, and ***1′-2′*** were separately expressed in *Escherichia coli* and purified. At 10 μM of ***1′-2′*** and 20 μM of 2, we observed a 33 fold increase in binding between ***2*** and ***1′-2′*** upon addition of 10 μM of ***1*** (Fig. 1G), a fold increase comparable to naturally occurring allosteric systems (*33*). To assess the sensitivity

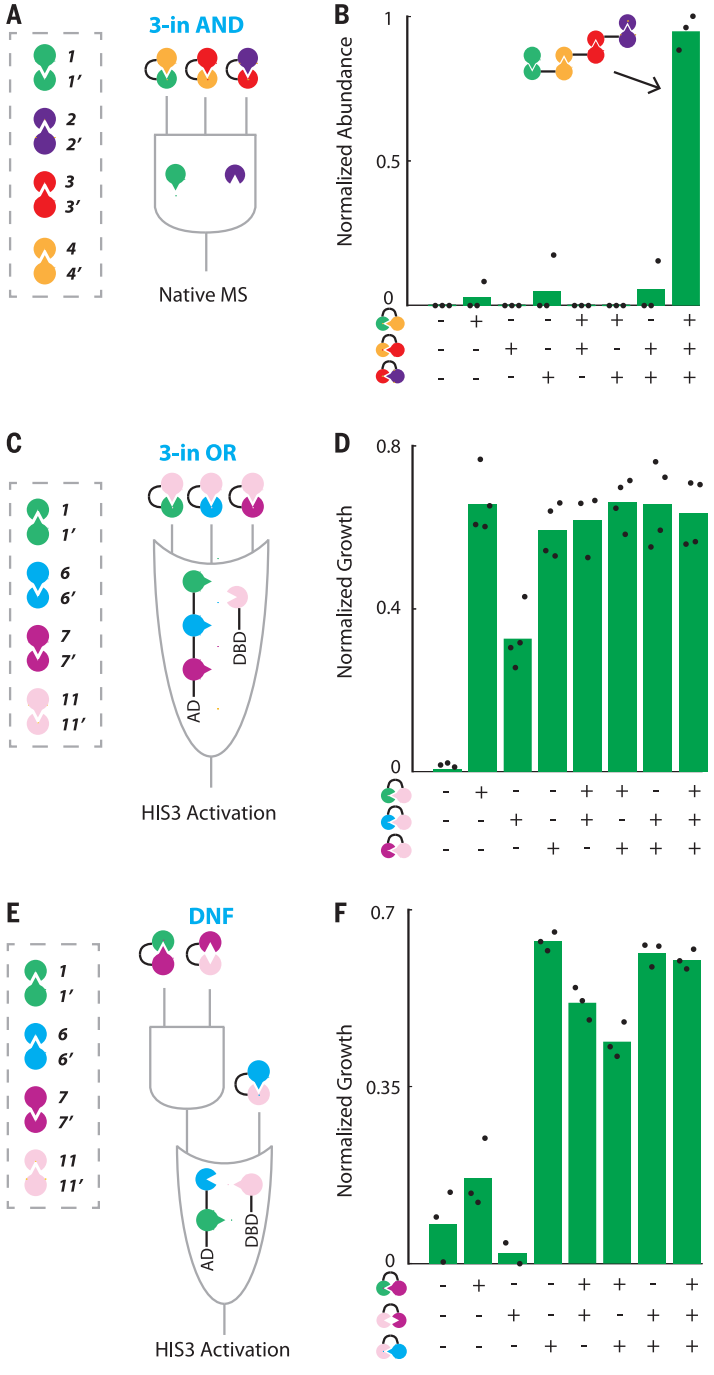

Fig. 3. Three-input CIPHR logic gates. (**A**) Schematic of a three-input AND gate. (**B**) nMS results indicating proper activation of the three-input AND gate only in the presence of all three inputs. (**C**) Schematic of a three-input OR gate. (**D**) Y2H results confirming activation of the three-input OR gate with any of the inputs. (**E**) Schematic of a DNF gate. (**F**) Y2H results confirming proper activation of the gate. For each gate, black dots represent individual measurements with their average values shown in green bars. For Y2H-based measurements [(D) and (F)], the growth measurements are corrected over background growth. Components in gray boxes indicate the DHD pairs used.

of binding to stoichiometric imbalance, 10 μM ***1*** and ***2*** were titrated with increasing concentrations of ***1′-2′*** (Fig. 1H) and the species formed were determined by nMS. The heterotrimeric ***1:1′-2′:2*** complex was observed over a wide range of ***1′-2′*** concentrations (Fig. 1H). Even in the presence of a 6-fold excess of ***1′-2′***, there was no decrease in the amount of ***1:1′-2′:2*** formed, and neither ***1:1′-2′*** nor ***1′-2′:2*** was detected (Fig. 1H). We define a cooperativity parameter c as the ratio of the affinities in the presence and absence of the other monomer, which in our model directly relates to the free energy of opening of the dimerizer ($c = e^{\Delta G_{open}/RT}$; see supplementary materials). The estimated c value from fits of the thermodynamic model to nMS data (Fig. 1H, cyan line) is 991,000 ± 21 (for reference, the c value of the naturally occurring N-Wasp system is 350 but system differences complicate quantitative comparisons). This value of c corresponds to ΔG_{open} of 8.2 kcal/mol, which is about half the measured unfolding free energy of ***1′-2′*** (table S3), suggesting that binding may not require complete unfolding of the four-helix bundle state of the dimerizer.

To investigate the cooperativity of the induced dimerizer system in living cells, we used a two-hybrid–like assay in yeast. ***11′*** was fused to the DNA-binding domain ZF43 (*14*), ***7*** to the transactivation domain VP16, and the dimerizer ***11-7′*** was placed under the control of a progesterone-responsive element. Association of the DNA-binding and activation domains results in transcription of red fluorescent protein (RFP) (Fig. 1I). Treating cells with increasing amount of progesterone resulted in up to a 4.5-fold increase in RFP signal, with only a small drop at saturating progesterone concentrations (Fig. 1J). On the basis of calibration curves, under these conditions, ***11-7′*** is expected to be in >5-fold molar excess over ***11′*** and ***7*** (fig. S4), suggesting that ***11-7′*** binds cooperatively to ***11′*** and ***7*** in cells. Thus, the cooperativity of the dimerizer system makes it robust to fluctuating component stoichiometries in cells.

With dimerizers displaying cooperative binding, we reasoned that the lack of dependence on stoichiometric excesses of one of the components should extend to more complex gates. Using nMS, we investigated the cooperativity of a two-input AND gate constructed with the two dimerizers ***1′-3′*** and ***3-2′*** as inputs and monomers ***1*** and ***2*** brought together by the two inputs (Fig. 1K). As the concentration of the 2 inputs increased, the amount of heterotetrameric complex plateaued at a stoichiometry of

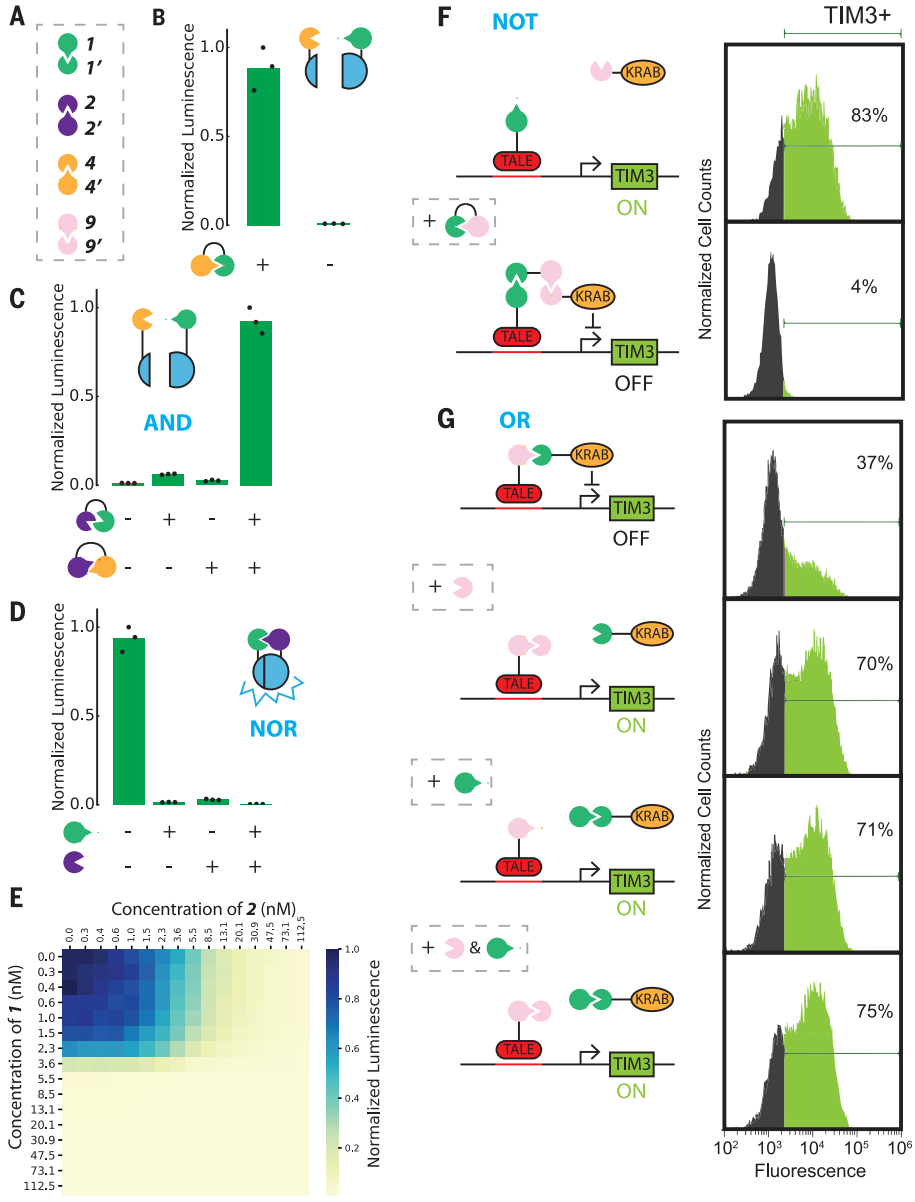

Fig. 4. Transferability of CIPHR logic gates. (**A**) Four pairs of DHDs were modularly combined to construct CIPHR logic gates that can be used to control different functions: catalytic activity of split luciferase (**B** to **E**) and gene expression in primary human T cells (**F** and **G**). (B) the induced dimerization system, (C) AND gate, and (D) NOR gate coupled to NanoBiT split luciferase system, tested by in vitro translation and monitoring luminescence. (E) In vitro titration of the two inputs of the NOR gate in D while keeping ***1′***-smBiT and ***2′***-lgBiT fixed at 5 nM. NOT gate (F) and OR gate (G) using a split TALE-KRAB repression system to control expression of TIM3 proteins in primary human T cells, tested by flow cytometry.

2:1, and then largely remained constant with a small drop at molar ratio of 6:1. Only very small amounts of partial complexes (heterotrimers and heterodimers) were observed, further indicating high cooperativity (Fig. 1L). We constructed a three-input AND gate from ***1′-4′***, ***4-3′***, and ***3-2′***, which together control the association of ***1*** and ***2*** (Fig. 1M). Similar to the two-input AND gate, the abundance of full, pentameric complexes only decreased slightly at greater than stoichiometric concentrations of inputs with no detectable competing tetrameric complexes (Fig. 1N).

We explored the modular combination of DHDs (table S1) to generate a range of two-input cooperatively inducible protein heterodimer (CIPHR) logic gates. Monomers from individual DHDs were linked to effector proteins of interest by genetic fusion such that the inputs (linked heterodimer subunits) control colocalization or dissociation of the effector proteins. Taking advantage of previously measured all-by-all specificity matrices for the DHDs (*32*), we explored constructing gates from two interaction modalities: cognate binding between designed protein pairs and competitive binding involving multispecific interactions (Fig. 2A).

We began by constructing AND and OR gates, reading out gate function using a yeast-two-hybrid (Y2H) setup similar to previously described yeast-four-hybrid systems (*38*, *39*). To construct an AND gate, we fused ***2*** to the Gal4 activation domain (AD) and ***1*** to the Gal4 DNA-binding domain (DBD). In this scheme, the colocalization of AD and DBD, and the resulting transcriptional activation of the *His3* gene, should require the expression of both input proteins (***1′-5***, ***5′-2′***). Indeed, growth in medium lacking histidine required expression of both inputs (Fig. 2B). An OR gate was similarly constructed by linking the ***1-6*** fusion to the AD and ***7′*** to the DBD. Expression of either of the inputs, ***1′-7*** or ***6′-7***, resulted in growth by driving association of AD with DBD (Fig. 2C).

We explored the construction of additional Boolean logic gates by exploiting binding affinity hierarchies identified in all-by-all Y2H experiments (*32*). ***8*** alone formed a homodimer, but in the presence of ***8′*** it dissociated to form the ***8:8′*** heterodimer (fig. S5A). We constructed a NOT gate by fusing ***8*** to both AD and DBD; the ***8:8*** homodimer supported yeast growth but in the presence of coexpressed ***8′*** input protein, the interaction was broken and growth was slowed (Fig. 2D). On the basis of the affinity hierarchy ***9:9′*** ≈ ***10:10′*** > ***9:10′*** (fig. S5B), we constructed a NOR gate in which ***9*** was fused to the AD and ***10′*** to the DBD, with ***9′*** and ***10*** as the two inputs. Either or both inputs outcompeted the ***9:10′*** interaction and hindered yeast growth (Fig. 2E). On the basis of the affinity hierarchy ***9′:1′*** > ***9:9′*** ≈ ***1:1′*** > ***9:1*** (fig. S5B), an XNOR gate was constructed by fusing ***9*** to AD, ***1*** to DBD, and using ***9′*** and ***1′*** as the two inputs: the presence of either outcompeted the ***9:1*** binding and blocked growth, but when both were expressed they instead interacted with each other and growth was observed (Fig. 2F). Similarly, a NAND gate was designed based on the interaction hierarchy ***1′:10′*** > ***1:1′*** ≈ ***10:10′*** (fig. S5B). Neither ***1*** nor ***10*** alone could outcompete the ***1′:10′*** interaction and hence growth occured, but when both were expressed, the free energy of formation of both ***1:1′*** and ***10:10′*** outweighed that of ***1′:10′*** and growth was blocked (Fig. 2G).

We next investigated three-input CIPHR logic gates. We first used nMS to characterize a three-input AND gate (Fig. 1M) in which monomers ***1*** and ***2*** are brought into proximity by the three inputs ***1′-4′***, ***4-3′***, and ***3-2′***. We experimentally tested all eight possible input combinations (Fig. 3A) with both ***1*** and ***2*** present, quantifying all complexes using nMS. Consistent with three-input AND gate function, ***1*** and ***2*** only showed significant coassembly when all three inputs were present (Fig. 3B).

To test three-input CIPHR gate function in cells, we designed two additional gates using the same four pairs of DHDs and tested them by Y2H. To make a three-input OR gate, ***1′-6-7*** was fused to AD and ***11′*** to DBD. Any one of the three inputs (***11-1***, ***11-6′***, or ***11-7′***) connects the AD to the DBD through ***1′***, ***6***, or ***7***, respectively (Fig. 3C). Y2H results confirmed the expected behavior of this logic gate in cells: any of the input proteins induced cell growth (Fig. 3D). We additionally constructed a CIPHR-disjunctive normal form [DNF (***A*** AND ***B***) OR ***C***] gate by fusing ***1′-6*** to AD and ***11′*** to DBD with inputs ***11-7′***, ***7-1***, or ***11-6′*** (Fig. 3E). In Y2H experiments, the DNF gate functioned as designed, with low yeast growth levels when no input or only one of the ***11-7′*** and ***7-1*** input proteins was present and high yeast growth levels otherwise (Fig. 3F).

To test the transferability of CIPHR logic gates, we explored the ability of CIPHR logic gates to reconstitute split enzyme activity by controlling the association of the two halves of the NanoBiT split luciferase system (*40*–*42*). Monomers from ***1:1′***, ***2:2′***, ***4:4′***, and ***9:9′*** (Fig. 4A) were fused in pairs to the two split domains (smBiT and lgBiT) and produced by in vitro transcription and translation, which facilitated a rapid testing cycle enabling the full 4×4 interaction affinity hierarchy to be determined by monitoring luciferase activity after mixing (fig. S6A). On the basis of this hierarchy, we constructed and experimentally verified an induced dimerization circuit with ***4***-smBiT, ***1***-lgBiT, and ***1′-4′*** as the input (Fig. 4B and fig. S6, C and D); characterization of the time dependence of the response revealed a 7-fold increase in signal 5 min after adding inputs (fig. S6D). We also constructed an AND gate with ***4***-smBiT, ***1***-lgBiT, and ***1′-2*** and ***2′-4′*** as the inputs (Fig. 4C) and a NOR gate with ***1′***-smBiT, ***2′***-lgBiT, and ***1*** and ***2*** as the inputs (Fig. 4D), both of which had the designed dependence of gate function (i.e., luciferase activity) on the inputs. We investigated the response of the NOR gate to varying concentrations of the inputs against the NanoBiT components held at 5 nM and found a sharp drop in signal around 5 nM for both inputs, consistent with NOR logic (Fig. 4E and fig. S6E).

Engineered T cell therapies are promising therapeutic modalities (*43*–*45*) but their efficacy for treating solid tumors is limited at least in part by T cell exhaustion (*46*, *47*). Immune checkpoint genes including *TIM3* are believed to play critical roles in modulating T cell exhaustion (*48*–*50*). To put the transcription of such proteins under the control of the CIPHR logic gates, we took advantage of potent and selective transcriptional repressors of immune checkpoint genes in primary T cells that combine sequence-specific transcription activator-like effector (TALE) DNA-binding domains with the Krüppel-associated box (KRAB) repressor domain (*51*). Repression activity is preserved in split systems pairing a DNA recognition domain fused to a DHD monomer with a repressor domain fused to the complementary DHD monomer (*51*). We reasoned that this system could be exploited to engineer programmable therapeutic devices by making the joining of the DNA recognition and transcriptional repression functionalities dependent on CIPHR gates. Use of a repressive domain effectively reverses the logic of CIPHR gates when expression level of the target gene is measured as the output.

To test the feasibility of this concept, we used a TALE-KRAB fusion engineered to repress the immune checkpoint gene *TIM3* (*51*). We designed a NOT gate with ***1*** fused to the TALE DNA recognition domain, ***9′*** fused to KRAB, and the ***1′-9*** dimerizer protein as the input (see fig. S7A for T cell DHD specificity matrix). In this scheme, ***1′-9*** brings KRAB to the promoter region bound by the TALE, therefore triggering repression of *TIM3* (Fig. 4F). Taking advantage of the interaction between ***9*** and ***1′***, we built an OR gate with ***9***-TALE and ***1′***-KRAB fusions; *TIM3* was repressed in the absence of inputs but upon addition of either ***9′*** or ***1***, the weaker ***9:1′*** interaction was outcompeted in favor of the stronger ***9:9′*** and ***1:1′*** interactions, restoring *TIM3* expression (Fig. 4G). These results suggest that the combination of CIPHR and TALE-KRAB systems could be directly applied to add signal-processing capabilities to adoptive T cell therapy.

The systematic design of logic gates described herein takes advantage of the strengths of de novo protein design. Because the building block heterodimers are designed de novo, many more

components for gate construction with nearly identical overall topology can be generated than are available by repurposing biological motifs. The encoding of specificity using designed hydrogen bond networks enables a wide range of binding affinities between monomers with similar structures, which in turn allows the construction of more complex gates that are based on competitive binding. From the protein biophysics perspective, our results highlight the strong synergy between de novo design of protein complexes and nMS and, more generally, the ability of de novo protein design to generate complex cooperative assemblies. For example, detecting and quantifying the 33-fold activation of binding in Fig. 1G depended critically on the ability to resolve all species formed in solution by nMS. Analysis of the three-input logic gates in Fig. 3B required distinguishing the designed heteropentameric assemblies, which are composed of five distinct protein chains, from the very large number of alternative possible heterotetrameric, trimeric, and dimeric complexes. The ability to generate highly cooperative and well-defined assemblies composed of five distinct polypeptide chains demonstrates that de novo protein design is starting to approach the complexity of naturally occurring protein assemblies, which are responsible for much of biological function.

Unlike nucleic acid–based logic gates, CIPHR gates can be directly coupled to arbitrary protein actuation domains, offering greater diversity in the types of functional outputs. We illustrate here the coupling to transcriptional activation and repression and split enzyme reconstitution; in principle, any function that can be modulated by protein-protein association can be put under the control of the CIPHR gates. Because the designed components are hyperstable proteins and no additional cellular machinery is required, the gates should function in a wide range of conditions inside and outside of cells (here, we have demonstrated function with purified components in cell-free extracts, yeast cells, and T cells). The small size of DHDs and thus their genetic payload makes them attractive for mammalian cell engineering. The sophistication of the circuits could be further increased by proteolytic activation as in recent elegant studies using protease-based protein circuits (*30*, *31*); our purely protein interaction–based circuits have advantages in bioorthogonality, demonstrated scalability to three inputs, composability (the output, like the input and the computing machinery, consists of interactions between building blocks with common design features), and extensibility because an essentially unlimited repertoire of heterodimeric building blocks can be created using de novo design.

REFERENCES AND NOTES

1. R. Nussinov, *Mol. Biosyst.* **8**, 22–26 (2012).
2. A. W. Reinke, J. Baek, O. Ashenberg, A. E. Keating, *Science* **340**, 730–734 (2013).
3. Y. E. Antebi *et al*., *Cell* **170**, 1184–1196.e24 (2017).
4. B. Z. Harris, W. A. Lim, *J. Cell Sci.* **114**, 3219–3231 (2001).
5. G. Seelig, D. Soloveichik, D. Y. Zhang, E. Winfree, *Science* **314**, 1585–1588 (2006).
6. L. Qian, E. Winfree, *Science* **332**, 1196–1201 (2011).
7. M. B. Elowitz, S. Leibler, *Nature* **403**, 335–338 (2000).
8. T. S. Gardner, C. R. Cantor, J. J. Collins, *Nature* **403**, 339–342 (2000).
9. A. Tamsir, J. J. Tabor, C. A. Voigt, *Nature* **469**, 212–215 (2011).
10. P. Siuti, J. Yazbek, T. K. Lu, *Nat. Biotechnol.* **31**, 448–452 (2013).
11. J. Bonnet, P. Yin, M. E. Ortiz, P. Subsoontorn, D. Endy, *Science* **340**, 599–603 (2013).
12. B. H. Weinberg *et al*., *Nat. Biotechnol.* **35**, 453–462 (2017).
13. S. Ausländer, D. Ausländer, M. Müller, M. Wieland, M. Fussenegger, *Nature* **487**, 123–127 (2012).
14. A. S. Khalil *et al*., *Cell* **150**, 647–658 (2012).
15. N. Roquet, A. P. Soleimany, A. C. Ferris, S. Aaronson, T. K. Lu, *Science* **353**, aad8559 (2016).
16. L. B. Andrews, A. A. K. Nielsen, C. A. Voigt, *Science* **361**, eaap8987 (2018).
17. B. Angelici, E. Mailand, B. Haefliger, Y. Benenson, *Cell Rep.* **16**, 2525–2537 (2016).
18. J. J. Lohmueller, T. Z. Armel, P. A. Silver, *Nucleic Acids Res.* **40**, 5180–5187 (2012).
19. A. A. Green, P. A. Silver, J. J. Collins, P. Yin, *Cell* **159**, 925–939 (2014).
20. A. A. Green *et al*., *Nature* **548**, 117–121 (2017).
21. K. Rinaudo *et al*., *Nat. Biotechnol.* **25**, 795–801 (2007).
22. L. Wroblewska *et al*., *Nat. Biotechnol.* **33**, 839–841 (2015).
23. S.-H. Park, A. Zarrinpar, W. A. Lim, *Science* **299**, 1061–1064 (2003).
24. P. L. Howard, M. C. Chia, S. Del Rizzo, F.-F. Liu, T. Pawson, *Proc. Natl. Acad. Sci. U.S.A.* **100**, 11267–11272 (2003).
25. B. Groves, A. Khakhar, C. M. Nadel, R. G. Gardner, G. Seelig, *eLife* **5**, e15200 (2016).
26. L. Morsut *et al*., *Cell* **164**, 780–791 (2016).
27. J. E. Dueber, B. J. Yeh, K. Chak, W. A. Lim, *Science* **301**, 1904–1908 (2003).
28. J. E. Dueber, E. A. Mirsky, W. A. Lim, *Nat. Biotechnol.* **25**, 660–662 (2007).
29. A. J. Smith, F. Thomas, D. Shoemark, D. N. Woolfson, N. J. Savery, *ACS Synth. Biol.* **8**, 1284–1293 (2019).
30. X. J. Gao, L. S. Chong, M. S. Kim, M. B. Elowitz, *Science* **361**, 1252–1258 (2018).
31. T. Fink *et al*., *Nat. Chem. Biol.* **15**, 115–122 (2019).
32. Z. Chen *et al*., *Nature* **565**, 106–111 (2019).
33. K. E. Prehoda, J. A. Scott, R. D. Mullins, W. A. Lim, *Science* **290**, 801–806 (2000).
34. B. Yu *et al*., *Cell* **140**, 246–256 (2010).
35. K. N. Dyer *et al*., *Methods Mol. Biol.* **1091**, 245–258 (2014).
36. B. T. Ruotolo, C. V. Robinson, *Curr. Opin. Chem. Biol.* **10**, 402–408 (2006).
37. Z. L. VanAernum *et al*., *Nat. Protoc.* **15**, 1132–1157; Rapid online (2020).
38. A. Pause, B. Peterson, G. Schaffar, R. Stearman, R. D. Klausner, *Proc. Natl. Acad. Sci. U.S.A.* **96**, 9533–9538 (1999).
39. B. Sandrock, J. M. Egly, *J. Biol. Chem.* **276**, 35328–35333 (2001).
40. A. S. Dixon *et al*., *ACS Chem. Biol.* **11**, 400–408 (2016).
41. Y.-C. Kwon, M. C. Jewett, *Sci. Rep.* **5**, 8663 (2015).
42. J. R. Porter, C. I. Stains, B. W. Jester, I. Ghosh, *J. Am. Chem. Soc.* **130**, 6488–6497 (2008).
43. S. L. Maude *et al*., *N. Engl. J. Med.* **378**, 439–448 (2018).
44. S. S. Neelapu *et al*., *N. Engl. J. Med.* **377**, 2531–2544 (2017).
45. J. A. Fraietta *et al*., *Nat. Med.* **24**, 563–571 (2018).
46. C. H. June, R. S. O'Connor, O. U. Kawalekar, S. Ghassemi, M. C. Milone, *Science* **359**, 1361–1365 (2018).
47. A. H. Long *et al*., *Nat. Med.* **21**, 581–590 (2015).
48. E. J. Wherry, M. Kurachi, *Nat. Rev. Immunol.* **15**, 486–499 (2015).
49. E. J. Wherry *et al*., *Immunity* **27**, 670–684 (2007).
50. K. E. Pauken *et al*., *Science* **354**, 1160–1165 (2016).
51. M. S. Wilken *et al*., Regulatory DNA keyholes enable specific and persistent multi-gene expression programs in primary T cells without genome modification. bioRxiv 2020.02.19.956730 [Preprint]. 20 February 2020; https://doi.org/10.1101/2020.02.19.956730.
52. Z. Chen *et al*., Code used to simulate the cooperative binding system for: De novo design of protein logic gates, Zenodo (2020); https://doi.org/10.5281/zenodo.3697264.

ACKNOWLEDGMENTS

We thank A. Ng, T. Nguyen, D. Younger, M. Xie, and B. Groves for assistance with yeast experiments; C. Chow for assistance with protein purification; W. Lim for discussions on protein-binding cooperativity; M. Elowitz, R. Schulman, and N. Woodall for feedback on the manuscript; S. Bermeo, M. Lajoie, R. Langan, and A. Ljubetič for useful discussions; and S. Pennington for making the media for Y2H assays. **Funding:** This work was supported by the Howard Hughes Medical Institute (D.B.), the generosity of Eric and Wendy Schmidt by recommendation of the Schmidt Futures program (D.B. and Z.C.), IPD-WA State funding Y5/07-5568 (D.B.), NIH BTRR Yeast Resource Grant Y8-12/61-3650 (Z.C. and R.D.K.), Bruce and Jeannie Nordstrom/Patty and Jimmy Barrier Gift for the Institute for Protein Design (Z.C. and R.D.K.), Spark ABCA4/63-3819 (Z.C.), NIH P41 grant GM103533 (R.D.K.), Open Philanthropy (D.B. and B.I.M.W.), EMBO/80-7223 (B.I.M.W.), Burroughs Wellcome Fund Career Award at the Scientific Interface (S.E.B.), the Army Research Office W911NF-18-1-0200 (M.C.J.), the Air Force Research Laboratory Center of Excellence grant FA8650-15-2-5518 (M.C.J), the David and Lucile Packard Foundation (M.C.J.), and the Camille Dreyfus Teacher-Scholar Program (M.C.J.). A.H. was supported by the Department of Defense (DOD) through the National Defense Science & Engineering Graduate Fellowship (NDSEG) Program. T cell engineering work was supported by a charitable contribution from GlaxoSmithKline to the Altius Institute for Biomedical Sciences (J.R.P., H.L., M.W., C.C., J.A.S.) and NHLBI grant 7R33HL120752 (J.A.S). V.H.W. was supported by NIH grant P41 GM128577 and Ohio Eminent Scholar funds. H.E.-S. was supported by the Defense Advanced Research Projects Agency, contract no. HR0011-16-2-0045, and is a Chan-Zuckerberg investigator. SAXS data were collected at the Advanced Light Source (ALS) at LBNL, supported by the following grants from the NIH: P30 GM124169-01, ALS-ENABLE P30 GM124169, and S10OD018483; NCI SBDR (CA92584); and DOE-BER IDAT (DE-AC02-05CH11231). **Author contributions:** Z.C., S.E.B., and D.B. conceived of the idea; Z.C. and D.B. designed the research; Z.C. and D.B. wrote the manuscript with help from R.D.K and S.E.B.; Z.C. and R.D.K. performed biophysical characterizations with help from B.I.M.W.; Z.C. performed Y2H experiments; A.H. performed NanoBiT experiments and analyzed data with M.C.J.; F.B., M.J., and Z.L.V. performed nMS experiments and analyzed data with V.H.W.; J.R.P., M.W., and C.C. performed and analyzed data from T cell experiments with transcriptional repressors, supervised by S.G. and J.A.S.; G.D. performed the yeast titration assay and analyzed data with H.E.-S.; all authors discussed the results and commented on the manuscript. **Competing interests:** Z.C, S.E.B., and D.B. are coinventors on patent application PCT/US19/59654 that incorporates discoveries described in this manuscript. D.B. is a cofounder of and holds equity in Lyell Immunopharma and Sana Biotechnology. J.P., M.W., C.C., S.G., and J.A.S. are co-inventors on U.S. patent application 62/937,011 that includes discoveries described in this manuscript. J.P. H.L., and S.E.B. hold equity in Lyell Immunopharma. **Data and materials availability:** Raw data from nMS experiments have been deposited to http://files.ipd.uw.edu/pub/de_novo_logic_2019/190522_native_ms_raw.zip. Code used to simulate the cooperative binding system has been deposited at Zenodo (*52*). Plasmids used in this study are available upon request from the corresponding author.

SUPPLEMENTARY MATERIALS

science.sciencemag.org/content/368/6486/78/suppl/DC1
Materials and Methods
Supplementary Text
Figs. S1 to S7
Tables S1 to S8
References (*53*–*71*)

5 June 2019; accepted 5 March 2020
10.1126/science.aay2790

CANCER

Cysteine depletion induces pancreatic tumor ferroptosis in mice

Michael A. Badgley[1,2]*, Daniel M. Kremer[3,4]†, H. Carlo Maurer[1,2,5]†, Kathleen E. DelGiorno[6], Ho-Joon Lee[3,4], Vinee Purohit[3,4], Irina R. Sagalovskiy[1,2], Alice Ma[1,2], Jonathan Kapilian[1,2], Christina E. M. Firl[1,2], Amanda R. Decker[1,2], Steve A. Sastra[1,2], Carmine F. Palermo[1,2], Leonardo R. Andrade[7], Peter Sajjakulnukit[3,4], Li Zhang[4,8], Zachary P. Tolstyka[3,4], Tal Hirschhorn[9], Candice Lamb[10], Tong Liu[2,11,12], Wei Gu[2,11,12], E. Scott Seeley[13,14], Everett Stone[10,15], George Georgiou[15], Uri Manor[7], Alina Iuga[2,12], Geoffrey M. Wahl[6], Brent R. Stockwell[9], Costas A. Lyssiotis[3,4,16], Kenneth P. Olive[1,2]‡

Ferroptosis is a form of cell death that results from the catastrophic accumulation of lipid reactive oxygen species (ROS). Oncogenic signaling elevates lipid ROS production in many tumor types and is counteracted by metabolites that are derived from the amino acid cysteine. In this work, we show that the import of oxidized cysteine (cystine) via system x_C^- is a critical dependency of pancreatic ductal adenocarcinoma (PDAC), which is a leading cause of cancer mortality. PDAC cells used cysteine to synthesize glutathione and coenzyme A, which, together, down-regulated ferroptosis. Studying genetically engineered mice, we found that the deletion of a system x_C^- subunit, *Slc7a11*, induced tumor-selective ferroptosis and inhibited PDAC growth. This was replicated through the administration of cyst(e)inase, a drug that depletes cysteine and cystine, demonstrating a translatable means to induce ferroptosis in PDAC.

Pancreatic ductal adenocarcinoma (PDAC) is a deadly cancer that is resistant to traditional therapies. More than 90% of PDAC cases harbor mutations in *KRAS* that both promote proliferation and alter cellular metabolism. A by-product of mutant-KRAS signaling is the increased production of reactive oxygen species (ROS), which can damage cellular components. To compensate, PDAC cells up-regulate metabolic programs that detoxify ROS using cysteine-derived metabolites such as glutathione (GSH) (*1*). Most cellular cysteine is acquired through the system x_C^- antiporter, which exchanges extracellular, oxidized cysteine (cystine) for intracellular glutamate. Yet, germline deletion of the system x_C^- gene, *Slc7a11*, is well tolerated in unstressed mice (*2*), which suggests that normal cells have low basal cystine import requirements. We hypothesized that cystine import is a critical dependency of PDAC that may be selectively targeted as an anticancer therapy.

To investigate the role of cysteine metabolism in PDAC, we measured the viability of human PDAC cell lines cultured for 24 hours in media with varying concentrations of cystine or the system x_C^- inhibitor imidazole ketone erastin (IKE) (Fig. 1, A and B) (*3*). In four of five PDAC lines, cystine starvation reduced cell viability by >80%; this was largely prevented by addition of the lipophilic antioxidant Trolox. Cystine-starved cells underwent catastrophic destabilization of their plasma membranes, without visual evidence of nuclear fragmentation (movie S1). IKE treatment mimicked the effects of cystine withdrawal, quickly killing most cells from the four sensitive PDAC lines in a manner that was visually identical to that of cystine starvation but distinct from staurosporine-induced apoptosis (fig. S1A and movies S2 and S3). Neither cystine starvation nor system x_C^- inhibition (collectively referred to as cysteine depletion) induced caspase 3 cleavage (fig. S1B), which indicates that the cell death was not apoptotic. Rather, the oxidative cell death resembled ferroptosis, a form of iron-dependent, non-apoptotic cell death previously associated with system x_C^- inhibition (*4*). We found that cotreatment of human PDAC cells with either deferoxamine (DFO, an iron chelator), ferrostatin-1 (Fer1, a ferroptosis inhibitor), or N-acetylcysteine (NAC, a cell-permeable analog of cysteine) markedly reduced cell death from cysteine depletion, whereas inhibitors of apoptosis or necroptosis had little impact on cell death, consistent with previous reports (Fig. 1C and fig. S1, C to E) (*5*). Autophagy inhibition had variable effects in different lines, likely reflecting the known effect of ferritinophagy on ferroptosis (*6*). Using the fluorescent probe C11-BODIPY, we observed a large increase in lipid oxidation (a hallmark of ferroptosis) prior to cell death in response to cysteine depletion; this was prevented by cotreatment with Trolox, Fer-1, NAC, and DFO (Fig. 1D and fig. S2, A and B). By contrast, elevated total ROS levels induced by cysteine depletion were not prevented by these agents, which argues against a more general oxidative process (fig. S2C). We conclude from these experiments that most PDAC lines rely on cysteine to prevent ferroptotic cell death. An analysis of *SLC7A11* expression across human datasets revealed a modest overexpression in PDAC versus normal tissues, enrichment in the malignant epithelial compartment of PDAC, and an association with signatures of redox stress (fig. S3). Across multiple human cancers, *SLC7A11* was frequently overexpressed and associated with reduced survival (fig. S4).

To learn whether pancreatic tumors in mice depend on system x_c^- for survival, we employed a dual recombinase genetic engineering strategy based on the KPC mouse model (*7*). $Kras^{FSF.G12D/+}$; $Tp53^{R172H/+}$; $Pdx1FlpO^{tg/+}$; $Slc7a11^{Fl/Fl}$; $Rosa26^{CreERT2/+}$ (KPFSR) mice (fig. S5) spontaneously develop PDAC driven by FlpO-dependent activation of mutant *Kras* and germline expression of mutant *Tp53*. These tumors are identical in genotype and phenotype to the KPC model, but the administration of tamoxifen induces systemic deletion of *Slc7a11* through the action of Cre recombinase expressed from the *Rosa26* locus (figs. S5 and S6, A to C). We randomized KPFSR mice bearing 4 to 7 mm tumors to receive six daily doses of vehicle or tamoxifen and monitored tumor growth by ultrasound (*8*). We found that deletion of *Slc7a11* in established tumors of KPFSR mice nearly doubled median survival compared with vehicle treatment (Fig. 2A; $P = 0.0295$, $n = 10$ per group). Most recombined tumors exhibited a period of stable disease or partial response—and one underwent a complete regression—but these responses were never observed in vehicle-treated mice (Fig. 2B and figs. S6, D to F, and S7A). Critically, the addition of NAC to the drinking water of tamoxifen-treated mice restored baseline survival and eliminated tumor responses, supporting a link to cysteine metabolism (Fig. 2, A and B). At necropsy, escaped tumors exhibited evidence of incomplete *Slc7a11* recombination by polymerase chain reaction and restored protein

[1]Division of Digestive and Liver Diseases, Department of Medicine, Columbia University Medical Center, New York, NY 10032, USA. [2]Herbert Irving Comprehensive Cancer Center, Columbia University Medical Center, New York, NY 10032, USA. [3]Department of Molecular and Integrative Physiology, University of Michigan, Ann Arbor, MI 48109, USA. [4]Rogel Cancer Center, University of Michigan, Ann Arbor, MI 48109, USA. [5]Klinikum rechts der Isar, II, Medizinische Klinik, Technische Universität München, 81675, Munich, Germany. [6]Gene Expression Laboratory, Salk Institute for Biological Studies, La Jolla, CA 92037, USA. [7]Waitt Advanced Biophotonics Center, Salk Institute for Biological Studies, La Jolla, CA 92037, USA. [8]Michigan Regional Comprehensive Metabolomics Resource Core, University of Michigan, Ann Arbor, MI 48105, USA. [9]Departments of Biological Sciences and Chemistry, Columbia University, New York, NY 10027, USA. [10]Department of Chemical Engineering, University of Texas at Austin, Austin, TX 78712, USA. [11]Institute for Cancer Genetics, Columbia University Medical Center, New York, NY 10032, USA. [12]Department of Pathology, Columbia University Medical Center, New York, NY 10032, USA. [13]Department of Pathology, University of California, San Francisco, CA 94143, USA. [14]Salvo Therapeutics, San Francisco, CA 94117, USA. [15]Department of Molecular Biosciences, University of Texas at Austin, Austin, TX 78712, USA. [16]Department of Internal Medicine, Division of Gastroenterology, University of Michigan, Ann Arbor, MI 48109, USA.
*Present address: Department of Biochemistry and Molecular Pharmacology, Langone Medical Center, New York University, New York, NY 10016, USA. †These authors contributed equally to this work.
‡Corresponding author. Email: kenolive@columbia.edu

expression by Western blotting, which suggests the outgrowth of unrecombined tumor cells (fig. S7, B and C).

The study of in vivo ferroptosis has been hindered by the lack of a validated, selective biomarker and the absence of a histopathological characterization of the phenomenon in tissues. Within tamoxifen-treated KPFSR tumors, we observed numerous lesions of ballooned epithelial cells with lipid droplet-like structures and intermittent megamitochondria, often juxtaposed to necrotic regions—a phenotype only occasionally observed in vehicle-treated KPFSR and untreated KPC tumors (Fig. 2, C and D, and fig. S7C). These lesions exhibited no alterations in apoptosis or proliferation markers (fig. S8, A and B), but they did display accumulation of 4-hydroxynonenal (4HN) (fig. S8, C to E), a by-product of lipid peroxidation, making them candidates for in vivo ferroptosis. Critically, no pathologies were observed in nonpancreatic tissues of tamoxifen-treated KPFSR mice, indicating a tumor-selective phenotype. Transmission electron microscopy (TEM) and Oil Red O staining of tamoxifen-treated KPFSR tumors confirmed the presence of abnormally large lipid droplets (Fig. 2D and fig. S8F). TEM also revealed structural aberrations in the mitochondria of malignant epithelial cells, including disrupted cristae and compromised membrane integrity (Fig. 2E), which is consistent with the results of prior in vitro studies (*9*). Finally, we performed laser capture microdissection and RNA sequencing to isolate malignant epithelial cells from KPFSR tumors. We found that genes up-regulated in response to *Slc7a11* deletion were enriched in a ferroptotic expression signature from erastin-treated HT-1080 cells (Fig. 2F) (*10*), whereas apoptotic gene sets were not enriched (table S1). We conclude that the phenotype observed in tamoxifen-treated KPFSR tumors is a histologically identifiable, in vivo manifestation of ferroptosis.

Prior studies have indicated that cysteine regulates ferroptosis primarily through the synthesis of GSH, a critical cofactor for the lipid peroxide–detoxifying enzyme GPX4 (*3*). We found that cysteine depletion rapidly reduced GSH levels in two human PDAC cell lines (fig. S9A). Furthermore, cotreatment with the membrane-permeable GSH analog glutathione ethyl ester prevented lipid oxidation and ferroptosis (fig. S9, B to E). However, inhibition of GSH biosynthesis using buthionine sulfoximine (BSO) (fig. S9F) did not induce lipid ROS or reduce cell viability (Fig. 3, A and B), which demonstrates that GSH loss is not sufficient to induce ferroptosis in PDAC cells (*11*). To investigate whether additional cysteine-derived metabolites contribute to the regulation of ferroptosis, we traced the metabolism of exogenous cystine by using ^{13}C-labeled cystine and measuring labeled metabolites by mass spectrometry. In addition to exhibiting rapid flux into GSH pools, cystine was also converted to coenzyme A (CoA) over 24 hours (Fig. 3 C and D); no flux was observed into taurine, lactate, citrate, or glutamate (fig. S9G). CoA is synthesized from cysteine via the pantothenate pathway and plays a role in many metabolic pathways, particularly lipid metabolism. Both CoA and its derivative coenzyme Q_{10} (CoQ_{10}) have been shown to affect sensitivity to ferroptosis (*12*, *13*). We found that system x_C^- inhibition reduced CoA levels and increased levels of pantothenate (Fig. 3E), a metabolite upstream of cysteine incorporation in CoA synthesis. Moreover, treatment of PDAC cells with exogenous CoA (*14*) prevented IKE-induced ferroptosis (Fig. 3F) whereas pantothenate kinase inhibition with PANKi sensitized cells to IKE (fig. S10, A to C). Notably, PANKi combined synergistically with BSO to induce ferroptosis (Fig. 3G and fig. S10D). Cotreatment with idebenone (a membrane-permeable analog of CoQ_{10}) or a monounsaturated fatty acid blocked BSO/PANKi-induced ferroptosis, whereas saturated or polyunsaturated fatty acids did not (fig. S10E), similar to prior observations with IKE (*15*). Together, these experiments demonstrate that CoA and GSH cooperate to regulate ferroptosis in human PDAC cells (fig. S10H).

Finally, we sought a pharmacological means to target cysteine metabolism in pancreatic tumors. Drug delivery is compromised in PDAC because of the effects of fibrosis on tissue perfusion (*16*). Although current system x_C^- inhibitors are not optimized for the PDAC microenvironment, the engineered enzyme cyst(e)inase is well-tolerated in mammals, has a long half-life, and potently degrades both cystine and cysteine in circulation (*17*). In vitro, cyst(e)inase treatment induced lipid oxidation and reduced the viability of IKE-sensitive PDAC lines; this was largely prevented by cotreatment with ferroptosis inhibitors (Fig. 4, A to C, and fig. S11, A and B). To determine the effects of cyst(e)inase on pancreatic tumors in vivo, we treated tumor-bearing KPC mice for 10 days with vehicle, low-dose cyst(e)inase, or high-dose cyst(e)inase (n = 2 for each treatment). Histopathological examination

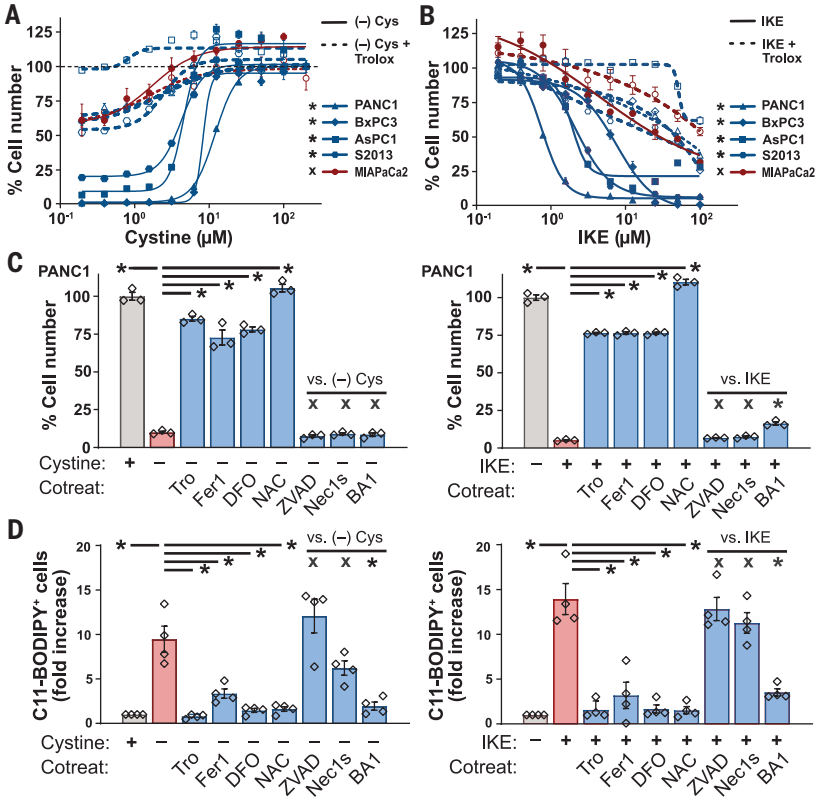

Fig. 1. Pancreatic cancer cells require exogenous cystine to avert ferroptosis. (**A** and **B**) Viability of human PDAC lines after 24 hours culture in varying concentrations of cystine (A) or IKE (B), alone or in combination with 100 μM Trolox. Student's *t* test was performed, comparing maximal cytotoxicity ± Trolox. (**C**) Viability of PANC-1 cells cultured for 24 hours in cystine-free media (left) or treated with 10 μM IKE (right), alone or in combination with 100 μM Trolox (Tro), 500 nM ferrostatin-1 (Fer1), 100 μM deferoxamine (DFO), 1mM N-acetyl cysteine (NAC), 50 μM ZVAD-FMK, 1 nM Bafilomycin A1 (BA1), or 10 μM Necrostatin-1s (Nec1s). Tukey test was performed. (**D**) Flow cytometry of C11-BODIPY fluorescence in PANC-1, AsPC-1, BxPC-3, and S-2013 cells after 6 to 8 hours of treatment with conditions from (C). Tukey test was performed. All data are means ± SEM of three independent experiments. *P < 0.05; x, no significant difference.

of cyst(e)inase-treated tumors revealed a severe ferroptosis phenotype, with extensive lipid droplet formation, stromal disruption, decompressed blood vessels, and necrosis (Fig. 4, D and E, and fig. S12, A and B). TEM revealed enlarged lipid droplet formation, extracellular lipid droplets, and mitochondrial defects, preferentially in cyst(e)inase-treated KPC tumors (Fig. 4, F to I). Ferroptotic lesions were generally 4HN positive and cleaved caspase 3 negative (fig. S13A). Finally, four additional KPC mice were treated with high-dose cyst(e)inase, and their tumor growth was monitored by ultrasound. Notably, all four tumors exhibited stabilizations or regressions, whereas historical vehicle-treated controls never stabilized (Fig. 4J). Thus, we conclude that the

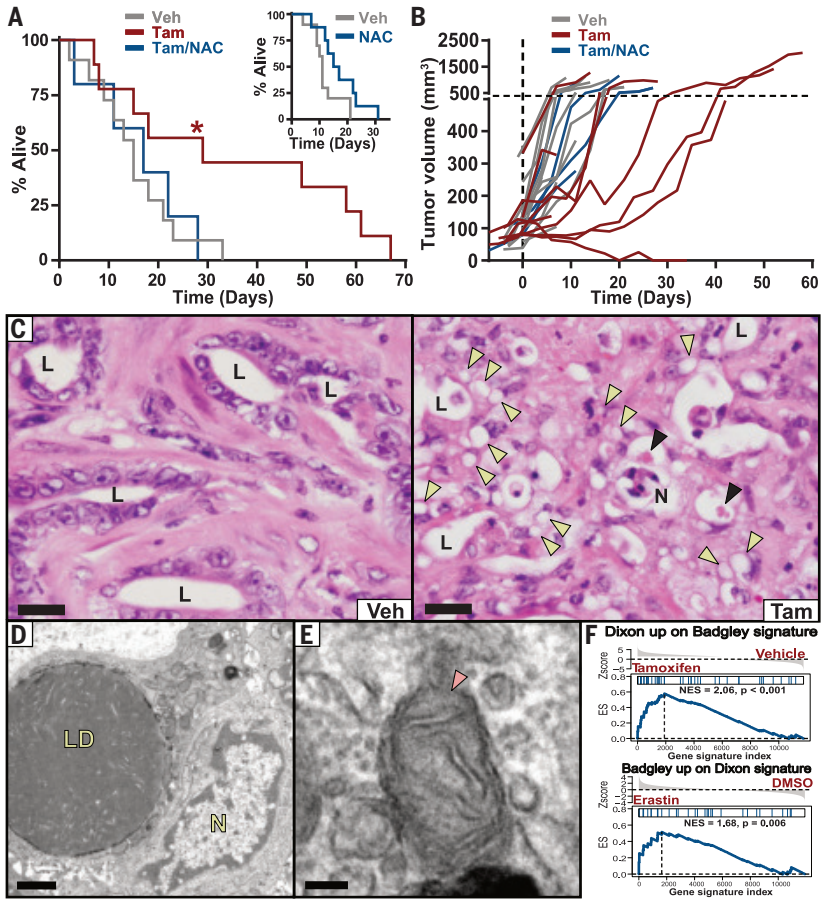

Fig. 2. Deletion of *Slc7a11* in KPC mice induces tumor ferroptosis and extends survival. (**A**) Survival of KPFSR mice treated with vehicle (Veh) (n = 11, median 15 days), tamoxifen (Tam) (n = 9, median 29 days), or tamoxifen/NAC (n = 5, median 17 days). *P < 0.0295, log-rank. Inset shows the survival of KPC mice treated with NAC alone (n = 8, median 16 days) versus historical saline-treated controls (n = 10, median 11 days). (**B**) Growth curves for each KPFSR tumor. (**C**) Hematoxylin and eosin (H&E)–stained sections of tumor tissue from KPFSR mice treated with vehicle (left) or tamoxifen (right). L, lumen of malignant epithelium; N, necrosis; yellow arrowheads, lipid droplets; black arrowheads, megamitochondria; scale bars, 20 μm. (**D** and **E**) TEM images from tamoxifen-treated KPFSR tumors. LD, lipid droplets; N, nucleus; arrowhead indicates damaged mitochondrion. Scale bar (D), 1μm; scale bar (E), 100 nm. (**F**) Gene set enrichment analysis. Top panel depicts enrichment of a published ferroptosis expression signature (Dixon) among genes differentially expressed in tamoxifen-treated KPFSR epithelia (Badgley) (P < 0.001). Bottom panel depicts the reciprocal comparison (P < 0.006). NES, normalized enrichment score; DMSO, dimethyl sulfoxide.

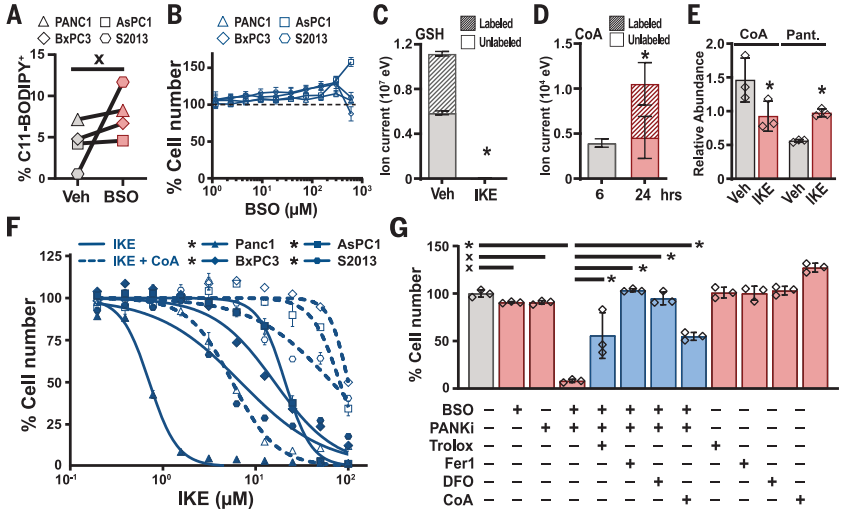

Fig. 3. Combination GSH and CoA inhibition induces ferroptosis in human PDAC cells. (**A**) Flow cytometry for C11-BODIPY fluorescence in four human PDAC lines treated for 6 hours with 150 μM BSO. Paired t test was performed. (**B**) Viability of human PDAC cells treated for 24 hours with indicated concentrations of BSO. (**C**) Liquid chromatography time-of-flight mass spectrometry (LC-TOF-MS) analysis of GSH in PANC-1 cells labeled for 6 hours with ^{13}C-cystine combined with vehicle or 5μM IKE. Student's t test was performed. (**D**) LC-TOF-MS analysis of CoA in PANC-1 cells labeled for 6 hours with ^{13}C-cystine, after 6 or 24 hours. Student's t test was performed. (**E**) Liquid chromatography triple quadrupole tandem mass spectrometry measurements of CoA and pantothenate (Pant.) levels in Panc-1 cells treated with vehicle and IKE for 6 hours. Student's t test was performed. (**F**) Viability of human PDAC cell lines treated with IKE, alone or in combination with 200 μM CoA. Student's t test comparing maximal cytotoxicity ± CoA was performed. (**G**) PANC-1 cells treated for 24 hours with combinations of 300 μM BSO and 5 μM PANKi along with Trolox, Fer-1, DFO, or CoA, as described in Fig. 1C. Tukey test was performed. In (A) to (G), *P < 0.05 and x indicates not significantly different. In (A), (B), (E), and (F), data are means ± SEM from three independent experiments. In (C) and (D), data are means ± SD from three biological replicates. In (E), *P < 0.05 comparing maximal cytotoxicity in CoA-treated versus untreated conditions for each line, Student's t test. In (F), *P < 0.05, one-way ANOVA with posthoc Tukey test.

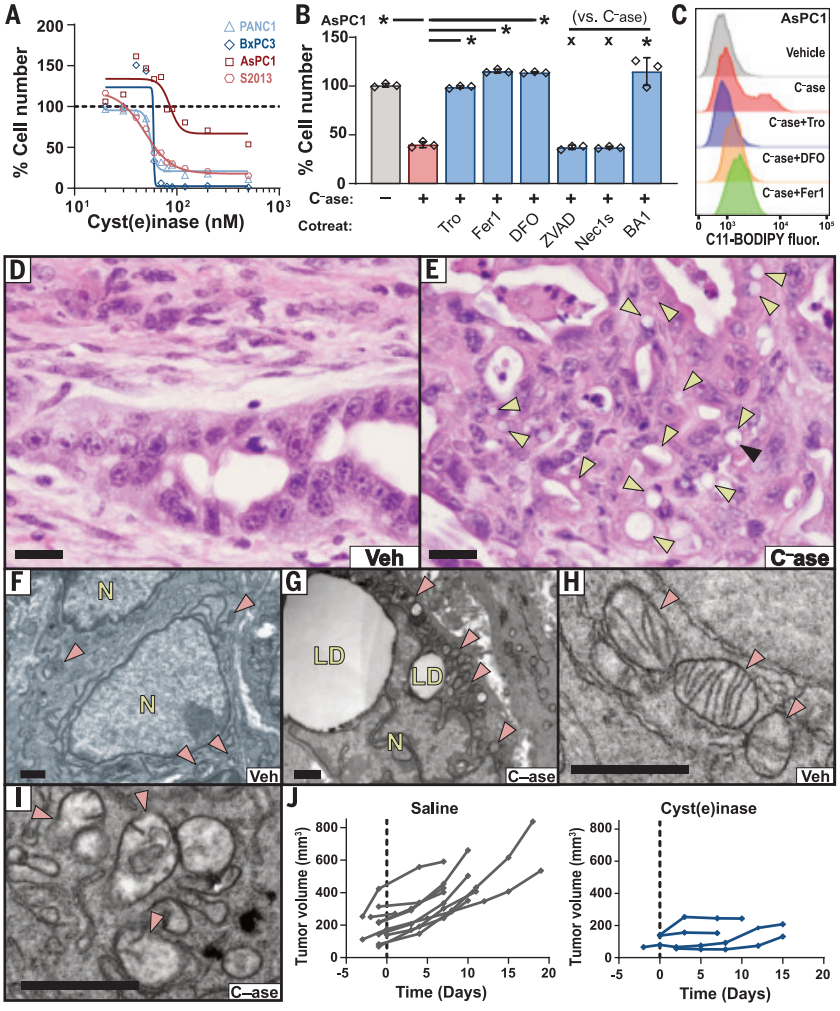

Fig. 4. Cyst(e)inase treatment induces tumor-selective ferroptosis in KPC mice. (**A**) Viability of human PDAC lines cultured with varying concentrations of cyst(e)inase for 48 hours (AsPC1) or 72 hours (PANC-1, BxPC3, and S2-013). (**B**) Viability of AsPC1 cells treated with 90 nM cyst(e)inase (C⁻ase) for 72 hours, alone or in combination with indicated agents, under conditions described in Fig. 1C. (**C**) C11-BODIPY fluorescence was measured by flow cytometry in AsPC-1 cells after 24 hours of treatment with 90 nM cyst(e)inase, alone or in combination with indicated agents, under conditions described in Fig. 1C. (**D** and **E**) H&E-stained sections of pancreatic tumors from KPC mice treated with vehicle or cyst(e)inase. Yellow arrowheads indicate lipid droplets; black arrowhead indicates megamitochondrion; scale bars, 20 μm. (**F** to **I**) TEM of pancreatic tumors from the KPC model treated with vehicle [(F) and (H)] or cyst(e)inase [(G) and (I)]. Red arrowheads indicate mitochondria; LD, lipid droplets; N, nucleus; scale bars, 1 μm. (**J**) Tumor growth curves from KPC mice treated with saline (historical controls) or 100 mg/kg cyst(e)inase, every other day, intraperitoneally. For (A) and (B), data depict mean of three biological replicates. *P < 0.05; x, not significant.

therapeutic depletion of cysteine (cystine) can induce ferroptosis in Kras/p53 mutant pancreatic tumors in mice.

In summary, our data add to a growing body of evidence showing that certain cancers, including PDAC, rely on cysteine metabolism to avert ferroptosis. Previously, *SLC7A11* deletion via CRISPR-Cas9 was shown to induce ferroptosis in cultured PDAC cells and slow xenograft engraftment and growth (*18*), and system x_C^- inhibition was shown to limit the growth of lymphoma xenografts, inducing a lipid oxidative signature and other indicators of ferroptosis (*15*). However, cysteine depletion in a PDAC xenograft model had little effect on tumor growth (*19*), perhaps indicating that the nutrient-deprived, hypoxic microenvironment of autochthonous pancreatic tumors may contribute to the tumor-selective cysteine dependency we observed in genetically engineered mouse models of PDAC. Although it is not yet known whether human PDAC is also susceptible to ferroptosis from cysteine depletion, the clinical development of cyst(e)inase for treatment of the metabolic disorder cystinuria provides a pathway for future translation of this concept.

REFERENCES AND NOTES

1. G. M. DeNicola *et al.*, *Nature* **475**, 106–109 (2011).
2. H. Sato *et al.*, *J. Biol. Chem.* **280**, 37423–37429 (2005).
3. W. S. Yang *et al.*, *Cell* **156**, 317–331 (2014).
4. S. J. Dixon *et al.*, *Cell* **149**, 1060–1072 (2012).
5. M. Gao *et al.*, *Cell Res.* **26**, 1021–1032 (2016).
6. J. P. Friedmann Angeli *et al.*, *Nat. Cell Biol.* **16**, 1180–1191 (2014).
7. S. R. Hingorani *et al.*, *Cancer Cell* **7**, 469–483 (2005).
8. S. A. Sastra, K. P. Olive, *Methods Mol. Biol.* **980**, 249–266 (2013).
9. M. Gao *et al.*, *Mol. Cell* **73**, 354–363.e3 (2019).
10. S. J. Dixon *et al.*, *eLife* **3**, e02523 (2014).
11. I. S. Harris *et al.*, *Cell Metab.* **29**, 1166–1181.e6 (2019).
12. K. Shimada *et al.*, *Nat. Chem. Biol.* **12**, 497–503 (2016).
13. J. I. Leu, M. E. Murphy, D. L. George, *Proc. Natl. Acad. Sci. U.S.A.* **116**, 8390–8396 (2019).
14. B. Srinivasan *et al.*, *Nat. Chem. Biol.* **11**, 784–792 (2015).
15. Y. Zhang *et al.*, *Cell Chem. Biol.* **26**, 623–633e9 (2019).
16. K. P. Olive *et al.*, *Science* **324**, 1457–1461 (2009).
17. S. L. Cramer *et al.*, *Nat. Med.* **23**, 120–127 (2017).
18. B. Daher *et al.*, *Cancer Res.* **79**, 3877–3890 (2019).
19. S. Kshattry *et al.*, *NPJ Precis. Onc.* **3**, 16 (2019).

ACKNOWLEDGMENTS

We thank members of the Olive, Lyssiotis, and Stockwell laboratories for technical advice and thoughtful critiques. We also thank K. L. Olive for manuscript editing and S. W. Novak for advice on electron microscopy interpretation. **Funding:** This work was supported by the NIH/NCI Cancer Center Support Grant P30CA013696 and utilized the Confocal and Specialized Microscopy, Molecular Pathology, Flow Cytometry Core, and OPTIC shared resources. M.A.B. was supported by a training grant (T32 A009503) and a predoctoral fellowship (F31 CA180738). D.M.K. was supported by a Department of Education GAANN fellowship through the University of Michigan Program in Chemical Biology. K.P.O. was supported by the Lustgarten Foundation for Pancreatic Cancer Research (2011 Innovator Award) and the NIH/NCI (1R01CA215607). C.A.L. was supported by a Pancreatic Cancer Action Network/AACR Pathway to Leadership award (13-70-25-LYSS), a Dale F. Frey Award for Breakthrough Scientists from the Damon Runyon Cancer Research Foundation (DFS-09-14), a Junior Scholar Award from The V Foundation for Cancer Research (V2016-009), a Kimmel Scholar Award from the Sidney Kimmel Foundation for Cancer Research (SKF-16-005), and NIH grant U24-DK097153. V.P. was supported by a PRCRP Horizon award by the Department of Defense (W81XWH-17-1-0497). L.R.A. and U.M. were supported by NCI CCSG (CA014195) and the Waitt Foundation. B.R.S. is supported by the NCI/NIH (R35CA209896 and P01CA087497). G.M.W. and K.E.D. were funded by a Cancer Center Core Grant (CA014195), the NIH/NCI (R35 CA197687), and funding from the Freeberg Foundation and the Hirschberg Foundation. K.E.D. was also funded by the Salk Women and Special Science Award. **Author contributions:** M.A.B. and K.P.O. conceived and supervised the overall project; M.A.B., D.M.K., I.R.S., A.M., J.K., C.E.M.F., A.R.D., T.H., and T.L. performed in vitro studies with supervision from C.A.L., W.G., B.R.S., and K.P.O.; M.A.B., S.A.S., and C.F.P. performed in vivo studies; D.M.K., V.P., H.-J.L., P.S., L.Z., and Z.P.T. performed and analyzed mass spectrometry studies with supervision from C.A.L.; H.C.M. performed computation analyses; K.E.D. and L.R.A. performed and analyzed the electron microscopy data with supervision from U.M. and G.M.W.; E.S.S. generated the Pdx1-FlpO strain; C.L. generated the cyst(e)inase reagent with supervision from G.G. and E.S.; B.R.S. provided erastin analog material; A.I. and K.P.O. performed pathology analyses; and M.A.B. and K.P.O. wrote the manuscript and drafted the figures with input from all authors. **Competing interests:** B.R.S. holds equity in and serves as a consultant to Inzen Therapeutics and is an inventor on patents and applications related to ferroptosis, including the following U.S. patents and corresponding applications and patents in other countries, all submitted by Columbia University: 10,259,775, 10,233,171, 9,580,398, 20190292135, 20190135782, 20170233370, 20160297748, 20150079035, 20080299076, 9,938,245, 20160332974, 9,695,133, 20150175558, 8,546,421, 20100081654, 8,535,897, 20110008803, 8,518,959, 20090214465, 8,124,365, 7,358,262, 20080220454, 7,615,554, 20190315681, and 20070161644. G.G. and E.S. have an equity interest in Aeglea Biotherapeutics, a company that has licensed the commercial development of Cyst(e)inase, and are inventors on U.S. patents and corresponding applications and patents in other countries, all submitted by the University of Texas, related to L-cyst(e)inase: 10,363,311 and 20180327734. The other authors declare no competing interests, financial or otherwise. **Data and materials availability:** Cyst(e)inase is available from G.G. and E.S. under a material transfer agreement with the University of Texas.

RNA sequencing datasets are available at Gene Expression Omnibus (accession no. GSE119628). All other data are available in the text or the supplementary materials. Mouse strains comprising the KPC and KPFSR models (other than Pdx1-FlpO) were provided through material transfer agreements with EUCOMM (Slc7a11^{Flox}), Univ. Cincinnati (Pdx1Cre), and MIT (all others).

SUPPLEMENTARY MATERIALS
science.sciencemag.org/content/368/6486/85/suppl/DC1
Materials and Methods
Figs. S1 to S13
Table S1
References (*20*–*43*)
Movies S1 to S3

13 February 2019; resubmitted 25 October 2019
Accepted 8 March 2020
10.1126/science.aaw9872

NEUROSCIENCE

Facial expressions of emotion states and their neuronal correlates in mice

Nejc Dolensek[1,2], Daniel A. Gehrlach[1,3], Alexandra S. Klein[1,3], Nadine Gogolla[1]*

Understanding the neurobiological underpinnings of emotion relies on objective readouts of the emotional state of an individual, which remains a major challenge especially in animal models. We found that mice exhibit stereotyped facial expressions in response to emotionally salient events, as well as upon targeted manipulations in emotion-relevant neuronal circuits. Facial expressions were classified into distinct categories using machine learning and reflected the changing intrinsic value of the same sensory stimulus encountered under different homeostatic or affective conditions. Facial expressions revealed emotion features such as intensity, valence, and persistence. Two-photon imaging uncovered insular cortical neuron activity that correlated with specific facial expressions and may encode distinct emotions. Facial expressions thus provide a means to infer emotion states and their neuronal correlates in mice.

Emotions are patterns of behavioral, hormonal, and autonomic responses aimed at promoting survival. Emotions result from brain states that reflect the dynamic integration of external cues, bodily signals, and cognitive processes (*1*–*5*). Although emotions have been subject to intensive research efforts in neuroscience, psychology, and philosophy (*1*, *4*, *6*, *7*), we still lack a mechanistic understanding of how emotions arise in neuronal circuits (*3*, *4*, *8*, *9*). The functional dissection and causal interrogation of the neuronal circuit underpinnings of emotion rely on research in animal models. However, whether animals experience emotions similar to those of humans and how to best define or investigate emotions are still matters of controversy (*3*, *5*, *8*–*10*). Although most researchers would agree that externally observable behaviors indicate that forms of evolutionarily conserved "emotion states" exist across species (*1*, *3*, *5*), investigating emotions using modern neuroscientific tools has been hindered by a lack of rapid and precise readouts of emotion states in model organisms, such as mice (*3*).

In humans and monkeys, facial expressions have been proposed to provide universal indicators of emotions (*11*, *12*). Rodents may also use their orofacial musculature to signal longer-lasting internal states (*13*–*15*). We asked whether mice reacted to emotionally salient stimuli with stereotyped facial expressions and whether these reflect core emotion properties, such as intensity, valence, flexibility, and persistence (*3*, *4*). We then investigated neuronal correlates of inferred emotion states in the insular cortex, an area of the brain that in humans has been implicated in subjective affective experiences (*16*, *17*).

To study facial expressions, we exposed mice to a diverse set of sensory stimuli that can be assumed to trigger changes in emotion state. In addition to these triggers, we also monitored spontaneous behavioral expressions of emotion states, such as the exhibition of established fear behaviors. These "emotion events" of different types therefore included painful tail shocks, sweet sucrose, bitter quinine, and lithium chloride injections, which induce visceral malaise (*14*, *18*), as well as freezing and escape behaviors (see methods). We video monitored the faces of head-fixed mice (Fig. 1A and fig. S1, A and B). Mice reacted to each emotion event with a noticeable facial movement visible to naïve human observers (Fig. 1B, fig. S2A, and movie S1). However, the valence or type of the underlying emotion event was not intuitively recognizable (fig. S2, B and C) and required extensive experience (Fig. 1B).

To achieve objective and temporally precise classification of facial expressions we used machine vision. We chose "histogram of oriented gradients" (HOG) (*19*) descriptors to represent the statistics of local image features in a standardized way and provide one numerical vector for each video frame (see materials and methods for advantages of the HOG method). This allowed us to compare facial expressions of mice reacting to emotion events quantitatively through comparison of their corresponding HOG descriptors.

We first assessed the facial expressions resulting from each type of emotion event separately by comparing all video frames collected in the vicinity (before and after) of three repetitions of the same event in individual mice. Pairwise correlations of all frames in these clips rendered two discrete clusters of highly similar facial expressions: One cluster belonged to the pre-event epochs, and the second cluster belonged to the epochs during or immediately after the event (Fig. 1, C and D). No distinct clusters and thus no consistent change in facial expressions were detected when frames were selected in the same temporal sequence but from mice recorded during a baseline period (see "neutral" condition, Fig. 1D, top).

Next, we examined whether facial expressions were specific to the underlying emotion and visualized frames from all of the emotion events using t-distributed stochastic neighbor embedding (t-SNE). We observed a clean separation into discrete frame clusters for each event type within individual mice, suggesting emotion-specific facial expressions (Fig. 1E and fig. S3).

To test whether the underlying emotion event in any given mouse could be predicted solely from its facial expressions, we trained a random forest classifier (see materials and methods). The decoder could predict each underlying emotion event across different mice reaching accuracies >90%. Performance dropped on average below 15% if the decoder was trained on temporally shuffled data (Fig. 1F, fig. S4, and table S1).

These results raised the question of whether the observed expressions may reflect separate basic emotion states, similar to emotion categories in humans (*7*, *10*). We collected the most characteristic video frames following each type of emotion event separately and averaged the corresponding HOG vectors into a single descriptor (Fig. 2A and materials and methods), which we termed "emotion prototype." We constructed prototypical HOG descriptors assuming the following event ≈ *emotion state* contingencies: quinine ≈ *disgust*, sucrose ≈ *pleasure*, tail shock ≈ *pain*, lithium chloride ≈ *malaise*, escape ≈ *active fear*, and freezing ≈ *passive fear*.

We first tested the sufficiency of the prototypes to capture the characteristics of the distinct facial expressions across individuals (Fig. 2, B and C, fig. S5, and table S1). We

[1]Circuits for Emotion Research Group, Max Planck Institute of Neurobiology, Am Klopferspitz 18, 82152 Martinsried, Germany. [2]Graduate School of Systemic Neurosciences, Ludwig-Maximilians University Munich, Germany. [3]International Max-Planck Research School for Molecular Life Sciences, Munich, Germany.
*Corresponding author. Email: ngogolla@neuro.mpg.de

measured the similarity of facial expressions to the emotion prototypes and, indeed, each single prototype was specific to only one emotion state, except for the active fear prototype, which resembled facial expressions evoked by bitter, pain, and escape and may thus capture features of diverse emotion states (Fig. 2C). Comparing each frame of any video sequence across time to an emotion prototype captured

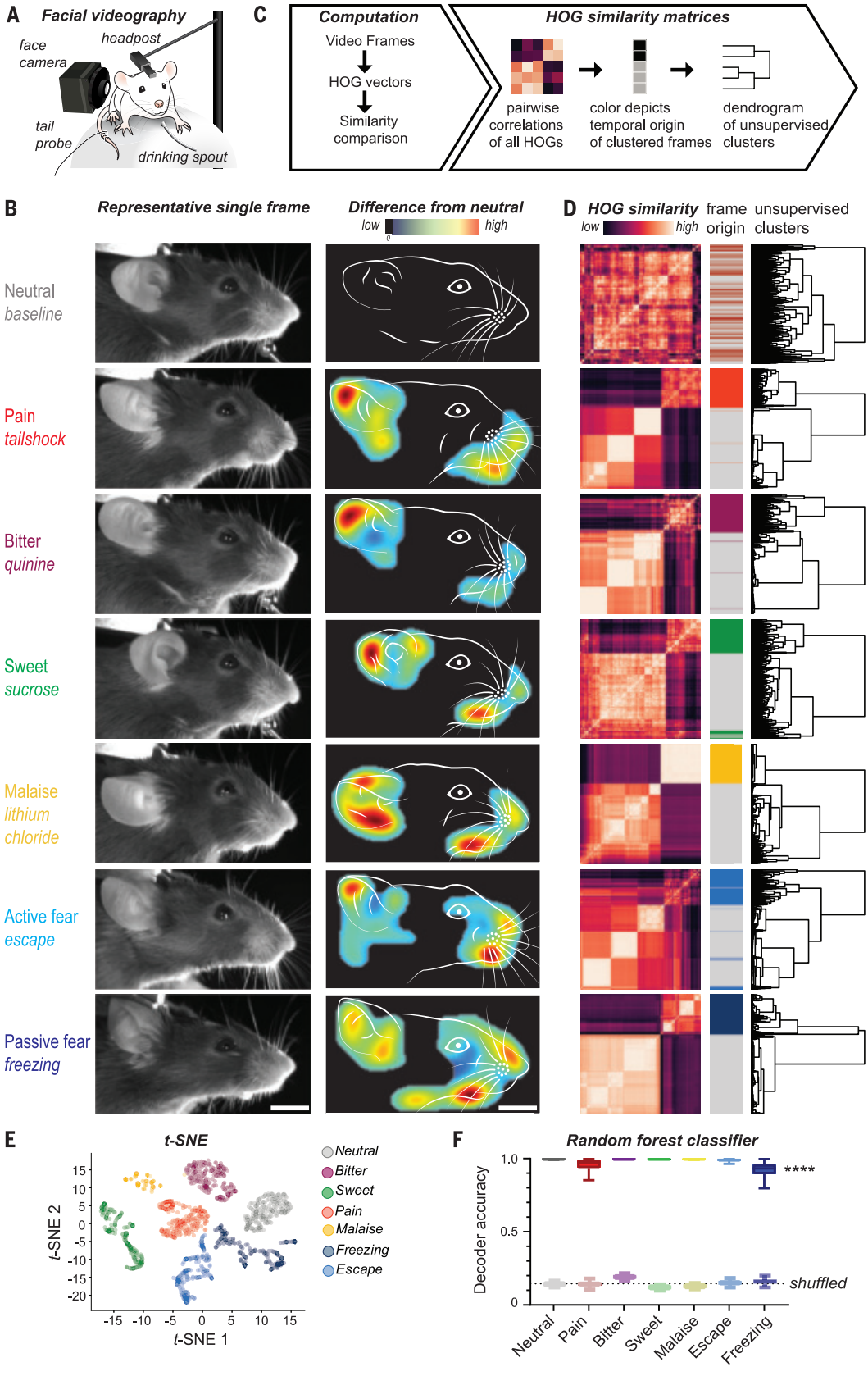

Fig. 1. Emotion-driven facial expressions in mice. (**A**) Facial videography setup. (**B**) (Left) Single representative video frames from individual mice captured during baseline (top) or upon different emotion events to illustrate characteristic changes. Images derived from $N = 2$ mice. Similar facial expressions were observed in all animals reported here. (Right) Line drawing of faces from the same frames. Heat-map overlays denote areas of largest difference compared to the neutral expression. Scale bar: 6 mm. (**C**) Computational strategy to compare facial expressions. (**D**) Similarity matrices containing pairwise similarity coefficients for all frames obtained in the vicinity of three events for each condition within one animal. To the right, post hoc temporal assignments for each frame are shown in color during the event and in gray before each event. Dendrograms represent hierarchical clustering. (**E**) t-SNE visualization of frames obtained from all emotion events in an individual mouse. (**F**) A random forest classifier reliably predicts and distinguishes between all event-related facial expressions. The classifier reaches high decoding accuracies (neutral, bitter, and sweet: 99 ± 1%; pain: 96 ± 5%; freezing: 92 ± 7%; malaise and escape: 99 ± 2%). Decoder performance dropped if the decoder was trained on temporally shuffled data (neutral: 14 ± 1%; bitter: 19 ± 1%; sweet 12 ± 1%; malaise: 13 ± 1%; pain: 14 ± 2%; freezing: 16 ± 2%; escape: 15 ± 1%). Mann-Whitney test revealed a significant (****$P < 0.0001$) difference in classifier's prediction performance between the real and shuffled data for each single facial expression.

the dynamics of facial expressions at high resolution (fig. S6 and movie S2).

Although our results so far suggested that facial expressions may relate to internal emotion states, an alternative explanation could be that facial expressions are stereotyped, reflex-like reactions. We therefore aimed to test whether facial expressions reflected fundamental features of emotions (*3*, *4*), such as intensity, valence, generalization, flexibility, and persistence (Fig. 2, D to G).

Scalability refers to the observation that emotions vary by intensity (*3*, *5*). We thus varied the stimulus strength and quantified the similarity of the resulting facial expressions to our prototypes. The similarity to prototypical descriptors increased significantly and in a graded manner when the strength of tail shocks, or the concentration of sucrose or quinine solutions, increased (Fig. 2D and table S1), although the sequence of stimulation did

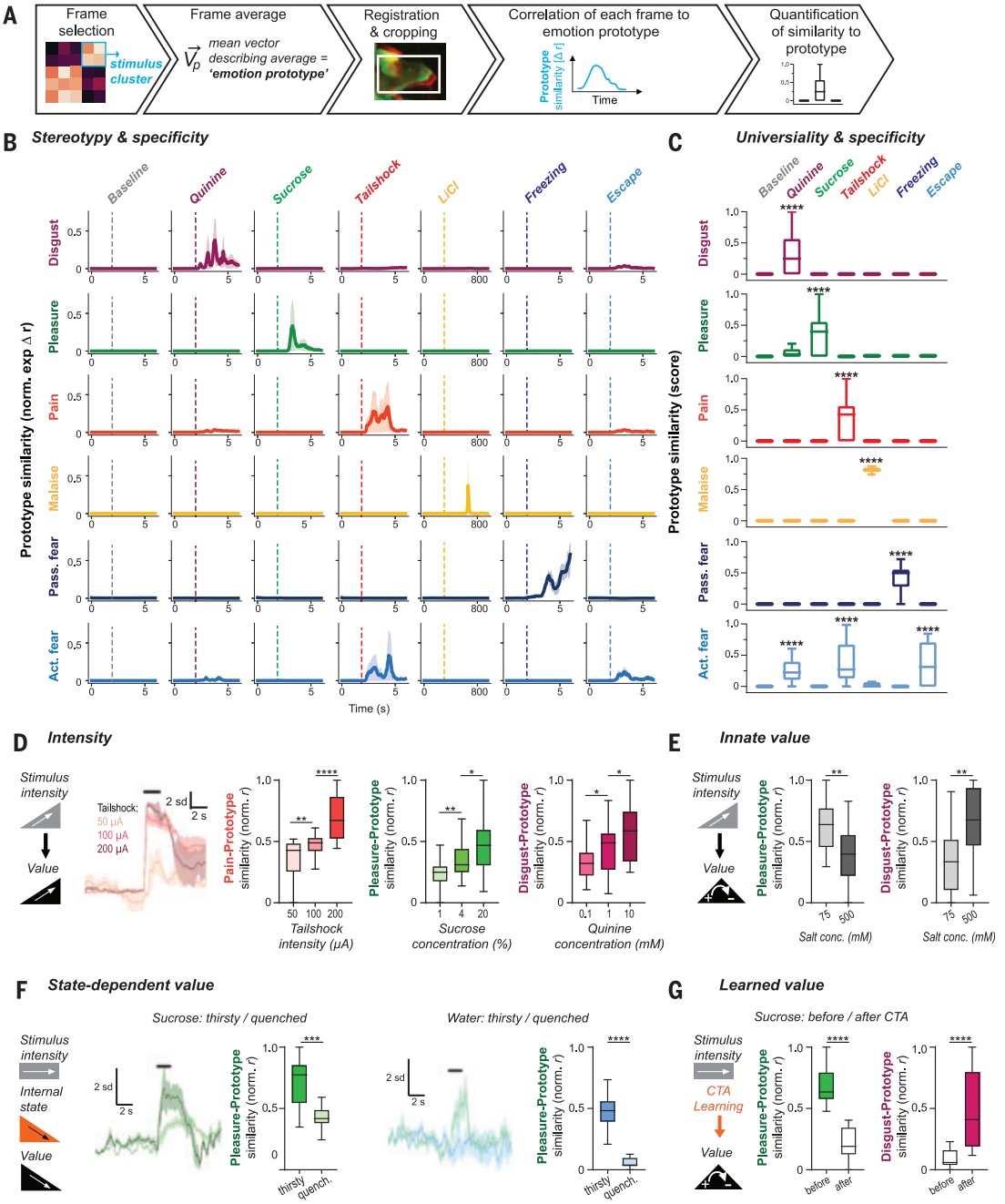

Fig. 2. Facial expressions reflect core features of emotion states. (**A**) Schematic of emotion prototype creation. (**B**) Similarities of facial expressions for each event type (three occurrences each) in one exemplary mouse to each emotion prototype. (**C**) Prototypes are valid and specific universally across mice. To calculate a similarity score, data from N = 9 mice and n = 27 trials per stimulus were averaged, then min-max normalized; the highest similarity value was set to 1, and the maximal baseline value and negative values were set to 0. Facial expressions were highly experience specific [ordinary one-way analysis of variance, ****P < 0.0001, Dunnett's post hoc comparisons revealed significant differences (****P < 0.0001) to the neutral condition only for the event matching the prototype, except for escape which carried components of pain and disgust.] (**D**) Sensory stimuli of increasing strength elicit more intense facial expressions. (Left) Example traces of face similarities to the pain prototype in one example mouse experiencing increasingly strong tail shocks. To the right, box-and-whisker plots quantifying the facial expression similarity to the pain prototype upon increasing tail shock intensities (N = 9 mice, n = 27 trials per intensity); the pleasure similarity upon drinking solutions of increasing sucrose content (N = 9 mice, n = 27 trials per concentration); and disgust similarity upon drinking solutions of increasing quinine content (N = 10 mice, n = 30 trials per concentration). (**E**) Drinking solutions of low salt content (75 mM) evoke pleasure-like facial expression (left) but little disgust-like facial expressions (right). The inverse pattern was observed upon drinking solutions with high salt content (500 mM). N = 5 mice, n = 15 trials per concentration. (**F**) Facial expressions reveal the changing affect upon experiencing sucrose or water in either thirsty or quenched states. N = 5 mice, n = 15 trials per state. (**G**) Facial expressions reveal associative aversion learning. Mice expressed highly pleasurable and low disgust facial expressions when drinking sucrose solutions before CTA. After CTA, mice exhibited disgusted facial expressions and low pleasure when drinking sucrose. N = 5 mice, n = 15 trials per timepoint. In all panels: *P ≤ 0.05, **P ≤ 0.01, ***P ≤ 0.001, ****P < 0.0001, two-tailed Mann-Whitney tests. Box-and-whisker plots in the style of Tukey containing trial averages. Line graphs are z-scored face similarities normalized to the 2 s preceding the stimulus, averaged across three trials in a single animal. Shaded areas are SEM.

not influence the facial expression intensity at the chosen intertrial intervals (fig. S7, A and B).

Another property of emotions is their valence—namely, they are experienced as good or bad in humans and trigger approach or retreat in animals (*3*, *5*, *14*, *18*). Salt is appetitive for rodents at low concentrations but aversive at high concentrations. Facial expressions reflected the innate valence of salt at different concentrations, because salt at low concentration elicited facial expressions of high similarity to our prototypical "pleasure" facial expression and weak similarity to our "disgust" prototype, whereas the opposite was observed for high salt concentrations (Fig. 2E and table S1). Facial expressions are thus decoupled from the underlying stimulus and generalize between different sensory experiences. Both sucrose and low-concentration salt solution elicited pleasure-like expressions, whereas quinine and high-concentration salt solution both evoked disgust.

Emotions reflect an integrated account of external and internal information (*3*, *9*) and are thus flexible. We next varied the internal state of the animal but kept the stimulus constant. When mice drank an identically concentrated sucrose solution or water in either thirsty or quenched states, both liquids elicited significantly stronger pleasure-like facial expressions when mice were thirsty than when they were quenched (Fig. 2F and table S1).

Emotions are thought to arise from predictions about how internal or external events may affect the well-being of the individual (or the well-being of closely related conspecifics) (*1*, *9*, *10*). These predictions can depend on the innate or learnt value of stimuli. We already saw how the innate value of salt depended on

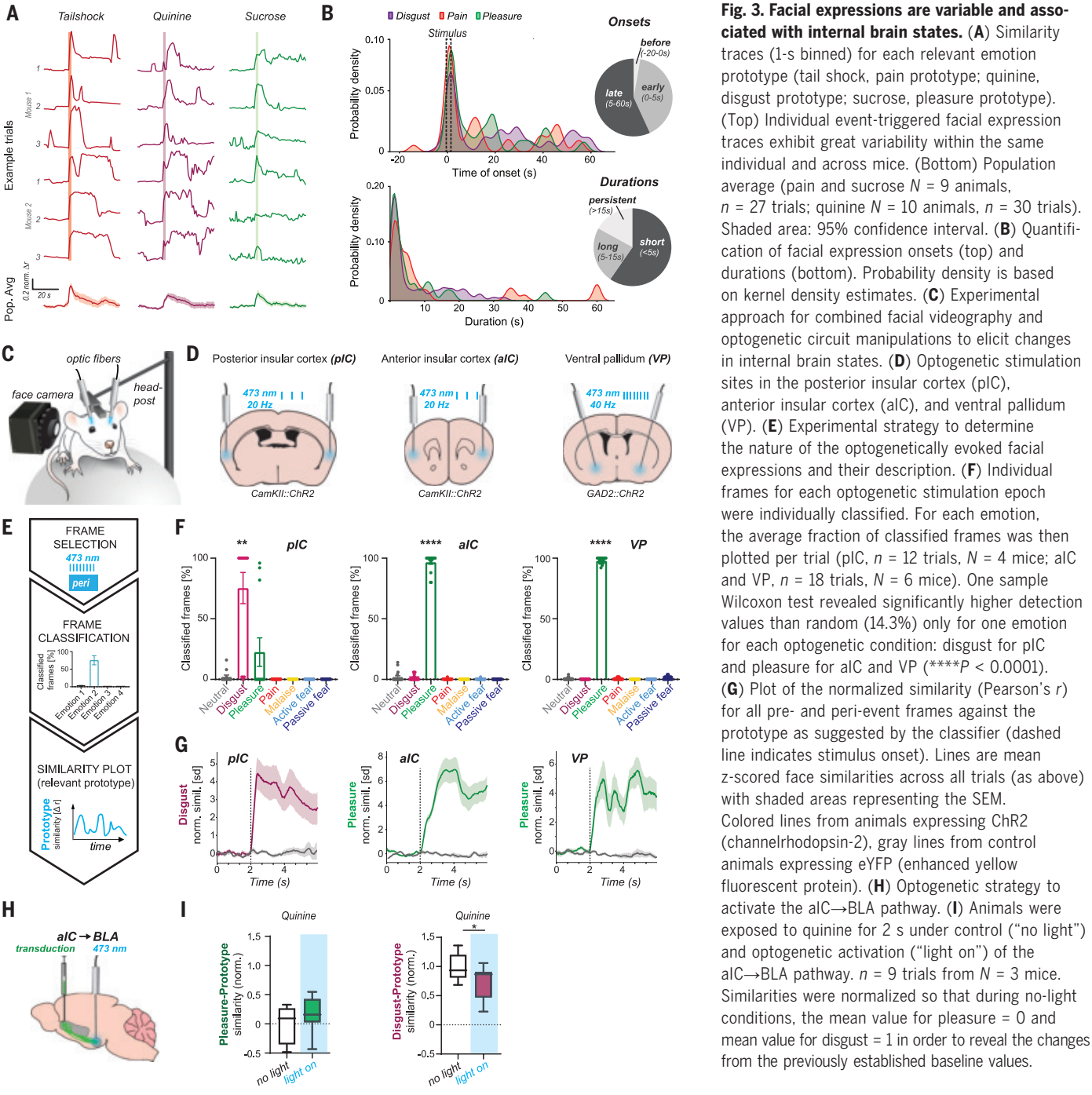

Fig. 3. Facial expressions are variable and associated with internal brain states. (**A**) Similarity traces (1-s binned) for each relevant emotion prototype (tail shock, pain prototype; quinine, disgust prototype; sucrose, pleasure prototype). (Top) Individual event-triggered facial expression traces exhibit great variability within the same individual and across mice. (Bottom) Population average (pain and sucrose N = 9 animals, n = 27 trials; quinine N = 10 animals, n = 30 trials). Shaded area: 95% confidence interval. (**B**) Quantification of facial expression onsets (top) and durations (bottom). Probability density is based on kernel density estimates. (**C**) Experimental approach for combined facial videography and optogenetic circuit manipulations to elicit changes in internal brain states. (**D**) Optogenetic stimulation sites in the posterior insular cortex (pIC), anterior insular cortex (aIC), and ventral pallidum (VP). (**E**) Experimental strategy to determine the nature of the optogenetically evoked facial expressions and their description. (**F**) Individual frames for each optogenetic stimulation epoch were individually classified. For each emotion, the average fraction of classified frames was then plotted per trial (pIC, n = 12 trials, N = 4 mice; aIC and VP, n = 18 trials, N = 6 mice). One sample Wilcoxon test revealed significantly higher detection values than random (14.3%) only for one emotion for each optogenetic condition: disgust for pIC and pleasure for aIC and VP (****P < 0.0001). (**G**) Plot of the normalized similarity (Pearson's r) for all pre- and peri-event frames against the prototype as suggested by the classifier (dashed line indicates stimulus onset). Lines are mean z-scored face similarities across all trials (as above) with shaded areas representing the SEM. Colored lines from animals expressing ChR2 (channelrhodopsin-2), gray lines from control animals expressing eYFP (enhanced yellow fluorescent protein). (**H**) Optogenetic strategy to activate the aIC→BLA pathway. (**I**) Animals were exposed to quinine for 2 s under control ("no light") and optogenetic activation ("light on") of the aIC→BLA pathway. n = 9 trials from N = 3 mice. Similarities were normalized so that during no-light conditions, the mean value for pleasure = 0 and mean value for disgust = 1 in order to reveal the changes from the previously established baseline values.

its concentration. Would learning affect facial expressions in a similar way? We exposed mice to sucrose solution and then injected them with malaise-inducing lithium chloride to induce conditioned taste aversion (CTA). Sucrose before CTA learning elicited pleasure but not disgust. After CTA learning, mice displayed disgusted facial expressions in response to sucrose and thus their expressions reflected the learnt change in subjective value of sucrose (Fig. 2G and table S1).

Emotions are thought to reflect complex internal brain states. Because we cannot control all emotion-relevant information streams, one would hypothesize that even under identical stimulus conditions, the triggered emotion state should vary. We therefore analyzed the variability of stimulus-triggered facial expressions. Within the same mouse but also across different mice, repeating the same stimulus elicited facial expressions that varied

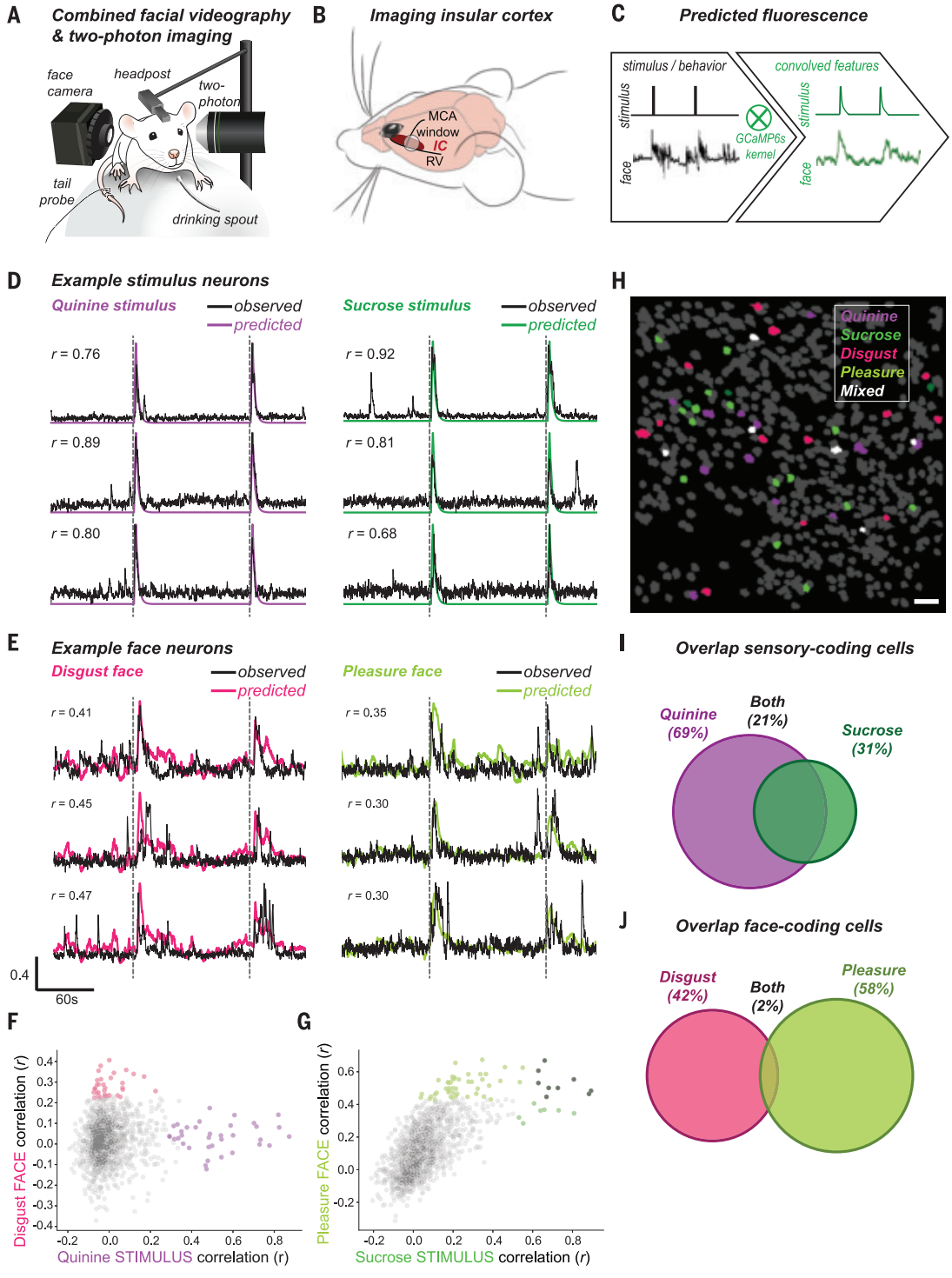

Fig. 4. Neuronal correlates of emotion state in the posterior insular cortex. (**A**) Illustration of combined facial videography with awake two-photon calcium imaging. (**B**) Schematic of the chronic window implant above the posterior insular cortex (IC, red) with respect to major blood vessels: medial cerebral artery (MCA) and rhinal vein (RV). (**C**) Schematic of neuronal activity prediction through stimulus and face convolution with GCaMP6s kernel. (**D** and **E**) Representative normalized fluorescence traces (black) overlaid with predicted stimulus or facial expression traces (colored). R values are Pearson's *r* for the correlation between normalized fluorescence and the overlaid convolved trace. (**F**) Scatter plot containing 1198 neurons from two animals experiencing quinine, plotted on the basis of their correlation to the convolved stimulus trace (quinine) and convolved face similarity trace (disgust prototype) for three stimulus presentations. A subset of neurons correlated strongly to the disgust similarity trace is labeled pink. A subset of neurons correlated strongly to the quinine stimulus trace is colored purple (for thresholds, see materials and methods). (**G**) Same as (F), but with sucrose stimulus. Neurons most strongly correlated to the pleasurable facial expression are labeled light green, neurons most strongly correlated to sucrose stimulus are in dark green, and the subset of neurons highly correlated to both are colored black (for thresholds, see materials and methods). (**H**) An example field of view from one animal with labeled regions of interest (ROIs) (gray circular shapes). Neurons, as identified and labeled in (F) and (G), are overlaid with the appropriate color. White ROIs indicate neurons with mixed coding properties (mostly multisensory neurons). (**I** and **J**) Venn diagrams representing the overlap in coding properties between sensory-coding cells (I) and face-coding cells (J). Scale bar: 100 μm.

in intensity, onset, and duration (Fig. 3, A and B). Facial expressions could wane and spontaneously reappear, possibly reflecting dynamic fluctuations in the underlying emotion state (Fig. 3A). Although the great majority of stimulus presentations resulted in immediate facial expressions (~90% of stimuli evoked facial expressions within 5s of stimulus onset), a considerable number of overall facial expressions occurred late after the stimulus (>5 s after stimulus start). Similarly, the duration of facial expressions was highly variable. Most facial expressions triggered by 2-s-long sensory stimuli lasted for less than 5 s (~60%); however, a substantial fraction of facial expressions lasted for relatively long periods (5- to 15-s duration, ~23%), or even persisted for more than 15 s (~17%) (Fig. 3B).

Direct brain stimulations can evoke specific emotions (*20*, *21*). We used optogenetics to test whether manipulating activity in emotion-relevant neuronal circuits could drive facial expressions (Fig. 3, C and D). We activated subregions and specific projections of the insular cortex (IC) that have been shown in humans and animals to evoke emotional sensations and behaviors (*20*, *22*–*25*). Furthermore, we manipulated the γ-aminobutyric acid–releasing neurons in the ventral pallidum (VP) that process rewarding properties of pleasant stimuli (*26*) (Fig. 3D). Each region-specific optogenetic manipulation evoked strong facial expressions (fig. S8 and movie S3). To analyze whether the evoked facial expressions would fall into our previously created emotion-state categories, we used the same random forest classifier as in Fig. 1F and categorized all frames during the optogenetic stimulations (Fig. 3, E and F). For each of these three manipulations, the classifier identified one specific emotion to be displayed—namely, pleasure—for the anterior IC and VP, but disgust for the posterior IC stimulations (Fig. 3F and table S1). When we compared the optogenetically evoked facial expressions to our emotion prototypes, we found a similar temporal build-up and persistence of the facial expressions to those triggered externally (Fig. 3G and movie S3). Projections from the insular cortex to the amygdala can influence the emotional value of tastants (*25*). Indeed, in agreement with this earlier report, the activation of the anterior IC→basolateral amygdala (aIC→BLA) pathway during the exposure to quinine attenuated the expression of disgust (Fig. 3, H and I).

Our data so far suggest that facial expressions are sensitive reflections of internal emotion states, which correspond to brain states. Therefore, we assumed that facial expressions should have neuronal correlates in emotion-relevant brain regions. The insular cortex is a critical brain region for emotional experience and behavior (*16*, *17*, *20*–*24*). We combined facial videography with two-photon calcium imaging in the posterior IC (pIC) to search for neuronal correlates of facial expressions (Fig. 4, A and B, and fig. S9). We identified single neurons that reliably encoded sensory stimuli in the pIC (Fig. 4, C to G), consistent with previous studies (*22*, *27*). We also identified neurons that exhibited strong correlations to the facial expression dynamics and only low correlations with the stimuli (Fig. 4, D to G). Indeed, these "face" neurons captured the characteristic persistence and spontaneity of the facial expression. Although a substantial fraction of stimulus neurons was multisensory, face-responsive neurons were highly segregated and exhibited almost no overlap.

In this study, we have identified facial expressions as reliable indicators of emotion states and their neuronal correlates in mice. But why do mice exhibit facial expressions? Charles Darwin suggested that facial expressions reveal affective processes across species, implying an evolutionarily conserved function of these behaviors (*1*). Though often discussed in the context of social communication, facial expressions may have evolved first as parts of emotional action programs, preparing for motor behaviors and adapting sensory acquisition to changes in the internal or external milieu (*2*, *28*, *29*). Indeed, head-fixed mice, which do not socially interact, consistently respond to emotionally salient events with stereotyped facial expressions. Although the value of facial expressions for uncovering emotional processes in humans remains controversial (*30*), this may be partially due to the volitional control that humans exert over emotions and their expression. It would therefore be interesting to examine how facial expressions are modified by the presence of conspecifics in mice.

Direct observation of facial expressions is possible in quasi–real time (fig. S10) and allows for the mechanistic investigation of the neural underpinnings of emotions in mice. Correlation of emotional facial expressions with neuronal activity recordings and closed-loop manipulations are promising approaches to search for and test the causal role of the neuronal substrates of basic emotional building blocks, such as intensity, valence, and persistence.

Our data suggest that facial expressions can be classified into different basic categories. An important question for future studies may be to what degree emotion states are dimensional or categorical states at the level of not only behavioral expressions but also the underlying brain circuitries. The relatively simple implementation of HOG feature descriptors may become a useful addition to studying emotional facial or postural expressions in other laboratory animals, such as rats, shrews, lemurs, and monkeys. It may also help in identifying unknown, species-specific emotion states and assist in moving toward a more universal and evolutionarily based definition and understanding of emotions and their neural underpinnings across species.

REFERENCES AND NOTES

1. C. Darwin, *The Expression of the Emotions in Man and Animals* (London, Murray, 1872).
2. A. Damasio, G. B. Carvalho, *Nat. Rev. Neurosci.* **14**, 143–152 (2013).
3. D. J. Anderson, R. Adolphs, *Cell* **157**, 187–200 (2014).
4. Ralph Adolphs & David J. Anderson, *The Neuroscience of Emotion: A New Synthesis* (Princeton Univ. Press, 2018).
5. R. Adolphs, *Soc. Cogn. Affect. Neurosci.* **12**, 24–31 (2017).
6. J. A. Russell, *J. Pers. Soc. Psychol.* **39**, 1161–1178 (1980).
7. P. Ekman, *Cogn. Emotion* **6**, 169–200 (1992).
8. J. LeDoux, *Neuron* **73**, 653–676 (2012).
9. L. F. Barrett, A. B. Satpute, *Neurosci. Lett.* **693**, 9–18 (2019).
10. J. Panksepp, *Neurosci. Biobehav. Rev.* **35**, 1791–1804 (2011).
11. P. Ekman, *Philos. Trans. R. Soc. Lond. B Biol. Sci.* **335**, 63–69 (1992).
12. L. A. Parr, B. M. Waller, J. Fugate, *Curr. Opin. Neurobiol.* **15**, 716–720 (2005).
13. D. J. Langford *et al.*, *Nat. Methods* **7**, 447–449 (2010).
14. A. Faure, J. M. Richard, K. C. Berridge, *PLOS ONE* **5**, e11223 (2010).
15. K. Finlayson, J. F. Lampe, S. Hintze, H. Würbel, L. Melotti, *PLOS ONE* **11**, e0166446 (2016).
16. J. Chikazoe, D. H. Lee, N. Kriegeskorte, A. K. Anderson, *Nat. Neurosci.* **17**, 1114–1122 (2014).
17. N. Gogolla, *Curr. Biol.* **27**, R580–R586 (2017).
18. P. Tovote, J. P. Fadok, A. Lüthi, *Nat. Rev. Neurosci.* **16**, 317–331 (2015).
19. N. Dalal, B. Triggs, in *2005 IEEE Computer Society Conference on Computer Vision and Pattern Recognition, CVPR 2005* (2005), vol. 1, pp. 886–893.
20. F. Caruana, A. Jezzini, B. Sbriscia-Fioretti, G. Rizzolatti, V. Gallese, *Curr. Biol.* **21**, 195–199 (2011).
21. C. Fausto, *Emot. Rev.* **11**, 27–38 (2019).
22. D. A. Gehrlach *et al.*, *Nat. Neurosci.* **22**, 1424–1437 (2019).
23. J. Yih, D. E. Beam, K. C. R. Fox, J. Parvizi, *Soc. Cogn. Affect. Neurosci.* **14**, 339–351 (2019).
24. Y. Peng *et al.*, *Nature* **527**, 512–515 (2015).
25. L. Wang *et al.*, *Nature* **558**, 127–131 (2018).
26. L. Faget *et al.*, *Nat. Commun.* **9**, 849 (2018).
27. X. Chen, M. Gabitto, Y. Peng, N. J. P. Ryba, C. S. Zuker, *Science* **333**, 1262–1266 (2011).
28. C. Montag, J. Panksepp, *Motiv. Emot.* **40**, 760–766 (2016).
29. J. M. Susskind *et al.*, *Nat. Neurosci.* **11**, 843–850 (2008).
30. L. F. Barrett, R. Adolphs, S. Marsella, A. M. Martinez, S. D. Pollak, *Psychol. Sci. Public Interest* **20**, 1–68 (2019).
31. N. Dolensek, N. Gogolla, GogollaLab/MouseFacialExpressionAnalysis, Version 1.0, Zenodo (2020).

ACKNOWLEDGMENTS

We thank members of the Gogolla laboratory, K. Branson, P. Dayan, W. Denk, M. Hübener, E. Mace, D. Mearns, R. Portugues, and A. Sirota for discussions; J. Kuhl (somedonkey.com) for illustrations; and T. Black, F. Lyonnaz, A. Podgornik, and C. Weiand for technical assistance. **Funding:** Supported by the Max-Planck Society, the European Research Council (ERC) under the European Union's Horizon 2020 research and innovation program (ERC-2017-STG, grant agreement no. 758448 to N.G.), the Deutsche Forschungsgemeinschaft (SPP1665), the German Israeli Foundation (Grant I-1301-418.13/2015), and the ANR-DFG project "SAFENET" (ANR-17-CE37-0021). **Author contributions:** N.G. and N.D. conceived the project and designed the experiments. N.D. performed all experiments and developed and performed all facial expression analysis. D.A.G. and A.S.K. helped with the optogenetic experiments. N.G. wrote the manuscript with assistance from N.D. **Competing interests:** The authors declare no competing financial interests. **Data and materials availability:** All data are available in the manuscript or the supplementary materials. The facial expression analysis code is available on Github (https://github.com/GogollaLab) and at Zenodo (*31*). Viruses were packaged at the University of North Carolina (UNC) Vector Core and made available under a material transfer agreement.

SUPPLEMENTARY MATERIALS

science.sciencemag.org/content/368/6486/89/suppl/DC1
Materials and Methods
Figs. S1 to S10
Table S1
Movies S1 to S3
References (*32*–*41*)

22 October 2019; accepted 11 February 2020
10.1126/science.aaz9468

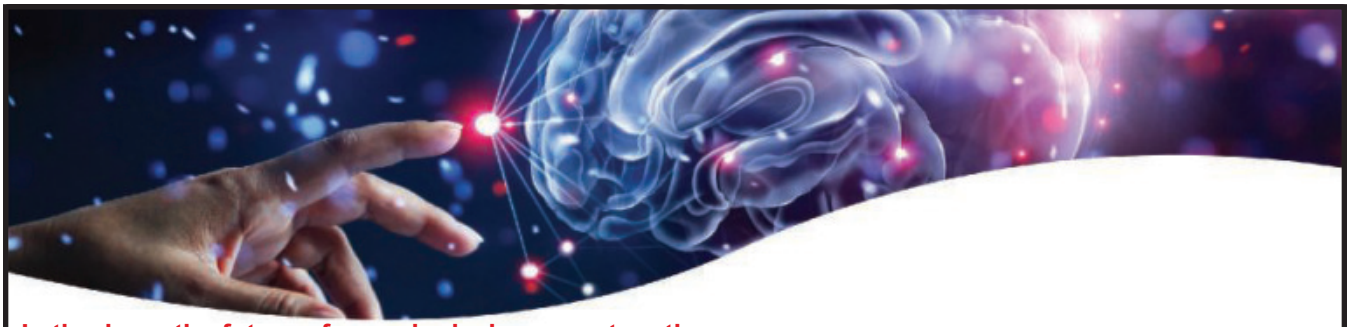

Let's shape the future of neurological surgery together.

Faculty Positions in Neuroscience

Rutgers University Department of Neurosurgery at Robert Wood Johnson and New Jersey Medical Schools and Rutgers Brain Health Institute seek to recruit outstanding federally-funded faculty who will help execute our mission of building a world-class translational neuroscience research program in one of the leading academic medical centers in the United States. Openings will be filled at the rank of Assistant, Associate, or Full Professor. The recent merging of the two departments of Neurosurgery at Robert Wood Johnson and New Jersey Medical Schools, under the leadership of newly recruited Chair, Dr. Anil Nanda, has led to the formation of a department composed of basic and translational research scientists, clinician scientists, and clinicians working collaboratively on high-impact basic and clinical research. The scientific focus of the Department is on bench-to-bedside research to understand mechanisms of disease development, progression, and prevention in the areas of epilepsy, traumatic brain injury, stroke, spinal cord injury, and cancer; and to translate research findings into novel therapeutic approaches with a particular focus on neuromodulation, metabolism, and epigenetics. In addition, we apply neuroimaging techniques in understanding disease processes and monitoring their response to therapy. These research topics are also part of the four focus areas at the Rutgers Brain Health Institute, which is the home for the overall Rutgers neuroscience initiative, and is a growing interdisciplinary institute consisting of more than 250 principal investigators with neuroscience laboratories across various campuses of Rutgers University and Rutgers federally-funded research program in epilepsy, traumatic brain injury, stroke, spinal cord injury, brain cancer, or neuroimaging.

Applicants must have a PhD, MD, or equivalent doctoral degree, with demonstrated ability to lead an independent, federally-funded research program in epilepsy, traumatic brain injury, stroke, spinal cord injury, or brain cancer. We offer substantial resources and outstanding core facilities to support these positions. Candidates applying for a position at the Assistant Professor level are expected to have K99/R00 grants or equivalent and develop a rigorous extramurally funded research program. Candidates at the Associate and Full Professor level are expected to have an established federal grant portfolio that can be transferred to Rutgers. Rutgers values a culturally diverse faculty; we strongly encourage applications from female and minority candidates. Applications for these positions will be screened immediately and the search will continue to be considered until September 2020.

Direct Contact Information: Applicants should submit a 1-page letter of interest, current Curriculum Vitae including a complete list of publications, and a 3-page research statement.

Detlev Boison, Ph.D., Professor, Vice Chair of Research and Training, Department of Neurosurgery detlev.boison@rutgers.edu

Rutgers, The State University of New Jersey, is an Affirmative Action/Equal Opportunity Employer, M/F/D/V.

RUTGERS
RW.JBarnabas HEALTH

Science Careers
FROM THE JOURNAL SCIENCE AAAS

Confused about your next career move?

Download Free Career Advice Booklets!

ScienceCareers.org/booklets

By **Ye Zhou**

Making allowances for COVID-19

On 18 March, I woke up and checked my email. A decision letter from a journal editor caught my eye. "We are not able at this stage to accept your manuscript for publication. I invite you to address the reviewer comments and make the necessary changes and improvements in a major revision of your manuscript," it read. All three reviewers requested additional experiments, and the editor gave us 3 weeks to submit a revised manuscript. Under normal circumstances, such a decision would be disappointing but the experiments doable. Not in these days of COVID-19—and certainly not by the deadline we had been given.

I am a research group leader at a university in Shenzhen, China. I last saw my group members in January, when we took off for 2 weeks of vacation for the Chinese New Year. We planned to return to the university in early February. However, the unexpected spread of the new coronavirus disrupted our lives and work arrangements. Our university and lab are closed, and we have no idea when they will reopen.

During the holiday, I went to my hometown—a city roughly 600 kilometers from Wuhan, where the virus first emerged. As more and more cities were blocked to travel I flew to my current home in Hong Kong, a short commute from the campus in Shenzhen. The Hong Kong authorities then issued quarantine orders to all people entering the city from mainland China, making it impossible for me to travel to Shenzhen. My students and postdocs have faced similar problems, with some of them unable to leave their hometowns. Others are in Shenzhen, but they are not allowed to enter our lab.

"Should we rethink our standard peer-review procedures?"

The outbreak has led us to reassess what we can reasonably accomplish. I'd already planned to spend time this year editing two books. Now, I have time to write my own chapters and track the progress of other contributors. Before COVID-19 disrupted our lives, my students and postdocs were busy with lab work. With their activities now restricted to home, I've asked them to organize their experimental data, read some literature in depth, and write a review article that we're collaboratively piecing together through video calls, messages, and emails. We've also been working to submit research manuscripts.

We can make good use of the time. But the decision letter I received on 18 March was a reminder of what we can't do—and the consequences for our progress as researchers. Some of the comments on our manuscript, which we submitted in early February, are reasonable and can help us improve it. However, several ask us to add more data that are not important for the main conclusion. I feel the work is publishable without the additional experiments.

I can ask the editor for an extension. But I'm also left wondering something: As labs shut down in many countries for an indefinite period of time, should editors be more accommodating when authors can't access their lab space? The first author of our manuscript is a postdoc who would benefit from the publication of his work. Is it fair to ask him to wait for months to resubmit and risk the chance that he'll be scooped by other researchers?

I also see the other side of the coin. I serve as an associate editor for several scientific journals, and I've received more requests for deadline extensions recently. I have also been considering how to balance the reviewer comments with the difficulties authors face during the pandemic. For each manuscript I'm shepherding through the peer-review process, I find myself asking a few questions: Are additional experiments truly necessary? Can I ask reviewers to reconsider their requests for more data if the authors have already presented a compelling body of work?

I don't have all of the answers. But I think these are important questions for the scientific community to grapple with during the weeks and months to come. As we deal with massive disruptions to daily life because of a pandemic, should we rethink our standard peer-review procedures? Can we accept that not every additional experiment is needed for a manuscript to be publishable? ■

Ye Zhou is a professor at Shenzhen University in China. Do you have a career story to share? Send it to SciCareerEditor@aaas.org.

ILLUSTRATION: ROBERT NEUBECKER

WHAT DO YOU AND THOMAS EDISON HAVE IN COMMON?

AAAS.

By investing in AAAS you join Thomas Edison and the many distinguished individuals whose vision led to the creation of AAAS and our world-renowned journal, *Science*, more than 150 years ago.

Like Edison, you can create a legacy that will last well into the future through planned giving to AAAS. By making AAAS a beneficiary of your will, trust, retirement plan, or life insurance policy, you make a strong investment in our ability to advance science in the service of society for years to come.

To discuss your legacy planning, contact Juli Staiano, Chief Philanthropy Officer, at (202) 326-6636, or jstaiano@aaas.org, or visit **aaas.org/1848society** for more information.

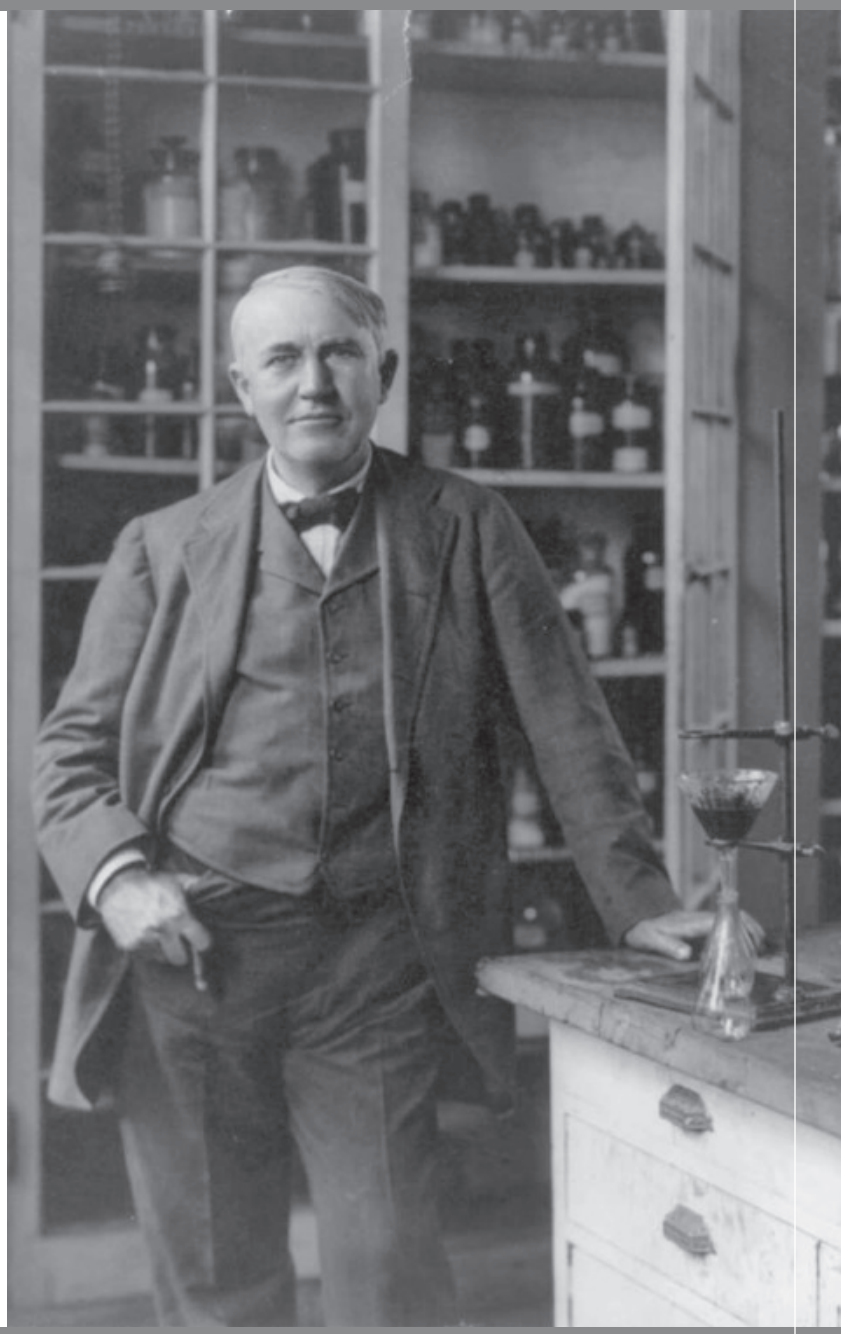

1848 SOCIETY AAAS

"I feel great knowing that I will leave behind a legacy that will be channeled through the AAAS. It also means a lot to me to be able to honor my late parents, too."

–PETER ECKEL
Member, 1848 Society and AAAS Member since 1988

Custom Lentivirus Generation

One-Stop-CRO for CAR-T Research

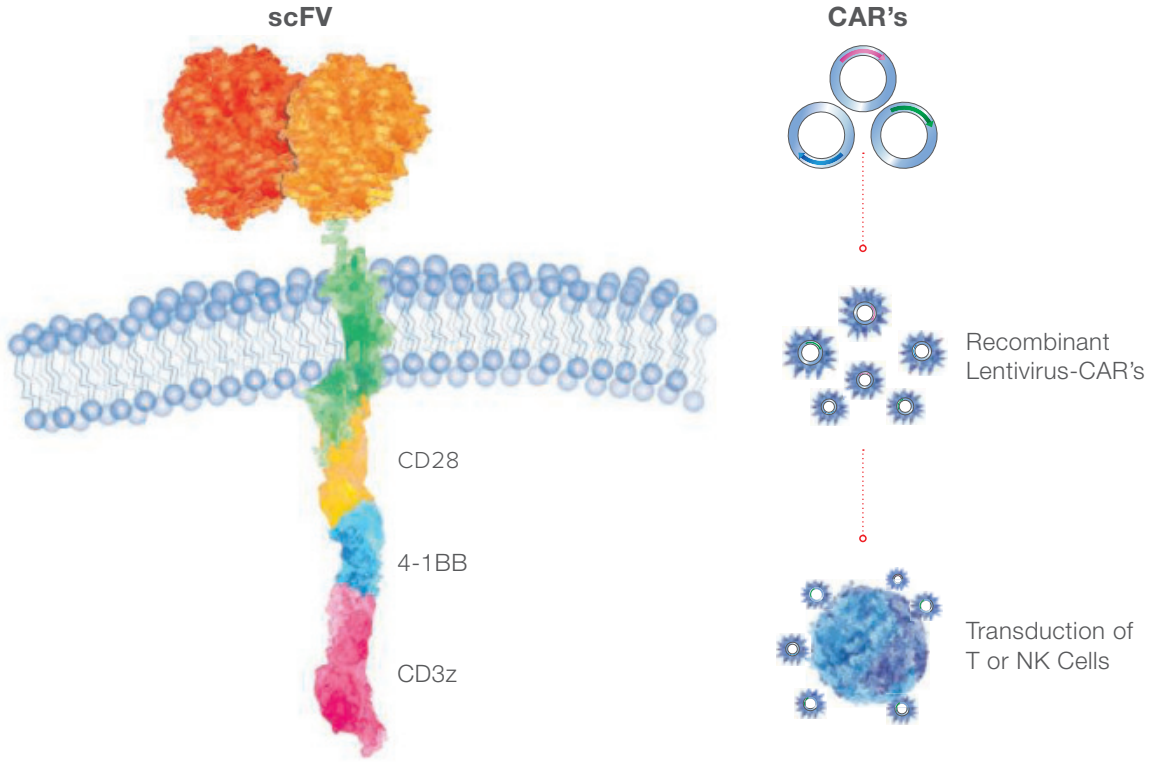

ProMab Biotechnologies commits to stay at the forefront of CAR-T technologies by providing an all-inclusive pre-clinical research program for CAR-T development. Our CAR-T platform utilizes lentivirus as it has become widely used as a vector to deliver specific genes of interest and to compliment gene and cell therapy applications.

Our standardized and highly optimized platform enables ProMab to produce recombinant lentivirus with many benefits:

- Custom vector engineering from gene synthesis to plasmid production
- High titer: 10^8 to 10^10 particles/ml
- Fast turnaround time: 2 to 3 weeks
- Variety of analytical options
- Ready to use CAR-T lentivirus
- Downstream to CAR-T or stable cell line development services

All products are for research only

Discover more | www.promab.com

ProMab Biotechnologies, Inc.
2600 Hilltop Dr, Building B, Richmond, CA 94806
1.866.339.0871 | info@promab.com